FRIEDRICH-SCHILLER-
UNIVERSITÄT
JENA

Approaching $\mathcal{N} = 1$ Super-Yang-Mills theory with improved lattice actions

Dissertation

zur Erlangung des akademischen Grades
doctor rerum naturalium (Dr. rer. nat.)

vorgelegt dem Rat der
Physikalisch-Astronomischen Fakultät
der Friedrich-Schiller-Universität Jena

von M.Sc. Marc Julian Steinhauser
geboren am 18.10.1991 in Biberach (Riß)

Gutachter:

1. Prof. Dr. Andreas Wipf (Friedrich-Schiller-Universität Jena)
2. Prof. Dr. Gernot Münster (Westfälische Wilhelms-Universität Münster)
3. Prof. Dr. Anosh Joseph (Indian Institute of Science Education and Research Mohali)

Tag der Disputation: 19.02.2021

"*Supersymmetry was (and is) a beautiful mathematical idea. The problem with applying supersymmetry is that it is too good for this world.*"

Frank Wilczek, Nobel laureate in Physics 2004

Abstract

Investigations of the non-perturbative effects of $\mathcal{N} = 1$ Super-Yang-Mills (SYM) theory on the lattice are demanding. The lattice breaks translation invariance to a discrete subgroup and consequently also supersymmetry. With a fine-tuning of the Wilson fermions to a critical point, it can be achieved that supersymmetry (as well as chiral symmetry) are restored in the continuum limit. This thesis is intended to contribute to weaken the associated restrictions.

A significant fraction of the runtime is spent in the inversion of the huge Wilson Dirac matrix. By adopting a multigrid library to our needs, we could accelerate this task by a factor of 20. Further improvements were mainly motivated by the $\mathcal{N} = 1$ SYM theory itself. Unbroken supersymmetry in the continuum arranges the bound states in supermultiplets. When supersymmetry is broken, for example by the lattice discretization, then the mass-degeneracy ends. Based on this observation, we tried to modify the fermionic lattice action to minimize the mass difference of states within a supermultiplet and thus the supersymmetry breaking.

The first extension of the Wilson Dirac operator was a clover term. It is known from the Symanzik improvement program that a proper choice of the coefficient reduces the lattice discretization artifacts to the order $\mathcal{O}(a^2)$ in the lattice spacing. There are several possibilities to determine this coefficient and we compared them with a heuristic parameter scan. With the latter no distinct value could be determined.

As an alternative, we added a twisted mass term to the Wilson Dirac operator. When the difference of the untwisted mass parameter to its critical value corresponds to the value of the parity-breaking mass, then the two mesonic partners a-η' and a-f_0 approach at finite lattice spacing the same mass. After we observed this improvement of the supermultiplet in the numerical data, we also found an analytical proof. Additionally we investigated the eigenvalues of the free Dirac operator with twists in the mass term and the Wilson term. There we found an $\mathcal{O}(a)$ improvement when those two terms are orthogonal to each other.

With the 45°-mass-twisted Wilson Dirac operator, we performed simulations on a $16^3 \times 32$ lattice and analyzed all states of the Veneziano-Yankielowicz and Farrar-Gabadadze-Schwetz supermultiplet. Extrapolated to the critical point, mass-degenerated ground states are found and the first excited states have comparable masses.

Zusammenfassung

Simulationen der $\mathcal{N} = 1$ Super-Yang-Mills (SYM) Theorie auf dem Gitter zur Untersuchung von nicht-perturbativen Effekten ist herausfordernd. Das Gitter bricht die Translationsinvarianz in eine diskrete Untergruppe und dadurch wird auch die Supersymmetrie gebrochen. Durch ein Fine-Tuning der Wilson-Fermionen zum kritischen Punkt kann erreicht werden, dass die Supersymmetrie (und die chirale Symmetrie) im Kontinuumslimes wieder hergestellt werden. Diese Arbeit soll dazu beitragen, die damit verbundenen Einschränkungen zu mildern.

Ein erheblicher Anteil der Laufzeit wird durch die häufige Invertierung der riesigen Wilson-Dirac-Matrix verbraucht. Durch die Anpassung einer Multigrid-Bibliothek an unsere Bedürfnisse, konnten wir diese Berechnung um den Faktor 20 beschleunigen. Weitere Verbesserungen waren hauptsächlich von der $\mathcal{N} = 1$ SYM Theorie selbst motiviert. Bei ungebrochener Supersymmetrie im Kontinuum sind die gebundenen Zustände in Supermultipletts angeordnet. Wenn die Supersymmetrie gebrochen ist, bspw. durch die Gitterdiskretisierung, dann endet diese Massenentartung. Darauf aufbauend haben wir versucht die fermionische Gitterwirkung anzupassen, um die Massendifferenz innerhalb eines Supermultipletts und damit die Supersymmetriebrechung zu minimieren.

Die erste Erweiterung des Wilson-Dirac-Operators war ein Clover-Term. Vom Symanzik-Verbesserungsprogramm ist bekannt, dass eine geeignete Wahl des Koeffizienten zu einer Reduktion der Gitterartefakte auf die Ordnung $\mathcal{O}(a^2)$ im Gitterabstand führt. Es gibt mehrere Möglichkeiten diesen Koeffizienten zu bestimmen und wir haben diese mit einem heuristischen Parameterscan verglichen. Mit dem Letzteren konnten wir keinen aussagekräftigen Wert ermitteln.

Als Alternative haben wir einen Massenterm mit Twist zum Wilson-Dirac-Operator hinzugefügt. Wenn die Differenz des ungetwisteten Massenparameters zu seinem kritischen Wert dem Wert der paritätsbrechenden Masse entspricht, dann erreichen die beiden mesonischen Partner a-η' und a-f_0 bei einem endlichen Gitterabstand dieselbe Masse. Nachdem wir diese Verbesserung des Supermultipletts in den numerischen Daten beobachtet haben, sind wir auf einen analytischen Beweis gestoßen. Zusätzlich haben wir die Eigenwerte des freien Dirac-Operators mit Twists in dem Massenterm und dem Wilson-Term untersucht. Dort fanden wir eine $\mathcal{O}(a)$ Verbesserung, wenn die beiden Terme orthogonal zueinander gewählt werden.

Mit dem 45°-massengetwisteten Wilson-Dirac-Operator haben wir Simulationen auf einem $16^3 \times 32$ Gitter durchgeführt und alle Zustände des Veneziano-Yankielowicz-Supermultipletts und Farrar-Gabadadze-Schwetz-Supermultipletts untersucht. Durch Extrapolation zum kritischen Punkt haben wir eine Massenentartung der Grundzustände gefunden und auch die ersten angeregten Zustände haben vergleichbare Massen.

Contents

CHAPTER 1

Introduction

Our current knowledge of particle physics is based on experimental observations and theoretical investigations. On small scales, quantum theory is an extraordinary successful description of nature. The standard model (SM) of particle physics contains three types of interactions, namely the electromagnetic, the strong and the weak nuclear force. Symmetries are a fundamental ingredient in its formulation as $\mathrm{SU}(3) \times \mathrm{SU}(2) \times \mathrm{U}(1)$ gauge theory. Only the gravitational interaction described by general relativity has no satisfactory description compatible with the SM despite an intense search for a *theory of everything*. However, the gravitational force is much weaker than the other interactions in terrestrial experiments. Only the strong gravitation of a black hole or energies near the Planck scale $\mathcal{O}(10^{19}\mathrm{GeV})$ would require a theory of quantum gravity.

The SM very successfully describes all processes mediated by the electromagnetic, weak and strong forces at low energies $\lesssim 10\,\mathrm{TeV}$, but its 19 free parameters, which are only fixed by experimental measurements, motivate the search for a more fundamental theory. Furthermore, several open questions cannot be answered within the scope of the SM. The Higgs boson was discovered in 2012 by ATLAS and CMS collaborations [1, 2] with mass $m_\mathrm{H} = (125.18 \pm 0.16)\,\mathrm{GeV}$ [3]. Since the Higgs field is a scalar, this value seems unreasonably light. A one-loop calculation reveals a quadratic divergence and a mass of the order of the Planck mass would be more likely [4, 5]. The situation improves considerably in a supersymmetric theory, where every bosonic particle has a fermionic superpartner with the same quantum numbers (besides the spin) and vice versa. In a supersymmetric standard model a small Higgs mass is more natural to accommodate since at leading order bosonic and fermionic divergences cancel such that there is no quadratic divergence [6–8]. Another urgent problem of modern physics is the large amount of dark matter in our universe seen by cosmological observations [9, 10]. Most likely, dark matter cannot be detected through electroweak or strong interactions and only its gravitational force is observable. It outweighs the visible matter by a factor of six, making up about 27 percent of the total mass-energy of the universe [11]. Supersymmetric

models naturally provide a dark matter candidate, the so-called lightest supersymmetric particle (LSP) [12]. This particle is stable and cannot decay if R-parity is conserved [13]. Furthermore, supersymmetry brings the possibility of unifying the gauge theories of the SM at high energies in a so-called grand unified theory (GUT), which can be achieved by a modified running of the coupling constants [14]. Another fine-tuning problem arises in QCD, where the θ-term of the Lagrangian would break CP-invariance [15, 16]. No CP-violation is observed in experiments and therefore the value of θ should be unnaturally small or zero. With the help of supersymmetry, natural explanations for a vanishing θ angle exist [17, 18].

A straightforward extension of the SM is the minimal supersymmetric standard model (MSSM). This phenomenologically relevant model contains one supercharge [13]. Supersymmetry and the accompanying cancellation of quantum corrections simplify perturbative calculations of the electroweak subsector. Although supersymmetry has been studied for many years, the low-energy region of the strongly coupled subsector is only explored a little, because it is inaccessible with perturbation theory. It is inevitable to perform calculations with a non-perturbative method. An extraordinarily successful method to study strongly interacting theories from first principles is lattice gauge theory. The present work is intended to shed some light on the rich non-perturbative phenomena of an important building block of the MSSM: four-dimensional $\mathcal{N} = 1$ Super-Yang-Mills (SYM) theory with gauge group SU(3). It is the supersymmetric extension of pure Yang-Mills (YM) theory describing gluons in interaction with their superpartners, the so-called gluinos. As members of the same $\mathcal{N} = 1$ vector supermultiplet the gluons and gluinos are (in perturbation theory) massless. Both are in the adjoint representation of the gauge group and on-shell the degrees of freedom match. The latter statement holds true since the gluinos are Majorana fermions. Similar to QCD, the theory is asymptotically free and shows confinement.

Early analytic studies of supersymmetric lattice systems go back to Dondi and Nicolai [19], who studied the discretized Wess-Zumino model. Subsequently, the restoration of supersymmetry in the continuum limit and the spectrum of particles have been studied for these Yukawa-type lattice models [20–26]. Early simulations of four-dimensional $\mathcal{N} = 1$ SYM theory with quenched fermions were performed in [27, 28]. Clearly, dynamical fermions are an integral part in any supersymmetric field theory and the inclusion of light dynamical fermions in simulations is essential [29].

Extensive investigations and simulations of $\mathcal{N} = 1$ SYM theory with gauge group SU(2) and with dynamical fermions where performed by the DESY-Münster collaboration during the past 20 years. In [30] the chiral symmetry breaking was investigated and two ground states were spotted. A comprehensive lattice study including the mass spectrum was first

presented in [31] and concluded with [32]. Later, those results were refined with the help of a variational analysis [33]. Ward identities were exploited in [34] to determine the gluino mass as well as the mixing coefficient of the supercurrent. An investigation of the theory at finite temperature revealed that deconfinement and chiral symmetry restoration occur at the same temperature [35]. This insight was confirmed recently using the gradient flow [36]. Also the compactified theory with periodic boundary conditions was examined [37].

The lattice studies are supplemented with a one-loop calculation of the supersymmetric Ward identities [38], the analysis of the adjoint pion within partially quenched chiral perturbation theory [39] and the perturbative calculation of the clover coefficient [40]. More recently the spectrum of the low-lying bound states [41] and supersymmetric Ward identities [42] have been calculated for $\mathcal{N} = 1$ SYM with gauge group SU(3). Additionally, the measurement of baryonic states has been started [43, 44].

Besides these studies with Wilson fermions, first investigations and simulations with domain wall and overlap fermions have been presented in [45–48] and [49, 50]. With Ginsparg-Wilson fermions no fine-tuning should be necessary to end up with a supersymmetric continuum theory [51]. In addition to the numerical studies, there exist also many analytical results, e.g. concerning the chiral condensate and beta function [52–54].

A dimensional reduction of $\mathcal{N} = 1$ SYM theory from four to two spacetime dimensions leads to the $\mathcal{N} = (2, 2)$ SYM theory and the two theories have supermultiplets of identical length. The mass spectrum of the reduced theory [55], the Ward identities [56], the dynamical breaking of supersymmetry [57] and the large-N_c behavior [58] were investigated in detail. Certain field theories with extended supersymmetry can be formulated such that some (nilpotent) supersymmetry transformations are preserved exactly on the lattice [59, 60]. Two-dimensional $\mathcal{N} = (2, 2)$ SYM theory [61–65] and its extensions with fermions in the fundamental [66, 67] or adjoint [68] representation are fields of application. Other examples for models with an exact supersymmetry are the four-dimensional $\mathcal{N} = 4$ SYM theory [69–73] and its cousins, the four-dimensional $\mathcal{N} = 2^*$ SYM theory [74] and the two-dimensional $\mathcal{N} = (8, 8)$ SYM [75, 76]. Further supersymmetric models under investigation are for example the $\mathcal{N} = 2$ Landau-Ginzburg model [77], the supersymmetric nonlinear O(3) sigma model [78, 79] and applications in gauge-gravity duality [80, 81].

In the present work we aim with analytical and numerical investigations for a better understanding of the low-energy properties of $\mathcal{N} = 1$ SYM theory. Unfortunately all lattice regularizations break supersymmetry explicitly and, as a result of this breaking, one observes a mass-splitting within a given supermultiplet. Concretely we propose and carefully study a deformation of the $\mathcal{N} = 1$ SYM lattice action by twisting the mass term. We provide an analytical proof and numerical evidence that the twisting leads to a sizable improvement of the mass-degeneracy within the Veneziano-Yankielowicz supermultiplet.

As a result, the fine-tuning problem to the chiral and supersymmetric continuum limit is less severe. Originally the concept of a twisted mass was introduced to lattice QCD in [82] with the aim to remove exceptional configurations. Later, $\mathcal{O}(a)$ improvement at maximal twisting angle $\pm\pi/2$ was recognized as particularly interesting for measuring physical quantities [83]. Also a study of the two-dimensional Wess-Zumino model with a twisted lattice action revealed a dramatic suppression of the discretization errors for optimal twisting [22].

An alternative approach to improve the lattice formulation is the addition of a clover term to the Wilson fermions. With this modification, the lattice artifacts can be reduced from order $\mathcal{O}(a)$ to $\mathcal{O}(a^2)$ in the lattice spacing a, when the coefficient of the clover term is chosen appropriately [84–86]. Various perturbative and non-perturbative values of the numerical value of this coefficient exist in the literature for different lattice actions. As a complement, we try to find an optimal value by a heuristic parameter scan.

This thesis is structured as follows. Chapter 2 introduces the foundations of the following investigations and starts with a short introduction to (non-supersymmetric) YM theory in section 2.1. In the next section 2.2, the concept and properties of supersymmetry are summarized in a general context. Afterwards those two ingredients are combined in section 2.3 about the $\mathcal{N} = 1$ SYM theory and its predicted mass spectrum. Subsequently, the two-dimensional $\mathcal{N} = (2, 2)$ is addressed briefly in section 2.4. As a connection between the continuum theory in Minkowski spacetime and the lattice formulation, section 2.5 covers Euclidean field theory.

Chapter 3 consists of two parts. In the first part 3.1, basics of lattice field theory such as the Monte Carlo sampling 3.1.1, rational approximation, conjugate gradient and multigrid algorithm 3.1.2 are recapitulated. Furthermore the procedure of mass spectroscopy 3.1.3 and smearing 3.1.4 are addressed. The second part 3.2 of this chapter deals with specific challenges of $\mathcal{N} = 1$ SYM theory on the lattice and the applied lattice formulations of the gauge fields (section 3.2.1) and Majorana fermions (section 3.2.2). In section 3.2.3 the properties of the mass-twisted Wilson Dirac operator, which we employed in many simulations, are discussed. This chapter is concluded with an overview of the investigated lattice observables 3.2.4.

Our analytical investigations are found in chapter 4. First, the transformation of the mesonic correlators under a chiral rotation is calculated 4.1, which reveals as a key finding the special twist $\alpha = 45°$. Subsequently, we apply in section 4.2 supersymmetry transformations to the states of the Veneziano-Yankielowicz supermultiplet to check that the chiral rotation does not spoil the supermultiplet structure. We complete our analytical chapter with the calculation of the eigenvalues of the free Wilson Dirac operator with twists and find hints for $\mathcal{O}(a)$ improvement 4.3.

In chapter 5, preparatory examinations pave the way for the physical results. The parameter scans of the clover fermions and twisted-mass fermions are shown in the sections 5.1 and 5.2. In the following, technical topics such as the sign of the Pfaffian in section 5.3, the scale setting in section 5.4, and the finite size effects in section 5.5 are analyzed. Further insights are gained with the double-twisted Wilson Dirac operator in section 5.6. The last part 5.7 contains numerical studies of the fermion smearing (section 5.7.1) and multigrid acceleration (section 5.7.2).

Chapter 6 covers the numerical results and is divided into two parts. In the first part 6.1, we present briefly results obtained in the two-dimensional $\mathcal{N} = (2, 2)$ SYM theory before turning to the four-dimensional $\mathcal{N} = 1$ SYM theory in part 6.2. The promising direction of 45° mass twist is explored with the mesonic states 6.2.1, the gluino-glue 6.2.2 and the glueballs 6.2.3. Finally, all those results are combined in an extrapolation to the critical point, see section 6.2.4.

We conclude with chapter 7 and give an outlook. In the appendix, our conventions (A), the calculation of the properties of the untwisted (B.1) and mass-twisted (B.2) Wilson Dirac operator, and the details of the supersymmetry transformation of the gluino-glue (C) can be found. In addition, it is shown that the Euclidean (continuum) action is invariant under supersymmetry (D). We provide a proof that the pion is the lightest meson (E), an overview of our ensembles (G), short notes on the data analysis (H), and benchmarks of the strong and weak scaling (I).

The compilation of this thesis is solely due to the author. However large parts of the work were in collaboration with Andreas Wipf, Björn Wellegehausen and André Sternbeck. We published different interim results in conference proceedings [87–89]. A publication encompassing most $\mathcal{N} = 1$ SYM results shall appear in JHEP and is available as a preprint [90]. The $\mathcal{N} = (2, 2)$ SYM results are published together with Daniel August [55]. All numerical simulations are based on a code developed over many years mainly by Björn Wellegehausen and during my PhD I was involved in its extension. The simulations were performed at Leibniz Supercomputing Center on SuperMUC and SuperMUC-NG, the clusters Ara and Omega of the University of Jena, and on compute servers of the theoretical physics institute.

CHAPTER 2

Basics

This chapter serves a twofold purpose. Firstly, it recapitulates the basic knowledge required for the study of supersymmetric Yang-Mills theory. Secondly, we can fix our notation for the upcoming chapters.

In the beginning, Yang-Mills theory without supersymmetry is addressed in Minkowski spacetime. Afterwards, the concept of supersymmetry is introduced in a general manner. Subsequent to those two sections, these topics are combined to discuss Super-Yang-Mills theory in four and two spacetime dimensions. In the last section, we turn to Euclidean field theories.

2.1 Yang-Mills theory

Our understanding of the standard model (SM) of particle physics is based on gauge theories. Yang and Mills introduced in [91] the concept of non-Abelian Lie groups to treat quantum chromodynamics (QCD). The gauge invariance in QCD permits local transformations $\Omega(x) \in \mathrm{SU}(3)$. Requiring that the gauge transformations

$$\psi(x) \mapsto \psi'(x) = \Omega(x)\,\psi(x)\,, \qquad \bar{\psi}(x) \mapsto \bar{\psi}'(x) = \bar{\psi}(x)\,\Omega^\dagger(x) \tag{2.1}$$

leave the fermionic action

$$S_\mathrm{F}[\psi, \bar{\psi}, A] = \int \mathrm{d}^4x\, \bar{\psi}(x)\Big(\mathrm{i}\gamma^\mu\big(\partial_\mu - \mathrm{i}gA_\mu(x)\big) - m\Big)\psi(x) \tag{2.2}$$

invariant leads to the definition of the covariant derivative

$$D_\mu(x) = \partial_\mu - \mathrm{i}gA_\mu(x) \tag{2.3}$$

and the transformations

$$A_\mu(x) \mapsto A'_\mu(x) = \Omega(x)\,A_\mu(x)\,\Omega^\dagger(x) - \mathrm{i}\big(\partial_\mu\Omega(x)\big)\,\Omega^\dagger(x)\,, \tag{2.4}$$

$$D_\mu(x) \mapsto D'_\mu(x) = \Omega(x)\,D_\mu(x)\,\Omega^\dagger(x)\,. \tag{2.5}$$

Pure Yang-Mills (YM) theory consists only of the gauge field $A_\mu(x)$, which describes gluons in QCD. With the covariant derivative of eq. (2.3) we define the field strength tensor

$$F_{\mu\nu}(x) \equiv \frac{\mathrm{i}}{g}[D_\mu(x), D_\nu(x)] = \partial_\mu A_\nu(x) - \partial_\nu A_\mu(x) - \mathrm{i}g[A_\mu(x), A_\nu(x)]\,. \tag{2.6}$$

Under a gauge transformation it transforms as the covariant derivative in eq. (2.5),

$$F_{\mu\nu}(x) \mapsto F'_{\mu\nu}(x) = \Omega(x)\, F_{\mu\nu}(x)\, \Omega^\dagger(x)\,. \tag{2.7}$$

Then we can define the gauge action

$$S_\mathrm{G}[A] = -\frac{1}{4}\int \mathrm{d}^4x\, \mathrm{tr}\Big(F_{\mu\nu}(x)F^{\mu\nu}(x)\Big)\,, \tag{2.8}$$

which is invariant under Lorentz and gauge transformations. For the lattice formulation it is beneficial to rescale the gauge fields $A_\mu(x) \mapsto \frac{1}{g}A_\mu(x)$, such that the action takes the form

$$S_\mathrm{G}[A] = -\frac{1}{4g^2}\int \mathrm{d}^4x\, \mathrm{tr}\Big(F_{\mu\nu}(x)F^{\mu\nu}(x)\Big)\,, \tag{2.9}$$

where the covariant derivative is now $D_\mu(x) = \partial_\mu - \mathrm{i}A_\mu(x)$.

2.2 Supersymmetry

A general spacetime symmetry is an element of the Poincaré group

$$\mathrm{iL} = \Big\{(\Lambda, a)\,\Big|\, a \in \mathbb{R}^d,\ \Lambda \in \mathrm{O}(1, d-1),\ \Lambda^\mathrm{T}\eta\Lambda = \eta\Big\}\,, \tag{2.10}$$

where we assume flat spacetime with the signature $(+,-,\ldots,-)$. In a Poincaré transformation $x^\mu \mapsto \Lambda^\mu{}_\nu x^\nu + a^\mu$, a Lorentz transformation is combined linearly with a translation. The corresponding generators of the individual transformations

$$(\Lambda, 0) = \mathrm{e}^{\frac{\mathrm{i}}{2}\omega^{\mu\nu}M_{\mu\nu}}, \qquad (\mathbb{1}, a) = \mathrm{e}^{\mathrm{i}a^\mu P_\mu} \tag{2.11}$$

are the momenta P_μ and the antisymmetric matrices $M_{\mu\nu}$ with the elements

$$[M_{\mu\nu}]_{\rho\sigma} = -\mathrm{i}(\eta_{\mu\rho}\eta_{\nu\sigma} - \eta_{\nu\rho}\eta_{\mu\sigma})\,, \tag{2.12}$$

describing infinitesimal rotations and boosts. Those generators obey the Poincaré algebra

$$\begin{aligned}
[P_\mu, P_\nu] &= 0\,,\\
[M_{\mu\nu}, M_{\rho\sigma}] &= \mathrm{i}(\eta_{\mu\rho}M_{\nu\sigma} + \eta_{\nu\sigma}M_{\mu\rho} - \eta_{\mu\sigma}M_{\nu\rho} - \eta_{\nu\rho}M_{\mu\sigma})\,,\\
[M_{\mu\nu}, P_\rho] &= \mathrm{i}(\eta_{\mu\rho}P_\nu - \eta_{\nu\rho}P_\mu)\,.
\end{aligned} \tag{2.13}$$

The Coleman-Mandula theorem prohibits in $d > 2$ dimensions the non-trivial combination of spacetime symmetry with internal symmetries. In short, a direct product of the Poincaré group and an internal symmetry group is the most general symmetry group of the scattering matrix [92]. However, this theorem can be circumvented with the help of fermionic generators and the usage of the anti-commutator [93, 94]. Consequently, the Poincaré group can be extended. Therefore the infinitesimal parameter ϵ of the supersymmetry transformation δ_ϵ has to be an anti-commuting spinor. The supercharge $\mathcal{Q}$ is the generator of supersymmetry transformations and has $2^{\lfloor d/2 \rfloor}$ components. It enters the supersymmetry transformation via $\delta_\epsilon(\ldots) = \bar{\epsilon}\mathcal{Q}(\ldots)$. Models with extended supersymmetry contain multiple supercharges $\mathcal{Q}^i$, $i = 1, \ldots, \mathcal{N}$, but we focus on the $\mathcal{N} = 1$ SYM theory with a single supercharge. The superalgebra is a $\mathbb{Z}_2$ graded Lie algebra, which consists of

$$[P_\mu, \mathcal{Q}_\alpha] = 0\,, \tag{2.14}$$

$$[M_{\mu\nu}, \mathcal{Q}_\alpha] = \frac{1}{4\mathrm{i}} \left(\Sigma_{\mu\nu}\mathcal{Q}\right)_\alpha\,, \tag{2.15}$$

$$\{\mathcal{Q}_\alpha, \bar{\mathcal{Q}}_\beta\} = 2(\gamma^\mu)_{\alpha\beta} P_\mu\,, \tag{2.16}$$

and the Poincaré algebra given in eq. (2.13) [95]. The definition of the Dirac matrices γ^μ can be found in appendix A and their commutator is $\Sigma_{\mu\nu} \equiv [\gamma_\mu, \gamma_\nu]$. From the superalgebra, properties of the supercharge $\mathcal{Q}$ can be derived. Eq. (2.14) implies that the supercharge is translation-invariant. As can be seen in eq. (2.15), the supercharge transforms under a Lorentz transformation like a spin-$\frac{1}{2}$ particle. The product of two spinor operators in eq. (2.16) has to transform like a vector operator and the only allowed vector operator is the momentum operator P_μ. Thus the composition of two supersymmetry transformations leads to a translation.

In the following we will address further important properties of supersymmetry. First of all, every supersymmetry transformation transforms a fermion $|\mathcal{F}\rangle$ into a boson $|\mathcal{B}\rangle$ and vice versa:

$$\mathcal{Q}|\mathcal{B}\rangle = |\mathcal{F}\rangle\,, \qquad \mathcal{Q}|\mathcal{F}\rangle = |\mathcal{B}\rangle\,. \tag{2.17}$$

All quantum numbers of two superpartners are identical, except their spin. In particular, the O'Raifeartaigh theorem [96] states that superpartners have identical mass as long as supersymmetry is unbroken. With the help of eq. (2.14) we can prove that

$$m_\mathcal{B}^2|\mathcal{B}\rangle = P_\mu P^\mu|\mathcal{B}\rangle = P_\mu P^\mu \mathcal{Q}|\mathcal{F}\rangle = \mathcal{Q}P_\mu P^\mu|\mathcal{F}\rangle = m_\mathcal{F}^2\mathcal{Q}|\mathcal{F}\rangle = m_\mathcal{F}^2|\mathcal{B}\rangle\,. \tag{2.18}$$

This means that two massive superpartners have degenerate mass, $m_\mathcal{B} = m_\mathcal{F}$. All particles which are transformed into each other by supersymmetry are grouped in a so-called supermultiplet. We can deduce with eq. (2.16) that the energy

$$E = \langle\psi|P_0|\psi\rangle = \frac{1}{8}\sum_\alpha \langle\psi|\{\mathcal{Q}_\alpha, \mathcal{Q}_\alpha^\dagger\}|\psi\rangle = \frac{1}{8}\sum_\alpha \left(\|\mathcal{Q}_\alpha^\dagger|\psi\rangle\|^2 + \|\mathcal{Q}_\alpha|\psi\rangle\|^2\right) \geq 0 \tag{2.19}$$

of all states is non-negative. The translation-invariant vacuum $|0\rangle$ is the only state with zero energy and it is annihilated by all supercharges if supersymmetry is unbroken, $\mathcal{Q}_\alpha|0\rangle = \mathcal{Q}_\alpha^\dagger|0\rangle = 0$. Conversely the energy of the lowest state is an order parameter and supersymmetry is broken if $E_0 > 0$. The discrepancy between the calculated cosmological constant and its observed value can be explained by supersymmetry without any renormalization or unnatural addition [97]. Experimental data suggests that the cosmological constant is $1.1 \times 10^{-52}\,\mathrm{m}^{-2}$ [11].

States with positive energy cannot be invariant under supersymmetry and thus each particle requires a superpartner. Concretely, each supermultiplet with $P_\mu \neq 0$ has the same amount of bosonic and fermionic degrees of freedom. Only in the vacuum, the number of bosonic and fermionic ground states can differ due to its invariance under translations, $P_\mu = 0$. The Witten index

$$I_\mathrm{W} = \mathrm{tr}\Big((-1)^F\Big) = n_\mathrm{B}^0 - n_\mathrm{F}^0 \tag{2.20}$$

with the fermion number F and the trace over the Hilbert space is a useful quantity [98]. Because all states with positive energy come in pairs, only the difference of the bosonic and fermionic ground states remains. Consequently the Witten index can be used to distinguish between scenarios of supersymmetry breaking. If the Witten index is non-zero, supersymmetry cannot be broken spontaneously and at least one fermionic ($I_\mathrm{W} < 0$) or bosonic ($I_\mathrm{W} > 0$) ground state is present. In this scenario, supersymmetry can only be broken explicitly by adding terms to the Lagrangian. For vanishing Witten index, $I_\mathrm{W} = 0$, supersymmetry may be broken ($n_\mathrm{B}^0 = n_\mathrm{F}^0 = 0$) or unbroken ($n_\mathrm{B}^0 = n_\mathrm{F}^0 \neq 0$). In section 2.3 we will show that the $\mathcal{N} = 1$ SYM theory with gauge group $\mathrm{SU}(N_\mathrm{c})$ has the Witten index $I_\mathrm{W} = N_\mathrm{c}$ and thus no spontaneous supersymmetry breaking is possible.

One further important feature of supersymmetric theories is the non-renormalization theorem [99], which states that supersymmetry is unbroken at all orders of perturbation theory if the classical theory is supersymmetric. The underlying mechanism is the cancellation of bosonic and fermionic loops at each order. Accordingly, supersymmetry cannot be broken perturbatively. In the discussion of the Witten index, we already mentioned the spontaneous and explicit breaking of supersymmetry. A further variant is the so-called soft supersymmetry breaking, which affects only the low-energy regime of a theory and the supersymmetry stays intact in the ultraviolet regime, i.e. the solution to the hierarchy problem of the Higgs mass keeps its validity. Such a soft supersymmetry breaking can be achieved by adding a mass to all superpartners. If this additional mass is large enough, the superpartners become so heavy that they cannot be observed with today's accelerator facilities and the postulated supersymmetry remains compatible with the experimental data. Superpartners may have masses of tens of TeV [100]. Still, an open question is the nature of a presumable soft supersymmetry breaking [101, 102].

2.3 Four-dimensional $\mathcal{N} = 1$ Super-Yang-Mills theory

In four-dimensional Minkowski spacetime the on-shell action of $\mathcal{N} = 1$ SYM theory reads

$$S^{\mathrm{M}}_{\mathrm{SYM}} = \int \mathrm{d}^4x \ \mathrm{tr}\left(-\frac{1}{4}F_{\mu\nu}F^{\mu\nu} + \frac{\mathrm{i}}{2}\bar{\lambda}\not{D}\lambda - \frac{m}{2}\bar{\lambda}\lambda\right) \tag{2.21}$$

and its structure resembles the action of Quantum Chromodynamics (QCD). In the supersymmetric theory the fermion and the gauge boson are members of the same vector supermultiplet. The fermion in the $\mathcal{N} = 1$ SYM theory is called gluino and described by a Majorana field $\lambda(x)$, which transforms in the same adjoint representation as the gauge potential $A_\mu(x)$. A Majorana fermion is characterized by $\lambda = \lambda^C$, that means it is its own anti-particle. The action in eq. (2.21) contains a finite gluino mass m which breaks supersymmetry softly. On the lattice this mass is fine-tuned such that after continuum extrapolation a supersymmetric limit is reached which at the same time is chirally symmetric.

For the same gauge group $\mathrm{SU}(N_\mathrm{c})$, the chiral symmetry of $\mathcal{N} = 1$ SYM theory has a different breaking pattern in comparison to QCD. For vanishing gluino mass the classical theory has a global $\mathrm{U}(1)_\mathrm{A}$ symmetry $\lambda \mapsto \mathrm{e}^{\mathrm{i}\alpha\gamma_5}\lambda$. The axial anomaly reduces this $\mathrm{U}(1)_\mathrm{A}$ via instantons to the discrete subgroup $\mathbb{Z}_{2N_\mathrm{c}}$,

$$\lambda \mapsto \mathrm{e}^{2\pi\mathrm{i}n\gamma_5/2N_\mathrm{c}}\lambda \quad \text{with} \quad n \in \{1, \ldots, 2N_\mathrm{c}\}\,. \tag{2.22}$$

A gluino condensate $\langle\bar{\lambda}\lambda\rangle \neq 0$ spontaneously breaks this remnant symmetry further to a $\mathbb{Z}_2$ symmetry [103, 104]. Therefore N_c physically equivalent vacua are expected, which differ in their phase of the gluino condensate [30]. Thus the Witten index is $I_\mathrm{W} = N_\mathrm{c}$. A gluino mass $m \neq 0$ lifts this degeneracy and the chiral condensate Σ becomes $\gtrless 0$ for $m \gtrless 0$ [30].

A key point of the action (2.21), is its invariance under the supersymmetry transformation

$$\delta_\epsilon A_\mu(x) = \mathrm{i}\bar{\epsilon}\gamma_\mu\lambda(x)\,, \quad \delta_\epsilon\lambda(x) = \frac{1}{4}\Sigma_{\mu\nu}F^{\mu\nu}(x)\epsilon\,, \quad \delta_\epsilon\bar{\lambda}(x) = -\frac{1}{4}\bar{\epsilon}\,\Sigma_{\mu\nu}F^{\mu\nu}(x)\,. \tag{2.23}$$

Therein, ϵ is a constant majorana-valued anticommuting parameter. We can check that the supersymmetry transformation of each field respects the following criteria. Firstly, each bosonic field is transformed into a fermionic field and vice versa. Secondly, the transformations are in accordance to the mass dimensions of the fields $[\epsilon] = L^{1/2}$, $[\partial_\mu] = [A_\mu] = L^{-1}$, $[\lambda] = L^{-3/2}$ and $[F_{\mu\nu}] = L^{-2}$. Thirdly, the open indices match to guarantee the correct Lorentz transformations. Finally, the Hermiticity is implemented by appropriate imaginary units. In appendix D, we will show that the $\mathcal{N} = 1$ SYM Lagrangian transforms under these supersymmetry transformations into a total derivative and thus

Table 2.1: Veneziano-Yankielowicz supermultiplet.

1 bosonic scalar	$s=1,\ l=1,\ 0^{++}$	gluinoball	a-$f_0 \sim \bar{\lambda}\lambda$
1 bosonic pseudoscalar	$s=0,\ l=0,\ 0^{-+}$	gluinoball	a-$\eta' \sim \bar{\lambda}\gamma_5\lambda$
1 majorana-type	$s=\frac{1}{2},\ l=1,\ \frac{1}{2}^{\mathrm{i}+}$	gluino-glueball	$\tilde{\mathrm{g}}\mathrm{g} \sim F_{\mu\nu}\Sigma^{\mu\nu}\lambda$

Table 2.2: Farrar-Gabadadze-Schwetz supermultiplet.

1 bosonic scalar	$s=0,\ l=0,\ 0^{++}$	glueball	$0^{++} \sim F_{\mu\nu}F^{\mu\nu}$
1 bosonic pseudoscalar	$s=1,\ l=1,\ 0^{-+}$	glueball	$0^{-+} \sim \epsilon_{\mu\nu\rho\sigma}F^{\mu\nu}F^{\rho\sigma}$
1 majorana-type	$s=\frac{1}{2},\ l=0,\ \frac{1}{2}^{(-\mathrm{i})+}$	gluino-glueball	$\tilde{\mathrm{g}}\mathrm{g} \sim F_{\mu\nu}\Sigma^{\mu\nu}\lambda$

the action is invariant. When the off-shell Lagrangian

$$\mathcal{L}^{\mathrm{off}}_{\mathrm{SYM}} = -\frac{1}{4}\mathrm{tr}(F_{\mu\nu}F^{\mu\nu}) + \frac{\mathrm{i}}{2}\mathrm{tr}(\bar{\lambda}\not{D}\lambda) + \frac{1}{2}\mathrm{tr}(\mathcal{G}^2) \tag{2.24}$$

with the auxiliary field of mass dimension $[\mathcal{G}] = L^{-2}$ is considered, then the supersymmetry transformations are modified to

$$\begin{aligned} \delta_\epsilon A_\mu(x) &= \mathrm{i}\bar{\epsilon}\gamma_\mu\lambda(x)\,, & \delta_\epsilon\lambda(x) &= \frac{1}{4}\Sigma_{\mu\nu}F^{\mu\nu}(x)\epsilon + \mathrm{i}\mathcal{G}(x)\gamma_5\epsilon\,, \\ \delta_\epsilon\mathcal{G}(x) &= \bar{\epsilon}\gamma_5\not{D}\lambda(x)\,, & \delta_\epsilon\bar{\lambda}(x) &= -\frac{1}{4}\bar{\epsilon}\,\Sigma_{\mu\nu}F^{\mu\nu}(x) + \mathrm{i}\bar{\epsilon}\mathcal{G}(x)\gamma_5\,. \end{aligned} \tag{2.25}$$

At high energies or high temperatures, $\mathcal{N}=1$ SYM can be considered as a gas of free gluons and gluinos. On the other hand, at low energies it is a confining theory with color-singlet bound states similar to gauge theories without supersymmetry. The spectrum has been investigated with the method of effective field theory based on the theory's symmetries and application of anomaly matching. Three different types of bound states are expected to arise: pure glueballs, pure meson-like gluinoballs and gluino-glueballs.

Supersymmetry arranges these bound states in mass-degenerate supermultiplets. Veneziano and Yankielowicz (VY) predicted a chiral supermultiplet [105] of bound states listed in table 2.1. The names of the particles are chosen in analogy to QCD, with the prefix "a-" indicating the adjoint representation. As usual, the quantum numbers J^{PC} specify the total angular momentum J, the parity P and the charge conjugation C. Note that for Majorana fermions the intrinsic parity has to be imaginary [106].

Subsequently Farrar, Gabadadze and Schwetz (FGS) suggested the existence of a second supermultiplet [107] consisting of the particles listed in table 2.2. Based on symmetry arguments they suggested the more general effective Lagrangian

$$\mathcal{L}^{\mathrm{eff}}_{\mathrm{SYM}} = \frac{1}{\alpha}(S^\dagger S)^{1/3}\bigg|_D + \gamma\left[\left\{S\,\log\left(\frac{S}{\mu^3}\right) - S\right\}\bigg|_F + \mathrm{h.c.}\right] + \frac{1}{\delta}\left(-\frac{U^2}{(S^\dagger S)^{1/3}}\right)\bigg|_D \tag{2.26}$$

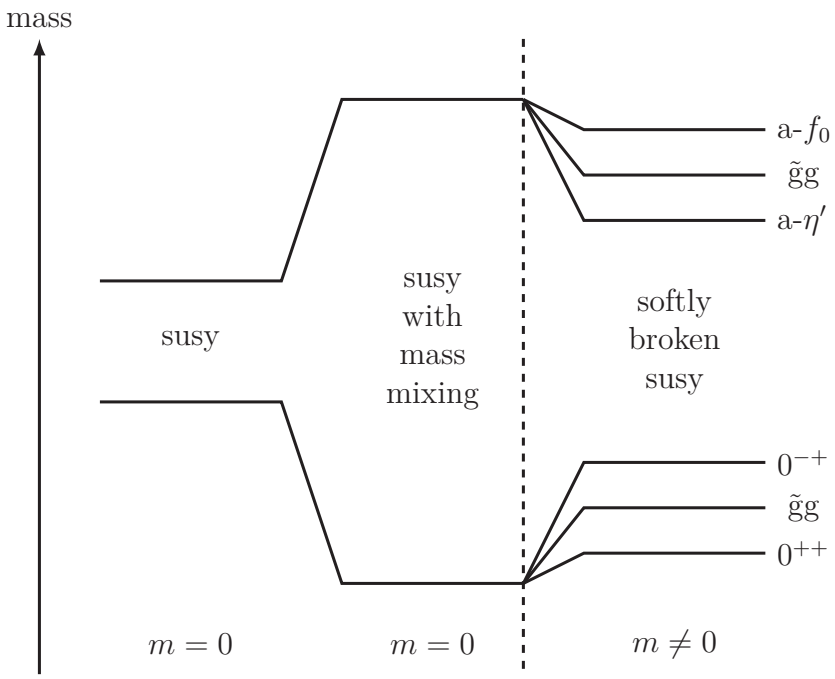

Figure 2.1: Mass hierarchy of the VY- and FGS-supermultiplets. To the left of the dashed line, where the gluino mass m vanishes, supersymmetry guarantees the mass-degeneracy within each supermultiplet and a mass mixing increases the mass difference between those two supermultiplets. On the right, the gluino mass is turned on to softly break supersymmetry. Consequently the states within each supermultiplets split. Note that the pseudoscalar states are shifted the most and the masses of the scalar states are modified the least. This figure is adopted from [108].

with chiral superfield S, real tensor superfield U, dynamically generated scale μ and further low-energy constants α, γ and δ.[1] Eq. (2.26) is written in superspace and the F-term with $\theta^1\theta^2$ resp. the D-term with $\theta^1\theta^2\bar{\theta}^1\bar{\theta}^2$ has to be taken as indicated. In the limit $\delta \to \infty$ the effective action of Veneziano and Yankielowicz is recovered. The effective Lagrangian (2.26) describes propagating massive fields, among others the scalar and pseudoscalar glueball. The physical states will be mixtures of states from the VY-supermultiplet and the FGS-supermultiplet with same quantum numbers [107].

Figure 2.1 combines those two supermultiplets and visualizes their mass hierarchy. Both multiplets are chiral Wess-Zumino supermultiplets consisting of a scalar, a pseudoscalar and a fermionic spin-$\frac{1}{2}$ particle. As proposed in [107], it is assumed that the FGS-supermultiplet is lighter than the VY-supermultiplet. Without a supersymmetry-breaking gluino mass, both supermultiplets have presumably different masses, but each is degenerated. The scalar, pseudoscalar and majorana-type states of both supermultiplets have the same quantum numbers and mixing occurs. In [108], it was calculated that mass mixing of the physical

[1] In [108], the same authors suggest an alternative formulation with two chiral superfields.

states increases the mass difference between the supermultiplets as sketched. As soon as a gluino mass is added, supersymmetry will be broken softly and the mass-degeneracy ends. By perturbation of the effective action with a small gluino mass, the authors of [108] found that the pseudoscalar mesonic state is lighter than the scalar mesonic state. In analogy to another proof with glueballs [109], they then conjectured that the lightest state is the scalar glueball. Thus the FGS-supermultiplet should be the lightest supermultiplet.

Generally, the ordering of the supermultiplet depends on free parameters of the effective action. In [110], it was shown that the effective Lagrangian can also be constructed such that the mass hierarchy of the two supermultiplet is inverted. These authors introduced a tunable mixing angle between the two supermultiplets and applied the large-N_c equivalence between SYM theory and QCD. They argued that this mixing should be small in accordance to QCD, where the η' is much lighter than the 0^{++} glueball. Consequently, the VY-supermultiplet should be the lightest supermultiplet.

Therefore, non-perturbative lattice simulations are a promising approach to shed light on the question of the lightest supermultiplet. For the numerical results in [33], an argument is found in favor of the FGS-supermultiplet to be the lightest: The lightest state in the scalar channel is dominantly a glueball. At the same time, their results agree with the argumentation of [110], because the mesonic contribution dominates the pseudoscalar ground state and has negligible mixing with the pseudoscalar glueball. Although in [110] the scalar and pseudoscalar channel were treated equally, the numerically found mixing angles are not equal. In summary, the mass hierarchy of the supermultiplets is not clarified yet and future lattice investigations may provide a definitive answer.

2.4 Two-dimensional $\mathcal{N} = (2,2)$ Super-Yang-Mills theory

With the idea of Kaluza and Klein [111, 112], the four-dimensional $\mathcal{N} = 1$ SYM theory can be reduced to the two-dimensional $\mathcal{N} = (2,2)$ SYM theory. Therefore the four-dimensional Majorana spinors are decomposed into two-dimensional spinors, $\lambda = \begin{pmatrix} \chi_1 \\ \chi_2 \end{pmatrix}$. The Kaluza-Klein reduction $\mathbb{R}^4 \to \mathbb{R}^2 \times \mathbb{T}^2$ compactifies two spatial dimensions and consequently the corresponding gauge fields become scalars $A_2 = \phi_1$, $A_3 = \phi_2$. By absorbing the compactified volume $V_{23} = \int \mathrm{d}x_2 \mathrm{d}x_3$ in the gauge coupling $g \to \sqrt{V_{23}} g$, the latter comes in units of length and leads to superrenormalizability. Dimensionally reducing the gauge term and the kinetic term of the four-dimensional Lagrangian (2.21) without any gluino-mass

results in the two-dimensional action

$$S_{2d} = \frac{1}{2g^2}\int \mathrm{d}^2x\,\mathrm{tr}\Big(-\frac{1}{2}F_{\mu\nu}F^{\mu\nu} - D_\mu\phi_m D^\mu\phi^m + \frac{1}{2}[\phi_m,\phi_n][\phi^m,\phi^n] + \mathrm{i}\bar{\chi}_m\sigma_2 D_0\chi_m \\ - \bar{\chi}_m\sigma_3 D_1\chi_m - \bar{\chi}_m(\mathrm{i}\sigma_1)^{mn}\sigma_1[\phi_1,\chi_n] - \bar{\chi}_m(\mathrm{i}\sigma_3)^{mn}\sigma_1[\phi_2,\chi_n]\Big)\,. \tag{2.27}$$

In the previous equation, the Dirac matrices are given by the Pauli matrices and the indices run over $\mu,\nu = 0,1$ and $m,n = 1,2$. To formulate the two-dimensional superalgebra, it is helpful to introduce light-cone coordinates $z = x_0 + x_1$ and $\bar{z} = x_0 - x_1$ [113]. Vectors V_μ are also rearranged to $V_z = \frac{1}{2}(V_0 + V_1)$ and $V_{\bar{z}} = \frac{1}{2}(V_0 - V_1)$. Decomposing the four-dimensional Majorana supercharge $\mathcal{Q}$ into two left-handed $\mathcal{Q}^1_+, \mathcal{Q}^2_+$ and two right-handed $\mathcal{Q}^1_-, \mathcal{Q}^2_-$ Majorana-Weyl spinors, we label our superalgebra as $\mathcal{N} = (2,2)$. With the definition $M = M_{01}$, the superalgebra is given by

$$\begin{aligned}
&\{\mathcal{Q}^i_+, \mathcal{Q}^j_+\} = 2\mathrm{i}\delta^{ij}P_z\,, && [\mathcal{Q}^i_+, M] = -\frac{1}{2}\mathcal{Q}^i_+\,, && [\mathcal{Q}^i_+, P_z] = 0\,, && [P_z, M] = -P_z\,,\\
&\{\mathcal{Q}^i_-, \mathcal{Q}^j_-\} = 2\mathrm{i}\delta^{ij}P_{\bar{z}}\,, && [\mathcal{Q}^i_-, M] = \frac{1}{2}\mathcal{Q}^i_-\,, && [\mathcal{Q}^i_-, P_{\bar{z}}] = 0\,, && [P_{\bar{z}}, M] = P_{\bar{z}}\,,\\
&\{\mathcal{Q}^i_+, \mathcal{Q}^j_-\} = 0\,, && [\mathcal{Q}^i_+, P_{\bar{z}}] = [\mathcal{Q}^i_-, P_z] = 0\,,
\end{aligned} \tag{2.28}$$

as the direct sum of the left algebra $(2,0)$ and the right algebra $(0,2)$. Although the dynamics of the reduced $\mathcal{N} = (2,2)$ SYM theory are different and the constituents of the particle operators differ, the supermultiplet structure is identical to $\mathcal{N} = 1$ SYM theory [55, 114]. The VY-supermultiplet consists of the a-η', a-f_0, and a mixture of gluino-glue and gluino-scalarball. In the FGS-supermultiplet all states contain the scalar fields and they are a glue-scalarball, a mixture of 0^{++}-glueball and pure scalarball, and a mixture of gluino-glue and gluino-scalarball [55, 114].

2.5 Euclidean field theory

For the lattice formulation of a theory, its definition in Euclidean spacetime is required [115]. Axiomatic field theory states that there exists an analytic continuation to Euclidean spacetime [116, 117]. Wightman functions $W(x_1,\ldots,x_n) = \langle 0|\phi(x_1)\ldots\phi(x_n)|0\rangle$ are vacuum expectation values of products of fields[2] $\phi(x_i)$ at spacetime coordinates $x_i = (t_i, \vec{x}_i)$. A Wightman function evaluated at Euclidean points $x^{\mathrm{E}}_i = (\vec{x}_i, -\mathrm{i}t_i)$ is called Schwinger function, $W(x^{\mathrm{E}}_1,\ldots,x^{\mathrm{E}}_n) = S(x_1,\ldots,x_n)$. With the Schwinger function

$$S(x_1,\ldots,x_n) = \frac{1}{Z}\int \mathcal{D}\phi\,\phi(x_1)\cdots\phi(x_n)\,\mathrm{e}^{-S_{\mathrm{E}}[\phi]} = \langle\phi(x_1)\cdots\phi(x_n)\rangle \tag{2.29}$$

[2] For simplicity in the notation, we consider scalar fields $\phi(x)$ here. Analogously, positivity can be defined for lattice fermions [118, 119] and gauge theories [120].

the Euclidean action $S_\mathrm{E}[\phi]$ is defined [121, 122]. The most important requirement in order that Euclidean correlation functions can be continued back to Minkowski spacetime is reflection positivity, also called Osterwalder-Schrader positivity [123]. We define a Euclidean scalar field operator[3] at spacetime coordinate $x = (\vec{x}, x_4)$ as $\phi(x) \equiv \mathrm{e}^{Hx^4}\phi(\vec{x}, 0)\,\mathrm{e}^{-Hx^4}$ with Euclidean spacetime translations e^{-Hx^4} and analogously the Hermitean conjugated operator $O^\dagger(x) \equiv \mathrm{e}^{Hx^4}O^\dagger(\vec{x}, 0)\,\mathrm{e}^{-Hx^4}$. The Euclidean time reflection is then given by

$$\theta(\vec{x}, x^4) = (\vec{x}, -x^4)\,, \tag{2.30}$$

$$\Theta\phi(x) = \phi^*(\theta x)\,, \tag{2.31}$$

$$\Theta(cF) = c^*\,\Theta F\,, \tag{2.32}$$

$$\Theta(FG) = \Theta F\,\Theta G\,, \tag{2.33}$$

where the asterisk stands for complex conjugation, F, G are functionals of fields and c is a complex number [124]. The time reflection Θ is the Euclidean equivalent of conjugate transpose (dagger) in Minkowski spacetime. It is evident, that Hermitean conjugation of the Minkowskian time evolution operator $\mathrm{e}^{\mathrm{i}Ht}$ reverses the time, $t \leftrightarrow -t$, and the same does the time reflection Θ with e^{Hx^4}. Now we can define the reflection positivity condition [123, 124]:

$$\Big\langle (\Theta F)\, F \Big\rangle \geq 0\,. \tag{2.34}$$

Given the expectation value $\langle\ \rangle$ of a Euclidean reflection-positive classical field theory, then there exists a Hilbert space $\mathcal{H}$ and a Poincaré group representation $U(a;\Lambda)$ with positive energy such that

$$\Big\langle (\Theta F)\, T(\vec{x}, x^4)\, F \Big\rangle = \Big\langle F,\ U(t, \vec{x})\, F \Big\rangle_{\mathcal{H}}\,, \tag{2.35}$$

where $T(\vec{x}, x^4)$ is a Euclidean spacetime translation and $U(t, \vec{x}; \mathbb{1}) = \mathrm{e}^{-\mathrm{i}tH + \mathrm{i}\vec{x}\vec{P}}$ is a Minkowski spacetime translation [115]. For $t = 0$, $\vec{x} = \vec{0}$ this theorem guarantees the existence of the Hilbert space $\mathcal{H}$ with positive inner product. Or, the other way around, it shows that a self-adjoint transfer matrix $T(t, \vec{x})$ exists on the lattice. With the help of the transfer matrix T we can define the Euclidean lattice Hamiltonian

$$T = \mathrm{e}^{-Ha}\,, \tag{2.36}$$

where a is the lattice spacing.

[3] In the Schrödinger picture the operators O_S and its Hermitean conjugate $O_\mathrm{S}^\dagger$ are time-independent, while the states $|\phi_\mathrm{S}(t)\rangle = \mathrm{e}^{-\mathrm{i}H_\mathrm{S}t}|\phi_\mathrm{S}(0)\rangle$ evolve in time. Conversely, in the Heisenberg picture considered here the states $|\phi_\mathrm{H}\rangle$ are constant and the operators are time-dependent $O_\mathrm{H}(t) = \mathrm{e}^{\mathrm{i}H_\mathrm{S}t}\,O_\mathrm{S}\,\mathrm{e}^{-\mathrm{i}H_\mathrm{S}t}$ and similarly its conjugate transpose $O_\mathrm{H}^\dagger(t) = \mathrm{e}^{\mathrm{i}H_\mathrm{S}t}\,O_\mathrm{S}^\dagger\,\mathrm{e}^{-\mathrm{i}H_\mathrm{S}t}$ [124].

Returning to the YM theory introduced in section 2.1, the Euclidean Lagrangian after the Wick rotation $t \mapsto -\mathrm{i}x_4$ is

$$\mathcal{L}_{\mathrm{E}}[A] = \frac{1}{4}\mathrm{tr}\left(F_{\mu\nu}F^{\mu\nu}\right) . \tag{2.37}$$

Note that the definitions of the field strength $F_{\mu\nu}$ and the covariant derivative D_μ are not affected by the Wick rotation. The Euclidean continuum on-shell action of $\mathcal{N} = 1$ SYM theory is

$$S^{\mathrm{E}}_{\mathrm{SYM}} = \int \mathrm{d}^4x \ \mathrm{tr}\left(\frac{1}{4}F_{\mu\nu}F^{\mu\nu} + \frac{1}{2}\bar{\lambda}\not{D}\lambda + \frac{m}{2}\bar{\lambda}\lambda\right) . \tag{2.38}$$

To fulfill the Clifford algebra after the transition from Minkowski to Euclidean metric, the Dirac matrices have to be modified according to $\gamma^i \mapsto \mathrm{i}\gamma^i$, $\gamma^0 \mapsto \gamma^4$.

At this point, the Majorana nature of the spinors in $\mathcal{N} = 1$ SYM theory has to be addressed. In Minkowski spacetime the relation $\lambda = \lambda^C = \mathcal{C}\bar{\lambda}^{\mathrm{T}}$ resp. $\bar{\lambda} = \lambda^\dagger\gamma^0 = \lambda^{\mathrm{T}}\mathcal{C}$ hold. Consequently a Majorana spinor has only two complex parameters and is therefore sometimes referred to as a half Dirac spinor. Euclidean spacetime does not allow the definition of Majorana fermions [125]. Therefore a simple Wick rotation of the Minkowskian quantum field theory to imaginary times is not sufficient, unlike for Dirac spinors. A solution is to employ the Euclidean action (2.38) and to ensure the correct degrees of freedom for the spinor by requiring the formal Majorana condition $\bar{\lambda} = \lambda^{\mathrm{T}}\mathcal{C}$ while giving up the reality condition $\bar{\lambda} = \lambda^\dagger\gamma^0$ [126–128].

In the next chapter, the ingredients of lattice gauge theory are introduced. Together with the foundations presented in this chapter, the formulation of $\mathcal{N} = 1$ SYM theory on the lattice and the necessary fine-tuning process with Wilson fermions are addressed in section 3.2.

CHAPTER 3

Method

This chapter is intended to give an overview of the lattice techniques and methods in use. Additionally, some input parameters and our default values are discussed. For further details of the foundations, see textbooks like [124, 129–131].

In the first part of this chapter, we summarize basics of lattice field theory with $\mathcal{N} = 1$ SYM theory in mind. Therefore generality is restricted sometimes in favor of a straight-forward presentation. After section 3.1.1 about Monte Carlo sampling, we address the rational approximation, the conjugate gradient and the multigrid approach in 3.1.2. Further topics in 3.1.3 include the fundamentals of mass spectroscopy and approximations of the propagator. Subsequently, smearing methods for the improvement of the lattice interpolators are presented 3.1.4.

The second part 3.2 focuses on the additional requirements and implementation of $\mathcal{N} = 1$ SYM theory on the lattice. In detail, the gauge and fermion actions are introduced including their properties. Finally, the lattice observables are defined.

3.1 Lattice field theory

Lattice simulations are used to simulate theories like the $\mathcal{N} = 1$ SYM theory or QCD in a Euclidean spacetime. For our purpose we choose a four-dimensional hyper-cubic lattice Λ with lattice spacing a and coordinates $x^\mu = an^\mu, n \in \mathbb{Z}^4$. In temporal direction, we choose a lattice extent N_T, which is typically twice as long as the spatial extent N_S. We want to work at zero temperature and that way the effects of finite temperature (corresponding to the inverse temporal lattice length $L = aN_T$) are reduced. Furthermore the longer time extent is useful for the evaluation of the correlators in hadron spectroscopy.

For the lattice points, periodic boundary conditions are imposed leading to a torus with discrete translation invariance. Furthermore periodic boundary conditions are chosen for bosonic fields and spatial directions of fermionic fields. For the *temporal* direction of fermionic fields anti-periodic boundary conditions are required.

The lattice brings a natural regularization. On the one hand, the finite lattice spacing leads to a UV cutoff $\frac{1}{a}$ and on the other hand, the finite lattice volume $V = |\Lambda|$ is a regulator in the IR. At the same time, all lattice momenta can be restricted to the first Brillouin zone, $p_i = \frac{2\pi n_i}{aN_S},\ 0 \leq n_i < N_S$.

The fermionic fields of the theory under investigation are placed on the lattice sites. Two fermions of neighboring sites may interact for example through a discretized derivative. To build gauge invariant objects, parallel transporters between those sites are required. Such a parallel transporter contains the gauge field $A_\mu(x) = A^a_\mu(x)T^a$ and is defined as

$$\mathcal{U}_\mu(x) \equiv \mathrm{e}^{\mathrm{i}g\int_x^{x+\hat{\mu}} A_\mu(y)\,\mathrm{d}y^\mu}\,. \tag{3.1}$$

In this sense, the group-valued gauge links of the lattice are related to the underlying continuum gauge fields, which are elements of the Lie algebra. The trace of the product of gauge links along a closed path is a gauge invariant object, which will be used to construct the discretized bosonic actions. A so-called plaquette

$$\mathcal{U}_{\mu\nu}(n) \equiv \mathcal{U}_\mu(n)\,\mathcal{U}_\nu(n+\hat{\mu})\,\mathcal{U}_{-\mu}(n+\hat{\mu}+\hat{\nu})\,\mathcal{U}_{-\nu}(n+\hat{\nu}) \tag{3.2}$$

is the product of four links along the shortest loop.

3.1.1 Monte Carlo sampling

For the numerical simulation, the Euclidean action S_E of eq. (2.38) is discretized on a spacetime lattice Λ. The corresponding Euclidean partition functions is

$$Z = \int_\Lambda \mathcal{D}\mathcal{U}\,\mathcal{D}\lambda\,\mathrm{e}^{-S_\mathrm{E}[\mathcal{U},\lambda]}\,. \tag{3.3}$$

Since the Majorana fermions $\bar{\lambda} = \lambda^\mathrm{T}\mathcal{C}$ and λ are not independent, the path integral measure contains only $\mathcal{D}\lambda$. With the partition function, the expectation value

$$\langle O\rangle = \frac{1}{Z}\int_\Lambda \mathcal{D}\mathcal{U}\,\mathcal{D}\lambda\,O[\mathcal{U},\lambda]\,\mathrm{e}^{-S_\mathrm{E}[\mathcal{U},\lambda]} \tag{3.4}$$

of an observable $O[\mathcal{U},\lambda]$ can be defined, which is a very high-dimensional integral. As a statistical Boltzmann weight, the exponential suppresses a lot of the configuration space and thus the integral can be evaluated efficiently, for example with importance sampling [132, 133]. Path integrals in theories with fermions contain Grassmann numbers and the application of importance sampling is difficult. A possibility would be a polymer representation, but due to the Pauli principle the contributions have alternating signs [124, 134, 135]. Thus it is favorable to calculate the Grassmann integral analytically and sample the effective bosonic theory with Markov Chain Monte Carlo (MCMC)

methods [124]. Integrating out the Majorana fermions[4] gives the partition function [136]

$$Z = \int_\Lambda \mathcal{D}\mathcal{U}\,\mathcal{D}\lambda\, \mathrm{e}^{-S_\mathrm{B}[\mathcal{U}]-\frac{1}{2}\mathrm{tr}(\lambda^\mathrm{T}\mathcal{C}D[\mathcal{U}]\lambda)} \propto \int_\Lambda \mathcal{D}\mathcal{U}\,\mathrm{Pf}(\mathcal{C}D[\mathcal{U}])\,\mathrm{e}^{-S_\mathrm{B}[\mathcal{U}]}\,. \tag{3.5}$$

Note that the generalized trace in the previous equation contains besides the summation of the internal indices also the sum over spacetime. Up to a sign, the occurring Pfaffian is proportional to the square root of the determinant. Therefore, a Majorana fermion is sometimes called a half Dirac spinor. In order to apply algorithms, which require Hermitean matrices, we define $M \equiv DD^\dagger$ and rewrite the Pfaffian [137]

$$\mathrm{Pf}(\mathcal{C}D[\mathcal{U}]) = \mathrm{phase}\Big(\mathrm{Pf}(\mathcal{C}D[\mathcal{U}])\Big)\Big|\mathrm{Pf}(\mathcal{C}D[\mathcal{U}])\Big| = \mathrm{phase}\Big(\mathrm{Pf}(\mathcal{C}D[\mathcal{U}])\Big)\Big|(\det M[\mathcal{U}])^{1/4}\Big|\,. \tag{3.6}$$

If $\mathrm{phase}\Big(\mathrm{Pf}(\mathcal{C}D[\mathcal{U}])\Big)$ is complex or negative, then a so-called sign-problem occurs and the interpretation of the measure as a Boltzmann weight loses its validity. A mild sign-problem may be compensated by reweighting [138].

An explicit calculation of the occurring Pfaffian in eq. (3.5) would be numerically too costly. By introducing so-called pseudofermions, the Pfaffian can be approximated as a Gaussian distribution [139], such that

$$Z \propto \int_\Lambda \mathcal{D}\mathcal{U}\,\mathcal{D}\phi\, e^{-S_\mathrm{B}[\mathcal{U}]-\mathrm{tr}\left(\phi^\dagger M^{-1/4}\phi\right)}\,. \tag{3.7}$$

Pseudofermions are bosonic fields with the same degrees of freedom as the fermions they describe. To approximate the fourth root, a rational approximation (see section 3.1.2) is performed.

After this detour about the treatment of the fermionic fields on the lattice, we return to the Monte Carlo procedure to calculate an observable, see (3.4). A Markov chain describes a stochastic process, whose future probabilities depend only on its current state. Additionally, the detailed balance condition is requested such that the stochastic process is reversible under infinitesimal time-reversal. On the resulting field configurations $C_n[\mathcal{U}]$ of a reversible Markov chain, the ensemble mean of an observable

$$\langle O\rangle \approx \frac{1}{N}\sum_{n=1}^{N} O[C_n] \tag{3.8}$$

is an approximation of the expectation value (3.4). The Markov chain guarantees that in the limit $N \to \infty$ the correct expectation value is approached. An estimate for the deviation with N configurations [129, 133] is

$$\langle O\rangle - \frac{1}{N}\sum_{n=1}^{N} O[C_n] \propto \mathcal{O}\left(\frac{1}{\sqrt{N}}\right)\,. \tag{3.9}$$

[4] Dirac fermions will not be discussed here. Similar equations as for Majorana fermions hold and the determinant instead of the Pfaffian appears. For further details, many textbooks for lattice QCD are available [124, 129–131].

For theories with spinors, the fermionic expectation value is given by Wick's theorem as the solution of an integral of Gaussian type with Grassmann numbers [140]. Within the scope of this thesis we will encounter Wick contractions with two, resp. four, Majorana[5] spinors (written with multi-indices):

$$\langle \lambda_I \bar{\lambda}_J \rangle_{\mathrm{F}} = D^{-1}_{IJ} \,, \qquad \langle \lambda_I \bar{\lambda}_J \lambda_K \bar{\lambda}_L \rangle_{\mathrm{F}} = D^{-1}_{IJ} D^{-1}_{KL} - D^{-1}_{IK} D^{-1}_{JL} + D^{-1}_{IL} D^{-1}_{JK} \,. \tag{3.10}$$

Higher orders can be computed from the generating functional

$$W[\theta] = \int \mathcal{D}\lambda \, \mathrm{e}^{-\frac{1}{2}\mathrm{tr}\bar{\lambda} D \lambda + \mathrm{tr}\bar{\theta}\lambda} = \int \mathcal{D}\lambda \, \mathrm{e}^{-\frac{1}{2}\mathrm{tr}\lambda^{\mathrm{T}} \mathcal{C} D \lambda + \frac{1}{2}\mathrm{tr}\,\theta^{\mathrm{T}} \mathcal{C} \lambda + \frac{1}{2}\mathrm{tr}\lambda^{\mathrm{T}} \mathcal{C}\theta} \propto \mathrm{Pf}(\mathcal{C}D)\, \mathrm{e}^{\frac{1}{2}\mathrm{tr}\,\theta^{\mathrm{T}} \mathcal{C} D^{-1} \theta} \,.$$

Next, we will present an efficient algorithm for obtaining configurations of a Euclidean action with fermions. The Hybrid Monte Carlo (HMC) algorithm is often used to generate configurations according to the Markov chain condition [141]. If a rational approximation is required like in eq. (3.7), then the slightly modified algorithm is called Rational Hybrid Monte Carlo (RHMC) [142]. For each configuration, Hamiltonian equations of motion resembling molecular dynamics are integrated along a fictive trajectory. The molecular dynamics method combines classical dynamics with the ergodicity hypothesis to sample the correct statistical distribution [143, 144].

At the beginning of a (R)HMC step, the pseudofermion field $\phi = D\chi$ is generated from Gaussian distributed fields χ. Afterwards the (fictive) canonical conjugated momenta P of the Hamiltonian

$$H[P, \mathcal{U}] = S_{\mathrm{G}}[\mathcal{U}] + \frac{P^2}{2} + \phi^\dagger (DD^\dagger)^{-1/4} \phi \tag{3.11}$$

are initialized according to a Gaussian probability distribution. Then the molecular dynamical equations of the momenta P and gauge fields $\mathcal{U}$ are evolved. At the end of the trajectory, a Metropolis step [145] with probability $\min\left(1, \mathrm{e}^{-\delta H}\right)$ decides whether the configuration is accepted or rejected. The calculation of

$$\delta H = H' - H = \frac{P'^2}{2} - \frac{P^2}{2} + S_{\mathrm{G}}[\mathcal{U}'] - S_{\mathrm{G}}[\mathcal{U}] + \phi^\dagger \left((D'D'^\dagger)^{-1/4} - (DD^\dagger)^{-1/4} \right) \phi \tag{3.12}$$

requires the calculation of $(DD^\dagger)^{-1/4}$, which we calculate with a rational approximation (see section 3.1.2). This final accept-reject step avoids that numerical integration errors propagate along the Markov chain. Nevertheless, the errors of the integrator of the Hamiltonian molecular dynamics influence the acceptance rate. To fulfill the detailed balance condition, the integrator has to be (up to machine precision) time-reversible and energy-conserving. Therefore, symplectic integrators are well-suited.

Several parameters enter the RHMC algorithm and their values influence how many independent configurations can be created with a fixed amount of computational time.

[5] Note that we restrict ourselves here again to Majorana spinors. For Dirac spinors, see textbooks such as [124, 129–131].

Our default values are summarized in table 3.1. Generally we measure on every fifth configuration to reduce auto-correlation. In total we need in three places a rational approximation: Firstly in the creation of the pseudofermions, secondly in the calculation of the force in the molecular dynamics and thirdly in the accept-reject step. The rational approximation for the pseudofermions and the accept-reject step should be performed with machine precision, whereas for the molecular dynamics a simpler approximation is sufficient. The latter choice is especially important, because the force has to be calculated very often and an appropriate choice saves computational time. For all approximations, the interval $I = [\lambda_{\min}, \lambda_{\max}]$ is chosen such that the smallest eigenvalue as well as the largest eigenvalue of the operator M are enclosed. Table 3.2 summarizes the default values of the mentioned parameters of the rational approximation.

If machine precision is used for the pseudofermions and the acceptance step, then the RHMC algorithm is as exact as the HMC algorithm. "Exact" is related to the creation of the Markov chain and its convergence [146]. The numerical simulations contain a statistical uncertainty based on the finite ensemble size and it can be reduced subsequently by the creation of additional configurations. On top of that, systematic errors enter our results. The influence of the lattice spacing and the resulting discretization errors can be reduced by choosing a smaller lattice constant or an improved lattice action (see section 3.2 for further details). Additionally, the finite lattice volume may lead to a shift of the particle masses as addressed in section 5.5.

Table 3.1: HMC parameters with their default values and further test values, which were used to check if the default values are well-suited. The quotient $\delta T = T/N$ defines the size of a single integration step. The second order integrator is the leap-frog integrator [147], the improved second order was published in [148], the fourth order can be found in [149] and the sixth order is taken from [150].

	default	test
trajectory length T	0.6	0.4, 0.8, 1.2, 1.6, 2.0
time steps N along trajectory	15	8, 12, 16
order for fermion field	improved 2	2, 4
order for gauge field	4	improved 2, 6

3.1.2 Rational approximation, conjugate gradient and multigrid

Many inversions of the linear system $D \cdot x = y$ with the Dirac operator D and a given y are required to generate the ensembles and perform measurements on them. By integrating out the fermions, pseudofermions are introduced and their calculation requires the Dirac

Table 3.2: Parameters of the rational approximation. Therefore N_R coefficients are used to approximate the function in the interval $[\lambda_\mathrm{min}, \lambda_\mathrm{max}]$ with the indicated digits for the determination of the Remez coefficients and the given precision to calculate the inverse.

	N_R	digits	λ_min	λ_max	precision
pseudofermions	25	100	10^{-5}	10	10^{-16}
force	10	60	10^{-4}	10	10^{-2}
acceptance step	25	100	10^{-5}	10	10^{-16}

matrix to a negative rational power, M^{-q} [139]. For $0 < q < 1$, a rational approximation

$$r(M) = M^{-q} \approx \alpha_0 + \sum_{r=1}^{N_\mathrm{R}} \frac{\alpha_r}{M + \beta_r \mathbb{1}} \tag{3.13}$$

can approximate the rational power after the coefficients α_r, β_r have been specified, e.g. with the Remez algorithm [151, 152]. Table 3.2 summarizes the default parameters, which are used for the various rational approximations to calculate the pseudofermions, the force and the acceptance step [137]. Each summand of the rational approximation needs an inversion. An exact calculation of this inverse is numerically too costly for such a huge matrix like the Dirac operator. Therefore, an iterative procedure is used and for Hermitean, positive definite matrices the CG algorithm [153] is well-suited. With the multi-shift CG solver all inversions of the rational approximation in eq. (3.13) can be calculated simultaneously with only a small overhead [154]. This variant of the CG algorithm utilizes that one Krylov space for all shifted systems $(M + \beta_r \mathbb{1}) \cdot x = y$ is sufficient and it needs like the original algorithm one single matrix-vector product per iteration. The condition number is the quotient of the maximal and minimal eigenvalue (by absolute value), $\kappa = \frac{|\lambda_\mathrm{max}|}{|\lambda_\mathrm{min}|}$, and an indicator how many iterations are required for the inversion.

Preconditioning is a possibility to accelerate the inversion by reducing the condition number. There exist two types of preconditioning, which can be applied independently, either as factorization of the fermion determinant in eq. (3.6) or in the inversion. Even-odd preconditioning [155–157] is used in both cases and independently of the usage of CG or multigrid algorithms (see below).

For the measurement of the mesonic observables on the lattice, a significant part of the runtime is spent to invert the Wilson Dirac operator. For a stochastic estimator one inversion is required and for a point source one per internal index, of which there are in total $\dim_\mathrm{f} \cdot \dim_\mathrm{s} \cdot \dim_\mathrm{c}$. In all our simulations only one flavor is present, $\dim_\mathrm{f} = 1$, and the spinor space dimension is $\dim_\mathrm{s} = 4$ in four spacetime dimensions. For the fundamental representation of $\mathrm{SU}(N_\mathrm{c})$ the color space has dimension $\dim_\mathrm{c}^\mathrm{fund} = N_\mathrm{c}$ and in the adjoint representation $\dim_\mathrm{c}^\mathrm{adj} = N_\mathrm{c}^2 - 1$. If γ_5-Hermiticity is not fulfilled (this is the case for $m_5 \neq 0$), then the backward running propagator has to be calculated separately

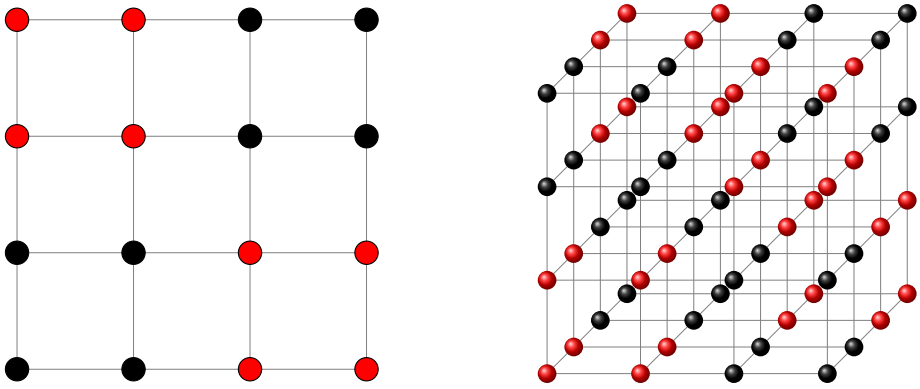

Figure 3.1: Left/Right: Red and black blocks of size 2^d in $d = 2/d = 3$ used in the Schwarz alternating procedure. In the algorithm all the red blocks are treated at once in alternation with the black blocks.

and the number of inversions for the point sources doubles. In the measurements of the observables, several inversions of the constant Dirac operator with different right-hand sides y are performed. In this context so-called multigrid algorithms can accelerate the calculations significantly compared to the CG algorithm. More precisely, we use the domain decomposition adaptive algebraic multigrid (DDαAMG) library [158, 159]. Only one setup of the coarsening is required for the measurements, where the Wilson Dirac operator stays constant.

Generally, the inversion of a matrix becomes harder when its condition number grows. In lattice simulations this happens typically when the critical point is approached. This so-called critical slowing down can be reduced with a multigrid algorithm. Its strength lies in the separate treatment of high and low modes by an alternating application of a domain decomposition smoother and a coarse-grid correction [160]. With the Schwarz alternating procedure (SAP) the lattice is decomposed into blocks (see figure 3.1), which is useful for the inversion of the UV-modes [161, 162]. The inverse block size acts as a cutoff for the low modes. Additionally to the domain decomposition smoother, a coarse-grid correction is performed to approximate the small eigenvalues and address the IR-modes that way. Therefore, a coarse-graining operator projects the current approximation of the vector x to a coarser lattice. The low modes are preserved mainly and on the coarse lattice the discretized Dirac equation $D \cdot x = y$ needs to be solved only with low precision. Finally the solution is projected back to the finer lattice and used as a starting guess for SAP.

The efficiency of this decomposition is based on the local coherence [163]. That means those eigenvectors of the Dirac operator, which correspond to small eigenvalues, have the tendency to agree on many blocks. Consequently the eigenvectors with small eigenvalues can be approximated with just $\mathcal{O}(20)$ eigenvectors [164] and with them the projection operator to the coarse grid as well as the coarse-grid Dirac operator are calculated. This

setup needs to be calculated only once in the beginning and can be used afterwards for all right-hand sides [165]. A benchmark test for $\mathcal{N} = 1$ SYM theory with a two-level multigrid can be found in section 5.7.2. In general the DDαMG allows more levels when the lattice is large enough.

For the generation of configurations multi-shift CG is our default solver, but we started to test the DDαAMG within the molecular dynamics of the RHMC. Along the Monte Carlo trajectory the gauge fields and the Wilson Dirac operator change. Therefore much more time-consuming setups of the coarsening operator are necessary. In addition, the precision for the inversion of the force is typically only 10^{-2}. Consequently the inversion stops after a few iterations and the ratio between setup time and inversion time is much higher than in the measurements. Finally, the reversibility may suffer since an update of the coarsening scheme in the trajectory propagates information. In [166] this problem was discussed in the context of the Schwarz Alternating Procedure (SAP).

The DDαMG solver has been extended to twisted-mass fermions [158], the rational approximation of a single quark [167] and a Davidson-type method to solve shifted linear systems efficiently [168].

3.1.3 Mass spectroscopy

To determine masses of compound particles on the lattice, two-point functions are considered. Using a basis $|n'\rangle$ we determine the expectation value of two interpolators O_i (corresponding to Hilbert space operators $\hat{O}_i$) separated by a temporal distance [129]:

$$\begin{aligned}\langle O_2(t)O_1(0)\rangle_T &= \frac{1}{Z_T}\sum_{n,n'}\langle n'|\mathrm{e}^{-(T-t)\hat{H}}\hat{O}_2|n\rangle\langle n|\mathrm{e}^{-t\hat{H}}\hat{O}_1|n'\rangle \\ &= \frac{1}{Z_T}\sum_{n,n'}\langle n'|\hat{O}_2|n\rangle\,\mathrm{e}^{-(T-t)E_{n'}}\langle n|\hat{O}_1|n'\rangle\,\mathrm{e}^{-tE_n} \\ &= \frac{\sum_{n,n'}\langle n'|\hat{O}_2|n\rangle\langle n|\hat{O}_1|n'\rangle\,\mathrm{e}^{-t(E_n-E_0)}\mathrm{e}^{-(T-t)(E_{n'}-E_0)}}{1+\mathrm{e}^{-T(E_1-E_0)}+\mathrm{e}^{-T(E_2-E_0)}+\ldots}\,. \end{aligned} \tag{3.14}$$

For a large temporal lattice extent T, the correlator is the sum of exponentials,

$$\lim_{T\to\infty}\langle O_2(t)O_1(0)\rangle_T = \sum_n\langle 0|\hat{O}_2|n\rangle\langle n|\hat{O}_1|0\rangle\,\mathrm{e}^{-t\Delta E_n}\,, \tag{3.15}$$

where we introduced $\Delta E_n \equiv E_n - E_0$ relative to the vacuum.[6] In order to extract masses from the lattice operators they have to be projected in momentum space

$$\tilde{O}(\vec{p},t) = \frac{1}{\sqrt{|\Lambda_3|}}\sum_{\vec{n}\in\Lambda_3} O(\vec{n},t)\,\mathrm{e}^{-\mathrm{i}a\vec{n}\cdot\vec{p}}$$

[6] Only energies relative to the vacuum energy E_0 occur, similar to an experiment where only energy differences can be measured. The absolute value of the vacuum energy is arbitrary since we can always add a constant term to the Hamiltonian without affecting the expectation value (3.14) [131].

to zero momentum. Projecting to $\vec{p} = \vec{0}$ corresponds to averaging the operator over the spatial lattice $\Lambda_3 = \{\vec{n} = (n_1, n_2, n_3) \,|\, n_i = 0, 1, \ldots, N_S\}$ with $t = \text{const}$ (a time-slice):

$$\tilde{O}(\vec{p} = \vec{0}, t) = \frac{1}{\sqrt{|\Lambda_3|}} \sum_{\vec{n} \in \Lambda_3} O(\vec{n}, t) \equiv S(t)\,. \tag{3.16}$$

Taking into account the boundary conditions and defining the renormalized mass $m_\mathrm{R} \equiv E_1 - E_0$ as well as the coefficients $a_0 = |\langle 0|S(t)|0\rangle|^2$, $a_1 = |\langle 1|S(t)|0\rangle|^2$ we get for $(E_2 - E_1)t \gg 1$ the symmetric/antisymmetric correlator

$$\begin{aligned}\langle S^\dagger(t_2) S(t_1)\rangle &= a_0 + a_1 \left(\mathrm{e}^{-|t_2 - t_1| m_\mathrm{R}} \pm \mathrm{e}^{-(T - |t_2 - t_1|) m_\mathrm{R}}\right) \\ &= a_0 + 2a_1\, \mathrm{e}^{-T m_\mathrm{R}/2} \begin{Bmatrix}\cosh \\ \sinh\end{Bmatrix} \left(m_\mathrm{R} \left(\frac{T}{2} - |t_2 - t_1|\right)\right),\end{aligned}$$

with the ground state as leading contribution [124]. To extract the mass we measure the connected two-point function

$$C(|t_2 - t_1|) = \langle S^\dagger(t_2) S(t_1)\rangle - \langle S^\dagger(t_2)\rangle\langle S(t_1)\rangle = 2a_1\, \mathrm{e}^{-T m_\mathrm{R}/2} \begin{Bmatrix}\cosh \\ \sinh\end{Bmatrix} \left(m_\mathrm{R} \left(\frac{T}{2} - |t_2 - t_1|\right)\right),$$

where the constant a_0 is canceled, and fit the correlator directly to the hyperbolic function [131]. In our fits we use the functions

$$\cosh1(t) = \mathrm{e}^{c_1} \cdot \cosh\left(d_1(T/2 - t)\right), \tag{3.17}$$

$$\cosh2(t) = \mathrm{e}^{c_1} \cdot \cosh\left(d_1(T/2 - t)\right) + \mathrm{e}^{c_2} \cdot \cosh\left(d_2(T/2 - t)\right), \tag{3.18}$$

$$\sinh1(t) = \mathrm{e}^{c_1} \cdot \sinh\left(d_1(T/2 - t)\right), \tag{3.19}$$

$$\sinh2(t) = \mathrm{e}^{c_1} \cdot \sinh\left(d_1(T/2 - t)\right) + \mathrm{e}^{c_2} \cdot \sinh\left(d_2(T/2 - t)\right), \tag{3.20}$$

with exponentials to guarantee positive factors. We refer to $d = \min(d_1, d_2)$ as the *dominant mass contribution*, which corresponds to the ground state mass on sufficiently large lattices. With d^*, we denote the mass contribution of the first excited state. To handle excited contributions at the border of the correlator as well as statistical noise and lattice artifacts in the center of the correlator, we adapt the fit range to $t \in [t_1, T/2 - t_2]$ and $t \in [T/2 + t_2, T - t_1]$. In section 5.5, the fit window $t_\mathrm{cut} = (t_1, t_2)$ will be discussed in the context of finite size effects. For an estimate of the fit interval, the effective mass m_eff is a helpful quantity. Calculated from

$$\frac{C(t)}{C(t+1)} = \frac{\cosh\left(m_\mathrm{eff}(T/2 - t)\right)}{\cosh\left(m_\mathrm{eff}(T/2 - (t+1))\right)} \tag{3.21}$$

for each t, it shows a plateau in the range where the ground state is the dominant contribution. An analogue equation with sinh can be used for antisymmetric correlators.

Approximating the propagator

To compute the correlation functions $C(t)$, we need the propagator $D_{\mathrm{W}}^{-1}(n',n)$ of the large Wilson Dirac operator. The explicit inversion of this $N_{\mathrm{int}}V \times N_{\mathrm{int}}V$ matrix would be computationally costly and very memory consuming. Although the Wilson Dirac operator is sparse, its inverse is not. For the calculation of the connected contributions it is sufficient to invert only one column, because the propagators on a gauge configuration are correlated. Therefore we place a point source $[S_0^{n_0,\alpha_0,a_0}(n)]_{\alpha a} = \delta_{n,n_0}\delta_{\alpha,\alpha_0}\delta_{a,a_0}$ for each internal degree of freedom at the position of the interpolator $O(n_0)$ and calculate with an iterative solver the point-to-all-propagator [129, 130]

$$[D_{\mathrm{W}}^{-1}(n',n_0)]_{\beta b,\alpha_0 a_0} = \sum_{n,\alpha,a} [D_{\mathrm{W}}^{-1}(n',n)]_{\beta b,\alpha a}[S_0^{n_0,\alpha_0,a_0}(n)]_{\alpha a}\,. \tag{3.22}$$

If the Wilson Dirac operator is γ_5-Hermitean, then the backward running propagator can be calculated simply by

$$[D_{\mathrm{W}}^{-1}(n',n_0)]^*_{\beta b,\alpha a} = \sum_{\mu,\nu} [\gamma_5]_{\alpha,\mu}[D_{\mathrm{W}}^{-1}(n_0,n')]_{\mu a,\nu b}[\gamma_5]_{\nu,\beta}\,. \tag{3.23}$$

For the disconnected contributions to the correlator, we use stochastic estimators [169, 170]. Based on N_{se} column vectors η^n of length $N_{\mathrm{int}}V$ the inverse of the Dirac Wilson operator can be approximated. The stochastic vectors are filled with white noise, that means their ensemble average fulfills

$$\langle \eta_i \rangle = \frac{1}{N_{\mathrm{se}}}\sum_{n=1}^{N_{\mathrm{se}}} [\eta^n]_i \approx 0 \qquad \text{and} \qquad \langle \eta_i^\dagger \eta_j \rangle = \frac{1}{N_{\mathrm{se}}}\sum_{n=1}^{N_{\mathrm{se}}} [\eta^n]_i^*[\eta^n]_j \approx \delta_{ij}\,. \tag{3.24}$$

Then we can invert the N_{se} equations $D_{\mathrm{W}} \cdot \chi^n = \eta^n$ and calculate the inverse Wilson Dirac operator by the ensemble average

$$[D_{\mathrm{W}}]^{-1}_{ij} \approx \sum_{k=1}^{N_{\mathrm{int}}V} [D_{\mathrm{W}}]^{-1}_{ik}\langle \eta_j^\dagger \eta_k \rangle = \langle \eta_j^\dagger \chi_i \rangle\,. \tag{3.25}$$

For the random noise, we chose complex random numbers $\frac{1}{\sqrt{2}}(\pm 1 \pm \mathrm{i})$ isomorphic to $\mathbb{Z}_4$. The equations (3.24)-(3.25) are exact in the limit $N_{\mathrm{se}} \to \infty$, but a finite number of stochastic estimators is sufficient for an adequate approximation of the so-called all-to-all-propagator. Typically, we perform the inversions involved in the calculation of the point sources and stochastic estimators with a precision of 10^{-12}.

3.1.4 Smearing

Many observables are hard to extract due to their bad signal-to-noise ratio. One possibility to improve this is to increase the ensemble size and reduce that way the impact of the

gauge field fluctuations. Additionally it is often beneficial to improve the overlap of the lattice operator and the physical state, which is measured. Typically this is done with smearing of the gauge fields and/or the fermions. With stout smearing

$$\mathcal{U}_\mu(n) \mapsto \mathcal{U}'_\mu(n) = \mathrm{e}^{\mathrm{i}B_\mu(n)}\,\mathcal{U}_\mu(n)\,, \tag{3.26}$$

the gauge links are broadened, which results in a suppression of unwanted states and excitations [171]. The matrix

$$B_\mu(n) = \frac{\mathrm{i}}{2}\left(\Omega^\dagger_\mu(n) - \Omega_\mu(n)\right) - \frac{\mathrm{i}}{2N_\mathrm{c}}\mathrm{tr}\left(\Omega^\dagger_\mu(n) - \Omega_\mu(n)\right) \tag{3.27}$$

contains $\Omega_\mu(n) = \tilde{W}_\mu(n)\,\mathcal{U}^\dagger_\mu(n)$, which is defined with the staples

$$\tilde{W}_\mu(n) = \sum_{\substack{\nu=1\\ \nu\neq\mu}}^{4} \rho_{\mu\nu}\Big(\mathcal{U}_\nu(n)\,\mathcal{U}_\mu(n+\hat{\nu})\,\mathcal{U}^\dagger_\nu(n+\hat{\mu}) + \mathcal{U}^\dagger_\nu(n-\hat{\nu})\,\mathcal{U}_\mu(n-\hat{\nu})\,\mathcal{U}_\nu(n-\hat{\nu}+\hat{\mu})\Big) \tag{3.28}$$

and the weights $\rho_{mn} = \rho$, $\rho_{4\mu} = \rho_{\mu 4} = 0$. Thus only the spatial directions are smeared and the traceless Hermitean matrix $B_\mu(n)$ guarantees that the smeared link is again an element of $\mathrm{SU}(N_\mathrm{c})$. In our simulations, we employ stout smearing for the mass spectroscopy of the gluino-glue and glueballs (see section 3.2.4 for the definition of these observables and sections 6.2.2 and 6.2.3 for their results). Alternative gauge field smearing procedures are APE smearing [172] and HYP smearing [173].

Also the shape of the fermionic source can be smeared to improve the matching with the physical size [174, 175]. In order to approximate a Gaussian shape, the starting point for the Wuppertal smearing [176–178] is the three-dimensional Klein-Gordon equation

$$K(n,n')\,S(n') = S_0^{n_0,\alpha_0,a_0}(n) \text{ with } K = \mathbb{1} - \kappa H\,. \tag{3.29}$$

This equation contains the hopping parameter $\kappa = \frac{1}{2(4+m)}$, the Hermitean hopping matrix

$$H(\vec{n},\vec{n}') = \sum_{i=1}^{3}\left(\mathcal{V}_i(\vec{n},n_t)\,\delta(\vec{n}+\hat{i},\vec{n}') + \mathcal{V}^\dagger_i(\vec{n}-\hat{i},n_t)\,\delta(\vec{n}-\hat{i},\vec{n}')\right)\,, \tag{3.30}$$

the smeared source with the components $[S(n)]_{\alpha,a}$ and the point source with $[S_0^{n_0,\alpha_0,a_0}(n)]_{\alpha,a} = \delta_{n,n_0}\delta_{\alpha,\alpha_0}\delta_{a,a_0}$. In the hopping matrix (3.30), the time coordinate $n_t = \mathrm{const} = [n_0]_4$ has the temporal value of the point source and the gauge link $\mathcal{V}_i$ is for $\mathcal{N}=1$ SYM theory in the adjoint representation, see definition in eq. (3.39). Instead of inverting K explicitly, the inverse is approximated by N_s Jacobi iterations with smearing parameter κ_s:

$$S^{(k)}(\vec{n},t) = (\mathbb{1} + \kappa_s H)\,S^{(k-1)}(\vec{n},t)\,. \tag{3.31}$$

Thus the smearing matrix is

$$M = (\mathbb{1} + \kappa_s H)^{N_s} \tag{3.32}$$

and the smeared source is calculated as $S(n) = M\, S_0^{n_0,\alpha_0,a_0}(n)$. Figuratively, the neighboring sites of the fixed time-slice of the source at n_t get connected by gauge links. Another similar approximation called Jacobi smearing [129, 179] uses the smearing matrix

$$M = \sum_{k=0}^{N_s} \kappa_s^k H^k \tag{3.33}$$

and a third possibility is the series expansion of the exponential $\mathrm{e}^{\kappa_s H}$ to the order $\mathcal{O}(\kappa_s^{N_s})$:

$$M = \sum_{k=0}^{N_s} \frac{1}{k!} (\kappa_s H)^k \,. \tag{3.34}$$

Like the gauge field smearing, source smearing does not influence the time-direction and acts only in the color space. Additional gauge field smearing may improve the fermion smearing through the gauge links entering the hopping matrix in eq. (3.30). We used mainly Jacobi smearing for the evaluation of the mesonic states to improve the noise of their disconnected contributions. A comparison of the three discussed types of fermion smearing showed no relevant difference, see section 5.7.1.

3.2 $\mathcal{N} = 1$ SYM theory on the lattice

The formulation of $\mathcal{N} = 1$ SYM theory on the lattice is challenging. Several important symmetries such as the (remnant) chiral symmetry are broken by the lattice. Other symmetries like the rotations and translations are realized only as a discrete subgroup of their continuum counterparts. The breaking of translation invariance implies furthermore the breaking of supersymmetry, see eq. (2.16). Another argument for broken supersymmetry is the failure of the Leibniz rule on the lattice [19]. Thus the supersymmetry transformation of the Lagrangian is not a total derivative at finite lattice spacing a. However, the additional terms proportional to a are irrelevant and vanish in the continuum limit [180].

Different lattice formulations are feasible, depending on the discretization of the continuum action and in particular on the choice of lattice fermions. In the present work we shall use the lattice formulation with Wilson fermions introduced by Curci and Veneziano [181]. At finite lattice spacing, supersymmetry and chiral symmetry are broken and this leads to a relevant counter-term, which is proportional to the gluino mass term. To compensate this, an explicit gluino mass term is added and fine-tuned such that the (renormalized) gluino becomes massless in the continuum limit. Since the gluino mass term is the only relevant operator, supersymmetry and chiral symmetry will be restored in this limit.

Unfortunately, confinement prevents the direct measurement of the gluino. Here we follow Veneziano and Yankielowicz who proposed to monitor instead the (unphysical)

adjoint pion mass, defined in a partially quenched approximation, similarly as in 1-flavor QCD [105]. Its mass squared $m^2_{\text{a-}\pi} \propto m^{\text{R}}$ is proportional to the renormalized gluino mass, which can be calculated in partially quenched chiral perturbation theory [39].[7] This quantity requires only low statistics and is easy to compute. To arrive at the continuum theory, several steps are required. First of all, the simulations are performed at different bare mass parameters to extrapolate to the critical point, where the adjoint pion and renormalized gluino have minimal mass. After that extrapolation the thermodynamic limit is required to remove finite volume effects. Finally, the continuum limit is performed to restore the continuum symmetries, among them supersymmetry and chiral symmetry.

Different lattice formulations of a continuum theory vary in their discretization errors and how fast the correct continuum limit is approached. The lattice action $S_{\text{lat}} = S_{\text{g}} + S_{\text{f}}$ consists of discretized gauge and fermionic actions. Next, the different gauge actions are presented and afterwards the fermion actions are addressed.

3.2.1 Gauge actions

In the scope of this work, we used sometimes the Wilson gauge action and mostly the Symanzik-improved Lüscher-Weisz gauge action.

Wilson gauge action

Defining the lattice coupling as $\beta = \frac{2N_{\text{c}}}{g^2}$, the Wilson gauge action is calculated via

$$S_{\text{g}}^{\text{W}}[\mathcal{U}] = \frac{\beta}{N_{\text{c}}} \sum_{\square} \text{tr}_{\text{c}} \left(\mathbb{1} - \text{Re}\mathcal{U}_{\square} \right) , \tag{3.35}$$

with the sum over all plaquettes $\square$ [183]. This lattice gauge action has discretization artifacts of order $\mathcal{O}(a^2)$ in the lattice spacing [129].

Symanzik-improved gauge action

With improved lattice actions, the discretization errors can be reduced and/or the symmetries can be enhanced [184, 185]. The Symanzik-improved lattice gauge action with rectangular paths over two plaquettes $\square\square$ is

$$S_{\text{g}}[\mathcal{U}] = \frac{\beta}{N_{\text{c}}} \left(c_0 \sum_{\square} \text{tr}_{\text{c}}(\mathbb{1} - \text{Re}\mathcal{U}_{\square}) + c_1 \sum_{\square\square} \text{tr}_{\text{c}}(\mathbb{1} - \text{Re}\mathcal{U}_{\square\square}) \right) . \tag{3.36}$$

The coefficients $c_0 = 1$ and $c_1 = 0$ would correspond to the Wilson gauge action (3.35). Choosing $c_0 = 1 - 8c_1$ and $c_1 = -\frac{1}{12}$ leads to a reduction of lattice artifacts and this choice

[7] The analog Gell-Mann-Oakes-Renner relation of QCD is $m_\pi^2 \propto m_q$ [182].

is known as the Lüscher-Weisz gauge action [84]:

$$S_{\mathrm{g}}^{\mathrm{LW}}[\mathcal{U}] = \frac{\beta}{N_{\mathrm{c}}} \left(\frac{5}{3} \sum_{\square} \mathrm{tr_c}(\mathbb{1} - \mathrm{Re}\,\mathcal{U}_{\square}) - \frac{1}{12} \sum_{\square\square} \mathrm{tr_c}(\mathbb{1} - \mathrm{Re}\,\mathcal{U}_{\square\square}) \right) . \tag{3.37}$$

Another variant with $c_0 = 3.648$ and $c_1 = -0.331$ was published by Iwasaki [186]. Note that the factor c_0 should be taken into account when the gauge coupling of a Symanzik-improved gauge action is compared to results with the Wilson gauge action.

3.2.2 Fermion actions

The generic fermionic action

$$S_{\mathrm{f}}[\lambda, \bar{\lambda}, \mathcal{U}] = \frac{a^4}{2} \sum_{n,n' \in \Lambda} \mathrm{tr_c}\, \bar{\lambda}(n) D(n,n') \lambda(n') \tag{3.38}$$

for the Majorana field (the gluino part) contains the lattice Dirac operator with gauge links in the adjoint representation

$$[\mathcal{V}_\mu(n)]^{ab} \equiv \mathrm{tr_c} \left[\mathcal{U}_\mu^\dagger(n) T^a \mathcal{U}_\mu(n) T^b \right] , \quad a,b = 1, \ldots, N_{\mathrm{c}}^2 - 1 . \tag{3.39}$$

Here the gauge links $\mathcal{U}_\mu(n)$ enter in the fundamental representation and T^a are the generators of the Lie algebra (see appendix A). Furthermore, we define $\gamma_{-\mu} \equiv -\gamma_\mu$ and $\mathcal{V}_{-\mu}(n) \equiv \mathcal{V}_\mu^\dagger(n - \hat{\mu})$ for a short notation. In the following paragraphs, the different formulations of the fermion action are addressed. Starting from Wilson fermions we try to improve the lattice formulation with a clover term or alternatively with twists in the mass term and/or Wilson term.

Naive fermions

By discretizing the derivatives in the fermionic part of the Euclidean continuum action (2.38) and taking into account the gauge transporters to assure gauge invariance [183], the naive lattice Dirac operator is

$$D(n,n') = m\, \delta_{n,n'} + \frac{1}{2a} \sum_{\mu=\pm 1}^{\pm 4} \gamma_\mu \mathcal{V}_\mu(n)\, \delta_{n+\hat{\mu},n'} . \tag{3.40}$$

When analyzed in momentum space, so-called doublers are identified by poles containing momentum components $p_\mu = \frac{\pi}{a}$ [129]. In four spacetime dimensions, there are 15 doublers which can be removed with a momentum dependent mass as suggested by Wilson.

Wilson fermions

The Wilson term damps all poles except $p = (0, 0, 0, 0)$ and consequently the Wilson Dirac operator

$$D_{\mathrm{W}}(n, n') = \left(\frac{4r}{a} + m\right) \delta_{n,n'} - \frac{1}{2a} \sum_{\mu=\pm 1}^{\pm 4} (\mathbb{1}r - \gamma_\mu)\, \mathcal{V}_\mu(n)\, \delta_{n+\hat{\mu},n'}\,, \tag{3.41}$$

describes one single fermion [183, 187]. By explicitly breaking chirality, Wilson fermions circumvent the Nielsen-Ninomiya theorem [188, 189]. For any Wilson parameter $0 < r \leq 1$ reflection positivity and the correct continuum limit are guaranteed [124]. If not stated otherwise, we set $r = 1$. In leading order the discretization errors are $\mathcal{O}(a)$ in the lattice spacing [129]. Within the scope of this work, two further types of lattice fermions with reduced lattice artifacts are used, namely clover fermions and twisted-mass fermions. Both variants are constructed in the following sections from the Wilson Dirac operator plus an irrelevant operator.

Clover fermions

With the help of the anti-symmetrized clover plaquette

$$\mathcal{F}_{\mu\nu}(n) = \frac{-\mathrm{i}}{8a^2}\Big(Q_{\mu\nu}(n) - Q_{\nu\mu}(n)\Big) \quad \text{with} \tag{3.42}$$

$$Q_{\mu\nu}(n) = \mathcal{V}_{\mu,\nu}(n) + \mathcal{V}_{\nu,-\mu}(n) + \mathcal{V}_{-\mu,-\nu}(n) + \mathcal{V}_{-\nu,\mu}(n) \tag{3.43}$$

consisting of four plaquettes (see figure 3.2), we define the clover Wilson Dirac operator:

$$D_{\mathrm{W}}^{\mathrm{cl}}(n, n') = \left(\frac{4}{a} + m\right) \delta_{n,n'} - \frac{1}{2a} \sum_{\mu=\pm 1}^{\pm 4} (\mathbb{1} - \gamma_\mu)\, \mathcal{V}_\mu(n)\, \delta_{n+\hat{\mu},n'} + c_{\mathrm{SW}} \frac{a}{4\mathrm{i}} \sum_{\mu<\nu} \mathcal{F}_{\mu\nu}(n) \Sigma_{\mu\nu} \delta_{n,n'}\,. \tag{3.44}$$

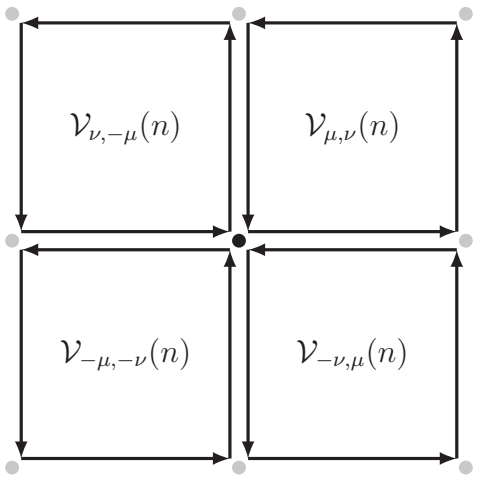

Figure 3.2: Sketch of the clover plaquette $Q_{\mu\nu}(n)$ in the adjoint representation consisting of four ordinary plaquettes $\mathcal{V}_{.,.}(n)$ anchored at the central (black) lattice site n.

Often, the Sheikholeslami-Wohlert coefficient c_{SW} is calculated with lattice perturbation theory such that $\mathcal{O}(a)$ discretization errors of quantities like the quark-gluon vertices vanish at a certain loop order [84–86]. Most of the time, the 1-loop order is already sufficient. Typically, the result depends on the chosen fermion representation and gauge action. A general 1-loop result for the Wilson gauge action and arbitrary fermion representation,

$$c_{\mathrm{SW}} = 1 + g^2 \left((0.167\,64 \pm 0.000\,03)\, C_{\mathrm{rep}} + (0.015\,03 \pm 0.000\,03)\, N_{\mathrm{c}} \right), \tag{3.45}$$

was calculated in [40] for $\mathcal{N} = 1$ SYM theory with gauge group SU(N_{c}). Therein, the quadratic Casimir invariant C_{rep} in the fundamental representation is $C_{\mathrm{fund}} = \frac{N_{\mathrm{c}}^2 - 1}{2N_{\mathrm{c}}}$ and in the adjoint representation $C_{\mathrm{adj}} = N_{\mathrm{c}}$. We performed some simulations with the clover coefficient determined that way (see the cyan line in figure 5.1 et seq.).

In order to use the Symanzik-improved Lüscher-Weisz gauge action of eq. (3.37), we preferred the following way of determining the value of c_{SW}. With the gauge-invariant definition of the tadpole factor $u_0 \equiv \left\langle \frac{\mathrm{tr_c}(\mathcal{U}_\Box)}{N_{\mathrm{c}}} \right\rangle^{1/4}$ the tadpole improvement at tree-level is $c_{\mathrm{SW}} = u_0^{-3}$ [32, 130, 190]. In the simulations the average is calculated self-consistently via the plaquette $\mathcal{U}_\Box$ from the current gauge field configuration and therefore c_{SW} varies for different bare mass parameters m. For the parameters of figure 5.1 this approach leads to values $c_{\mathrm{SW}} \in [2.09, 2.16]$ and they are highlighted with a green line.

Also non-perturbatively, the clover coefficient can be determined. With the help of the Schrödinger functional, the partially conserved axial current (PCAC) relation is measured on the lattice and the value of c_{SW} is tuned such that the contribution of order $\mathcal{O}(a)$ vanishes [191].

We tested a new heuristic approach to search for the clover coefficient, which is based on the following feature of $\mathcal{N} = 1$ SYM theory. Since the mass of the gluino vanishes in the continuum, its lattice mass is purely a consequence of broken supersymmetry and chiral symmetry. The same holds for the (unphysical) adjoint pion, whose mass squared is proportional to the renormalized gluino mass. We search the point of the lattice theory closest to the continuum, where the discretization errors and symmetry violations are expected to be minimal. To this end, the value of c_{SW} is varied for fixed bare gluino mass m such that the adjoint pion mass $m_{\text{a-}\pi}$ is minimized. This resembles the procedure of tuning the bare gluino mass m for Wilson fermions to the critical point.

To compare the different ways of determining c_{SW}, figure 3.3 collects from the literature several results for the Wilson gauge action. In the left panel, it is demonstrated for the Wilson gauge action with SU(2) that the perturbative and non-perturbative results approach each other in the limit $g \to 0$. By comparing the clover values of the fundamental representation to those of the adjoint representation, one clearly sees that the latter lie higher. Turning to the gauge group SU(3) depicted in the right panel, the perturbative values of c_{SW} grow even further.

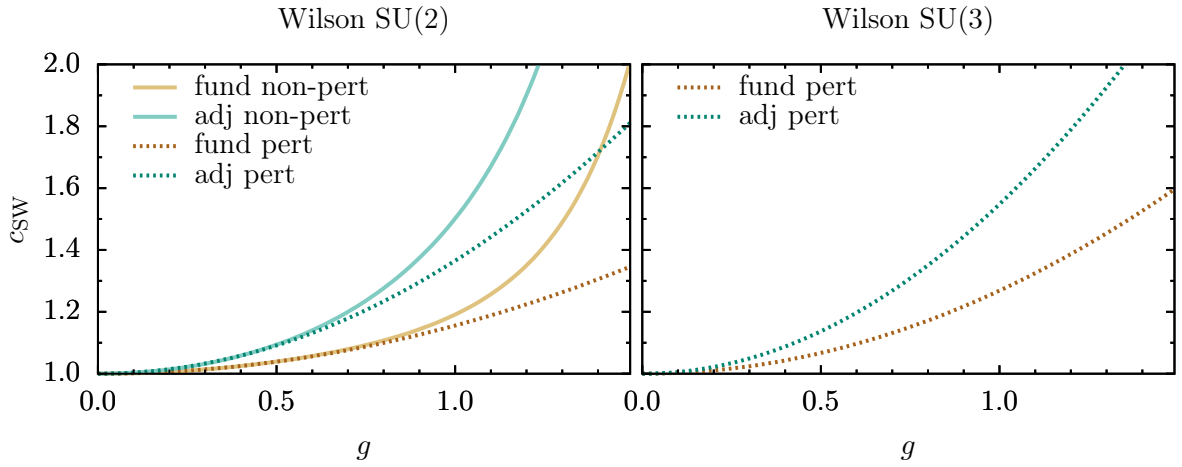

Figure 3.3: Left/Right: Clover coefficient for the Wilson gauge action with gauge group SU(2) resp. SU(3) and different representations. The non-perturbative results are from [192] and the perturbative 1-loop result is given in eq. (3.45) and taken from [40].

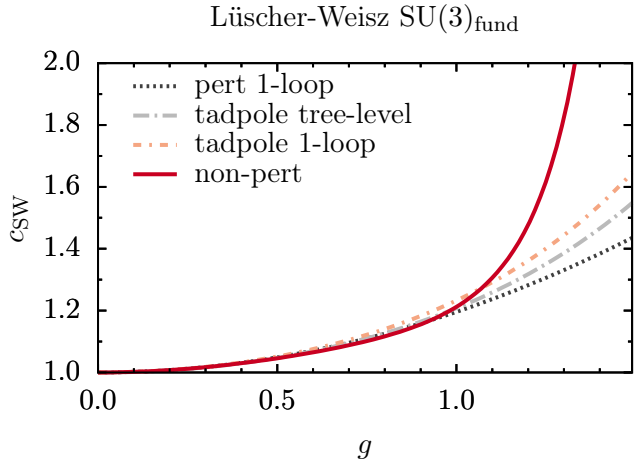

Figure 3.4: Approximations of c_{SW} for the Lüscher-Weisz gauge action with gauge group SU(3)$_{\mathrm{fund}}$. The corresponding functions are summarized in table 3.3.

Table 3.3: Different approximations of c_{SW} for the Lüscher-Weisz gauge action with gauge group SU(3)$_{\mathrm{fund}}$. The corresponding curves are plotted in figure 3.4.

type	reference	c_{SW}
perturbative 1-loop	[193]	$1 + 0.196g^2$
tadpole tree-level	[190]	u_0^{-3}
tadpole 1-loop	[130]	$u_0^{-3}\left(1 + g^2 u_0^{-4}(0.2659 - 1/4)\right)$
non-perturbative	[194]	$(1 - 0.1921g^2 - 0.1378g^4 + 0.0717g^6) \,/\, (1 - 0.3881g^2)$

No results exist in the literature for our favored choice of the Lüscher-Weisz gauge action in combination with Majorana fermions in the adjoint representation. In section 5.1 we search heuristically for an optimal clover coefficient, but no obvious value is found. The most promising option is the tadpole approximation at tree-level (see gray dashed line in figure 3.4), because it is universal and can be calculated directly from the gauge configuration during the simulations.

Mass-twisted fermions

The concept of twisted-mass was originally introduced to lattice QCD with the aim to remove exceptional configurations [82]. Later, $\mathcal{O}(a)$ improvement at maximal twisting angle $\pm\pi/2$ was discovered [83]. Our purpose is primary to reduce the effects of the explicit breaking of supersymmetry and chiral symmetry at finite lattice spacing. In section 4.1 the influence of the twisted formulation on the mesonic states is calculated analytically and in section 4.3 the eigenvalues of the free twisted Wilson Dirac operator are discussed in the context of $\mathcal{O}(a)$ improvement. The Wilson Dirac operator with parity-breaking mass term $\mathrm{i}m_5\gamma_5$ is

$$D_{\mathrm{W}}^{\mathrm{mtw}}(n,n') = \left(\frac{4}{a} + m + \mathrm{i}m_5\gamma_5\right)\delta_{n,n'} - \frac{1}{2a}\sum_{\mu=\pm1}^{\pm4}(\mathbb{1}-\gamma_\mu)\,\mathcal{V}_\mu(n)\,\delta_{n+\hat{\mu},n'} \tag{3.46}$$

similar to twisted-mass lattice QCD, but for one single Majorana fermion.[8] In terms of the polar mass $M \equiv \sqrt{m^2+m_5^2}$ and the twist angle $\alpha \equiv \arctan(m_5/m)$, the two mass terms can be combined[9] as

$$m + \mathrm{i}m_5\gamma_5 = M\mathrm{e}^{\mathrm{i}\alpha\gamma_5}\,. \tag{3.47}$$

A special feature of $\mathcal{N} = 1$ SYM motivates the additional twisted term: Particular values of the phase of the remnant chiral $\mathbb{Z}_{2N_c}$ symmetry (cf. eq. (2.22)) are favored in the gluino condensate. The chiral symmetry is broken explicitly by the bare gluino mass $m = M\cos(\alpha)$, which triggers a condensate $\sim\langle\bar{\lambda}\lambda\rangle$. A further condensate $\sim\langle\bar{\lambda}\mathrm{i}\gamma_5\lambda\rangle$ is triggered by the twisted mass $m_5 = M\sin(\alpha)$ and both condensates are related by a chiral rotation. With the twist angle α, we can control the "direction" of the favored condensate.

Whereas in twisted-mass lattice QCD simulations the twisted basis is rotated back to the physical basis for the calculation of observables, we interpret the m_5-mass term as a deformation which vanishes in the chiral limit $m \to m_{\mathrm{crit}},\ m_5 \to 0$. In section 5.2 we investigate numerically different "directions" in the (m, m_5)-plane for the extrapolation to the critical point and we show that for optimal twist angles the chiral partners a-η'

[8] In contrast to 2-flavor twisted-mass QCD, where the twist term contains the Pauli matrix τ_3, $\mathcal{N} = 1$ SYM theory contains only one flavor and thus τ_3 is absent.

[9] The polar mass M and the twist angle α are always in respect to the untwisted critical point at m_{crit}.

and a-f_0 have the same mass. This reduces the impact of explicitly broken chirality and supersymmetry at finite lattice spacing.

A similar twist was used in [22] for the supersymmetric Wess-Zumino model in two dimensions. There, a modified Wilson term was tuned such that the discretization errors in the eigenvalues of the free lattice Dirac operator are reduced to $\mathcal{O}(a^4)$. For the $\mathcal{N} = 1$ SYM theory, we perform an analogous calculation in section 4.3.

Double-twisted fermions

Later, we added a more general Dirac operator

$$\begin{aligned} D_{\mathrm{W}}^{\mathrm{dtw}}(n,n') &= \left(\frac{4}{a}(r + \mathrm{i}\gamma r_5) + m + \mathrm{i}m_5\gamma_5\right)\delta_{n,n'} - \frac{1}{2a}\sum_{\mu=\pm1}^{\pm4}\left(\mathbb{1}r + \mathrm{i}\gamma_5 r_5 - \gamma_\mu\right)\mathcal{V}_\mu(n)\delta_{n+\hat{\mu},n'} \\ &= \left(\frac{4R}{a}\,\mathrm{e}^{\mathrm{i}\varphi\gamma_5} + M\mathrm{e}^{\mathrm{i}\alpha\gamma_5}\right)\delta_{n,n'} - \frac{1}{2a}\sum_{\mu=\pm1}^{\pm4}\left(\mathbb{1}R\,\mathrm{e}^{\mathrm{i}\varphi\gamma_5} - \gamma_\mu\right)\mathcal{V}_\mu(n)\delta_{n+\hat{\mu},n'}\,. \end{aligned} \tag{3.48}$$

with twists in the mass term and Wilson term[10] to our investigations. A similar general action was discussed in [195]. For most numerical simulations the Wilson parameter was $(r, r_5) = (1, 0)$, see table G.4, and only some tests presented in section 5.6 are double-twisted. If both twist angles $\alpha = \varphi$ are identical, then a chiral rotation

$$\lambda \mapsto \mathrm{e}^{-\mathrm{i}\alpha\gamma_5/2}\lambda\,, \qquad \bar{\lambda} \mapsto \bar{\lambda}\,\mathrm{e}^{-\mathrm{i}\alpha\gamma_5/2}\,, \tag{3.49}$$

transforms the action with double-twisted Wilson Dirac operator (3.48) into the ordinary action with Wilson fermions:

$$\begin{aligned} S_{\mathrm{f}} &= \frac{a^4}{2}\sum_{n\in\Lambda}\bar{\lambda}(n)\left(\frac{4}{a}\,\mathrm{e}^{\mathrm{i}\alpha\gamma_5} + m\,\mathrm{e}^{\mathrm{i}\alpha\gamma_5}\right)\lambda(n) - \frac{a^3}{4}\sum_{n\in\Lambda}\sum_{\mu=\pm1}^{\pm4}\bar{\lambda}(n)\left(\mathbb{1}\,\mathrm{e}^{\mathrm{i}\alpha\gamma_5} - \gamma_\mu\right)\mathcal{V}_\mu(n)\,\lambda(n+\hat{\mu}) \\ &\mapsto \frac{a^4}{2}\sum_{n\in\Lambda}\bar{\lambda}(n)\left(\frac{4}{a} + m\right)\lambda(n) - \frac{a^3}{4}\sum_{n\in\Lambda}\sum_{\mu=\pm1}^{\pm4}\bar{\lambda}(n)\,(\mathbb{1} - \gamma_\mu)\mathcal{V}_\mu(n)\,\lambda(n+\hat{\mu})\,. \end{aligned}$$

As can be seen, the discrete derivative term $\sim \gamma_\mu$ stays always unchanged.

3.2.3 Properties of the twisted Wilson Dirac operator

In table 3.4 we compare the relevant properties of the Wilson Dirac operator with and without mass twist. Most differences result from the loss of γ_5-Hermiticity when a mass twist is added and only a modified γ_5-Hermiticity involving $\pm m_5$ holds. As a consequence, the complex eigenvalues do not come in complex-conjugated pairs and the determinant as well as the Pfaffian may have imaginary parts. Nevertheless, we shall demonstrate in

[10] The angle φ of the Wilson term determines the "direction" of the critical point, see section 5.6.

section 5.3 that only a very mild sign problem emerges. For the particular choice $\alpha = \varphi$ in the double-twisted Wilson Dirac operator (3.48), the chiral phase can be removed by a change of variables and therefore the Pfaffian becomes real again.

More details and some derivations can be found in the appendices B.1 and B.2. In section 4.3, the free twisted Wilson Dirac operator is analyzed to find a connection between the twist angle α and discretization errors.

Table 3.4: Properties of the untwisted and mass-twisted Wilson Dirac operator.

	D_{W} of eq. (3.41)	$D_{\mathrm{W}}^{\mathrm{mtw}}$ of eq. (3.46)
Hermiticity	$D_{\mathrm{W}}^{\dagger} \neq D_{\mathrm{W}}$	$(D_{\mathrm{W}}^{\mathrm{mtw}})^{\dagger} \neq D_{\mathrm{W}}^{\mathrm{mtw}}$
γ_5-commutator	$[D_{\mathrm{W}}, \gamma_5] \neq 0$	$[D_{\mathrm{W}}^{\mathrm{mtw}}, \gamma_5] \neq 0$
γ_5-Hermiticity	$\big(\gamma_5 D_{\mathrm{W}}\big)^{\dagger} = \gamma_5 D_{\mathrm{W}}$ $\big(D_{\mathrm{W}}^{-1}\big)^{\dagger} = \gamma_5 D_{\mathrm{W}}^{-1} \gamma_5$	$\big(\gamma_5 D_{\mathrm{W}}^{\mathrm{mtw}}(m_5)\big)^{\dagger} = \gamma_5 D_{\mathrm{W}}^{\mathrm{mtw}}(-m_5) = \gamma_5 D_{\mathrm{W}}^{\mathrm{mtw}}(m_5) - 2\mathrm{i}m_5$ $\big((D_{\mathrm{W}}^{\mathrm{mtw}})^{-1}\big)^{\dagger} = \big(D_{\mathrm{W}}^{\mathrm{mtw}} + 2\mathrm{i}m_5\gamma_5\big) \cdot \big(\gamma_5 D_{\mathrm{W}}^{\mathrm{mtw}} \gamma_5 D_{\mathrm{W}}^{\mathrm{mtw}} + 4m_5^2\big)^{-1}$
$\mathcal{C}$-antisymmetry	$\big(\mathcal{C}_- D_{\mathrm{W}}\big)^{\mathrm{T}} = -\mathcal{C}_- D_{\mathrm{W}}$	$\big(\mathcal{C}_- D_{\mathrm{W}}^{\mathrm{mtw}}\big)^{\mathrm{T}} = -\mathcal{C}_- D_{\mathrm{W}}^{\mathrm{mtw}}$
eigenvalues	double degenerated in complex conjugated pairs	complex
det	$\mathbb{R}^+$	$\mathbb{C}$
Pf	$\mathbb{R}$	$\mathbb{C}$

3.2.4 Lattice observables

An expectation value of an operator $O[\mathcal{U}, \lambda]$, which depends on the gauge field $\mathcal{U}$ as well as on the fermion field λ, is given by the path integral

$$\langle O \rangle = \langle \langle O \rangle_{\mathrm{F}} \rangle_{\mathcal{U}} = \frac{1}{Z} \int \mathcal{D}\mathcal{U}\, \mathrm{e}^{-S_{\mathrm{g}}[\mathcal{U}]}\, \mathcal{D}\lambda\, \mathrm{e}^{-S_{\mathrm{f}}[\mathcal{U},\lambda]}\, O[\mathcal{U}, \lambda]\,, \tag{3.50}$$

where first the fermionic integral is evaluated. The normalizing factor Z is the partition function given by the path integral $Z = \int \mathcal{D}\mathcal{U}\, \mathcal{D}\lambda\, \exp(-S[\mathcal{U}, \lambda])$ with the action $S[\mathcal{U}, \lambda] = S_{\mathrm{g}}[\mathcal{U}] + S_{\mathrm{f}}[\mathcal{U}, \lambda]$. The fermionic action is given by[11]

$$S_{\mathrm{f}}[\mathcal{U}, \lambda] = \frac{1}{2} \mathrm{tr}(\lambda^{\mathrm{T}} \mathcal{C} D[\mathcal{U}] \lambda) \equiv \frac{1}{2} \mathrm{tr}(\lambda^{\mathrm{T}} \tilde{D}[\mathcal{U}] \lambda) \tag{3.51}$$

with Wilson Dirac operator $D[\mathcal{U}]$ and the effective action after integrating out the Majorana fermions is $S_{\mathrm{eff}}[\mathcal{U}] = S_{\mathrm{g}}[\mathcal{U}] - \log(\mathrm{Pf}(\tilde{D}[\mathcal{U}]))$.

In our lattice investigations we measure different observables, the simplest ones consist only of the gauge field. The plaquette

$$\langle \mathcal{U}_{\square} \rangle = \frac{1}{V d(d-1)/2} \sum_{n \in \Lambda} \sum_{1 \leq \mu < \nu \leq d} \mathcal{U}_{\mu\nu}(n) \tag{3.52}$$

[11] Here, the trace contains again the spacetime summation.

is a useful observable to estimate the statistical fluctuations, auto-correlations[12] or to calculate the bosonic action

$$S_{\mathrm{B}} = \frac{1}{V} S_{\mathrm{g}}[\mathcal{U}] \,. \tag{3.53}$$

Observing the bosonic action can serve as an indicator for supersymmetry breaking, because the supersymmetric Ward identity $\langle \mathcal{Q} O \rangle = 0$ with the operator $[O(n)]_\alpha = \mathrm{tr_c}\Big(\bar{\lambda}^\beta(n)[\Sigma^{\mu\nu}]_{\beta\alpha} F_{\mu\nu}(n)\Big)$ reads

$$\langle S_{\mathrm{B}} \rangle_{\mathcal{U}} = \frac{3}{2} N_{\mathrm{G}} + \mathcal{O}\big(\beta^{-1}\big) \tag{3.54}$$

and involves the bosonic action as well as the number N_{G} of generators of the gauge group [55, 59, 196, 197]. Fermionic observables of interest include the gluino condensate

$$\Sigma = \frac{1}{V} \frac{\partial \ln(Z)}{\partial m} = -\frac{a^4}{2V} \sum_{n \in \Lambda} \Big\langle \bar{\lambda}(n) \lambda(n) \Big\rangle = \frac{1}{2V} \sum_{n \in \Lambda} \Big\langle \mathrm{tr}\, D^{-1}_{nn} \Big\rangle_{\mathrm{eff}} \,, \tag{3.55}$$

which is linked to the spontaneous breaking of the remnant chiral symmetry, see section 2.3. Similarly defined is the parity condensate

$$\Sigma^{\mathrm{P}} = -\frac{\mathrm{i} a^4}{2V} \sum_{n \in \Lambda} \Big\langle \bar{\lambda}(n) \gamma_5 \lambda(n) \Big\rangle = \frac{\mathrm{i}}{2V} \sum_{n \in \Lambda} \Big\langle \mathrm{tr}\, \gamma_5 D^{-1}_{nn} \Big\rangle_{\mathrm{eff}} \,. \tag{3.56}$$

Note that the chiral condensate (3.55) calculated with Wilson fermions needs an additive renormalization [129], but a subtracted condensate

$$\Sigma^{\mathrm{sub}} \equiv \Sigma - \frac{m_{\text{a-}\pi}}{m^{\mathrm{ref}}_{\text{a-}\pi}} \Sigma^{\mathrm{ref}} \tag{3.57}$$

with a reference point can be used instead.

For hadron spectroscopy (see section 3.1.3), interpolating lattice operators for the particles of interest are required. The Hermitean interpolating operators for mesons are bilinears of the form $O(n) = \bar{\lambda}(n) \Gamma \lambda(n)$. Specifically the interpolating operators for the adjoint mesonic states a-η' and a-f_0 are [181]

$$O_{\text{a-}\eta'}(n) = \mathrm{i} \bar{\lambda}(n) \gamma_5 \lambda(n) \qquad \text{and} \qquad O_{\text{a-}f_0}(n) = \bar{\lambda}(n) \lambda(n) \,. \tag{3.58}$$

For convenience, lattice units are used from now on if not stated otherwise. To return to physical units, all energies, masses and momenta have to be multiplied by the lattice constant a. We use the antisymmetric charge conjugation matrix $\mathcal{C}$ which commutes

[12] Note that the thermalization and autocorrelation of different observables may differ.

with γ_5, the definition $\bar{\lambda}=\lambda^{\mathrm{T}}\mathcal{C}$ and the antisymmetry of the product $\mathcal{C}\gamma_5$ to contract

$$\begin{aligned}\left\langle\bar{\lambda}_n\Gamma^1\lambda_n\bar{\lambda}_{n'}\Gamma^2\lambda_{n'}\right\rangle_{\mathrm{F}}&=\left\langle\lambda_n^{\mathrm{T}}\mathcal{C}\Gamma^1\lambda_n\lambda_{n'}^{\mathrm{T}}\mathcal{C}\Gamma^2\lambda_{n'}\right\rangle_{\mathrm{F}}\\&=\mathcal{C}_{\alpha_1\delta_1}\Gamma^1_{\delta_1\beta_1}\mathcal{C}_{\alpha_2\delta_2}\Gamma^2_{\delta_2\beta_2}\left\langle\lambda^{\mathrm{T}}_{n\alpha_1c_1}\lambda_{n\beta_1c_1}\lambda^{\mathrm{T}}_{n'\alpha_2c_2}\lambda_{n'\beta_2c_2}\right\rangle_{\mathrm{F}}\\&=\mathcal{C}_{\alpha_1\delta_1}\Gamma^1_{\delta_1\beta_1}\mathcal{C}_{\alpha_2\delta_2}\Gamma^2_{\delta_2\beta_2}\left(\tilde{D}^{-1}_{n\beta_1c_1,n\alpha_1c_1}\tilde{D}^{-1}_{n'\beta_2c_2,n'\alpha_2c_2}-\tilde{D}^{-1}_{n'\beta_2c_2,n\alpha_1c_1}\tilde{D}^{-1}_{n\beta_1c_1,n'\alpha_2c_2}\right)\\&\quad-\mathcal{C}_{\beta_1\delta_1}\Gamma^1_{\delta_1\alpha_1}\mathcal{C}_{\alpha_2\delta_2}\Gamma^2_{\delta_2\beta_2}\tilde{D}^{-1}_{n\alpha_1c_1,n'\alpha_2c_2}\tilde{D}^{-1}_{n'\beta_2c_2,n\beta_1c_1}\\&=\mathrm{tr}(\mathcal{C}\Gamma^1\tilde{D}^{-1}_{nn})\,\mathrm{tr}(\mathcal{C}\Gamma^2\tilde{D}^{-1}_{n'n'})-2\,\mathrm{tr}(\mathcal{C}\Gamma^1\tilde{D}^{-1}_{nn'}\mathcal{C}\Gamma^2\tilde{D}^{-1}_{n'n})\\&=\mathrm{tr}(\Gamma^1G_{nn})\,\mathrm{tr}(\Gamma^2G_{n'n'})-2\,\mathrm{tr}(\Gamma^1G_{nn'}\Gamma^2G_{n'n})\,.\end{aligned}\tag{3.59}$$

The fermion contraction leads to connected and disconnected contributions with products of the fermion lattice propagator $G_{nn'}\equiv D^{-1}_{nn'}$. In particular, the correlators between the source at $y=(\vec{y},0)$ and the sink at $x=(\vec{x},t)$ is

$$\begin{aligned}C(t)&=\left\langle\tilde{O}(\vec{p}=\vec{0},t)\,\tilde{O}^\dagger(\vec{p}=\vec{0},0)\right\rangle\\&=\frac{1}{|\Lambda_3|^2}\sum_{\vec{n},\vec{n}'\in\Lambda_3}\left\langle O(\vec{n},t)\,O^\dagger(\vec{n}',0)\right\rangle\\&=\frac{1}{|\Lambda_3|^2}\sum_{\vec{n},\vec{n}'\in\Lambda_3}\left\langle\bar{\lambda}(\vec{n},t)\Gamma\lambda(\vec{n},t)\,\bar{\lambda}(\vec{n}',0)\Gamma\lambda(\vec{n}',0)\right\rangle\\&\overset{(3.59)}{=}\frac{1}{|\Lambda_3|^2}\sum_{\vec{n},\vec{n}'\in\Lambda_3}\left\langle\mathrm{tr}(\Gamma G_{nn})\mathrm{tr}(\Gamma G_{n'n'})\right\rangle_{\mathcal{U}}-\frac{2}{|\Lambda_3|^2}\sum_{\vec{n},\vec{n}'\in\Lambda_3}\left\langle\mathrm{tr}(\Gamma G_{nn'}\Gamma G_{n'n})\right\rangle_{\mathcal{U}}\end{aligned}\tag{3.60}$$

with $\Gamma\in\{\mathbb{1}_4,\gamma_5\}$. For the connected[13] two-point correlator, the contribution of the position-independent vacuum expectation value

$$\frac{1}{|\Lambda_3|^2}\sum_{\vec{n},\vec{n}'\in\Lambda_3}\left\langle\mathrm{tr}(\Gamma G_{nn})\right\rangle_{\mathcal{U}}\left\langle\mathrm{tr}(\Gamma G_{n'n'})\right\rangle_{\mathcal{U}}\tag{3.61}$$

must be subtracted from the correlator in eq. (3.60) [131]. Instead of fitting the constant vacuum contribution (3.61), it is beneficial to calculate the large cancellations between $\langle\mathrm{tr}(\Gamma G_{nn})\mathrm{tr}(\Gamma G_{n'n'})\rangle_{\mathcal{U}}$ and $\langle\mathrm{tr}(\Gamma G_{nn})\rangle\langle\mathrm{tr}(\Gamma G_{n'n'})\rangle_{\mathcal{U}}$ numerically. This procedure is further stabilized when n' is consistently described by point sources and n is averaged over the whole lattice with the stochastic estimator technique. In parameter sets with small ensemble sizes these signals are too noisy and we use instead the (unphysical) correlators

$$C_{\text{a-}\pi}(t)=\frac{2}{|\Lambda_3|^2}\sum_{\vec{n},\vec{n}'\in\Lambda_3}\left\langle\mathrm{tr}(\gamma_5G_{nn'}\gamma_5G_{n'n})\right\rangle_{\mathcal{U}}\quad\text{and}\quad C_{\text{a-}a}(t)=\frac{2}{|\Lambda_3|^2}\sum_{\vec{n},\vec{n}'\in\Lambda_3}\left\langle\mathrm{tr}(G_{nn'}G_{n'n})\right\rangle_{\mathcal{U}},\tag{3.62}$$

[13] We encounter a misuse of language. Here "connected" is understood in the sense of QFT calculations, where $W=\ln Z$ is used to compute connected Feynman diagrams approaching zero at large spatial separation. This should not be confused with the term "connected" to distinguish between contributions like the last term of eq. (3.60) compared to the "disconnected" contributions of the first term.

which are defined in a partially-quenched framework and contain just the connected contributions.[14]

In $\mathcal{N}=1$ SYM theory there exist also mixed states containing bosonic and fermionic building blocks. To measure the gluino-glueballs we define the interpolating operator[15]

$$[O_{\tilde{\mathrm{gg}}}(n)]_\alpha = [\Sigma^{ij}]_{\alpha\beta}\,\mathrm{tr_c}\left(\mathcal{F}_{ij}(n)\lambda^\beta(n)\right) \tag{3.63}$$

with $\Sigma_{ij} \equiv [\gamma_i, \gamma_j]$ and the spatial part of the anti-symmetrized clover plaquette, see eq. (3.42). According to the fermionic nature of the gluino-glue interpolator, one Dirac index is open and it transforms with a γ_4 matrix under parity transformations [129]. Generally, a correlator built from $[O_{\tilde{\mathrm{gg}}}(n)]_\alpha$ and $[\bar{O}_{\tilde{\mathrm{gg}}}(n)]_\alpha$ couples to arbitrary parity and the lowest mass dominates the signal [124]. We introduce an additional matrix Γ to contract the spinor indices and select channels from the correlator

$$\begin{aligned} C_{\tilde{\mathrm{gg}}}(n,n') &= \left\langle \Gamma^{\mu\delta}[O_{\tilde{\mathrm{gg}}}(n)]_\mu\,[\bar{O}_{\tilde{\mathrm{gg}}}(n')]_\delta \right\rangle \\ &= -\left\langle [\Gamma^{\mathrm{T}}]^{\delta\mu}[\Sigma_{ij}]_{\mu\beta}\,\mathrm{tr_c}\Big(F^{ij}(n)T^a\Big)(G_{nn'})^{\beta\rho}_{ab}\,\mathrm{tr_c}\Big(F^{lm}(n')T^b\Big)[\Sigma_{lm}]_{\rho\delta}\right\rangle_{\mathcal{U}} . \end{aligned} \tag{3.64}$$

This gluino-glue correlator has a time-symmetric and a time-antisymmetric component, which are identified as the components of $\Gamma = \gamma_4$ and $\Gamma = \mathbb{1}_4$ respectively. In our simulations those two variants as well as the combinations $\Gamma = \frac{1}{2}(\mathbb{1}_4 \pm \gamma_4)$ are measured. It is reported that the antisymmetric component has a longer plateau in the effective mass and thus should be preferred for the determination of the ground state mass [198, 199]. The same authors expect at the same time that the symmetric component have a better signal for the excited states. Although the gluino-glue correlator has no disconnected contribution, it requires a medium amount of statistics because of sizable gauge field fluctuations.

Besides those states with gluino content, there exist pure glueball states in the FGS-supermultiplet. Typically, glueballs have noisy signals and thus require a large ensemble size. The signal can be enhanced by choosing a larger operator basis or by smearing of the gauge links (see chapter 3.1.4) [172, 200]. In the continuum, bosonic states transform under tensor representations of the rotation group SO(3), but the lattice discretization breaks this symmetry to the finite cubic group. With the help of the irreducible representations of the cubic symmetry group the eigenstates can be classified and a restoration of the rotation group in the continuum limit can be achieved [201]. For the scalar glueball $F_{\mu\nu}F^{\mu\nu}$ with quantum numbers $J^{PC} = 0^{++}$ we use the interpolating operator [200]

$$O_{0^{++}}(n) = \mathrm{Re}\Big(\mathrm{tr_c}\big(\mathcal{U}_{12}(n) + \mathcal{U}_{23}(n) + \mathcal{U}_{31}(n)\big)\Big) . \tag{3.65}$$

[14] The connected correlators (3.62) as two-flavor states do not allow any vacuum contribution as in eq. (3.61).

[15] The indices i, j run only over the spatial directions to avoid any contributions of multiple time-slices [28].

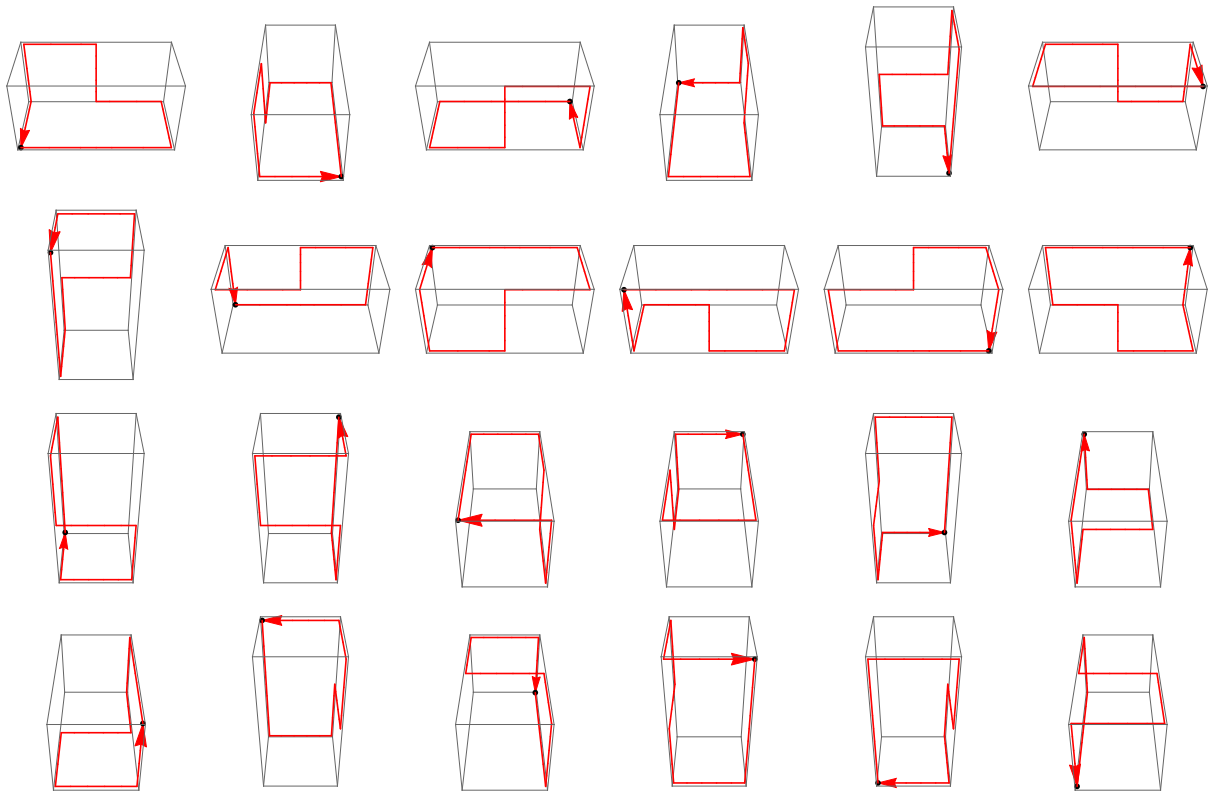

Figure 3.5: The three-dimensional standard path $\mathfrak{C}$ applied to the 24 elements of the cubic group for the calculation of the glueball 0^{-+}.

In the correlator of the scalar glueball, the disconnected vacuum contribution has to be subtracted [124] or an offset is required in the fit [130]. The pseudoscalar glueball $\tilde{F}_{\mu\nu}F^{\mu\nu}$ with quantum numbers $J^{PC} = 0^{-+}$ can be measured with the operator

$$O_{0^{-+}}(n) = \mathrm{Re}\sum_R \Big(\mathrm{tr_c}\Big(\mathcal{W}(\mathfrak{C}_R)\Big) - \mathrm{tr_c}\Big(\mathcal{W}(\mathrm{P}\mathfrak{C}_R)\Big)\Big) \tag{3.66}$$

using a specific standard loop along a suitable curve $\mathfrak{C}$ [200]. The sum extends over all rotations in the cubic group and the path $\mathfrak{C}_R$ is obtained by acting with the rotation R on the standard loop. The Wilson loops $\mathcal{W}$ are evaluated along the path $\mathfrak{C}_R$ and their reflections $\mathrm{P}\mathfrak{C}_R$, see figure 3.5

CHAPTER 4

Analytical calculations

Now that the foundations of the physical theory and the numerical methods are laid, this chapter contains analytical insights. In this sense, it establishes ties between the proposed twisted lattice formulation and the corresponding numerical results. At the same time, new properties are discovered.

First, the chiral transformation of the fermionic bilinears is analyzed and we prove that the twist angle $\alpha = 45°$ is special. Afterwards, the supersymmetry transformations of the lattice operators are calculated and the consequences of a mass twist are checked. Finally, the eigenvalues of the free Wilson Dirac operator are calculated analytically and they reveal the potential of $\mathcal{O}(a)$ improvement.

4.1 Chiral transformation of fermionic observables

Starting from the definition of the mass-twisted Wilson Dirac operator of eq. (3.46), the following reasoning shows that this lattice formulation is meaningful and describes the correct continuum theory. Afterwards, different choices of the twist angle α are discussed explicitly for the chiral partners of the VY-supermultiplet. For the analytical argument, it is helpful to twist also the irrelevant Wilson term with the same angle, which corresponds to $\alpha = \varphi$ in eq. (3.48).

In the continuum $\mathcal{N} = 1$ SYM theory, the scalar and pseudoscalar mesonic states are mass-degenerated. Therefore they have the same correlators and their operators can be combined in an arbitrary rotation of the operator basis.[16] Analogously, under the chiral $\mathrm{U(1)_A}$ rotation with angle $\frac{\alpha}{2}$ of the gluino field,

$$\lambda \mapsto \mathrm{e}^{\mathrm{i}\alpha\gamma_5/2}\lambda\,, \qquad \bar{\lambda} \mapsto \bar{\lambda}\,\mathrm{e}^{\mathrm{i}\alpha\gamma_5/2}\,, \tag{4.1}$$

[16] See for example [107], where the a-f_0 and a-η' are described by one common complex field A of the chiral multiplet S.

the Hermitean scalar and pseudo-scalar bilinear lattice operators form a doublet:

$$\begin{pmatrix} \bar{\lambda}\lambda \\ \mathrm{i}\bar{\lambda}\gamma_5\lambda \end{pmatrix} \mapsto \begin{pmatrix} \bar{\lambda}\mathrm{e}^{\mathrm{i}\alpha\gamma_5}\lambda \\ \mathrm{i}\bar{\lambda}\gamma_5\mathrm{e}^{\mathrm{i}\alpha\gamma_5}\lambda \end{pmatrix} = \begin{pmatrix} \cos\alpha & \sin\alpha \\ -\sin\alpha & \cos\alpha \end{pmatrix} \begin{pmatrix} \bar{\lambda}\lambda \\ \mathrm{i}\bar{\lambda}\gamma_5\lambda \end{pmatrix} . \tag{4.2}$$

Consequently, we can combine the two components of the doublet (4.2) linearly:

$$O_{a,b}(n) = a\bar{\lambda}_n\lambda_n + b\mathrm{i}\bar{\lambda}_n\gamma_5\lambda_n = O^\dagger_{a,b}(n) . \tag{4.3}$$

Here we assumed that a, b are real, which is the case for the mesonic states under investigation. Without twist the operators for a-f_0 and a-η' (compare to eq. (3.58)) have the form

$$O_{\text{a-}f_0}(n) = O_{1,0}(n) = \bar{\lambda}_n\lambda_n , \quad O_{\text{a-}\eta'}(n) = O_{0,1}(n) = \mathrm{i}\bar{\lambda}_n\gamma_5\lambda_n . \tag{4.4}$$

Adding a chiral rotation as in eq. (4.1) to the spinors, those bilinears become

$$O_{\text{a-}f_0}(n,\alpha) = \bar{\lambda}_n\mathrm{e}^{\mathrm{i}\alpha\gamma_5}\lambda_n = \cos(\alpha)\bar{\lambda}_n\lambda_n + \mathrm{i}\,\sin(\alpha)\bar{\lambda}_n\gamma_5\lambda_n = O_{\cos(\alpha),\sin(\alpha)}(n) , \tag{4.5}$$

$$O_{\text{a-}\eta'}(n,\alpha) = \mathrm{i}\bar{\lambda}_n\gamma_5\mathrm{e}^{\mathrm{i}\alpha\gamma_5}\lambda_n = \mathrm{i}\cos(\alpha)\bar{\lambda}_n\gamma_5\lambda_n - \sin(\alpha)\bar{\lambda}_n\lambda_n = O_{-\sin(\alpha),\cos(\alpha)}(n) . \tag{4.6}$$

Instead of implementing this rotation in the operator basis explicitly, this mixing is naturally contained in measurements with the twisted Wilson Dirac operator and the original lattice operators (3.58). If no anomaly enters the path integral, then a substitution of the integration variable leads to

$$\int_\Lambda \mathcal{D}\lambda\, \mathrm{e}^{-\frac{1}{2}\mathrm{tr}\bar{\lambda}D_\mathrm{W}\lambda}\, O[\mathrm{e}^{\mathrm{i}\alpha\gamma_5/2}\lambda] = \int_\Lambda \mathcal{D}\lambda\, \mathrm{e}^{-\frac{1}{2}\mathrm{tr}\bar{\lambda}D^{\mathrm{dtw}}_\mathrm{W}[-\alpha,-\alpha]\lambda}\, O[\lambda] \tag{4.7}$$

with an twist angle $-\alpha$ in the twisted action. This statement is correct near the continuum where the Wilson term is irrelevant. In section 5.6, we study the chiral and parity condensates to check if the anomaly may invalidate this argumentation.

Next, we demonstrate that this chiral twist can enhance the mass-degeneracy of the superpartners a-η' and a-f_0, which is non-trivial at finite lattice spacing. To interpret the results obtained with a twisted mass in the action it is helpful to study the twist on the level of observables *without* twisting the action. Then, we can calculate the (general) expectation values

$$\begin{aligned} M_{a,b}(n,n') \equiv \langle O_{a,b}(n)\, O^\dagger_{a,b}(n')\rangle_\mathrm{F} &= \langle (a\bar{\lambda}_n\lambda_n + b\mathrm{i}\bar{\lambda}_n\gamma_5\lambda_n)(a\bar{\lambda}_{n'}\lambda_{n'} + b\mathrm{i}\bar{\lambda}_{n'}\gamma_5\lambda_{n'})\rangle_\mathrm{F} \\ &= a^2\langle\bar{\lambda}_n\lambda_n\bar{\lambda}_{n'}\lambda_{n'}\rangle_\mathrm{F} - b^2\langle\bar{\lambda}_n\gamma_5\lambda_n\bar{\lambda}_{n'}\gamma_5\lambda_{n'}\rangle_\mathrm{F} \\ &\quad + ab\mathrm{i}\langle\bar{\lambda}_n\lambda_n\bar{\lambda}_{n'}\gamma_5\lambda_{n'}\rangle_\mathrm{F} + ab\mathrm{i}\langle\bar{\lambda}_n\gamma_5\lambda_n\bar{\lambda}_{n'}\lambda_{n'}\rangle_\mathrm{F} . \end{aligned} \tag{4.8}$$

The two terms in the last row have negative parity and thus must vanish. This can be seen explicitly, because the Green's function with parity transformed gauge field configuration $\mathcal{U}^P$ is related to the Green's function with the original configuration $\mathcal{U}$ as follows

$$G(\mathcal{U}^P;\vec{n},t;\vec{n}',t') = \gamma_4 G(\mathcal{U};-\vec{n},t;-\vec{n}',t')\gamma_4 . \tag{4.9}$$

For our parity-invariant theory[17], $\mathcal{U}$ and $\mathcal{U}^P$ have equal weight, such that indeed

$$\begin{aligned} C_{\text{a-}f_0,\text{a-}\eta'}(t) &= \frac{1}{|\Lambda_3|}\sum_{\vec{n}}\langle\bar{\lambda}(\vec{n},t)\lambda(\vec{n},t)\,\bar{\lambda}(\vec{0},0)\gamma_5\lambda(\vec{0},0)\rangle \\ &= \frac{1}{|\Lambda_3|}\sum_{\vec{n}}\Big\langle \operatorname{tr}(G(\vec{n},t;\vec{n},t))\operatorname{tr}(\gamma_5 G(\vec{0},0;\vec{0},0)) - 2\operatorname{tr}(G(\vec{n},t;\vec{0},0)\gamma_5 G(\vec{0},0;\vec{n},t))\Big\rangle_{\mathcal{U}} \\ &= -C_{\text{a-}f_0,\text{a-}\eta'}(t)\,, \end{aligned} \tag{4.10}$$

i.e. $C_{\text{a-}f_0,\text{a-}\eta'}(t)$ vanishes. Thus, we get the expectation values

$$\begin{aligned} \Big\langle O_{\text{a-}f_0}(n)\,O^\dagger_{\text{a-}f_0}(n')\Big\rangle(\alpha) &= \Big\langle M_{\cos(\alpha),\sin(\alpha)}(n,n')\Big\rangle_{\mathcal{U}}\,, \\ \Big\langle O_{\text{a-}\eta'}(n)\,O^\dagger_{\text{a-}\eta'}(n')\Big\rangle(\alpha) &= \Big\langle M_{-\sin(\alpha),\cos(\alpha)}(n,n')\Big\rangle_{\mathcal{U}}\,. \end{aligned} \tag{4.11}$$

We see immediately that for the angle $\alpha = 45°$,

$$\langle O_{\text{a-}f_0}(n)\,O^\dagger_{\text{a-}f_0}(n')\rangle_{\mathrm{F}}(45°) = \langle O_{\text{a-}\eta'}(n)\,O^\dagger_{\text{a-}\eta'}(n')\rangle_{\mathrm{F}}(45°)\,, \tag{4.12}$$

the two mesons in the supermultiplet have identical correlators and consequently the same mass. To contract the two non-vanishing terms in eq. (4.8), we use eq. (3.59). In the untwisted case with $\alpha = 0°$ the correlator for the a-f_0 contains traces of G only and the correlator for the a-η' traces of $\gamma_5 G$ only,

$$\begin{aligned} \langle O_{\text{a-}f_0}(n)\,O^\dagger_{\text{a-}f_0}(n')\rangle_{\mathrm{F}}(0°) &= M_{1,0}(n,n') = \operatorname{tr}(G_{nn})\operatorname{tr}(G_{n'n'}) - 2\operatorname{tr}(G_{nn'}G_{n'n})\,, \\ \langle O_{\text{a-}\eta'}(n)\,O^\dagger_{\text{a-}\eta'}(n')\rangle_{\mathrm{F}}(0°) &= M_{0,1}(n,n') = -\operatorname{tr}(\gamma_5 G_{nn})\operatorname{tr}(\gamma_5 G_{n'n'}) + 2\operatorname{tr}(\gamma_5 G_{nn'}\gamma_5 G_{n'n})\,. \end{aligned} \tag{4.13}$$

For maximal twist angle $\alpha = 90°$, we conclude from

$$\begin{aligned} \langle O_{\text{a-}f_0}(n)\,O^\dagger_{\text{a-}f_0}(n')\rangle_{\mathrm{F}}(90°) &= M_{0,1}(n,n') \;\; = -\operatorname{tr}(\gamma_5 G_{nn})\operatorname{tr}(\gamma_5 G_{n'n'}) + 2\operatorname{tr}(\gamma_5 G_{nn'}\gamma_5 G_{n'n})\,, \\ \langle O_{\text{a-}\eta'}(n)\,O^\dagger_{\text{a-}\eta'}(n')\rangle_{\mathrm{F}}(90°) &= M_{-1,0}(n,n') = \operatorname{tr}(G_{nn})\operatorname{tr}(G_{n'n'}) - 2\operatorname{tr}(G_{nn'}G_{n'n}) \end{aligned} \tag{4.14}$$

that a chiral rotation by 90° interchanges the mesonic states a-f_0 and a-η'. Finally, for twist angle $\alpha = 45°$ the identical correlators have the value

$$\begin{aligned} \langle O_{\text{a-}f_0}(n)\,O^\dagger_{\text{a-}f_0}(n')\rangle_{\mathrm{F}}(45°) &= \langle O_{\text{a-}\eta'}(n)\,O^\dagger_{\text{a-}\eta'}(n')\rangle_{\mathrm{F}}(45°) \\ &= \frac{1}{2}M_{1,1}(n,n') \\ &= \frac{1}{2}\operatorname{tr}(G_{nn})\operatorname{tr}(G_{n'n'}) - \operatorname{tr}(G_{nn'}G_{n'n}) \\ &\quad - \frac{1}{2}\operatorname{tr}(\gamma_5 G_{nn})\operatorname{tr}(\gamma_5 G_{n'n'}) + \operatorname{tr}(\gamma_5 G_{nn'}\gamma_5 G_{n'n})\,. \end{aligned} \tag{4.15}$$

[17] At the moment, the twist is only on the level of the observable and the action consists of the parity-invariant Wilson Dirac fermion action and for example the Wilson gauge action.

To summarize, we showed that a-η' and a-f_0 interchange their roles when the twist angle increases by 90°. In between, for $\alpha = 45°$, the two mesonic states have equal correlators. This demonstrates that for a suitably chosen twist angle the two superpartners in the VY-supermultiplet have equal mass without fine-tuning to a supersymmetric continuum limit.

In section 5.2 this mass-degeneracy is verified on the lattice, although at finite lattice spacing supersymmetry and chiral symmetry are broken. Actually, in the simulations we do not chirally rotate the fermion field in the observables (as we did in our analytic analysis here), but instead the twisted Wilson Dirac operator is used. We argued that (up to a twist of the irrelevant Wilson term and as long as the anomaly is negligible) this is equivalent to the previous calculation with chirally rotated fields in the observables. Even for the twisted-mass Wilson Dirac operator $D_{\mathrm{W}}^{\mathrm{mtw}}$, that is the operator $D_{\mathrm{W}}^{\mathrm{dtw}}$ with $\varphi = 0$ and $\alpha = \pi/4$, we find mass-degenerated connected mesonic states. Though, the chiral and parity condensates and consequently the noise in a-η' and a-f_0 differ, cf. section 5.6. This aspect can be improved with the flexibility of the double-twist as discussed there.

Finally, let us analyze how the third particle in the VY-supermultiplet is affected by a chiral rotation (4.1). The starting point is the interpolating operator (3.63) for the fermionic gluino-glue state with a twisted spinor,

$$[O_{\tilde{\mathrm{g}}\mathrm{g}}(n)]_\mu = [\Sigma_{ij}]_{\mu\nu}\,\mathrm{tr_c}\left(F^{ij}(n)\left[\mathrm{e}^{\mathrm{i}\alpha\gamma_5/2}\lambda(n)\right]^\nu\right)\,.$$

Consequently, the corresponding correlator has the form

$$\begin{aligned}
&\left\langle \Gamma^{\mu\delta}[O_{\tilde{\mathrm{g}}\mathrm{g}}(n)]_\mu\,[\bar{O}_{\tilde{\mathrm{g}}\mathrm{g}}(n')]_\delta\right\rangle \\
&= \left\langle \Gamma^{\mu\delta}[\Sigma_{ij}]_{\mu\nu}\mathrm{tr_c}(F^{ij}(n)\left[\mathrm{e}^{\mathrm{i}\alpha\gamma_5/2}\lambda(n)\right]^\nu)\left([\Sigma_{lm}]_{\omega\rho}\mathrm{tr_c}(F^{lm}(n')\left[\mathrm{e}^{\mathrm{i}\alpha\gamma_5/2}\lambda(n')\right]^\rho)\right)^\dagger[\gamma_4]_{\omega\delta}\right\rangle \\
&= -\left\langle \mathrm{tr}\left(\Gamma^{\mathrm{T}}\,F^{ij}(n)\Sigma_{ij}\mathrm{e}^{\mathrm{i}\alpha\gamma_5/2}G_{n,n'}e^{\mathrm{i}\alpha\gamma_5/2}F^{lm}(n')\Sigma_{lm}\right)\right\rangle_{\mathcal{U}}\,. \qquad (4.16)
\end{aligned}$$

With the cyclicity of the trace one easily sees that for the antisymmetric correlator with $\Gamma = \mathbb{1}_4$ a chiral phase factor $\mathrm{e}^{\mathrm{i}\alpha\gamma_5}$ arises and for the symmetric correlator with $\Gamma = \gamma_4$ the chiral twists cancel.

4.2 Supersymmetry transformation of the lattice operators

Two chiral Wess-Zumino supermultiplets are predicted from the analysis of $\mathcal{N} = 1$ SYM theory with low-energy effective actions (see section 2.3). The VY- and FGS-supermultiplets are independent of each other and closed under supersymmetry. Thus in each

supermultiplet, the fermionic states have to transform into the bosonic state and vice versa the bosonic state has to transform into a linear combination of the fermionic states.

The following calculation is primarily intended to check if a chiral rotation of the spinors spoils the expected transformations within the VY-supermultiplet. For clarity in the equations, we use the continuum notation of the supersymmetry transformations and do not write the chiral twist explicitly. The additional chiral phase factor, which is multiplied with each spinor field λ, can be carried through the whole calculation. No additional terms arise in the supersymmetry transformations and thus the supermultiplet stays intact. The bosonic glueball operators are not affected by the twist at all and therefore only the interesting VY-supermultiplet is presented in the following.

Remember that the transformations have to respect the mass dimensions, Hermiticity and Lorentz transformations as discussed in section 2.3. The mesonic states a-η' and a-f_0 have mass dimension L^{-3}. As we will see below, these states transform into the gluino-glue state $F_{\mu\nu}\Sigma^{\mu\nu}\lambda$ with mass dimension $L^{-7/2}$ times the infinitesimal spinor ϵ of mass dimension $[\epsilon] = L^{1/2}$. To calculate the supersymmetry transformations analytically, the off-shell formulation of eq. (2.25) is more practical. The transformation of the a-f_0 can be computed straightforwardly:

$$\begin{aligned}
\delta_\epsilon O_{\text{a-}f_0}(x) &= \Big(\delta_\epsilon\bar\lambda(x)\Big)\lambda(x) + \bar\lambda(x)\Big(\delta_\epsilon\lambda(x)\Big) \\
&= -\bar\epsilon\frac{1}{4}\Sigma_{\mu\nu}F^{\mu\nu}(x)\lambda(x) + \mathrm{i}\bar\epsilon\mathcal{G}(x)\gamma_5\lambda(x) + \bar\lambda(x)\frac{1}{4}\Sigma_{\mu\nu}F^{\mu\nu}(x)\epsilon + \bar\lambda(x)\mathrm{i}\mathcal{G}(x)\gamma_5\epsilon \\
&= -\frac{1}{2}\bar\epsilon\, O_{\tilde{\mathrm{g}}\mathrm{g}}(x) + 2\mathrm{i}\bar\epsilon\mathcal{G}(x)\gamma_5\lambda(x)\,. \qquad (4.17)
\end{aligned}$$

Analogously, the a-η' transforms as

$$\begin{aligned}
\delta_\epsilon O_{\text{a-}\eta'}(x) &= \mathrm{i}\Big(\delta_\epsilon\bar\lambda(x)\Big)\gamma_5\lambda(x) + \mathrm{i}\bar\lambda(x)\gamma_5\Big(\delta_\epsilon\lambda(x)\Big) \\
&= -\bar\epsilon\frac{\mathrm{i}}{4}\Sigma_{\mu\nu}F^{\mu\nu}(x)\gamma_5\lambda(x) - \bar\epsilon\mathcal{G}(x)\gamma_5^2\lambda(x) + \bar\lambda(x)\gamma_5\frac{\mathrm{i}}{4}\Sigma_{\mu\nu}F^{\mu\nu}(x)\epsilon - \bar\lambda(x)\gamma_5\mathcal{G}(x)\gamma_5\epsilon \\
&= \left(-\frac{1}{2}\bar\epsilon\,\gamma_5 O_{\tilde{\mathrm{g}}\mathrm{g}}(x) + 2\mathrm{i}\bar\epsilon\mathcal{G}(x)\lambda(x)\right)\mathrm{i}\,. \qquad (4.18)
\end{aligned}$$

To determine the supersymmetry transformation of the gluino-glue one needs the transformation of the field strength tensor,

$$\begin{aligned}
\delta_\epsilon F_{\mu\nu}(x) &= \partial_\mu\delta_\epsilon A_\nu(x) - \partial_\nu\delta A_\mu(x) - \mathrm{i}[\delta_\epsilon A_\mu(x), A_\nu(x)] - \mathrm{i}[A_\mu(x), \delta_\epsilon A_\nu(x)] \\
&= \partial_\mu\delta_\epsilon A_\nu(x) - \mathrm{i}[A_\mu(x), \delta_\epsilon A_\nu(x)] - \Big(\partial_\nu\delta A_\mu(x) - \mathrm{i}[A_\nu(x), \delta_\epsilon A_\mu(x)]\Big) \\
&= D_\mu(\delta A_\nu(x)) - D_\nu(\delta A_\mu(x)) \\
&= \mathrm{i}\bar\epsilon\,(\gamma_\nu D_\mu - \gamma_\mu D_\nu)\lambda(x)\,. \qquad (4.19)
\end{aligned}$$

After a longer calculation (see appendix C), one finds the transformation of the gluino-glue:

$$\delta_\epsilon\Big(O_{\tilde{\mathrm{g}}\mathrm{g}}(x) - 4\mathrm{i}\mathcal{G}(x)\gamma_5\lambda(x)\Big) = 2\mathrm{i}\partial\!\!\!/ O_{\text{a-}f_0}(x)\epsilon + 2\gamma_5\partial\!\!\!/ O_{\text{a-}\eta'}(x)\epsilon + \dots\,. \qquad (4.20)$$

The terms linear in the auxiliary field $\mathcal{G}$ as well as further terms indicated with the dots in eq. (4.20) vanish on-shell and thus the VY-supermultiplet defines a chiral supermultiplet. This is in accordance to the expectation that the components of the supermultiplet transform like the fields of the Wess-Zumino model [202]. Here, it should be emphasized again that this calculation leads to the conclusion that the twist keeps the supermultiplet structure intact.

After a Wick-rotation to Euclidean spacetime, the on-shell supersymmetry transformation of eq. (2.23) read [203–205]

$$\delta_\epsilon A_\mu(x) = \mathrm{i}\bar{\epsilon}\gamma_\mu\lambda(x)\,, \qquad \delta_\epsilon\lambda(x) = \frac{1}{4\mathrm{i}}\Sigma_{\mu\nu}F^{\mu\nu}(x)\epsilon\,, \qquad \delta_\epsilon\bar{\lambda}(x) = -\frac{1}{4\mathrm{i}}\bar{\epsilon}\,\Sigma_{\mu\nu}F^{\mu\nu}(x)\,. \tag{4.21}$$

Since Majorana spinors in four-dimensional Euclidean spacetime cannot be defined with the reality condition, the consistent condition $\bar{\lambda} = \lambda^{\mathrm{T}}\mathcal{C}$ is used instead [127]. For the bilinears with the four-dimensional Euclidean matrices (see appendix A) the same symmetries hold as in Minkowski spacetime:

$$\bar{\psi}\chi = \bar{\chi}\psi\,,\ \bar{\psi}\gamma_5\chi = \bar{\chi}\gamma_5\psi\,,\ \bar{\psi}\gamma_5\gamma_\mu\chi = \bar{\chi}\gamma_5\gamma_\mu\psi \text{ are symmetric and} \tag{4.22}$$

$$\bar{\psi}\gamma_\mu\chi = -\bar{\chi}\gamma_\mu\psi\,,\ \bar{\psi}\gamma_{\mu\nu}\chi = \bar{\chi}\gamma_{\mu\nu}\psi \text{ are antisymmetric.} \tag{4.23}$$

Furthermore, an analogous Euclidean Fierz identity exists and the above calculation can be transferred to Euclidean spacetime. At finite lattice spacing supersymmetry is broken and this will lead to additional terms in the transformation laws [205, 206].

4.3 Eigenvalues of the free twisted Wilson Dirac operator

For particular twists of the free lattice Dirac operator in lower-dimensional Wess-Zumino models an improvement up to order $\mathcal{O}(a^4)$ can be achieved [22, 207]. In order to see whether an improvement is also possible for the twisted lattice Dirac operator in $\mathcal{N}=1$ SYM theory we determine the eigenvalues of the operator $D_{\mathrm{W}}^{\mathrm{dtw}}$ (see eq. (3.48)) for free fermions, that is for trivial link variables $\mathcal{V}_\mu = \mathbb{1}$.[18] Then, we expand them in powers of the lattice spacing a to study the discretization errors in dependence on the twist angles α, φ and analyze if $\mathcal{O}(a)$ improvement is possible for particular choices.[19] We decompose the double-twisted lattice Dirac operator for free fermions,

$$D_{\mathrm{W}}^{\mathrm{dtw}} = \gamma^\mu\mathring{\partial}_\mu + M\,\mathrm{e}^{\mathrm{i}\alpha\gamma_5} - \frac{aR}{2}\,\mathrm{e}^{\mathrm{i}\varphi\gamma_5}\hat{\Delta} = \gamma^\mu\mathring{\partial}_\mu + X + \mathrm{i}\gamma_5 Y\,, \tag{4.24}$$

[18] In our simulations, $(r, r_5) = (1, 0)$ resp. $R = \sqrt{r^2 + r_5^2} = 1$ and $\varphi = 0°$ is chosen if not stated otherwise.
[19] In this section we use physical units to recognize the powers of a.

which contains the naive antisymmetric lattice derivative $\mathring{\partial}_\mu$ and the symmetric lattice Laplacian $\hat{\Delta}$ (we use the notation of [136]). The real operators X, Y in the last decomposition are

$$X = M\cos\alpha - \frac{aR}{2}\hat{\Delta}\cos\varphi\,, \quad Y = M\sin\alpha - \frac{aR}{2}\hat{\Delta}\sin\varphi\,. \tag{4.25}$$

The periodic eigenfunctions are constant spinors times plane waves on a $L^3 \times T$ lattice:

$$\psi_p(x) = u_p\,\mathrm{e}^{\mathrm{i}p_\mu x^\mu}\,, \quad p_0 = \frac{2\pi}{aN_T}\left(n_0 + \frac{1}{2}\right)\,, \quad p_i = \frac{2\pi}{aN_S}\,n_i\,. \tag{4.26}$$

Anti-periodic boundary conditions are imposed for fermions and thus the energy p_0 of their Matsubara modes is shifted compared to the spatial momenta p_i [129]. Plane waves are eigenfunctions of the derivative operators and the Laplacian,

$$\mathring{\partial}_\mu \mapsto \mathrm{i}\mathring{p}_\mu\,, \quad \mathring{p}_\mu = \frac{1}{a}\,\sin(ap_\mu)\,, \qquad \hat{\Delta} \mapsto -\hat{p}_\mu\hat{p}^\mu\,, \quad \hat{p}_\mu = \frac{2}{a}\,\sin\left(\frac{ap_\mu}{2}\right)\,. \tag{4.27}$$

In a sector with fixed momentum the operator X is a constant X_p which just shifts the eigenvalues of $D_{\mathrm{W}}^{\mathrm{dtw}}$ in eq. (4.24). Hence it suffices to determine the imaginary eigenvalues of the four-dimensional anti-Hermitean matrix $\mathcal{A}$ in $D_{\mathrm{W}}^{\mathrm{dtw}} = \mathcal{A} + X$ for fixed momentum,

$$\mathcal{A}_p u_p = (\mathrm{i}\gamma^\mu\mathring{p}_\mu + \mathrm{i}\gamma_5 Y_p)\,u_p = \mathrm{i}\mu_p u_p\,, \quad \mu_p \in \mathbb{R}\,. \tag{4.28}$$

Since $\mathcal{A}_p\mathcal{A}_p^\dagger = \mathring{p}^2 + Y_p^2$ is a multiple of the identity matrix we conclude that $\mu_p^2 = \mathring{p}^2 + Y_p^2$. In Euclidean spacetime there exists an antisymmetric charge conjugation matrix $\mathcal{C}_+$ with

$$\mathcal{C}_+\gamma_\mu^{\mathrm{T}}\mathcal{C}_+^{-1} = \gamma_\mu\,, \quad \mathcal{C}_+\gamma_5^{\mathrm{T}}\mathcal{C}_+^{-1} = \gamma_5\,. \tag{4.29}$$

Using that γ^μ and γ_5 are Hermitean, taking the complex conjugate of the eigenvalue equation (4.28), and acting with $\mathcal{C}_+$ on this equation we see that the charge conjugated constant spinor $\mathcal{C}_+u_p^*$ is a second eigenvector with the same eigenvalue $\mathrm{i}\mu_p$. Finally, since $\mathrm{tr}(\mathcal{A}_p) = 0$ we deduce, that $\mathcal{A}_p$ has two eigenvalues $\mathrm{i}\mu_p$ and two eigenvalues $-\mathrm{i}\mu_p$. We conclude that for fixed p_μ the twisted Dirac operator $D_{\mathrm{W}}^{\mathrm{dtw}} = \mathcal{A} + X$ has the double degenerated eigenvalues

$$\lambda_p = X_p + \mathrm{i}\mu_p \quad \text{and} \quad \lambda_p^* = X_p - \mathrm{i}\mu_p \quad \text{with} \quad \mu_p = \sqrt{\mathring{p}^2 + Y_p^2}\,. \tag{4.30}$$

Up to a possible sign the Pfaffian of the Dirac operator is the square root of its determinant and hence given by the product of all $|\lambda_p|^2$, where

$$|\lambda_p|^2 = \mathring{p}^2 + X_p^2 + Y_p^2 = \mathring{p}^2 + M^2 + \frac{(aR)^2}{4}\hat{p}^2\hat{p}^2 + (aR)M\hat{p}^2\cos(\alpha-\varphi)\,. \tag{4.31}$$

Inserting the small-a expansions of $\hat{p}_\mu$ and $\mathring{p}_\mu$ from eq. (4.27) gives rise to

$$|\lambda_p|^2 = p^2 + M^2 + (aR)Mp^2\cos(\alpha-\varphi) + \frac{a^2}{12}\left(3R^2(p_\mu p^\mu)^2 - 4\sum_\mu p_\mu^4\right) + \mathcal{O}(a^3)\,. \tag{4.32}$$

Table 4.1: Eigenvalues $|\lambda_p|^2$ of several lattice Dirac operators D_i, expanded in powers of the lattice spacing a. We defined $\kappa \equiv -\frac{1}{3}\sum_\mu p_\mu^4 + \frac{R^2}{4}\big(p_\mu p^\mu\big)^2$.

lattice Dirac operator	eigenvalues $\lvert\lambda_p\rvert^2$
$D_1 = \gamma^\mu \mathring{\partial}_\mu + M - \frac{aR}{2}\hat{\Delta}$	$p^2 + M^2 + aMRp^2 + \mathcal{O}(a^2)$
$D_2 = \gamma^\mu \mathring{\partial}_\mu + M - \frac{\mathrm{i}aR}{2}\gamma_5\hat{\Delta}$	$p^2 + M^2 + \kappa a^2 + \mathcal{O}(a^4)$
$D_3 = \gamma^\mu \mathring{\partial}_\mu + M\,\mathrm{e}^{\mathrm{i}\alpha\gamma_5} - \frac{aR}{2}\hat{\Delta}$	$p^2 + M^2 + aMRp^2\cos(\alpha) + \mathcal{O}(a^2)$
$D_4 = \gamma^\mu \mathring{\partial}_\mu + M\,\mathrm{e}^{\mathrm{i}\alpha\gamma_5} - \frac{aR}{2}\mathrm{e}^{\mathrm{i}\varphi\gamma_5}\hat{\Delta}$	$p^2 + M^2 + aMRp^2\cos(\alpha-\varphi) + \kappa a^2 + \mathcal{O}(a^3)$

Here we see explicitly that setting $\alpha - \varphi = 90°$ leads to an $\mathcal{O}(a)$ improvement in the fermionic sector – at least for free fermions.

Table 4.1 summarizes the values for $|\lambda_p|^2$ and their small-a expansions for various lattice Dirac operators considered in the present work. Starting from the Wilson Dirac operator D_1 with $\mathcal{O}(a)$ discretization errors, we can remove the leading discretization effects by choosing a 90°-twist like in D_2 (corresponding to fully twisted lattice QCD [83]) or by modifying the Wilson term like in D_3. In general, for free fermions $\mathcal{O}(a)$ improvement can be achieved when the mass term and Wilson term are orthogonal to each other, i.e. $\alpha - \varphi = 90° \pmod{180°}$ in D_4.

At this point, it is important to recall the relation between the twists of the mass term and the Wilson term. Starting from the general double-twisted action with Dirac operator (3.48), we add an additional twist to the spinors, $\lambda \mapsto \mathrm{e}^{\mathrm{i}\omega\gamma_5/2}\lambda$, $\bar{\lambda} \mapsto \bar{\lambda}\mathrm{e}^{\mathrm{i}\omega\gamma_5/2}$. This leads to the double-twisted fermion action

$$S^{\mathrm{dtw}} = \frac{a^4}{2}\sum_{n\in\Lambda}\bar{\lambda}_n\Big(\frac{4R}{a}\,\mathrm{e}^{\mathrm{i}(\varphi+\omega)\gamma_5} + M\,\mathrm{e}^{\mathrm{i}(\alpha+\omega)\gamma_5}\Big)\lambda_n - \frac{a^3}{4}\sum_{n\in\Lambda}\sum_{\mu=\pm1}^{\pm4}\bar{\lambda}_n\Big(\mathbb{1}R\,\mathrm{e}^{\mathrm{i}(\varphi+\omega)\gamma_5} - \gamma_\mu\Big)\mathcal{V}_\mu(n)\lambda_{n+\hat{\mu}}.$$

By choosing $\omega = -\varphi$ we recover the mass-twisted Wilson Dirac operator with angle $\alpha - \varphi$ and the choice $\omega = -\alpha$ leads to an operator with a non-vanishing angle $\varphi - \alpha$ in the Wilson term only. Hence one twist angle should be sufficient, but the relative angle between the mass term and the Wilson term matters and cannot be changed by a chiral rotation of the spinors. In the end, one angle can be transformed to zero and we prefer a remaining mass twist over a Wilson term twist to avoid problems with reflection positivity, which may arise for a complex Wilson term with $r_5 \neq 0$.

Unfortunately, the mass difference of the superpartners a-f_0 and a-η' is minimal for $\alpha = \varphi = 45°$ and not for $\alpha - \varphi = 90°$, see figure 5.10 and calculation in section 4.1. Since in the present work our main focus is on the restoration of supersymmetry and chirality we choose $(\alpha, \varphi) = (45°, 0°)$ for most of our simulations. Then $\mathcal{O}(a)$ discretization errors are not removed completely, but reduced by a factor of $\cos(45°) = 1/\sqrt{2} \approx 0.7071$.

CHAPTER 5

Technical investigations

For our simulations, we used two different modifications of Wilson fermions introduced in section 3.2.2, namely clover fermions and twisted fermions. In section 5.1, the former are applied and a parameter scan in the (m, c_{SW})-plane is performed to explore if an optimal parameter combination can be found. For the mass-twisted fermions, we start in section 5.2 with a parameter scan in the (m, m_5)-plane. As in the analytical calculation of section 4.1, the twist angle $\alpha = 45°$ stands out. More technical sections follow and deal with the sign of the Pfaffian (5.3), the scale setting (5.4), and the finite size effects (5.5). Afterwards, the possibilities of the double-twist are inspected in section 5.6. The remainder of this chapter highlights two improvements, the fermion smearing (5.7.1) and the DDαAMG algorithm (5.7.2). For an overview of the ensembles and parameters, see appendix G.

5.1 Clover fermions

In our early investigations of $\mathcal{N} = 1$ SYM theory, we extended the Wilson Dirac operator with a clover term, see section 3.2. Therefore we restructured the implementation of the Dirac operator in a modular way, such that terms can be added to the operator easily and a preconditioner can be chosen independently.

For the $\mathcal{O}(a)$ improvement of clover fermions, the Sheikholeslami-Wohlert coefficient c_{SW} has to be determined properly. Since for our combination of the Lüscher-Weisz gauge action with fermions in the adjoint representation no perturbative value is published in the literature, we use the possibility to determine the clover coefficient directly in the simulation via the tadpole factor u_0. To check if a better value of c_{SW} can be found, we perform a parameter scan in the (m, c_{SW})-plane.

In the heuristic parameter scan we try to minimize the adjoint pion mass for various clover coefficients $c_{\mathrm{SW}} \in [0, 3.7]$ by varying the bare gluino mass m. For this investigation, we fix the lattice size to $8^3 \times 16$ and the lattice coupling to $\beta = 4.2$. Figure 5.1 depicts the dominant mass contribution of the adjoint pion in the (m, c_{SW}) parameter space. In the

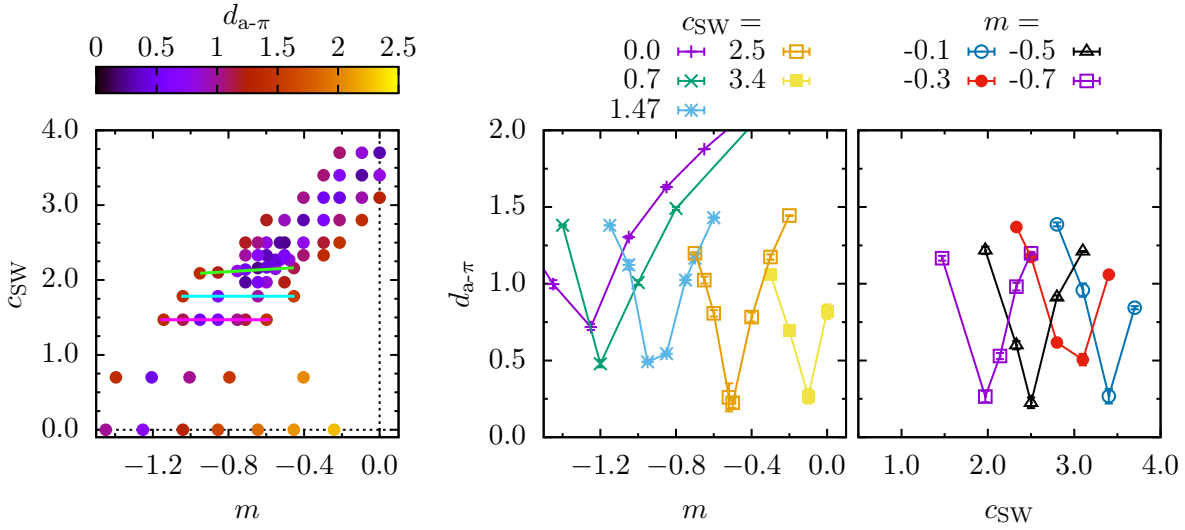

Figure 5.1: Parameter scan of the dominant mass contribution d of the adjoint pion. Left: The dependence on both parameters m, c_{SW} is depicted with color-coded $d_{\text{a-}\pi}$. The colored lines are discussed in the text. Center/Right: Same data as selected cuts with fixed c_{SW} resp. m. Markers are connected to guide the eye. Most error bars are smaller than the marker size.

left panel the value of $d_{\text{a-}\pi}$ is encoded in the color scale, while the middle and right panel show selected slices of constant c_{SW} resp. m. The different curves for fixed c_{SW} show that the critical point is shifted towards smaller mass parameters m for raising c_{SW} values. On the other hand, the right panel with curves of constant m, indicates that for all choices the lightest contribution to the adjoint pion has comparable magnitude. The red curve seems to lie higher, but an additional data point at $m \in [2.8, 3.1]$ should lead also to a lighter value with $d_{\text{a-}\pi} \approx 0.25$.

In summary, at least three outstanding combinations of the analyzed (m, c_{SW}) parameter space exist. In all of them only one parameter has to been tuned, otherwise any approach would not be practicable. Firstly, the choice $c_{\text{SW}} = 0$ without a clover term, corresponding to traditional Wilson fermions (horizontal dashed line). In this case no $\mathcal{O}(a)$ improvement can be achieved and the parameter m is tuned to find the critical point. Secondly, the clover coefficient c_{SW} may be tuned at fixed chiral tree-level mass parameter $m = 0$, see vertical dashed line. Finally, we could use the tadpole value $c_{\text{SW}} \approx 2.1$ and fine-tune m to the critical point there, which is highlighted in figure 5.1 with the green line. This variant lies between the two aforementioned extreme choices. If we exchanged the Symanzik-improved Lüscher-Weisz gauge action S_{g}^{LW} with the Wilson plaquette gauge action S_{g}^{W}, then the perturbative clover coefficient $c_{\text{SW}} = 1.7829$ of eq. (3.45) would be the most common choice, see cyan line. For comparison, we indicate with the magenta line the clover value $c_{\text{SW}} = 1.4697$, which is an estimate for the Lüscher-Weisz gauge action S_{g}^{LW} by using eq. (3.45) of the plaquette action with rescaled coupling $g^2 = \frac{2N_{\text{c}}}{\beta'}$ and with $\beta' = \frac{5}{3}\beta$.

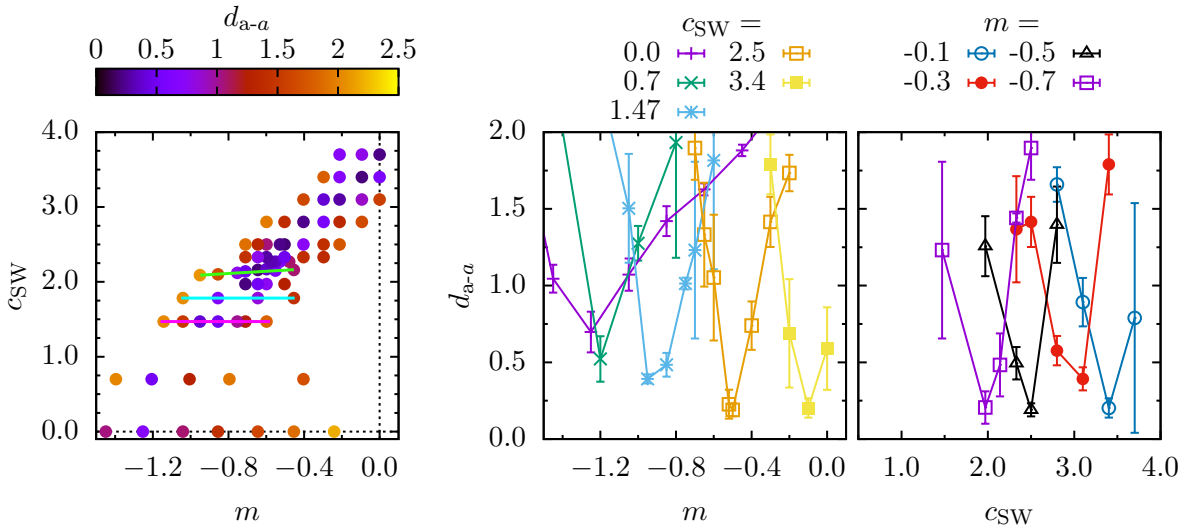

Figure 5.2: Parameter scan of the dominant mass contribution d of the a-a. Left: The dependence on both parameters m, c_{SW} is depicted with color-coded $d_{\text{a-}a}$. The colored lines are discussed in the text. Center/Right: Same data as selected cuts with fixed c_{SW} resp. m. Markers are connected to guide the eye.

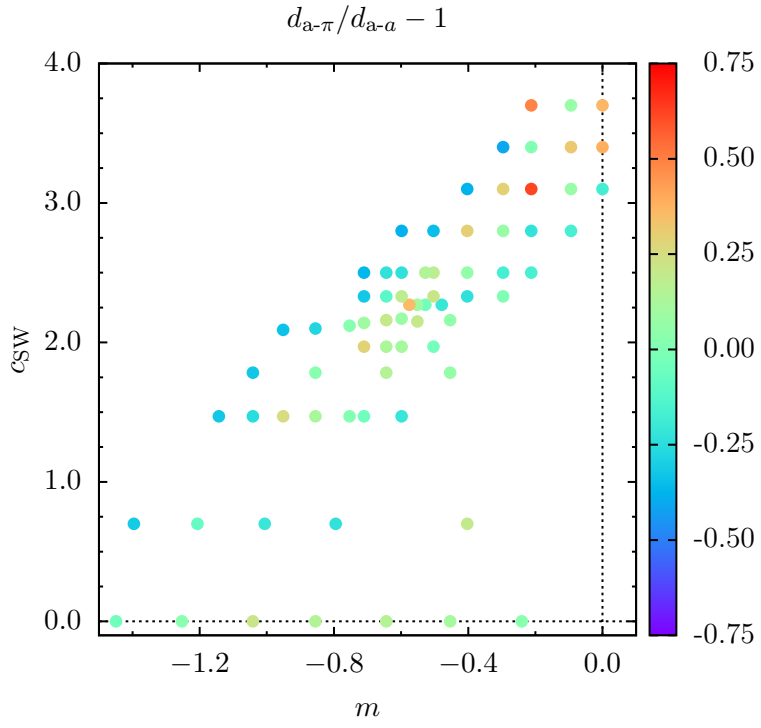

Figure 5.3: The data of figure 5.1 and 5.2 plotted as subtracted ratio $d_{\text{a-}\pi}/d_{\text{a-}a} - 1$. The light green data points signal that a-a and a-π have the same mass contributions.

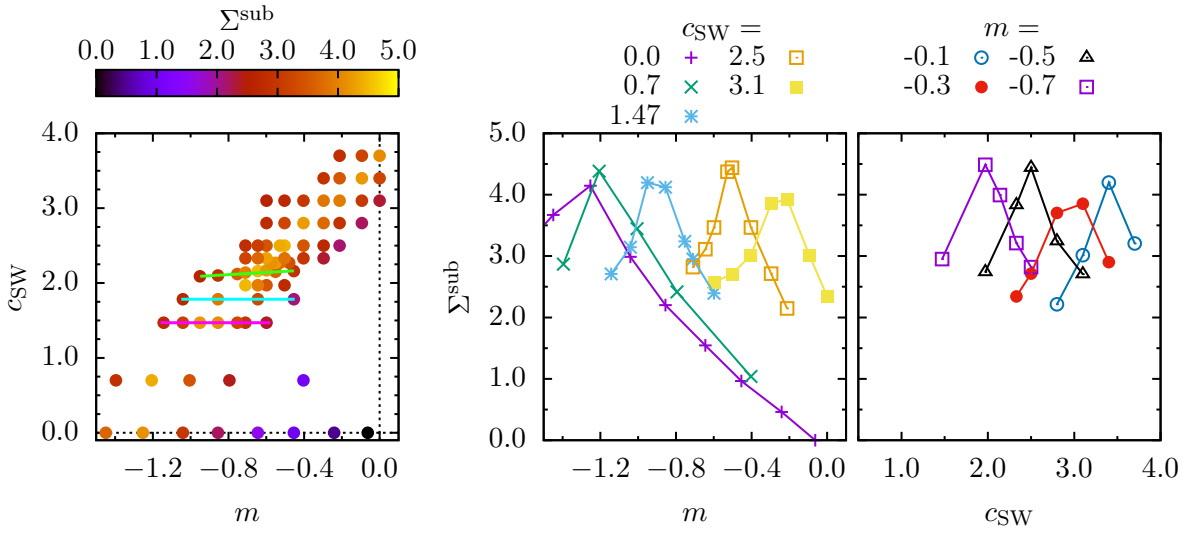

Figure 5.4: Parameter scan of the subtracted chiral condensate Σ^{sub}. Left: The dependence on both parameters m, c_{SW} is depicted with color-coded Σ^{sub}. The colored lines are discussed in the text. Center/Right: Same data as selected cuts with fixed c_{SW} resp. m. Markers are connected to guide the eye and error bars are neglected for better visibility.

To get a deeper insight into the different scenarios, we present further observables. Analogous results like for the a-π are shown in figure 5.2 for the a-a meson. In the central and right panel with the cuts of constant c_{SW} resp. m the error bars are larger compared to figure 5.1. Apart from that the data in the left panel looks very similar.

To visualize the differences, the subtracted ratio $d_{\text{a-}\pi}/d_{\text{a-}a} - 1$ is analyzed in figure 5.3. Two regions of this diagonally lying band attract attention. The outermost points to the top left have negative (blue) values indicating that the a-a is heavier than the a-π. Furthermore there is a large region in green, which corresponds to equal mass contributions. Only in the center of the band, some points are colored in red and signal that the adjoint pion is heavier than the adjoint a meson. This is unexpected, because the pion should be the lightest state as argued in appendix E. In section 5.2 we encounter again such an unexpected mass hierarchy. A careful analysis of the finite size effects is performed in section 5.5 to explore their origin.

Here, we restrict ourselves to the connected mesons, because the ensemble size in the parameter scan is not large enough for a meaningful signal of the physical mesons with their disconnected contributions. Furthermore, the subtracted chiral condensate (see eq. (3.57)) is evaluated in figure 5.4. Identically to the discussed mesonic states, the subtracted chiral condensate is extremal along the critical line. It is shrinking for constant m as well as constant c_{SW} departing from the critical line and its steepest descent is perpendicular to the critical line.

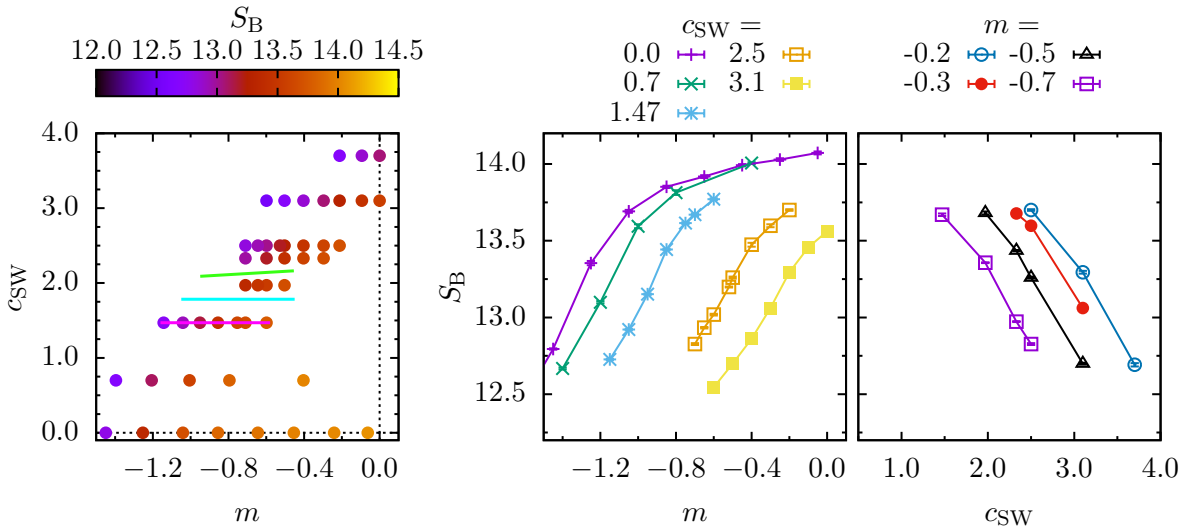

Figure 5.5: Parameter scan of the bosonic action S_B. The observable was measured only on some of the ensembles. Therefore the left plot contains fewer data points than the previous figures. Left: The dependence on both parameters m, c_{SW} is depicted with color-coded S_B. Center/Right: Same data as selected cuts with fixed c_{SW} resp. m. Markers are connected to guide the eye. Most error bars are smaller than the marker size.

Additionally, we investigated the bosonic action, which is part of the bosonic Ward identity (3.54). Its value for the adjoint representation of the gauge group SU(3) is predicted to be $S_B = 12$ and a deviation indicates broken supersymmetry. Along the critical line of the adjoint pion, its value stays approximately constant, see figure 5.5. In contrast to the other observables the bosonic action is not extremal there. It shrinks for constant mass m and increasing clover coefficient c_{SW} as well as for decreasing m and fixed c_{SW}. Thus the clover term reduces the deviation of the bosonic action to its predicted value and improves the bosonic Ward identity.

In conclusion, the discussed observables do not answer the question, which (heuristic) value is an optimal clover coefficient. Subsequent investigations with different lattice spacings and further observables are necessary to this end. A promising candidate would be the PCAC relation, which is well-suited, because of its sensitivity to discretization errors. So far this relation is not implemented in our code. Instead we focused on a different $\mathcal{N} = 1$ SYM specific fermion formulation inspired by observations, see the next section with the parameter scan of the mass-twisted Wilson Dirac operator.

We close this section with some remarks on the calculation of the clover coefficient with the tree-level tadpole formula presented in table 3.3. In our simulations, the clover coefficient is not a dynamical parameter. Instead, it is calculated for each ensemble at the beginning of the simulation on some configurations. When it plateaus, we freeze its value and start the Monte-Carlo history. As usual the first configurations of the thermalization are neglected for the measurements of the observables.

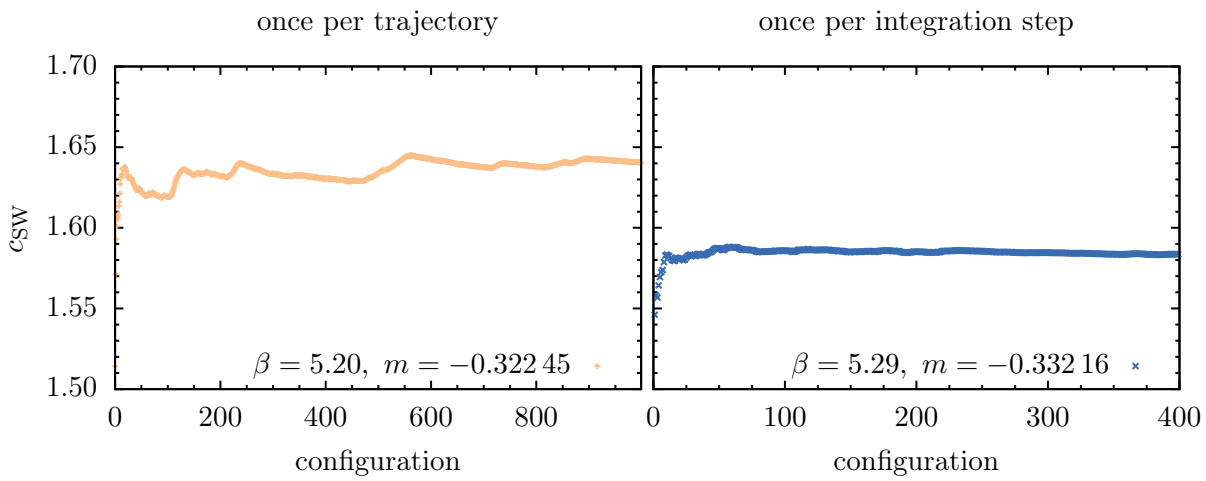

Figure 5.6: Clover coefficient c_{SW} versus the configuration number for two ensembles with mass parameter and lattice coupling given in the legend. The clover coefficient is calculated with the tree-level tadpole formula given in table 3.3. In the left/right panel, c_{SW} is updated once per trajectory (consisting of 12 integration steps) resp. once per integration step. This test was performed on a 8^4 lattice with two fundamental Dirac fermions, i.e. 2-flavor QCD, and without freezing c_{SW}.

For this initial clover setup, we tested different update frequencies. Figure 5.6 compares the value of c_{SW} along the Markov chain with updates either once per trajectory or once per integration step (i.e. as soon as the gauge field changes). In the left panel, it can be seen that the clover coefficient does not reach a thermalized constant value. On the contrary, more frequent updates help to plateau. Approximate 100 configurations are sufficient for thermalization with the chosen parameters in the right panel of the plot. Except for this test, we always used the frequent c_{SW} update once per integration step.

For stable simulations and roughly constant acceptance rates, we have to freeze the clover coefficient after its setup. To illustrate the effect of the freezing, figure 5.7 shows one ensemble with a thermalization length of 20 configurations and a neighboring ensemble with doubled thermalization length. The left panel shows a clear kink in the clover coefficient when the freezing starts and it may be estimated that the natural saturation without this artificial freeze would be some percent higher. Based on experience, this small deviation of the clover coefficient has no significant impact on the observables. In the right panel, the corresponding values of the plaquette are shown and it can be seen that the plaquette needs approximately 20 configurations to thermalize. There is no noticeable difference between those two data sets with 20 resp. 40 configurations before c_{SW} is frozen. Only in the interval between 20 and 40, the ensemble depicted in green fluctuates stronger, but in both cases the plaquette in this interval matches approximately the thermalized average at later times.

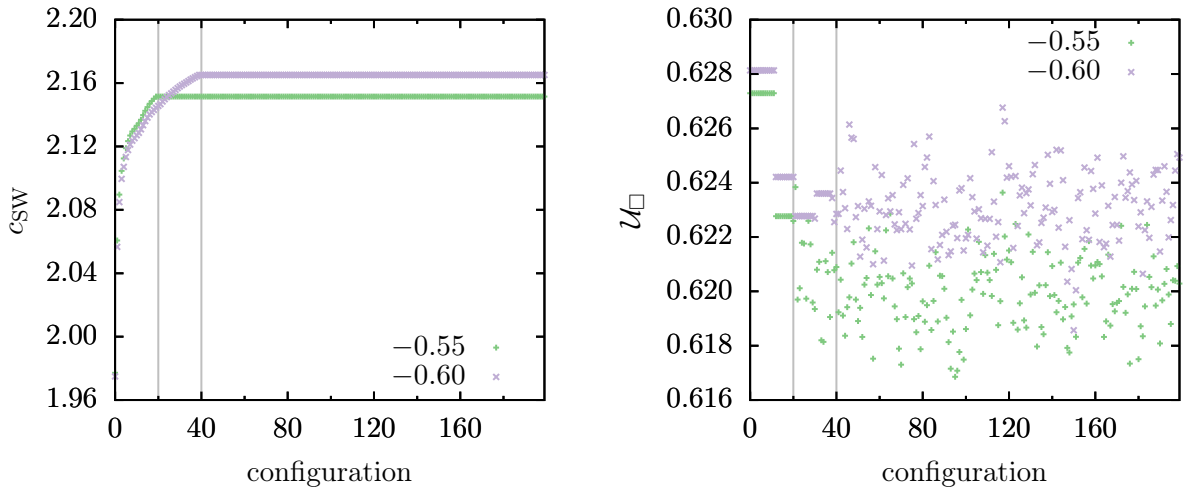

Figure 5.7: Left/Right: Clover coefficient c_{SW} resp. plaquette $\mathcal{U}_\square$ versus the configuration number for two ensembles at $\beta = 4.2$. The clover coefficient is calculated with the tree-level tadpole formula given in table 3.3 on the first configurations. For $m = -0.55$ (green symbols) resp. $m = -0.60$ (purple symbols) the latest clover coefficient is frozen after 20 resp. 40 configurations, highlighted by the vertical gray lines. For this reason the plaquette fluctuates stronger after 20 resp. 40 configurations. At those configuration numbers the plaquette is already approximately thermalized.

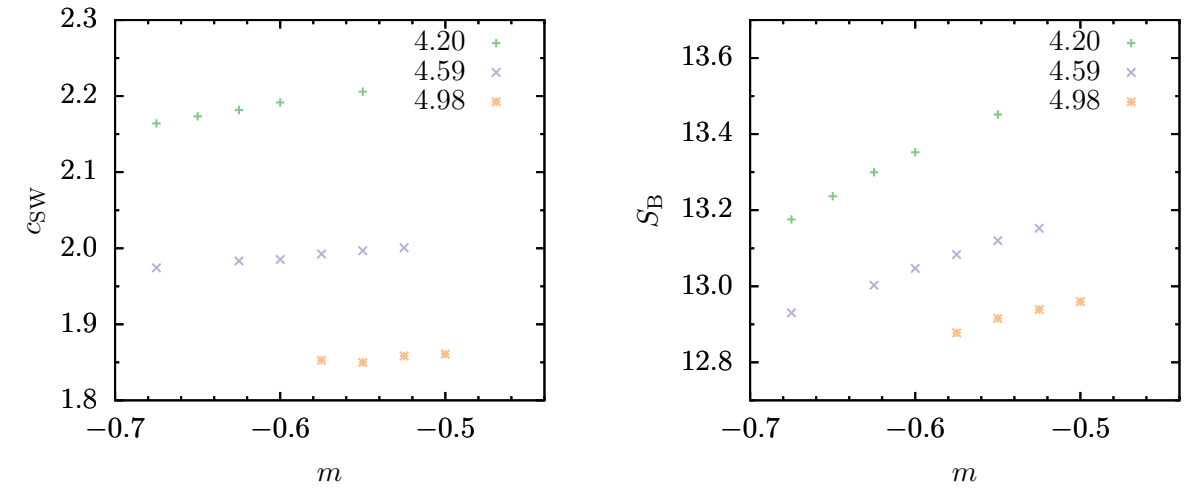

Figure 5.8: Left/Right: Clover coefficient c_{SW} resp. bosonic action S_B in dependence of the bare mass m. The data were measured on a $16^3 \times 32$ lattice with lattice couplings $\beta \in \{4.20, 4.59, 4.98\}$.

Finally we present in the left panel of figure 5.8 the dependence of the clover coefficient on the mass parameter m and the lattice coupling β. For comparison, the right panel shows the bosonic action S_B. Both observables shrink when the mass m is lowered, although the slope of c_{SW} is smaller.

To sum up, the parameter scan in the (m, c_{SW})-plane with the chosen observables gives no conclusive results. Especially, figure 5.3 with the subtracted ratio $d_{\text{a-}\pi}/d_{\text{a-}a} - 1$ does not reveal a region, where the mass contributions of the two chiral partners are identical. Thus, we conclude that the clover term does not lead to an improvement of the mass-degeneracy within the VY-supermultiplet. In the next section, we succeed with the twisted Wilson Dirac operator. The starting point is the same heuristic approach.

5.2 Twisted-mass parameter scan

To analyze the effect of a twisted mass term, we calculate the dominant mass contributions of the a-π and a-a in the (m, m_5) parameter space. Let us recall at this point that the connected mesonic states are not part of the physical spectrum of the $\mathcal{N} = 1$ SYM theory. But these auxiliary states are very useful, mainly because the signal-to-noise ratio of their correlators is much better compared to that of the physical mesonic states with disconnected contributions. Therefore we use the connected mesons for ensembles with low statistics, like in the parameter scan of this section. In addition, the connected diagrams contribute to the correlators of the physical states, see eq. (3.60) and (3.61). Hence, the connected mesonic states partly determine the behavior of the full physical states.

For the parameter scan we fix the lattice coupling to $\beta = 5.4$ and vary the mass parameters $m \in [-1.4, -0.6]$ and $m_5 \in [-0.4, 0.4]$ around the critical point, $(m, m_5) = (-0.967, 0.0)$. Due to the $(m_5 \leftrightarrow -m_5)$-symmetry, fine parameter steps are necessary only in the upper half-plane of the parameter space. Every gauge ensemble consists of approximately 200 thermalized configurations which is sufficient for a good signal-to-noise ratio of the connected correlators. To determine their dominant mass contribution d, all correlators are fitted to the ansatz (3.18). On the rather small $8^3 \times 16$ lattice, the quantity d is only a rough estimate for the ground state mass and the results for the latter are more qualitative than quantitative. However, the simulation results on a larger $16^3 \times 32$ lattice support our findings.

Note that we treat the twist as a deformation of the lattice action and do *not* rotate observables back, as is done in twisted-mass QCD. In the chiral limit $(m \to m_{\mathrm{crit}}, m_5 \to 0)$ the twisted Wilson Dirac operator $D_{\mathrm{W}}^{\mathrm{mtw}}$ (3.46) is equivalent to the untwisted Wilson Dirac operator D_{W} (3.41) such that both operators correspond to the same continuum theory. But the breaking of chiral symmetry and supersymmetry may be suppressed along certain paths ending at the critical parameters.

The left and center panels of figure 5.9 show the dominant mass contributions $d_{\text{a-}\pi}$ and $d_{\text{a-}a}$. In the right panel the subtracted ratio $d_{\text{a-}\pi}/d_{\text{a-}a} - 1$ near the critical point is shown. Three interesting choices for the twist angle α are highlighted with colored lines:

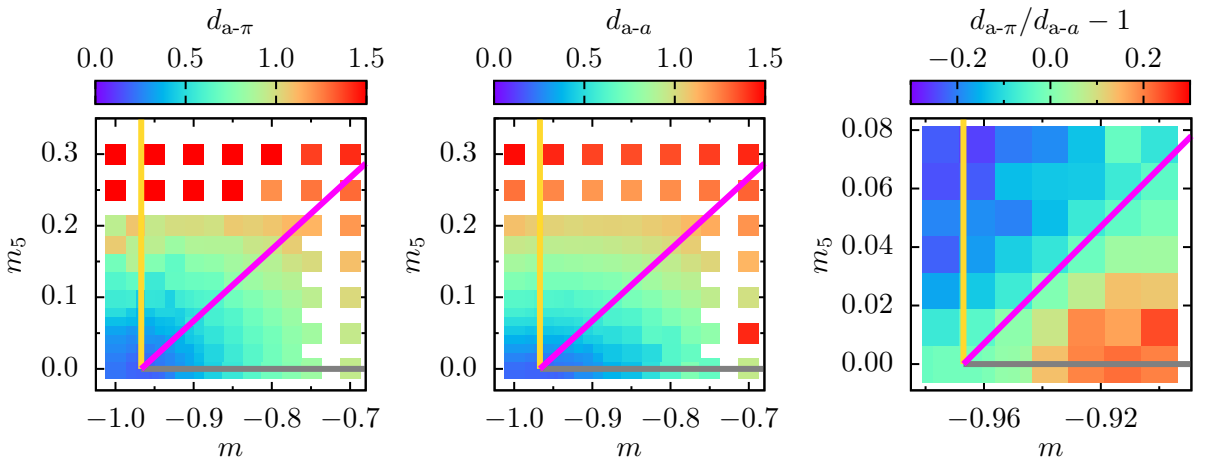

Figure 5.9: Parameter scan in m and m_5 on a $8^3 \times 16$ lattice. In the left and middle plot the dominant mass contribution d of the a-π (connected part of the a-η') resp. a-a (connected part of the a-f_0) are shown. The right plot combines those results in the subtracted ratio $d_{\text{a-}\pi}/d_{\text{a-}a} - 1$. Note the different axis ranges. The colored lines (gray, magenta and yellow) are discussed in the text.

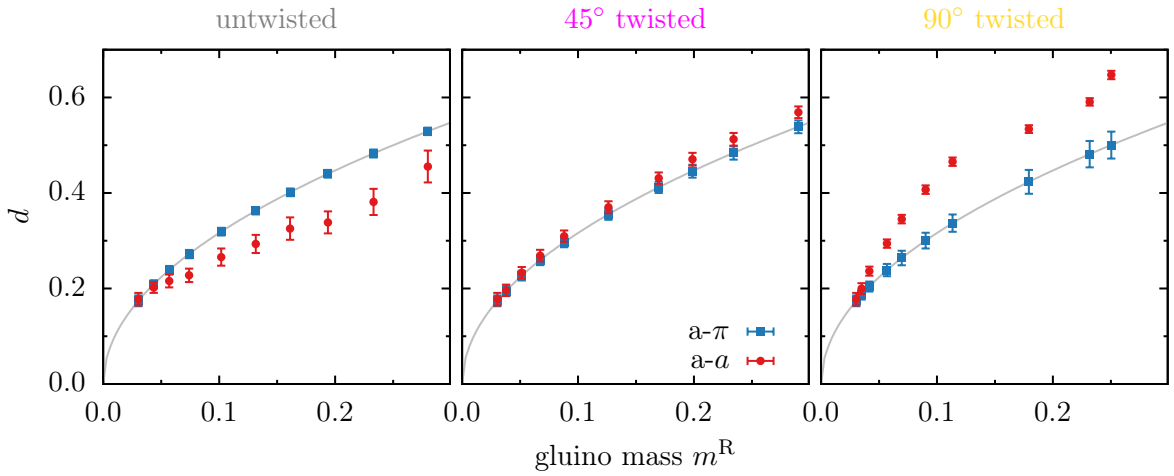

Figure 5.10: The three plots correspond to twist angles $\alpha \in \{0°, 45°, 90°\}$ marked in figure 5.9 with lines in gray, magenta and yellow. The same data of the $8^3 \times 16$ lattice is used and three clearly different mass hierarchies of the dominant contribution d are revealed. Some error bars are smaller than the symbol size. The gray curve $\sqrt{m^{\text{R}}}$ highlights the relation $m^{\text{R}} \propto m^2_{\text{a-}\pi}$.

- The data points for the untwisted case with $\alpha = 0°$ and $m_5 = 0$ along the gray line indicate that $d_{\text{a-}\pi}$ is greater than $d_{\text{a-}a}$.
- For $\alpha = 45°$ along the diagonal magenta line, the dominant mass contributions of the chiral partners a-π and a-a seem to match.
- At maximal twist, i.e., $\alpha = 90°$, where the bare gluino mass is kept fixed at its critical value, $m = m_{\text{crit}} = -0.967$, and only the twisted mass parameter m_5 is varied, $d_{\text{a-}a}$ is greater than $d_{\text{a-}\pi}$, see the vertical yellow line.

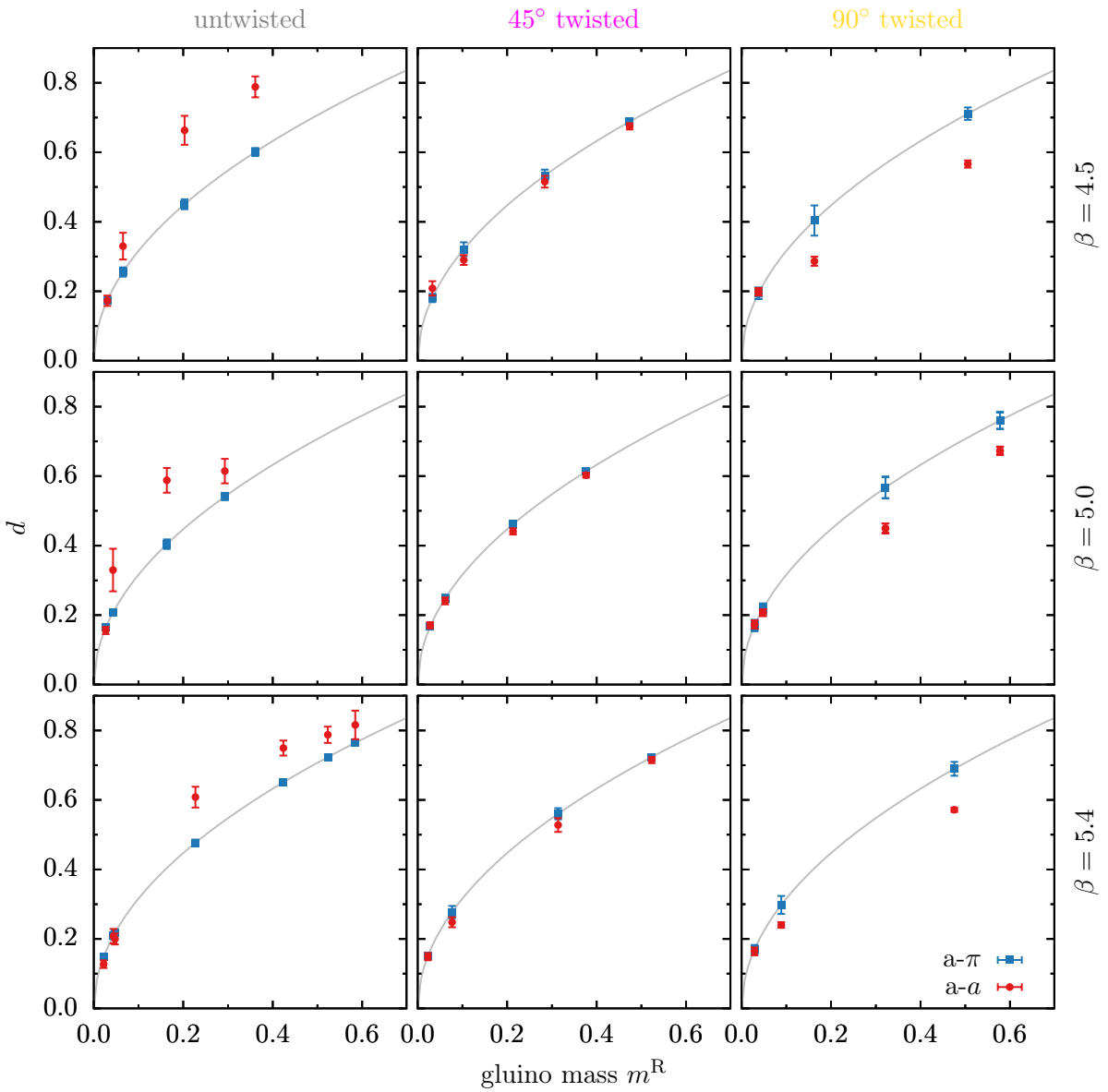

Figure 5.11: Connected mesons on the $16^3 \times 32$ lattice. From left to right the twist angle $\alpha \in \{0°, 45°, 90°\}$ rises. From top to bottom the lattice coupling $\beta \in \{4.5, 5.0, 5.4\}$ increases. Some error bars are smaller than the symbol size and some data points lie on top of each other. Only the first and last time slices are excluded in the correlator fit, i.e., $t_{\mathrm{cut}} = (1, 0)$.

The results clearly suggest that for $\alpha = 45°$ the chiral properties are improved considerably at finite lattice spacing. This interpretation is supported by the results shown in figure 5.10, where the dominant mass contributions $d_{\text{a-}\pi}$ and $d_{\text{a-}a}$ are shown versus the renormalized gluino mass $m^{\text{R}} \propto m^2_{\text{a-}\pi}$. At $\alpha = 45°$ the two chiral partners have equal mass contributions within errors. In contrast, for $\alpha = 0°$ and $\alpha = 90°$ we clearly see a split of the two mass contributions.[20]

To substantiate this observation on the small $8^3 \times 16$ lattice, we double the lattice in each direction and repeat our calculation for the gauge couplings $\beta \in \{4.5, 5.0, 5.4\}$ along the three aforementioned twist angles α. We see in figure 5.11 that without twist the dominant a-a contribution is greater than the a-π contribution, at $\alpha = 45°$ both contributions are equal, and at maximal twist $\alpha = 90°$ the a-a contribution is smaller than that of a-π. Compared to the results on the smaller volume in figure 5.10, the mass hierarchies for $\alpha = 0°$ and $\alpha = 90°$ are inverted, which was a finite size effect of the small lattice, but our findings for $\alpha = 45°$ remain and are barely affected by the lattice size.

In the subsequent sections, we will therefore focus on the twist angle $\alpha = 45°$ with improved chiral and supersymmetry properties at finite lattice spacing. Furthermore from section 4.3 we know this special twist reduces the discretization errors of order $\mathcal{O}(a)$ at tree-level which may reduce lattice spacing artifacts also at the non-perturbative level. Performing continuum extrapolations along the $\alpha = 45°$ direction might thus be beneficial.

What remains is a cross-check of our findings with other observables. The chiral condensate Σ and the parity condensate Σ^{p} are good candidates built from the gluino field, see eqs. (3.55) and (3.56). Note that the chiral condensate needs an additive renormalization and therefore the subtracted chiral condensate (3.57) is used. A parameter scan of those condensates along the three "directions", i.e., $\alpha \in \{0°, 45°, 90°\}$, is depicted in figure 5.12. In the left panel we notice that the subtracted chiral condensate is maximal at the critical point and falls off radially symmetrically. Particularly, this contains a mirror symmetry in $m_5 \leftrightarrow -m_5$ like for the dominant mass contribution $d_{\text{a-}\pi}$ of the adjoint pion. The parity condensate is shown in the right panel of figure 5.12. Along the gray data points with $m_5 = 0$ it vanishes, but if m_5 is increased the condensate decreases linearly and vice versa. The largest slope (yellow data points) is in direction of the m_5-axis.

From figure 5.12 we learn that the mass twist $\alpha = 45°$ is not a distinguished angle for the condensates. Only on-axis directions, that is 0° and 90°, are special. However, we will see in section 5.6 that for the double-twisted Wilson Dirac operator, $\alpha = \varphi = 45°$ is particular, because the absolute values of the condensates are equal there (see figure 5.26).

[20] See appendix E for a discussion of the expected mass hierarchy at $\alpha = 0°$ and also compare with figure 5.11.

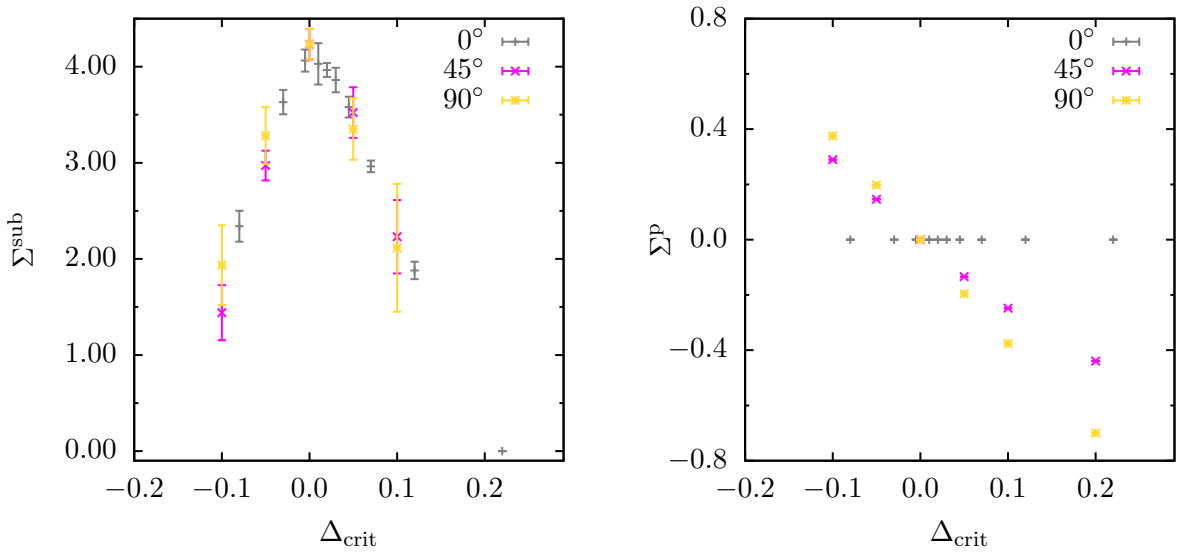

Figure 5.12: Left/Right: The subtracted chiral condensate Σ^{sub} resp. parity condensate Σ^{p} versus the distance $\Delta_{\mathrm{crit}} = (m - m_{\mathrm{crit}})\cos(\alpha) + m_5 \sin(\alpha)$ to the critical point. Note the different vertical axes. The different colors correspond to $\alpha = 0°$, $45°$ and $90°$. The error bars of the parity condensate are smaller than the symbol size.

5.3 Sign of the Pfaffian

In order to have a positive Boltzmann weight in the path integral, the Pfaffian must be positive. Otherwise our lattice calculations may suffer from a sign problem. In the continuum, the Pfaffian of $\mathcal{N} = 1$ SYM theory is real, but our twisted Wilson Dirac operator may have a complex Pfaffian. To check the severeness of that problem additional lattice calculations of the Pfaffian have been performed. Since the computational costs scale as $\mathcal{O}(N^3)$ and the memory requirement as $\mathcal{O}(N^2)$ with the size N of the Dirac matrix, the explicit calculation of the Pfaffian with the optimized serial algorithm [208] was only performed for lattice sizes from $2^3 \times 4$ to $7^3 \times 14$, see table 5.1. The computation time for one single Pfaffian on the $7^3 \times 14$ lattice is roughly 125 hours.

Table 5.1: Lattices $N_S^3 \times N_T$ and corresponding numbers of configurations on which the Pfaffian was calculated.

N_S	2	3	4	5	6	7
N_T	4	6	8	10	12	14
#	1000	1000	1000	400	100	20

The left panel of figure 5.13 shows the phase ω of $\mathrm{Pf}(\mathcal{C}D_{\mathrm{W}}^{\mathrm{mtw}}) = |\mathcal{C}D_{\mathrm{W}}^{\mathrm{mtw}}| \cdot \mathrm{e}^{\mathrm{i}\omega}$ for different lattice sizes and fixed simulation parameters $\beta = 5.4$ and $(m, m_5) = (-0.85, 0.1)$ with $m_{\text{a-}\pi} \approx 0.60$. Extrapolated to the typical lattice size of our calculations, $16^3 \times 32$, we find that the phase remains small: $1 - \cos(\omega) < 0.035$. That is, we expect no significant

sign problem for our simulations. In a further series of measurements with four different lattice couplings the Pfaffian is measured on a $4^3 \times 8$ lattice, each ensemble with 350 thermalized configurations. The corresponding results are summarized in the right plot of figure 5.13 and it can be deduced that the Pfaffian phase (and thus the risk of a sign problem) is smaller for larger lattice couplings β, i.e. closer to the continuum. Additionally, it is evident that the Pfaffian phase shrinks towards the critical point at $m_5 = 0$.

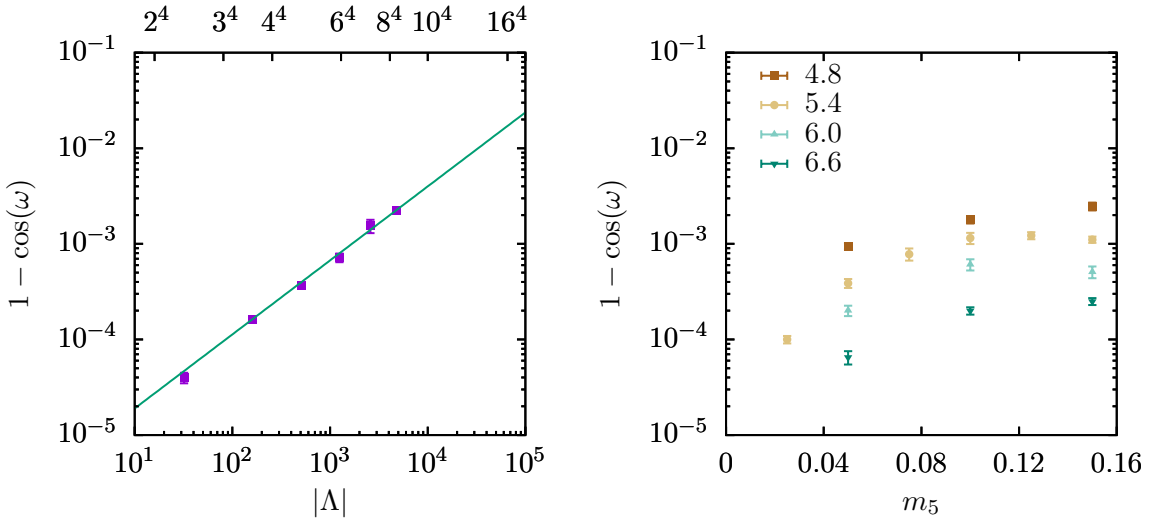

Figure 5.13: Left: Phase of the Pfaffian for different lattice sizes ranging from $2^3 \times 4$ to $7^3 \times 14$. The green line is an exponential fit to extrapolate the results to the lattice size $16^3 \times 32$. Right: Phase of the Pfaffian for different lattice couplings $\beta \in \{4.8, 5.4, 6.0, 6.6\}$ over m_5 on a $4^3 \times 8$ lattice. When approaching the critical point at $m_5 = 0$, the phase of the Pfaffian decreases. Error bars are mostly smaller than the symbol size.

5.4 Scale setting

In order to set the scale, the Sommer parameter and QCD units are used, i.e., $r_0 = 0.5\,\mathrm{fm}$ [209]. In the given context this is somewhat arbitrary but it allows for a direct comparison with results in the literature.

For our estimate of a/r_0, we calculate fundamental rectangular Wilson loops of different size and extract the static potential $V(R)$ for a range of spatial separations R [210]. In temporal direction all loops are sufficiently large such that $V(R)$ remains stable. Furthermore, different levels of stout smearing are applied to the gauge fields (with staple weight $\rho = 0.1$ [171]) and the Wilson mass is varied to allow for a safe extrapolation to the critical point, $m \to m_{\mathrm{crit}}$. For the different bare masses and levels of smearing, the results for $V(R)$ are separately fitted to

$$V(R) = V_0 + \sigma R - \frac{\alpha}{R}\,. \tag{5.1}$$

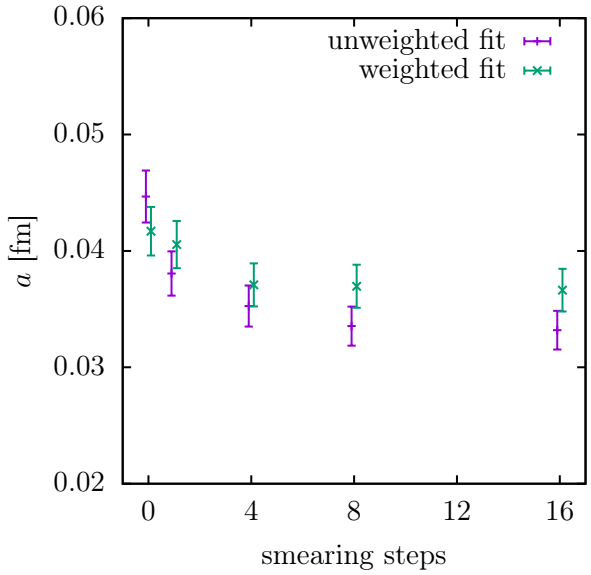

Figure 5.14: Lattice spacing a [fm] vs. number of gauge smearing steps. The values include an extrapolation to the critical point. To this end the parameter set (II) is fitted to $V(R)$ for different m, see table G.4 in appendix G.2. Unweighted and weighted fits to $V(R)$ leads to slightly different values of the lattice spacing a. Points are slightly displaced for better visibility.

From the fit parameters and setting

$$\frac{r_0}{a} \equiv \sqrt{\frac{1.65 - \alpha}{\sigma a^2}} \tag{5.2}$$

we obtain the lattice spacing and can extrapolate to the critical point. As an example, the lattice spacing for parameter set (II) is shown in figure 5.14 for different amounts of stout smearing and extrapolated to the critical point. We find that for a large number of stout smearing steps, the static potential changes its shape, but for a moderate number the values of the lattice spacing are all comparable. Combining the data in a linear fit leads to the lattice spacing $a = (0.040 \pm 0.002)\,\mathrm{fm}$ for this parameter set, which translates to a spatial length $L = aN_S = (0.64 \pm 0.03)\,\mathrm{fm}$ of the $16^3 \times 32$ lattice. In comparison to other lattice studies, e.g. [211], a box length $L < 1\,\mathrm{fm}$ appears small and finite size effects need to be analyzed carefully. This is provided in the following section.

5.5 Finite size effects

To analyze the finite size effects, we continue with parameter set (V) and show the correlators of a-π and a-a for $(m, m_5) = (-0.8950, 0.0000)$ in figure 5.15. Looking at the two panels, one clearly sees both correlators would not fit a simple cosh-shape. Up to $t = 5$ (and $T - t = 5$), contributions from higher states are visible, and the interval where a single exponential behavior dominates is rather short. For the fit, we choose a 2-cosh-ansatz (3.18) and vary the fit range with $t \in [t_1, T/2 - t_2]$ and $t \in [T/2 + t_2, T - t_1]$.

As an example, the 2-cosh fits for $t_1 = 2$ and $t_2 = 4$ are included in figure 5.15. Colored symbols refer to points inside the fit range, while gray symbols refer to points outside. Although cutting the inner time slices is not necessary, it turns out to be useful nonetheless:

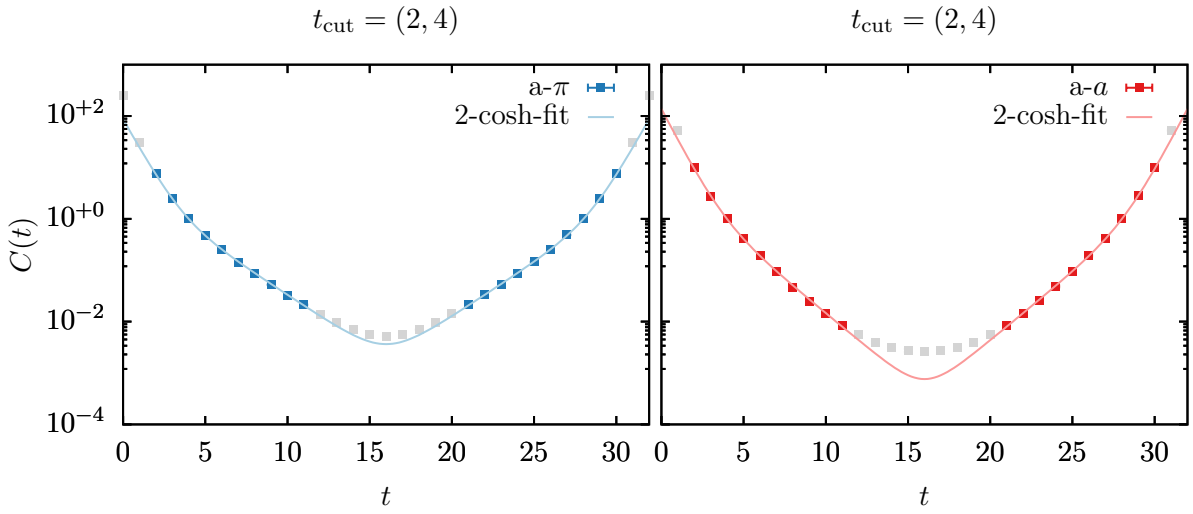

Figure 5.15: Left/Right: a-π resp. a-a correlator at $\beta = 5.4$ and $(m, m_5) = (-0.8950, 0.0)$ with 2-cosh-fits. The gray data points are excluded from the fit to reduce contributions from higher states and to stabilize the fit. Error bars are smaller than the symbol size.

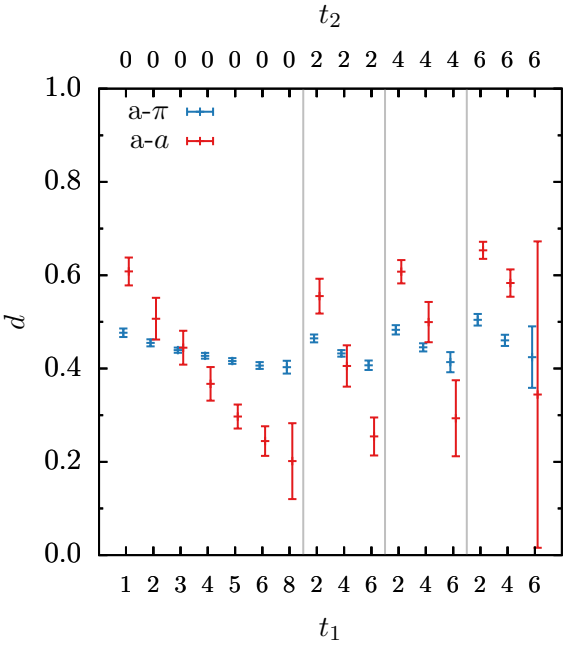

Figure 5.16: The dominant mass contribution d of a-π and a-a from 2-cosh-fits with different cuts $t_{\mathrm{cut}} = (t_1, t_2)$ at $\beta = 5.4$ and $(m, m_5) = (-0.8950, 0.0)$. The gray vertical lines separate regions with different values of t_2.

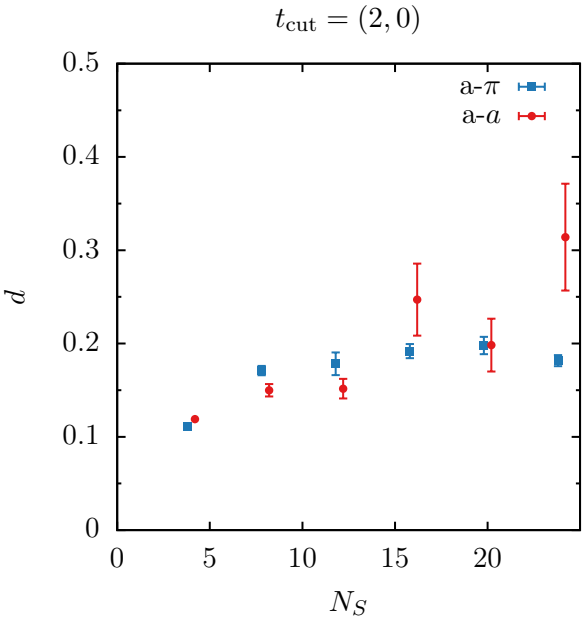

Figure 5.17: Dominant mass contribution of a-π and a-a for different lattice sizes $N_S^3 \times 2N_S$ with $N_S \in \{4, 8, 12, 16, 20, 24\}$. The bare gluino mass is $(m, m_5) = (-1.0506, 0.0)$ and the lattice coupling is $\beta = 5.0$. Points are slightly displaced for better visibility. Two time slices are excluded in the correlator fit at the boundary, i.e., $t_{\mathrm{cut}} = (2, 0)$.

Near the critical point, the correlators of the connected part of the mesonic states are flat while those of the disconnected part are dominated by statistical noise. Thus, a properly chosen fit window can reduce the influence of excited states at small t and lattice artifacts in the center of the correlator.

Results for $d_{\text{a-}\pi}$ and $d_{\text{a-}a}$, with different combinations of t_1 and t_2, are presented in figure 5.16. There, the upper t_2-axis divides the plot (vertical lines) into four domains and each domain shows d versus t_1 at constant t_2. We see that a variation of t_2 has a minor effect on the value of d, whereas there is a clear linear dependence on t_1. In particular for a-a this dependence is significant.

To estimate the finite size effects, the same 2-cosh-ansatz is used to analyze d as a function of the spatial lattice extent N_S. We performed simulations for $\beta = 5.0$ and $(m, m_5) = (-1.0506, 0.0)$ on lattices with spatial extent $N_S = 4, \ldots, 24$ and the results for the connected adjoint states are shown in figure 5.17. For the adjoint pion, d forms a plateau at approximately $d = 0.2$ for $N_S \geq 16$, while for the a-a the situation is not as clear. Finite size effects result in a too light adjoint pion mass which was also observed in [212, 213].

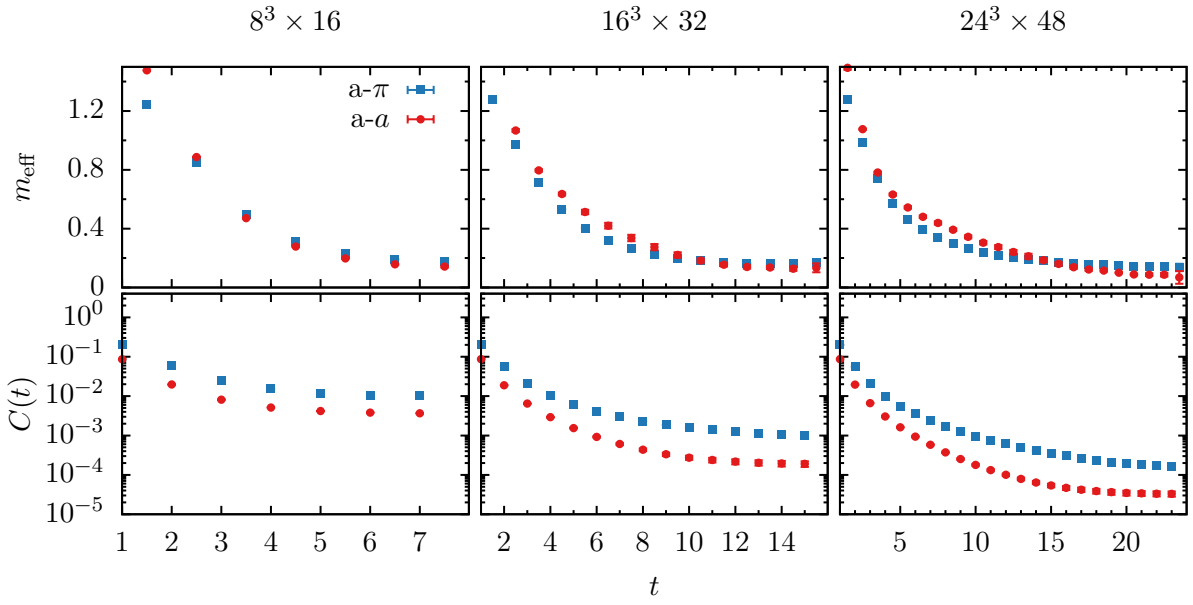

Figure 5.18: Top/Bottom: Effective masses/Correlators of the adjoint pion and the adjoint a meson at fixed bare gluino mass $m = -1.0506$ and lattice coupling $\beta = 5.0$, without any twist. From left to right the three columns show results from a $8^3 \times 16$, $16^3 \times 32$ and $24^3 \times 48$ lattice. Most error bars are smaller than the symbol size.

Volume effects are also apparent in the effective mass plots of a-π and a-a. Such plots, and the corresponding correlators, are shown in figure 5.18, again for $\beta = 5.0$, $(m, m_5) = (-1.0506, 0.0)$ and $N_S = 8, 16, 24$. Looking at the upper panels we notice an intersection of the effective mass values at a certain t. The effective mass of a-a falls off

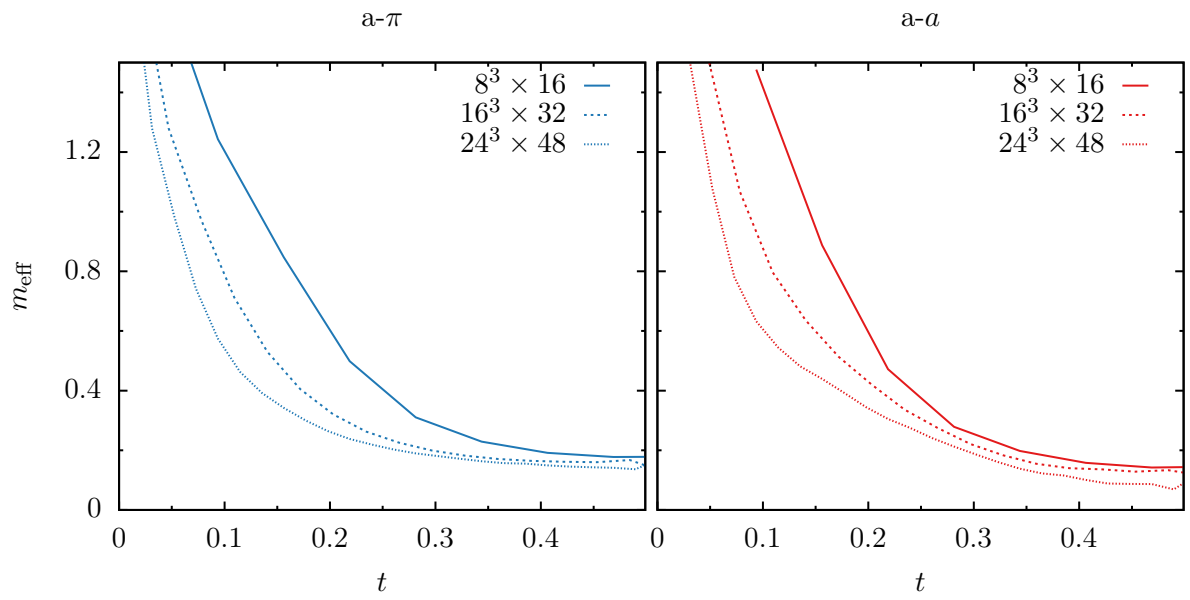

Figure 5.19: Effective masses at fixed bare gluino mass $m = -1.0506$ and lattice coupling $\beta = 5.0$, without any twist. The left/right panel compares a-π resp. a-a for different lattice sizes. To enhance visibility, the data points are connected by lines and symbols and error bars are omitted.

faster with t than that of a-π and approaches a lower value. Furthermore, the deviations seem to increase with increasing volume. This is in contrast to common expectations, because the a-π should be the lightest state, see appendix E for a further discussion. We suppose the relatively small volume ($L < 1\,\text{fm}$) causes a-a to appear lighter than a-π.

Further indications are provided by figure 5.19 showing separately for a-π and a-a the same data sets as figure 5.18 but plotted against the rescaled variable t/T such that finite size effects are better visible. We see that the effective mass curves of a-π settle on approximately the same value on all lattices and the length of the plateau increases with the lattice size. But for the a-a state the effective mass seems not to approach an unambiguous plateau, if at all. Rather m_{eff} and the plateau get smaller when increasing the lattice size which is unexpected. This indicates an enhanced correlation length and is in line with the correlator plots in the lower panels of figure 5.18. There, the a-a correlator on the largest lattice ($24^3 \times 48$) decays visibly faster than the a-π correlator for $0 < t \lesssim 15$ and reaches a very flat region at $t \gtrsim 20$. On the smaller lattices this effect is less pronounced. Again we see that finite size effects are small for a-π, while they are more distinct for a-a such that an unambiguous mass extraction is difficult despite the good signal-to-noise ratio.

For a comprehensive insight why the a-a correlator is so flat, a further test case follows. Still without any twist, the chosen parameters $m = -0.9856$ and $\beta = 5.0$ correspond to an adjoint pion mass $m_{\text{a-}\pi} \approx 0.5$. The correlators in the top row of figure 5.20 show the

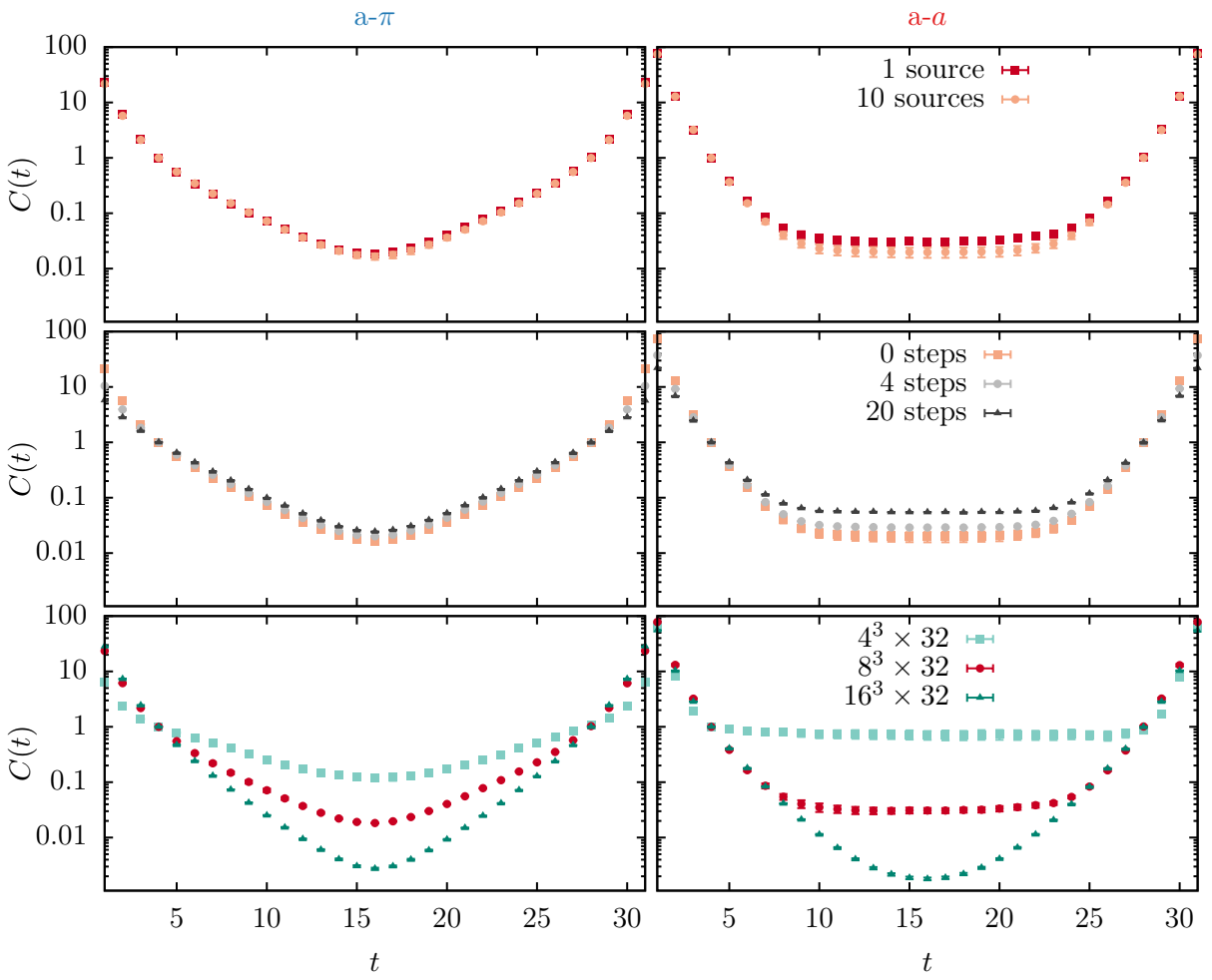

Figure 5.20: Left/Right: Correlators of a-π resp. a-a. Most error bars are smaller than the marker size. Top: Comparison of 1 and 10 point sources on the $8^3 \times 32$ lattice. Center: Comparison of the amount of Jacobi smearing on the $8^3 \times 32$ lattice. Bottom: Comparison of lattice sizes $4^3 \times 32$, $8^3 \times 32$ and $16^3 \times 32$ with one unsmeared point source.

expected shape for the a-π and a pronounced flat region for the a-a. Additional point sources lead to a lower minimum and reduce the flat range slightly. In the second row, different numbers of Jacobi smearing steps are compared. More smearing leads to flatter correlators and a marginal worsening of the flat region. Finally, the third row of figure 5.20 reveals the origin of the problem. Keeping the temporal extent $N_T = 32$ fixed, the number of spatial lattice points is varied, $N_S = 4, 8, 16$. Obviously, a large enough lattice removes the flat region of the a-a correlator completely. Furthermore, we see in the range $t \in [4, 8]$ a comparable slope of the correlators on the $8^3 \times 32$ and $16^3 \times 32$ lattices. Therefore, we have evidence that a suitable fit window helps to reduce the impact of finite size effects.

In conclusion, especially the adjoint a meson is affected by finite size effects on small volumes, where a very flat region appears in its correlator. As a consequence the extracted dominant mass contribution of a-a is underestimated. In appendix F, the correlators and

effective masses for twist angles $\alpha \in \{0°, 45°, 90°\}$ are discussed with regard to finite size effects. The mass-twisted Wilson Dirac operator improves the situation, because it leads to a mixing of the mesonic a-π and a-a. At optimal twist angle $\alpha = 45°$, the correlators of a-π and a-a have identical shapes and finite size effects are reduced.

Finally, we watch for signs of topological freezing which may occur at small lattice spacings $a \lesssim 0.05\,\mathrm{fm}$ [211]. In the top panel of figure 5.21, the Monte Carlo history of the chiral condensate Σ shows no evidence for a loss of ergodicity. Also the simple lattice definition of the topological charge $Q = \frac{1}{32\pi^2} \sum_n \epsilon_{\mu\nu\rho\sigma} F^a_{\mu\nu}(n) F^a_{\rho\sigma}(n)$, rounded to integers and depicted in the bottom panel, fluctuates a lot and indicates an efficient sampling [214]. Only the parity condensate Σ^{P} in the central panel does not fluctuate so uniformly as the other two observables.

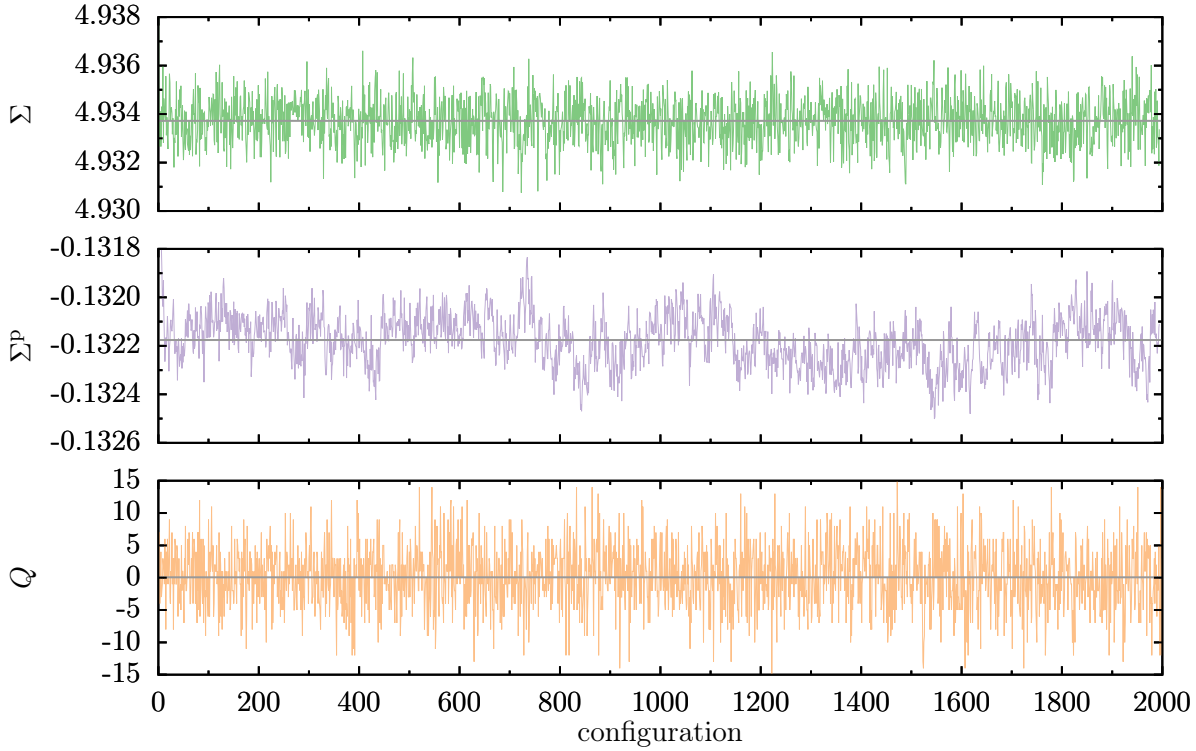

Figure 5.21: Chiral condensate (top), parity condensate (center) and topological charge (bottom) versus the Monte Carlo history. Note the different scales. The gray horizontal lines highlight the average values.

5.6 Double twist

For a deeper understanding of the twists, we study the double-twisted Wilson Dirac operator of eq. (3.48). Each parameter set can be specified either with absolute values (m, m_5) and (r, r_5), or with the angles (α, φ) with respect to the critical point. First, some

parameter studies are discussed. Afterwards, the freedom of the parameter choice is used to investigate the potential chiral anomaly and the relevance of the Wilson term.

In general, a modification of the Wilson parameters (r, r_5) requires a new fine-tuning, because the critical point is shifted. To exemplify, the Wilson parameters $(r, r_5) = \left(\frac{1}{\sqrt{2}}, \frac{1}{\sqrt{2}}\right)$, i.e. $\varphi = 45°$, are chosen and (m, m_5) are varied to find the mass parameters with minimal adjoint pion mass. The critical point is found at $(m, m_5) = (-0.7570, -0.7570)$, see figure 5.22. These values correspond to a rotation by $\varphi = 45°$ of the untwisted critical point at $(m_{\text{crit}}, m_5) = (-1.0706, 0.0000)$.

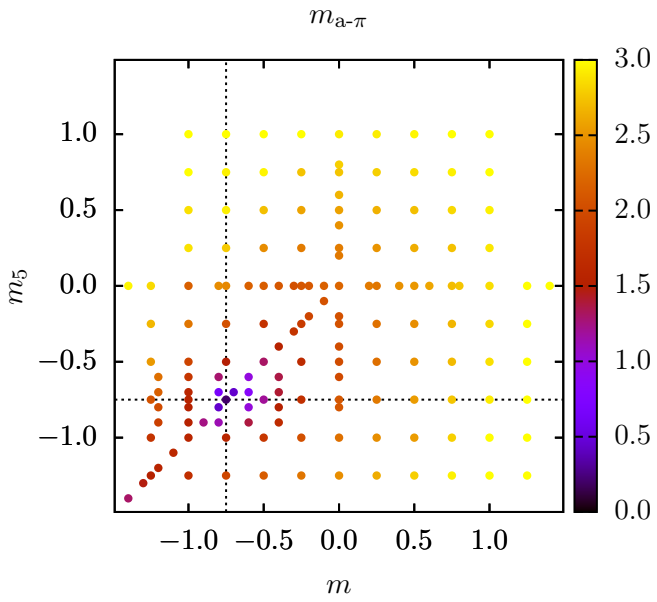

Figure 5.22: Parameter scan of the adjoint pion in the (m, m_5)-plane to find the critical point for the twisted Wilson parameter $(r, r_5) = \left(\frac{1}{\sqrt{2}}, \frac{1}{\sqrt{2}}\right)$ on the $8^3 \times 16$ lattice. The dotted black lines highlight the values of m and m_5, where the adjoint pion has its smallest mass.

We learn two lessons. Firstly, the critical point is rotated in the (m, m_5)-plane as soon as the Wilson term is twisted. Secondly, the critical points lie on a circle and their values can be calculated, $(m, m_5) = (m_{\text{crit}} \cos(\varphi), m_{\text{crit}} \sin(\varphi))$. Remember that the mass twist is always defined relatively to the (φ-dependent) critical point:

$$\alpha = \arctan\left(\frac{m_5 - m_{\text{crit}} \sin(\varphi)}{m - m_{\text{crit}} \cos(\varphi)}\right) . \tag{5.3}$$

In total 11 combinations (α, φ) of twist angles have been tested in more detail, listed in table 5.2. To visualize the chosen parameter sets, the critical point for each twist angle φ is marked in the left panel of figure 5.23 with a filled black circle and the colored rectangles depict the investigated regions of the (m, m_5)-plane. In the right panel of figure 5.23, the extracted masses of the adjoint pion are shown. Clearly, the lightest adjoint pion lies for each combination of (α, φ) on the dashed circle. In accordance to section 5.2, we find different mass hierarchies of a-π and a-a in dependence on the angle α. Independent of φ, we encounter a mass-degeneracy at $\alpha = \pm 45°$, see magenta rectangles in the left panel of figure 5.23.

Table 5.2: Investigated parameter combinations of the twist angles α, φ of the mass term and Wilson term.

α	$-45°$	$0°$	$0°$	$0°$	$45°$	$45°$	$45°$	$45°$	$90°$	$90°$	$90°$
φ	$45°$	$0°$	$45°$	$90°$	$-45°$	$0°$	$45°$	$135°$	$0°$	$45°$	$90°$

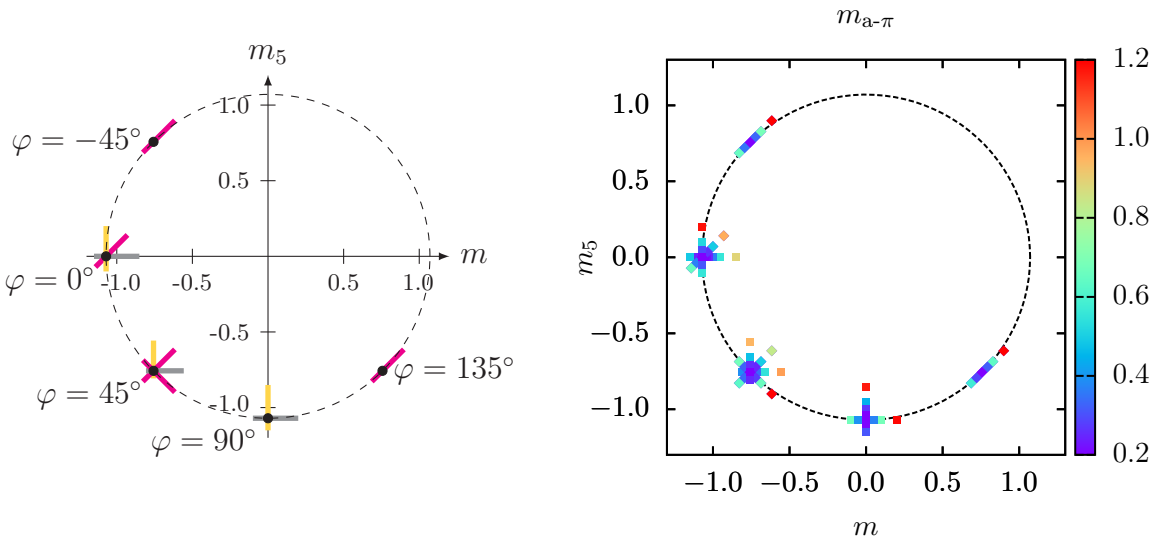

Figure 5.23: Left: Critical points (black filled circles) for different angles φ of the Wilson term in the (m, m_5)-plane. All critical points lie on the dashed circle with radius 1.0706. Rectangles mark the regions of (m, m_5), where simulations were performed. The colors indicate the different mass hierarchies of a-π and a-a at the angles $\alpha = 0°$ (gray), $\alpha \in \{-45°, 45°\}$ (magenta) and $\alpha = 90°$ (yellow), cf. figure 5.11. Right: The colored symbols show the adjoint pion mass for the different combinations of (α, φ) sketched on the left. All results are extracted from simulations on a $8^3 \times 16$ lattice with $\beta = 5.0$.

To quantify a possible anomaly and study the quality of the 45°-twist, we now consider the condensates and analyze the impact of the twist angles (α, φ) on them. Additionally to the twist combinations listed in table 5.2, we performed simulations at $(m, m_5) = -1.0506 \cdot (\cos(\varphi), \sin(\varphi))$, $\varphi = 10°, 20°, \ldots, 350°$. All those points are displaced from the critical point by $\Delta m = 0.02$ in direction of the origin. This special choice means $\alpha = \varphi$. The condensates are shown in figure 5.24 for the different twist combinations on the $8^3 \times 16$ lattice. Clearly, the chiral condensate Σ in the left panel has a $(m_5 \leftrightarrow -m_5)$-symmetry and its sign flips for $m \leftrightarrow -m$. For the parity condensate Σ^{P} in the right panel it is the other way around. Hence, the condensates have a φ-dependence, which can be explained as follows.

In the untwisted scenario, the chiral condensate is significantly larger than the parity condensate, because it is triggered by the Wilson term. Generalized to arbitrary angles φ, the (rotated) Wilson term always distinguishes one direction and consequently the

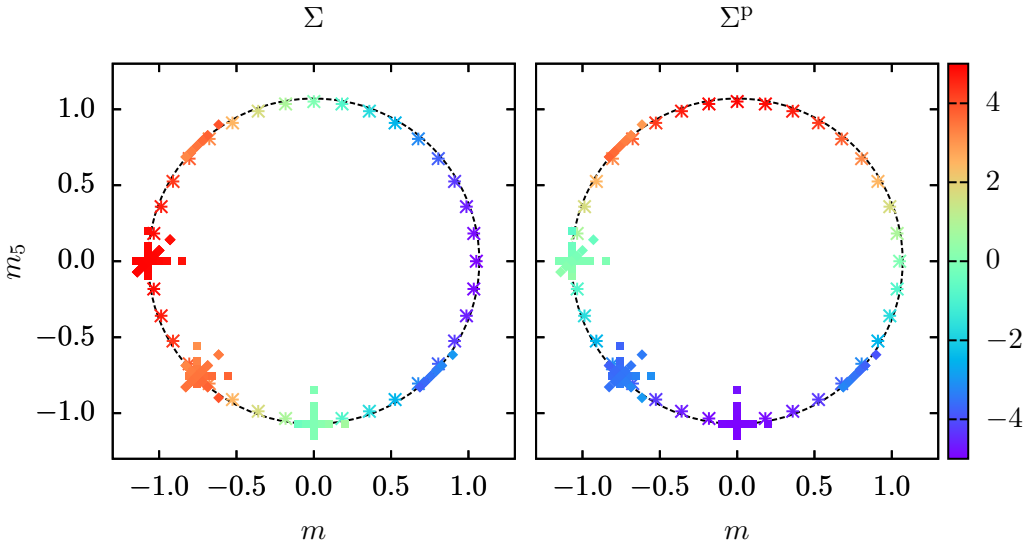

Figure 5.24: Left/Right: The chiral condensate Σ resp. parity condensate Σ^{P} for all different combinations of (α, φ) summarized in table 5.2. Additional ensembles with $(m, m_5) = -1.0506 \cdot (\cos(\varphi), \sin(\varphi))$, $\varphi = 10°, 20°, \ldots, 350°$ are depicted with asterisks. All results are extracted from simulations on a $8^3 \times 16$ lattice with $\beta = 5.0$.

chiral condensate, the parity condensate or a mixture of them is favored. A chiral transformation (4.1) rotates the doublet of bilinears, cf. eq. (4.2), and analogously the condensates (3.55) and (3.56) are rotated by $\alpha = \varphi$:

$$\begin{aligned} \Sigma(\varphi) &= \cos(\varphi)\langle\bar{\lambda}_n\lambda_n\rangle + \mathrm{i}\sin(\varphi)\langle\bar{\lambda}_n\gamma_5\lambda_n\rangle = \cos(\varphi)\Sigma + \sin(\varphi)\Sigma^{\mathrm{P}}\,, \\ \Sigma^{\mathrm{P}}(\varphi) &= \mathrm{i}\cos(\varphi)\langle\bar{\lambda}_n\gamma_5\lambda_n\rangle - \sin(\varphi)\langle\bar{\lambda}_n\lambda_n\rangle = \cos(\varphi)\Sigma^{\mathrm{P}} - \sin(\varphi)\Sigma\,. \end{aligned} \tag{5.4}$$

To check if our measured condensates obey eq. (5.4), the data of figure 5.24 is plotted in figure 5.25 versus the angle φ of the Wilson term. Without any twist, the chiral condensate has the magnitude $\Sigma(0°) = 4.952 \pm 0.001$ and the parity condensate $\Sigma^{\mathrm{P}}(0°) = (1.02 \pm 0.05) \times 10^{-6}$ is significantly smaller. The chiral condensate $\Sigma(\varphi)$ in the left panel is proportional to $\cos(\varphi)$, in accordance to eq. (5.4). Also the parity condensate $\Sigma^{\mathrm{P}}(\varphi) \sim -\sin(\varphi)$ in the right panel agrees with the prediction. Consequently the sum $|\Sigma(\varphi)|^2 + |\Sigma^{\mathrm{P}}(\varphi)|^2 = |\Sigma|^2 + |\Sigma^{\mathrm{P}}|^2$ can be used as a φ-independent condensate. Furthermore the difference

$$|\Sigma(\varphi)|^2 - |\Sigma^{\mathrm{P}}(\varphi)|^2 = |\Sigma|^2\Big(\cos^2(\varphi) - \sin^2(\varphi)\Big) - |\Sigma^{\mathrm{P}}|^2\Big(\cos^2(\varphi) - \sin^2(\varphi)\Big) \tag{5.5}$$

should vanish at $\varphi = \pm 45°$. When this difference is measured for the double-twist $\alpha = \varphi = 45°$ then a deviation from zero is only due to a potential non-invariance of the measure under the chiral rotation. The right panel of figure 5.26 is compatible with the chiral invariance of the measure. On the $8^3 \times 16$ lattice the deviation of $|\Sigma|^2 - |\Sigma^{\mathrm{P}}|^2$

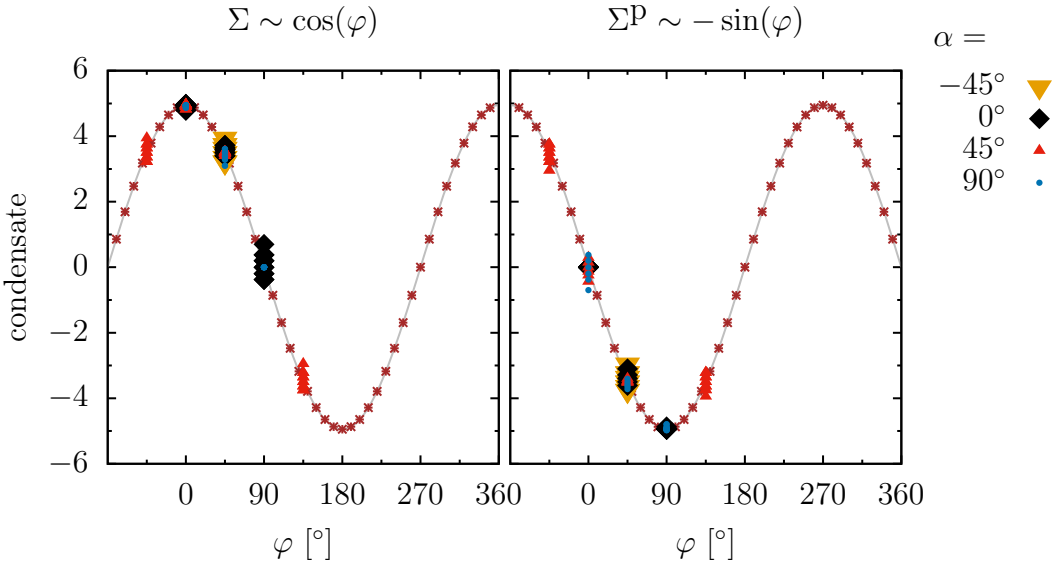

Figure 5.25: Left/Right: Chiral condensate Σ resp. parity condensate Σ^{P} versus twist angle φ with the same data used in figure 5.24. The different colors correspond to different twist angles α. Error bars are omitted and different marker sizes are chosen for clarity. The ensembles with $(m, m_5) = -1.0506 \cdot (\cos(\varphi), \sin(\varphi))$, $\varphi = 10°, 20°, \ldots, 350°$ are depicted with brown asterisks. Note that the horizontal axis starts at $\varphi = -90°$ and covers more than one period.

from zero is smaller than 10^{-4} and on the $16^3 \times 32$ lattice even below 10^{-5}. In the left panel of figure 5.26, a comparison of the fixed angle $\varphi = 45°$ with other mass twists α is shown. The deviation from zero for $\alpha \neq 45°$ demonstrates the influence of the mass twist on the condensates. All those choices approach $|\Sigma|^2 = |\Sigma^{\mathrm{P}}|^2$ in the chiral limit.

The similarity of the condensates for the double-twist $\alpha = \varphi = 45°$ can be used to our advantage when we analyze the physical mesonic states. Their vacuum contributions depend on the chiral condensate resp. parity condensate. In section 4.1 we argued analytically that a-η' and a-f_0 are identical when the spinors are rotated by 45°. Without twisting the Wilson term, that is for $\varphi = 0°$, the numerical data presented in section 5.2 showed that the connected part of a-η' and a-f_0 agree. At the same time, the chiral condensate Σ is much bigger than the parity condensate $\Sigma^{\mathrm{P}} \ll 1$, see figure 5.25 at $\varphi = 0°$. It follows that in the a-f_0 correlator large numbers of the order $\langle \mathrm{tr}(\Gamma G_{nn}) \rangle_{\mathcal{U}} \langle \mathrm{tr}(\Gamma G_{n'n'}) \rangle_{\mathcal{U}} \sim |\Lambda_3| \cdot \Sigma^2$ must be subtracted unlike for a-η', cf. figure 6.4. This explains the unequal noise in those two correlators at $\alpha = 45°$ – even though we would expect them to be equal according to the analytical calculation in section 4.1. For $\varphi = 90°$ the roles of the condensates are interchanged as can be seen in figure 5.27. The magnitude of $|\Sigma|^2 - |\Sigma^{\mathrm{P}}|^2$ for $\varphi = 90°$ in the right panel is reversed to the left panel with $\varphi = 0°$. Compare also the condensates in figure 5.25 at $\varphi = 0°$ and $\varphi = 90°$. Accordingly, the a-η' is noisier than the a-f_0 at $\varphi = 90°$.

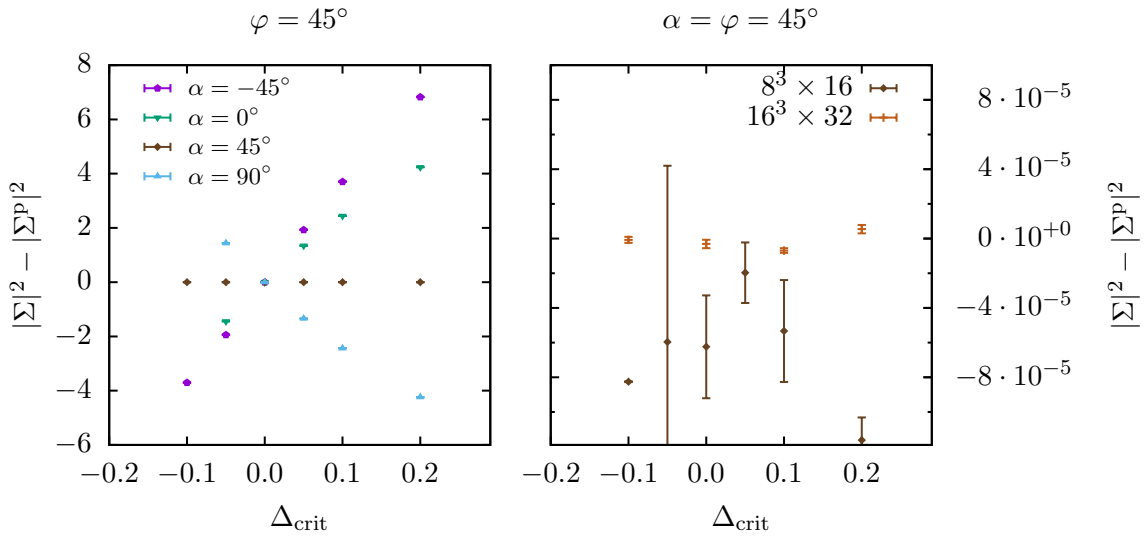

Figure 5.26: Difference of the absolute values squared of the chiral condensate Σ and the parity condensate Σ^{P} versus the distance to the critical point $\Delta_{\mathrm{crit}} = (m - m_{\mathrm{crit}}\cos(\varphi))\cos(\alpha) + (m_5 - m_{\mathrm{crit}}\sin(\varphi))\sin(\alpha)$. Left: Different twist angles α for fixed angle $\varphi = 45°$ on the $8^3 \times 16$ lattice. Right: Different lattice sizes for $\alpha = \varphi = 45°$, where the difference $|\Sigma|^2 - |\Sigma^{\mathrm{P}}|^2$ is expected to vanish.

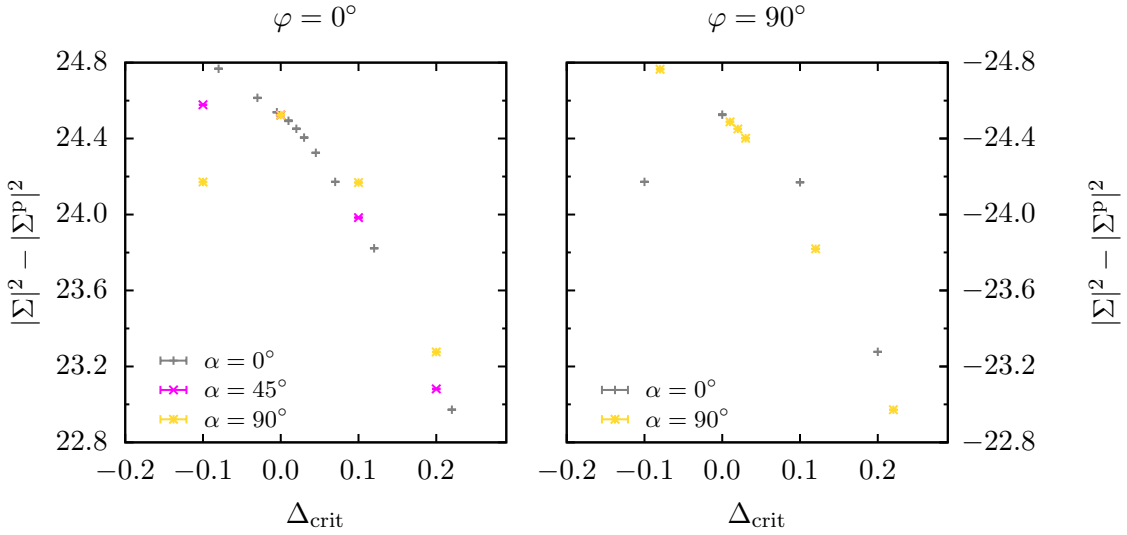

Figure 5.27: Difference of the absolute values squared of the chiral condensate Σ and the parity condensate Σ^{P} versus the distance to the critical point $\Delta_{\mathrm{crit}} = (m - m_{\mathrm{crit}}\cos(\varphi))\cos(\alpha) + (m_5 - m_{\mathrm{crit}}\sin(\varphi))\sin(\alpha)$ on the $8^3 \times 16$ lattice. Left/Right: Different twist angles α for fixed angle $\varphi = 0°$ resp. $\varphi = 90°$. Note that the vertical axis in the right plot is inverted for an easier comparison.

To summarize, the disconnected contributions of the two mesonic states are in the same order of magnitude when the mass term and the Wilson term are rotated by $\alpha = \varphi = 45°$. This implies an even better degeneracy of the a-η' and a-f_0. Additionally, the numerical data indicate smaller error bars in accordance with our analytical result in the free theory (section 4.3). Consequently, fewer discretization errors may be present and we can expect a faster continuum limit.

An alternative would be the choice $\alpha = 45° = -\varphi$, where the difference of the condensates is also significantly lower than in the scenario with $\varphi = 0°$, compare the left panel of figure 5.26 to the left panel of figure 5.27. The difference $|\Sigma|^2 - |\Sigma^{\mathrm{p}}|^2$ shrinks linearly towards the critical point (see purple symbols in figure 5.26) and for $\alpha - \varphi = 90°$ discretization improvements of $\mathcal{O}(a)$ may be possible as discussed in section 4.3.

Altogether, there are several interesting setups (α, φ) for future investigations compared to the untwisted Wilson Dirac operator:

1. $(45°, 0°)$: equal connected contributions to a-η' and a-f_0, $\mathcal{O}(a)$ errors may be reduced.
2. $(45°, 45°)$: equal connected and vacuum contributions to a-η' and a-f_0.
3. $(45°, -45°)$: equal connected contributions to a-η' and a-f_0, vacuum contributions become equal as the critical point is approached, possibility of $\mathcal{O}(a)$ improvement.

Although twisting the mass term with angle α and the Wilson term with angle φ are two different deformations, the choice $\alpha = \varphi$ corresponds in a redefinition of the spinors $\lambda \mapsto \mathrm{e}^{\mathrm{i}\frac{\alpha}{2}\gamma_5}\lambda$. In this scenario, we can shift the twist of the action completely into a twist of the observable (as long as no anomaly enters).[21] As the analytical calculation showed, in this case a-π and a-a as well as a-η' and a-f_0 are identical. For each of them only one observable remains, i.e. a connected meson being a mixture $\frac{1}{\sqrt{2}}(\text{a-}\pi + \text{a-}a)$ and the physical meson containing disconnected contributions is $\frac{1}{\sqrt{2}}(\text{a-}\eta' + \text{a-}f_0)$. While this may seem like a loss of one observable, it should be viewed conversely. The combination of those two superpartners is sufficient since they are mass-degenerated in the continuum theory anyway; compare to [107], where they are described by one common complex field.

5.7 Improvements

In this last section, we present two technical studies. First, the different types of fermion smearing introduced in section 3.1.4 are compared. Afterwards, the benchmark test of the DDαAMG algorithm is presented.

[21] One of the two twists can always be transformed away, but the relative angle between the mass term and the Wilson term stays unaltered.

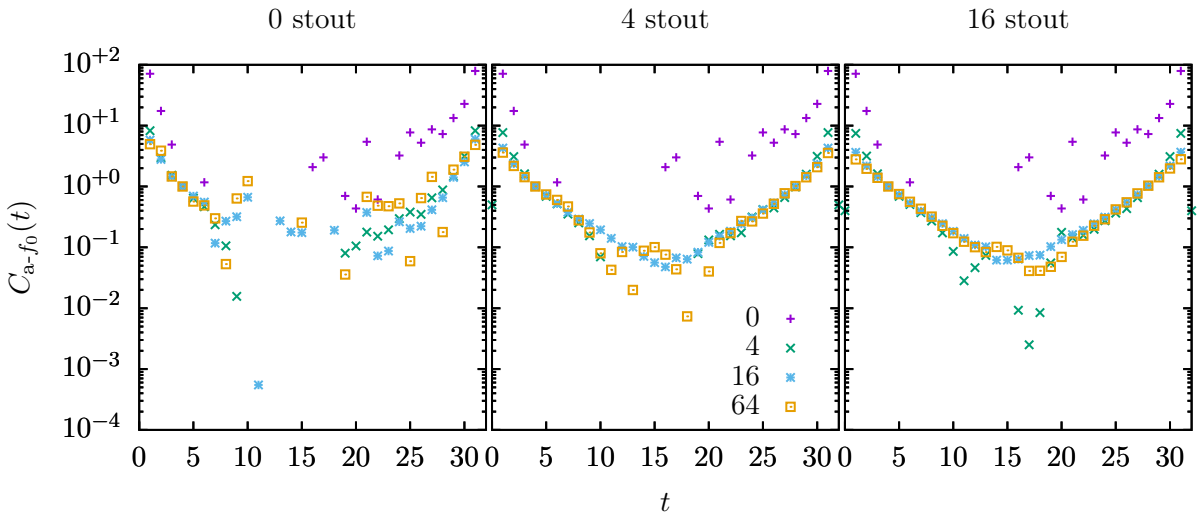

Figure 5.28: Left/Center/Right: a-f_0 correlator with 0/4/16 stout smearing steps. Each panel contains 4 data sets with $\{0, 4, 16, 64\}$ Jacobi smearing steps. No error bars are shown for clarity. The depicted correlators are extracted from 300 configurations on a $8^3 \times 32$ lattice.

5.7.1 Fermion smearing comparison

For this comparison, we use a $8^3 \times 32$ lattice with $\beta = 5.0$ and $(m, m_5) = (-1.0352, 0.0354)$, which has an adjoint pion mass $m_{\text{a-}\pi} \approx 0.3$. To demonstrate the impact of the smearing, we choose the a-f_0 which has the noisiest correlator.

In figure 5.28, its correlator with different combinations of Jacobi and stout smearing is depicted. The left panel evidences that Jacobi smearing without gauge link smearing is not sufficient for a clear signal. In the central panel with 4 stout smearing steps and the right panel with 16 stout smearing steps, it can be seen how the signal improves with the number of Jacobi smearing steps. Both choices of gauge smearing have the best correlator shape with 16 Jacobi smearing steps. When too many steps are applied, the signal worsens. This effect of over-smearing is more obvious in the central panel.

The comparison of the different types of fermion smearing are shown in figure 5.29. With the eye, almost no difference can be seen between Wuppertal (see eq. (3.32)) and Jacobi (see eq. (3.33)) fermion smearing. Most data points differ only within a few percent. In contrast, the results with JacobiExp (defined in eq. (3.34)) contain larger fluctuations when 4 resp. 16 steps of fermion smearing are applied. We choose the normal Jacobi smearing as our default.

The a-f_0 benefits the most from fermion smearing, because its unsmeared signal is noisier than a-η'. In contrast to the mesonic states, we observed only mild profits for the gluino-glue. On the other hand, applying gauge field smearing helps smoothing the latter.

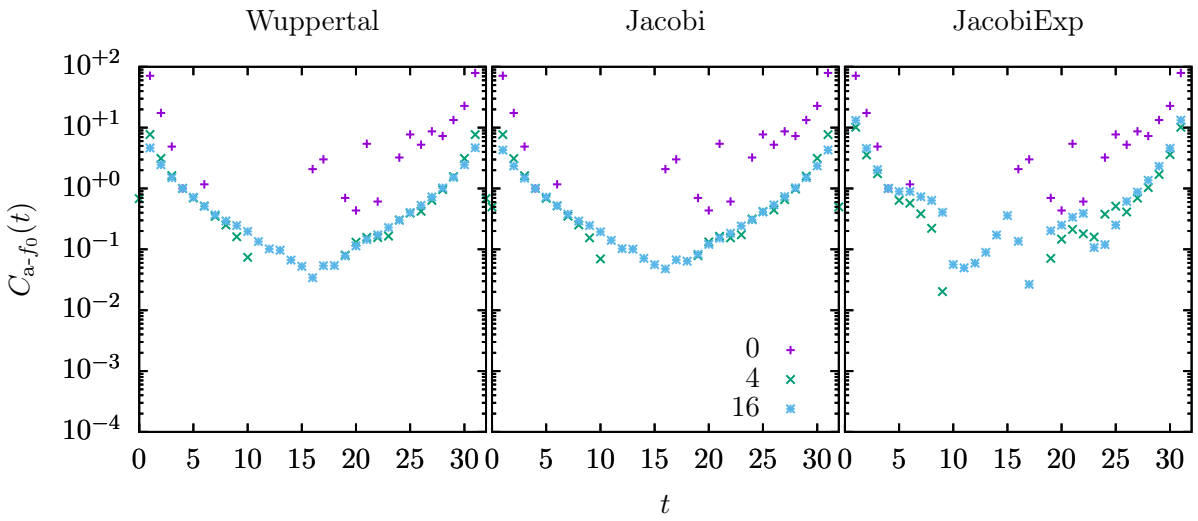

Figure 5.29: Left/Center/Right: a-f_0 correlator with Wuppertal/Jacobi/JacobiExp fermion smearing and 4 stout smearing steps. Each panel contains three data sets with $\{0, 4, 16\}$ Jacobi smearing steps. No error bars are shown for clarity. The depicted correlators are extracted from 300 configurations on a $8^3 \times 32$ lattice.

5.7.2 Multigrid acceleration

We are the first, who applied the DDαAMG library [158, 159] (see section 3.1.2) to a Wilson Dirac operator with fermions in the adjoint representation. Therefore we replaced all numerical values of the original library related to the fundamental representation of the gauge group SU(3) by a variable $\dim_c$. That way, the DDαAMG algorithm with general gauge group SU(N_c) and arbitrary representation became possible.

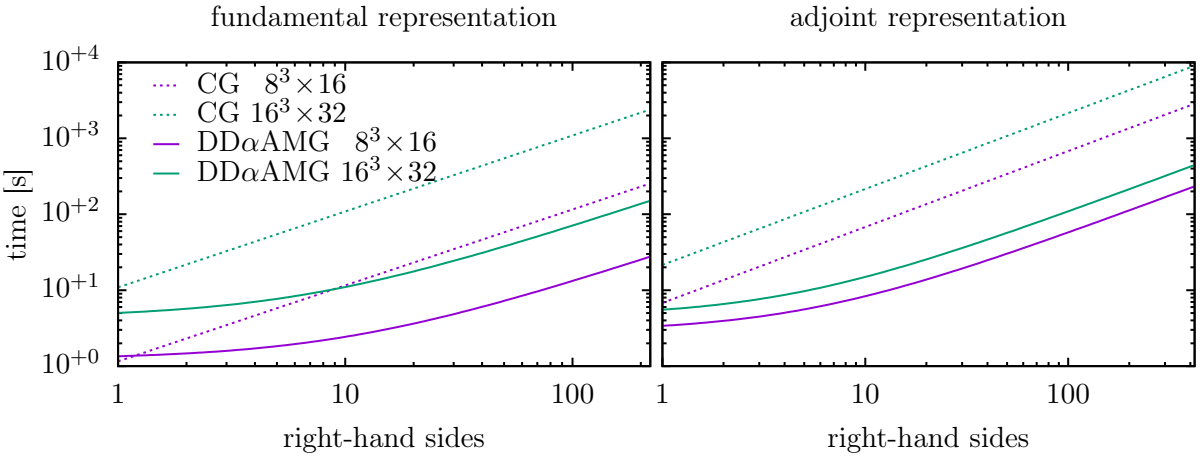

Figure 5.30: Left/Right: Measured time in seconds to invert the Wilson Dirac operator for different numbers of right-hand sides in the fundamental/adjoint representation of SU(3). The different colors correspond to the lattice sizes $8^3 \times 16$ resp. $16^3 \times 32$. Solid (dotted) lines are for the DDαAMG (CG) inverter. The linear functions are averages over approximately 25 configurations. Note the double-logarithmic scale.

To illustrate the performance boost by the DDαAMG inverter, we perform a benchmark test with the following setup: Inversion precision 10^{-12}, two multigrid levels, block size 2^4, mixed precision and the solver combination FGMRES with red-black SAP. Figure 5.30 shows the timings for the fundamental resp. adjoint test scenario with gauge group SU(3). For the former case, we simulate 2-flavors at $\beta = 5.0$ and $m = -0.5614$ with $m_{\pi^+} \approx 0.8$. The timings for the adjoint representation are for the parameters $\beta = 5.0$ and $m = -1.0606$ with $m_{\text{a-}\pi} \approx 0.2$. In both cases up to 100 stochastic estimators and 5 point sources are considered. For comparison, the timings of the CG algorithm and two different lattice sizes $8^3 \times 16$ and $16^3 \times 32$ are shown. On the $16^3 \times 32$ lattice, the DDαAMG solver is always faster than the CG algorithm. For the fundamental representation the DDαAMG setup of the coarsening has a bigger impact on the total time and for a single right-hand side on the $8^3 \times 16$ lattice the CG solver is slightly faster.[22] With more right-hand sides the impact of the setup time decreases.

In conclusion, the DDαAMG algorithm is especially beneficial on large lattices and in the adjoint representation, where this benchmark revealed a speed-up factor of 20. Additionally, it can reduce the critical slowing down. For the results presented in section 6.2, we used 150 stochastic estimators and 3 point sources.

[22] Note that the parameters chosen for the benchmark in the adjoint/fundamental representation correspond to different (adjoint) pion masses. The fundamental pion is heavier and that is why the inversion in this scenario required less iterations.

CHAPTER 6

Numerical results

We start this chapter with an overview of our investigations of the two-dimensional $\mathcal{N} = (2, 2)$ SYM theory in section 6.1 covering the mass spectrum and bosonic Ward identity. After this small detour, we return in section 6.2 to the four-dimensional $\mathcal{N} = 1$ SYM theory. Employing the Wilson Dirac operator with 45°-twisted mass the mesonic states (6.2.1), the gluino-glue (6.2.2) and the glueballs (6.2.3) are examined. In section 6.2.4 all results are collected and extrapolated to the chiral limit. An overview of the ensembles and parameters can be found in appendix G.

6.1 Two-dimensional $\mathcal{N} = (2, 2)$ Super-Yang-Mills theory

Our study of two-dimensional $\mathcal{N} = (2, 2)$ Super-Yang-Mills theory with gauge group SU(2) is also focused on the mass spectrum. As we have argued in section 2.4, the supermultiplet spectrum is expected to be analogous to the four-dimensional mother theory. A careful measurement of the fermion determinant revealed that no sign-problem is present [55, 114]. The only relevant operator of the lattice action is the scalar mass and we took its known critical value [215]. However, with an additional fine-tuning of the fermion mass, it was possible to damp the supersymmetry breaking terms and stabilize the positivity of the Boltzmann weight [55].

Figure 6.1 summarizes the spectroscopic results of the VY-supermultiplet for three different ensembles. The ground state masses of the mesonic states in the left panel tend to zero when extrapolated to the critical point at $m_{\mathrm{f}} = m_{\mathrm{f}}^{\mathrm{crit}}$. In the central panel, the excited states are depicted and they decrease slightly towards the critical point approaching values in the range $[0.2, 0.4]$. The gluino-glue states shown in the right panel fall in the same mass range, at which the symmetric signal is a little heavier than the antisymmetric one. Both gluino-glue states depend only marginally on the bare fermion mass m_{f}.

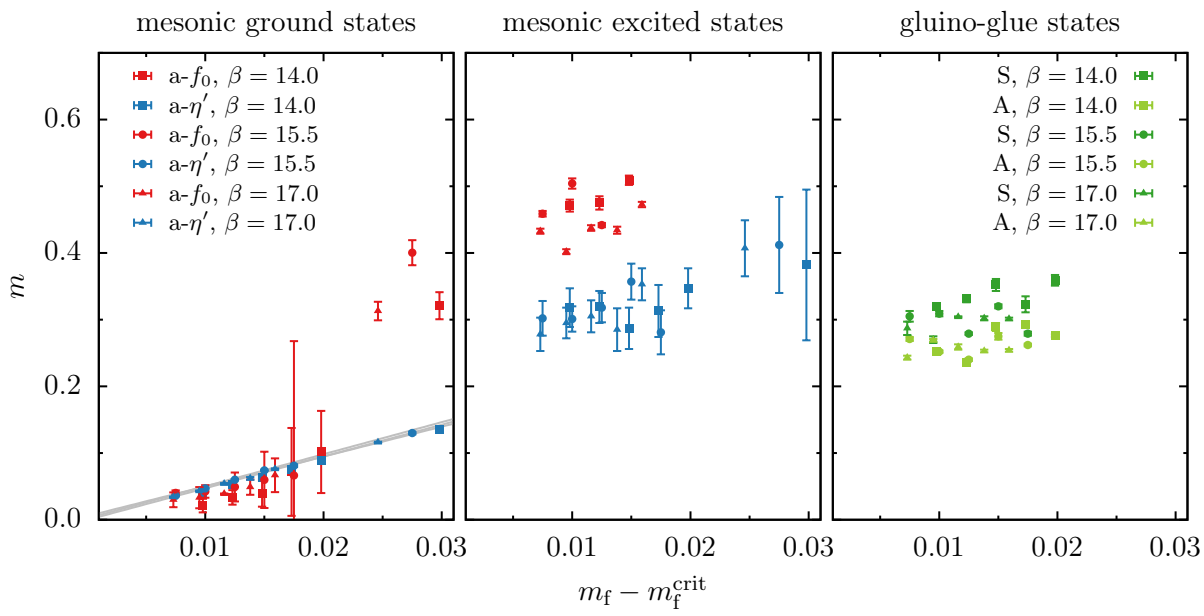

Figure 6.1: Left/Center: Ground/Excited state masses of the mesonic a-η' and a-f_0. Right: Symmetric (S) and antisymmetric (A) gluino-glue masses. All data sets are plotted versus the distance $m_\mathrm{f} - m_\mathrm{f}^\mathrm{crit}$ to the critical point and for three different lattice couplings $\beta \in \{14.0, 15.5, 17.0\}$. Each ensemble consists of 10 000 configurations on a 32×64 lattice. For the ground states of the a-η' linear fits to the critical point are included. Some error bars are smaller than the marker size. Data taken from [55].

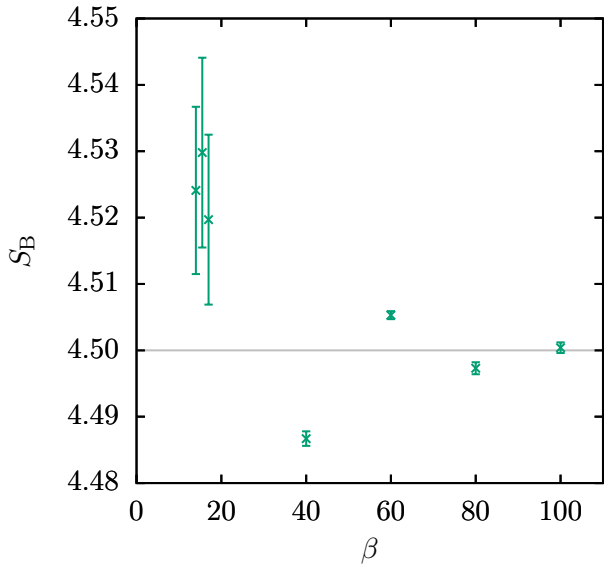

Figure 6.2: Bosonic Ward identity as a function of the lattice coupling β. In the limit $\beta \to \infty$ the value 4.5 (highlighted with the horizontal gray line) is expected for the adjoint representation of the gauge group SU(2). Data taken from [55].

Besides the gluino-glueball, all states of the FGS-supermultiplet are built from glueballs, scalarballs and glue-scalarballs. We observed that the corresponding correlators are so flat that no correlation can be detected. Consequently those massless states decouple from the theory. For the glueball in non-supersymmetric two-dimensional YM theory, analytical calculations support this finding [216, 217].

To summarize our spectroscopic study of $2d$ $\mathcal{N} = (2,2)$ SYM, we found that the FGS-supermultiplet decouples and in the chiral limit the VY-supermultiplet becomes massless. The excited mesonic states have a mass compatible with the gluino-glueball.

An additional effort is the analysis of lattice Ward identities to confirm the restoration of supersymmetry. In figure 6.2, this is demonstrated with the bosonic Ward identity, see eq. (3.54). Further details and other Ward identities can be found in [55].

6.2 Four-dimensional $\mathcal{N} = 1$ Super-Yang-Mills theory with twisted fermions

All the following numerical investigations are focused on the four-dimensional $\mathcal{N} = 1$ SYM theory with gauge group SU(3). QCD as well as its supersymmetric extension have three fundamental color degrees of freedom and with this in mind we chose $N_c = 3$ as well.

In this section we present, compare and discuss our lattice results with 45°-twisted mass term. Early simulations with a mass twist were performed at lattice coupling $\beta = 5.4$ on a $8^3 \times 16$ lattice [87, 88]. Those first results confirmed our claim of section 4.1 that a mass twist of $\alpha = 45°$ leads to degenerated masses of the mesonic states, but the lattice spacing $a \approx 0.026\,\text{fm}$ [218] was very small. Subsequent simulations on the $16^3 \times 32$ lattice aimed for a larger physical volume by additionally reducing the lattice coupling to $\beta = 5.0$ [88, 89]. In section 5.4 it turned out that the mentioned lattice parameters lead to a coarser lattice spacing $a = (0.040 \pm 0.002)\,\text{fm}$, but the lattice extent $L = (0.64 \pm 0.03)\,\text{fm}$ is still rather small. Thus the different results presented in the following sections may suffer from finite size effects (investigated in section 5.5), while lattice spacing artifacts are more or less absent. Nevertheless, all qualitative statements are expected to be transferable to smaller lattice couplings β. In appendix F, we analyze the correlators of the connected mesonic states for twist angles $\alpha \in \{0°, 45°, 90°\}$ and observe that with optimal twist angle $\alpha = 45°$ the finite size effects are less severe. Upcoming simulations should be performed with larger physical volumes to verify the spectroscopic results and state the quantitative numbers more precisely. Table G.4 in appendix G.2 lists the chosen lattice couplings, lattice sizes, mass parameters, Wilson parameters and ensemble sizes.

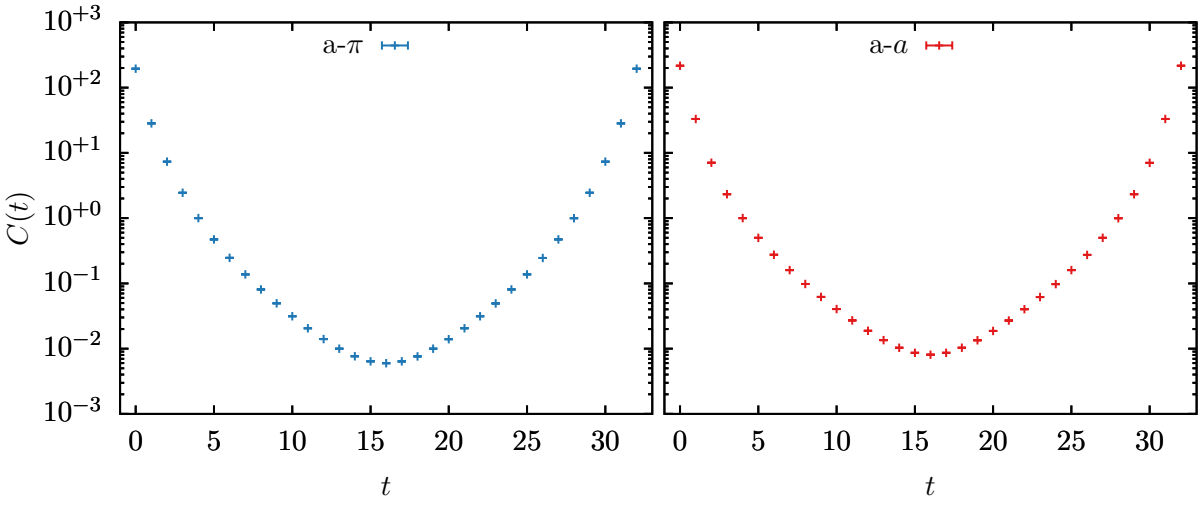

Figure 6.3: Left/Right: Correlator of the adjoint pion/a on the $16^3 \times 32$ lattice at $m^{\mathrm{R}} = 0.24$. Both correlators are normalized to $C(4) = 1$ for an easier comparison. Most error bars are smaller than the symbol size.

6.2.1 Mesonic states

For a better understanding of the mesonic states, we analyze the different contributions to the correlators. First, we present the connected contributions of the pseudoscalar and scalar mesons, which correspond to a-π and a-a. The shapes of the two correlators at $\alpha = 45°$ twist are very similar, see figure 6.3. Accordingly, the extracted dominant mass contributions are coincident. Only the excited contributions differ marginally, which may be a consequence of a slightly misplaced critical point.

Now, we analyze the physical states a-η' and a-f_0 of the VY-supermultiplet including their disconnected contributions, see eqs. (3.60) and (3.61). Compared to the connected contribution, the numerical effort for the disconnected part is rather large. We utilized three point sources and 150 stochastic estimators with an inversion precision of 10^{-12}. Figure 6.4 depicts all contributions entering the correlators of a-η' and a-f_0. The connected contribution in the top row is identical to the adjoint pion resp. a of figure 6.3. There are two contributions, $C_{\mathrm{d}}(t) = \langle \mathrm{tr}(\Gamma G_{nn})\mathrm{tr}(\Gamma G_{n'n'})\rangle_{\mathcal{U}}$ and $C_{\mathrm{v}}(t) = \langle \mathrm{tr}(\Gamma G_{nn})\rangle_{\mathcal{U}}\langle \mathrm{tr}(\Gamma G_{n'n'})\rangle_{\mathcal{U}}$, which bring large statistical uncertainties. Comparing the disconnected contribution $C_{\mathrm{d}}(t)$ of those particles in the second row, a clear difference in their order of magnitude can be seen – the numbers of a-f_0 are roughly a factor 1000 larger. The vacuum contribution $C_{\mathrm{v}}(t)$ in the third row looks very similar and the same observation holds.

After comparing the two different particles, let us examine the individual contributions to one particle and how they sum up. The disconnected contribution and the vacuum contribution seem to be identical in the logarithmic plot, even in the linear inset. But the difference between the disconnected and vacuum contribution is non-zero and enters

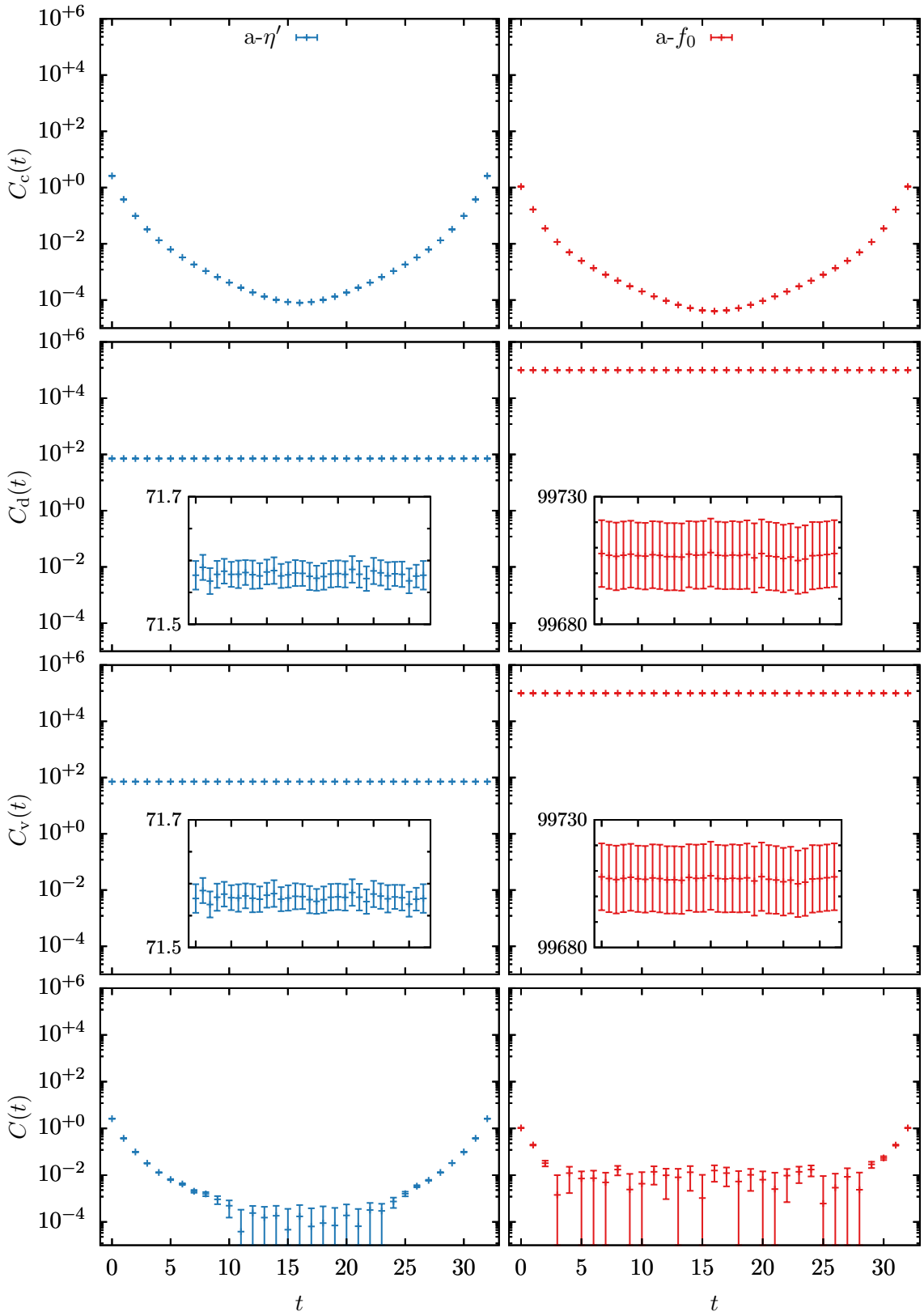

Figure 6.4: Left/Right: Correlator of the adjoint η' resp. f_0 on the $16^3 \times 32$ lattice at $m^R = 0.24$. From top to bottom, the individual contributions are shown: connected contribution $C_c(t)$, disconnected contribution $C_d(t)$, vacuum contribution $C_v(t)$ and their sum $C(t) = C_c(t) + C_d(t) - C_v(t)$. Some error bars are smaller than the symbol size.

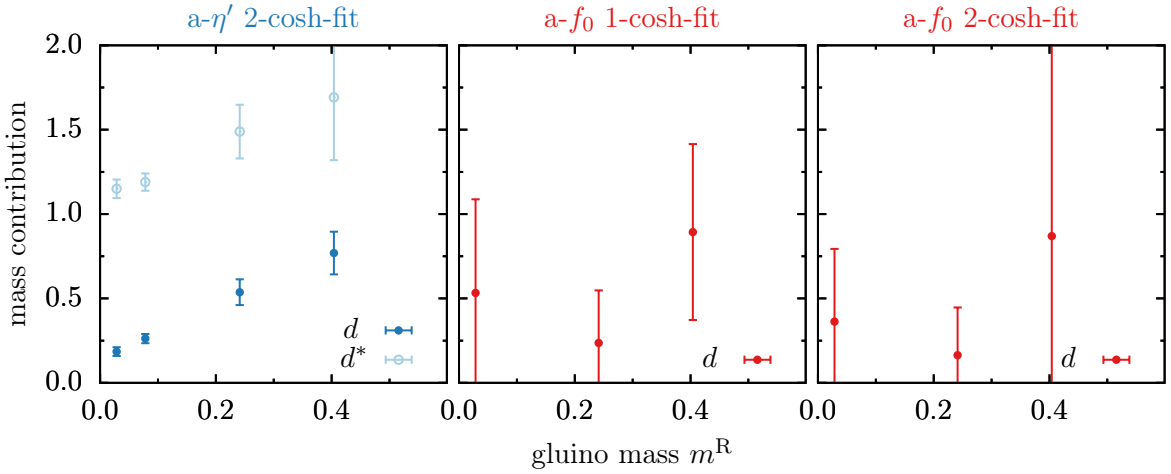

Figure 6.5: Masses for a-η' and a-f_0 from a $16^3 \times 32$ lattice at lattice coupling $\beta = 5.0$ and twist angle $\alpha = 45°$. Results are shown as a function of the renormalized gluino mass m^{R}. Left: Lowest contribution d and next higher mass contribution d^* of a-η' extracted by a 2-cosh-fit. Center/Right: Lowest contribution d of a-f_0 extracted by a 1-cosh-fit/2-cosh-fit. Two resp. four time slices are excluded in the correlator fit at the boundary resp. around the inner time slice, i.e., $t_{\mathrm{cut}} = (2, 4)$.

in the total correlator shown in the bottom row. This small difference is important and distinguishes the physical particles from the unphysical a-π and a-a.

Comparing the total correlators of a-η' and a-f_0, the latter contains considerably more noise, which is connected to the larger values in $C_{\mathrm{d}}(t)$ and $C_{\mathrm{v}}(t)$. Note that $\mathrm{avg}\left(C_{\mathrm{v}}^{\text{a-}\eta'}(t)\right) = |\Sigma^{\mathrm{P}}|^2 \cdot N_S^3$ and $\mathrm{avg}\left(C_{\mathrm{v}}^{\text{a-}f_0}(t)\right) = |\Sigma|^2 \cdot N_S^3$ are linked to the condensates and hence depend very sensitively on external conditions, see section 5.6 for an analysis. In principle the vacuum contribution is translation-invariant, but numerically we treat n and n' differently in the disconnected correlator and so we do in the vacuum contribution. More precisely n is summed over all lattice points and is calculated with stochastic estimators whereas n' is the sum over the randomly chosen positions of the point sources.

High statistics are a prerequisite for a reasonable mass estimate of the disconnected contributions. For the twist angle $\alpha = 45°$, we have medium ensemble sizes for a fixed lattice coupling $\beta = 5.0$ and the lattice size $16^3 \times 32$. Thereby the mass and twisted mass parameters were varied to extrapolate them towards their critical values (see table G.5b).

Results for the dominant mass contribution (i.e., for the approximate ground state mass) for a-η' and a-f_0 are shown in figure 6.5 versus the renormalized gluino mass. They are obtained from fits of the lattice two-point correlators to the same 2-cosh-ansatz as used above. For a-f_0, additional results from a 1-cosh-fit (see eq. (3.17)) are shown. For a-η' there are also results for the next higher state, d^*, included in figure 6.5.

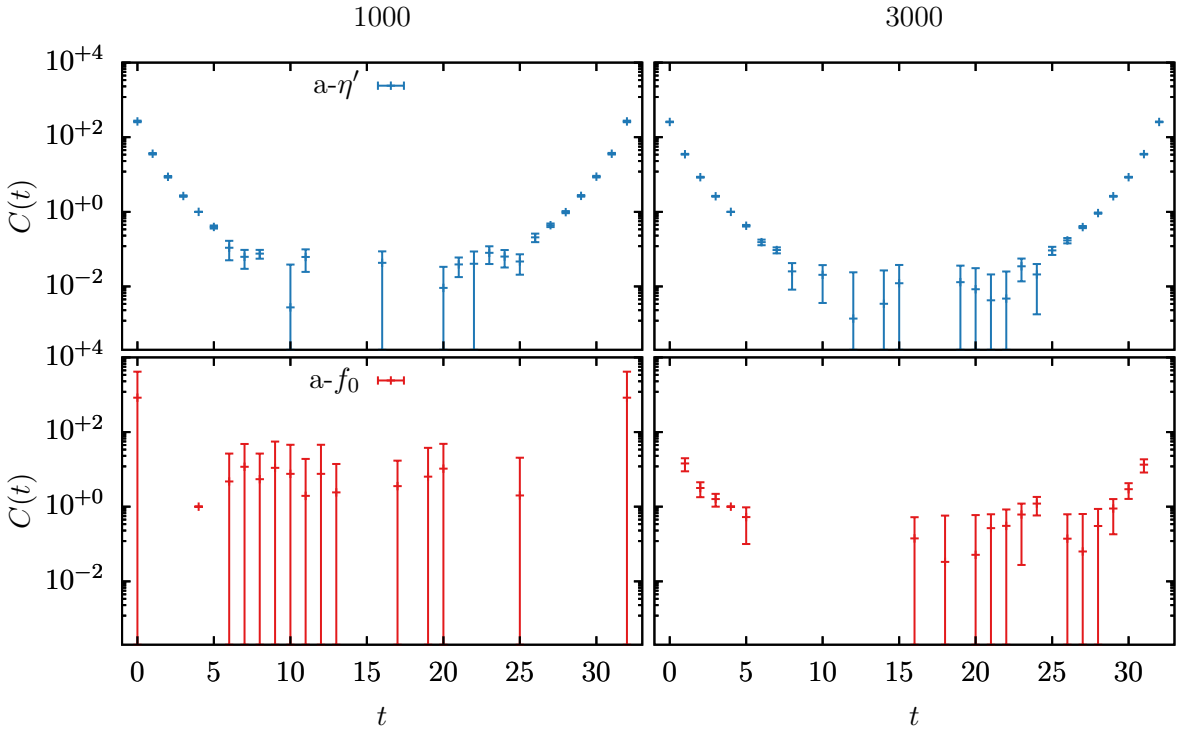

Figure 6.6: Top/Bottom: Correlators for a-η' resp. a-f_0 on the $16^3 \times 32$ lattice at $m^{\mathrm{R}} = 0.40$ ($m = -1.0105$, $m_5 = 0.0601$). Left/Right: Ensemble size 1000/3000. With higher statistics, the noise starts at lower values. Missing data points have negative sign. Correlators are rescaled such that $C(4) = 1$.

While for $d_{\text{a-}f_0}$ the uncertainties are large, both for the 2-cosh-fit and 1-cosh-fit, the results for a-η' are more precise such that a trend can be seen. For a-η', d and d^* clearly decrease with m^{R} and approach finite values at $m^{\mathrm{R}} = 0$. The ground state mass of a-η' near the critical point is approximately 0.2 in lattice units, while the mass of the next higher state tends towards a value above 1. For $d_{\text{a-}f_0}$, the lowest mass contribution is below 0.4 within errors, but strongly affected with noise and influenced by the higher contributions (see lower panels of figure 6.6). In section 6.2.4, we will revisit these chiral extrapolations and include other states beside the two mesonic states considered here.

On the generated ensembles with the chosen parameters, the correlators of the physical mesonic states are dominated by the connected contributions. We noticed that this dominance affects especially the ensembles next to the critical point. This may explain at the same time another observation, which indicates a reduction of statistical fluctuations when the critical point is approached.

To estimate the impact of the gauge fluctuations on the mesonic observables, figure 6.6 compares the correlators with different ensembles sizes. For the a-η' correlator in the upper panels, already 1000 configurations are sufficient for a clear signal of the first excited state at small t. The lowest state cannot be extracted in the center of the lattice due to missing

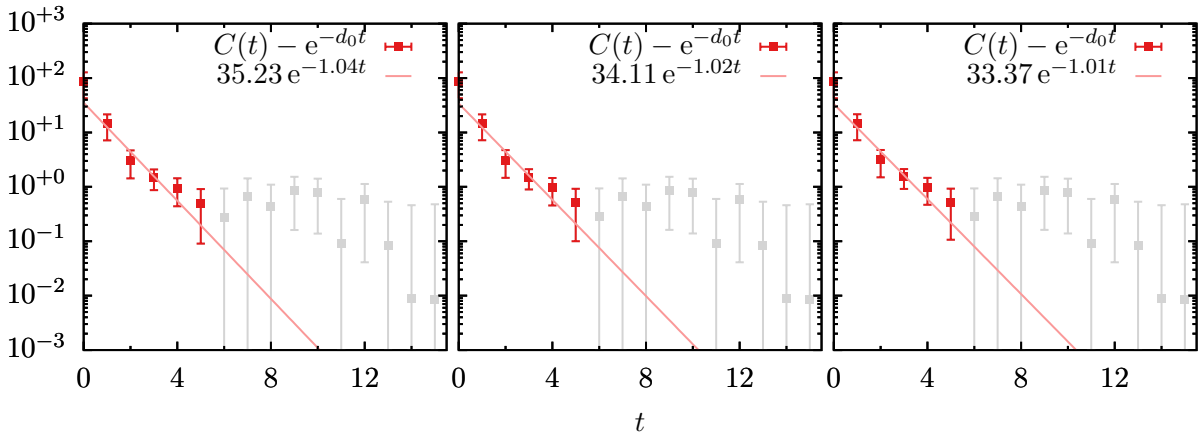

Figure 6.7: Exponential fit of the first excited state of the a-f_0 at $m^{\mathrm{R}} = 0.40$ in the interval $t \in [0, 5]$ by subtracting the ground state mass of the a-η'. In the left/center/right panel, the lowest dominant mass $d^0_{\text{a-}f_0} \in \{0.9 \cdot d^0_{\text{a-}\eta'}, 1.0 \cdot d^0_{\text{a-}\eta'}, 1.1 \cdot d^0_{\text{a-}\eta'}\}$ is assumed.

(negative) data points in the correlator, but with 3000 configurations the signal of the ground state improves slowly.

In the bottom row, the correlators of the a-f_0 reveal a stronger dependence on the ensemble size. The correlator with 1000 configurations is completely dominated by noise and 3000 configurations may allow a rough estimate of the first excited state. As already mentioned, our ensemble size is too small to extract the lowest state of a-f_0 reliably.

For a prediction of the first excited state of the a-f_0 without knowing the mass of the ground state, we cannot naively fit an exponential to the correlator at small times. The reason is that the correlator is a sum of exponentials $C(t) \approx a_0\,\mathrm{e}^{-d_0 t} + a_1\,\mathrm{e}^{-d_1 t}$. Approximately, we try to determine the first excited state by assuming $d^0_{\text{a-}f_0} = d^0_{\text{a-}\eta'}$ and check if $d^1_{\text{a-}f_0} \stackrel{?}{\approx} d^1_{\text{a-}\eta'}$ holds. By fitting $C(t) - a_0\,\mathrm{e}^{-d_0 t} \approx a_1\,\mathrm{e}^{-d_1 t}$ in the central panel of figure 6.7 we find for the ensemble with renormalized gluino mass $m^{\mathrm{R}} = 0.40$ the mass contribution $d^1_{\text{a-}f_0} \approx 1.02$. Repeating the same analysis with $d^0_{\text{a-}f_0} = 0.9 \cdot d^0_{\text{a-}\eta'}$ and $d^0_{\text{a-}f_0} = 1.1 \cdot d^0_{\text{a-}\eta'}$ to estimate the error leads to $d^1_{\text{a-}f_0} \approx 1.01 \ldots 1.04$, see left and right panel of figure 6.7. Thus the sensitivity to the ground state mass is rather low. The first excited contribution $d^1_{\text{a-}f_0}$ is in agreement with the value of the a-η' near the critical point, see figure 6.5. Nevertheless this is significantly lower than $d^1_{\text{a-}\eta'} \approx 1.73$ at $m^{\mathrm{R}} = 0.40$ but still in the range of allowed values, given all the other uncertainties and systematic errors (in particular due to the finite box size).

6.2.2 Gluino-glue

We continue with the third particle of the VY-supermultiplet, the gluino-glue $\tilde{\mathrm{g}}\mathrm{g}$. Figure 6.8 shows its dominant mass contribution for different numbers of stout smearing steps,

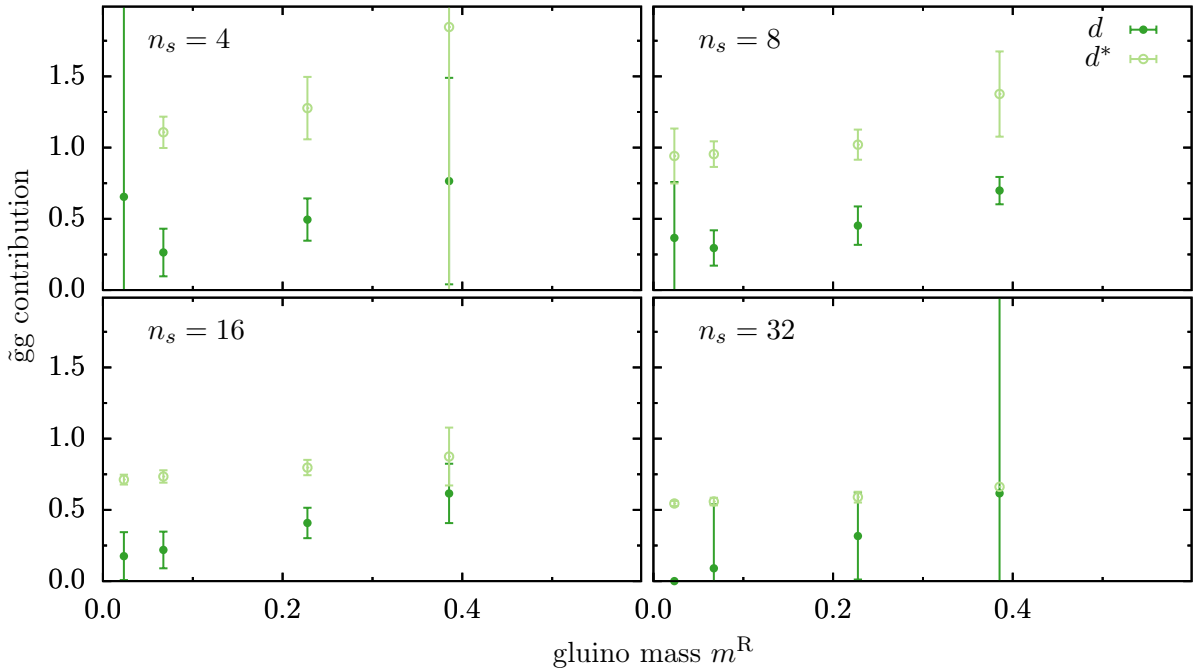

Figure 6.8: Symmetric gluino-glue from a $16^3 \times 32$ lattice and for twist angle $\alpha = 45°$ versus the gluino mass m^{R}. The different panels show data for $n_s = 4$, 8, 16 and 32 stout smearing steps. For the fits, two time-slices have been excluded at the boundary and around the inner time slice, i.e., $t_{\mathrm{cut}} = (2, 2)$.

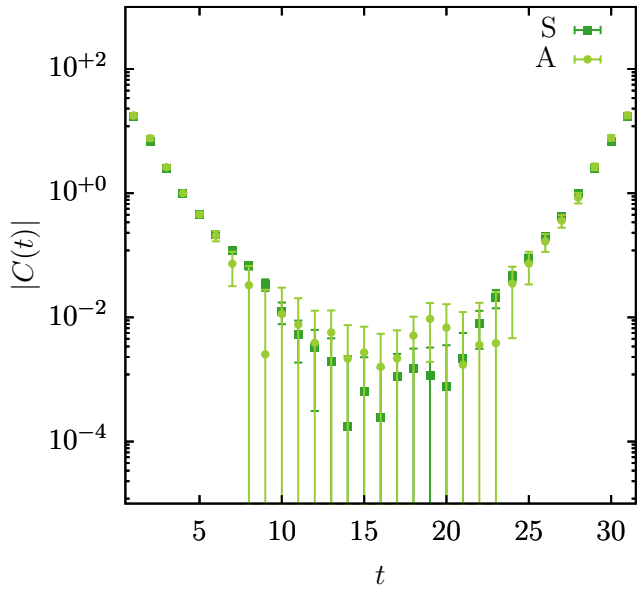

Figure 6.9: Comparison of time-symmetric (S) and time-antisymmetric (A) gluino-glue correlator at $m^{\mathrm{R}} = 0.40$ ($m = -1.0105$, $m_5 = 0.0601$) and for $n_s = 8$ stout smearing steps. Absolute values are shown for a better comparison of the cosh- and sinh-shaped correlators.

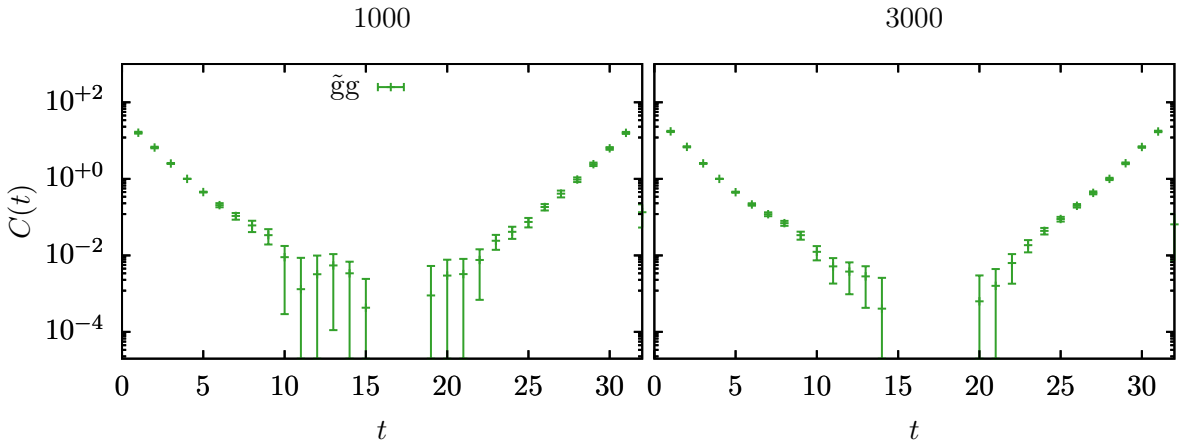

Figure 6.10: Correlators for the symmetric gluino-glue on the $16^3 \times 32$ lattice at $m^{\mathrm{R}} = 0.40$ ($m = -1.0105,\ m_5 = 0.0601$) with 8 steps of stout smearing. Left/Right: Ensemble size 1000/3000. Missing data points have negative sign.

specifically for $n_s = 4$, 8, 16 and 32 with staple weight $\rho = 0.1$. Gauge-link smearing smoothes the correlators and suppresses contributions from excited states, if a sufficient (but not too) large number of smearing steps is applied to the gauge links. Figure 6.8 suggests that 8-16 smearing steps are optimal for our simulation parameters. For both cases the lowest mass contribution of the gluino-glue near the critical point is between 0.2 and 0.4 in lattice units, and between 0.7 and 0.9 for the next higher state. In comparison, fits to correlators for only $n_s = 4$ smearing steps lead to higher uncertainties, while for $n_s = 32$ some fits even fail.

In figure 6.9, we compare (the absolute value of) the symmetric and antisymmetric correlators of the gluino-glue. Clearly, most data points lie on top of each other, but the noise of the antisymmetric correlator is increased at the inner time slices, where the sinh-shaped correlator crosses zero. Hence, no additional insight from the antisymmetric gluino-glue is expected and focusing on the symmetric gluino-glue should be sufficient.

In figure 6.10, the influence of the ensemble size on the correlator is analyzed. As can be seen in the left panel, already 1000 configurations with 8 levels of stout smearing are sufficient for a clear signal of the first excited state. With 3000 configurations an improvement in the center of the lattice is visible and therefore an extraction of the ground state mass becomes feasible.

6.2.3 Glueballs

Before continuing with a chiral extrapolation of the VY-supermultiplet states in the next section, let us present some results for the FGS-supermultiplet. This multiplet contains two glueballs and a further gluino-glueball, see table 2.2. Gauge link fluctuations in the

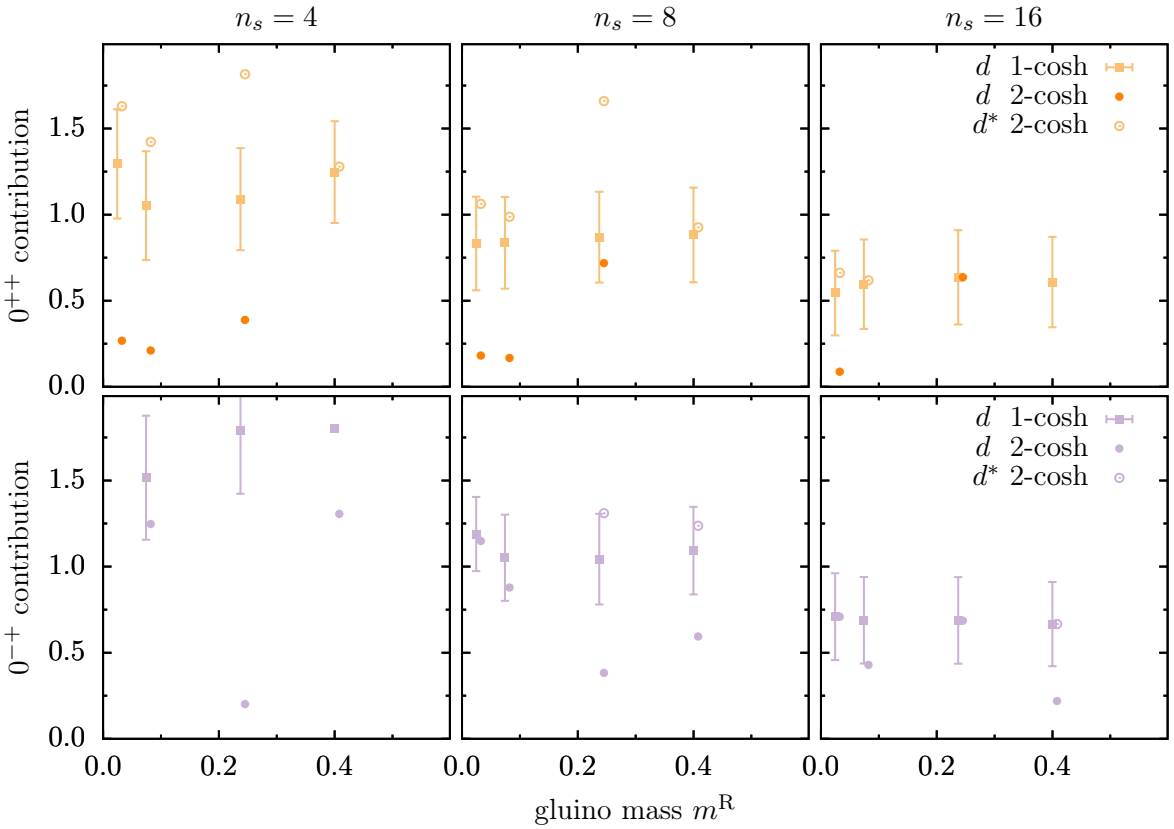

Figure 6.11: Top/Bottom: Scalar/Pseudoscalar glueball on the $16^3 \times 32$ lattice with twist angle $\alpha = 45°$ as a function of the gluino mass m^{R}. Data points are slightly displaced for better visibility. In the different panels, $n_s \in \{4, 8, 16\}$ steps of stout smearing are applied to smooth the data. Both 1-cosh-fit and 2-cosh-fit results are shown for comparison. Two resp. four time slices are ignored in the correlator fit at the lattice boundary resp. in the center, i.e., $t_{\mathrm{cut}} = (2, 4)$. For clarity some (over-estimated) error bars are not shown.

glueball interpolator fields require large ensemble sizes and thus a lattice determination is numerically demanding. A reasonable mass extraction would exceed our computational time budget. Hence all results presented here are exploratory and preliminary.

Figure 6.11 shows the dominant mass contributions for the glueballs with quantum numbers 0^{++} and 0^{-+}. Within errors, d does not depend on the renormalized gluino mass m^{R}. A similar observation holds for the next higher state d^* of the scalar glueball. Extrapolated to the critical point, the scalar glueball is lighter than the pseudoscalar glueball, cf. top and bottom rows of figure 6.11. Its dominant mass contribution d near the critical point lies between 0.2 and 0.3 in lattice units. The mass of the next higher state of the scalar glueball extrapolates to a value somewhere between 0.6 and 1.3.

Comparing the three columns of figure 6.11, we can estimate the effects of the different

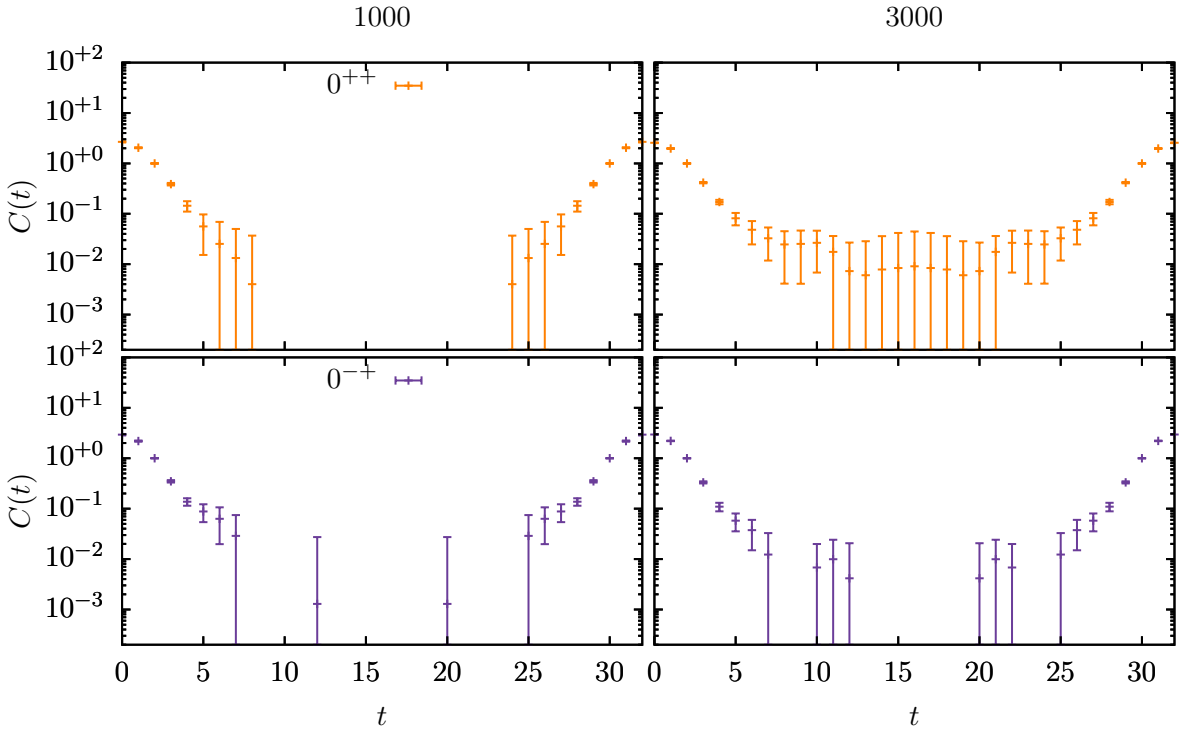

Figure 6.12: Top/Bottom: Correlators for 0^{++} resp. 0^{-+} glueball on the $16^3 \times 32$ lattice at $m^{\mathrm{R}} = 0.40$ ($m = -1.0105,\ m_5 = 0.0601$) with 8 steps of stout smearing. Left/Right: Ensemble size 1000/3000. Missing data points have negative sign.

number of stout smearing steps. Extrapolations to the critical mass are consistent with a horizontal line in all panels, that is a m^{R} dependency is not resolvable, but its value depends on the number of smearing steps. For the chiral extrapolations of all multiplet states in the next section we will choose the results with $n_s = 8$ stout smearing steps. Only for the lowest mass contribution of the 0^{++} glueball, the results with $n_s = 4$ are chosen, because there the mass hierarchy is better seen (compare panels in the top row of figure 6.11).

Fitting the dominant mass contribution of the 0^{-+} glueball is difficult, even with a 2-cosh-fit ansatz (see bottom row of figure 6.11). Maybe, the small lattice volume does not allow for a reasonable determination of the ground state mass. Therefore, only one (excited) contribution has been determined with a value between 0.7 and 1.5 in lattice units, depending on the number of stout smearing steps. In [33, 41] was reported that the lowest state of the pseudoscalar glueball is comparable with the first excited states of the mesonic states and gluino-glue. This is in accordance with our observations. Probably, a bigger operator basis with extended shapes may improve the signal-to-noise ratio and the overlap with a lower state.

Like for the other particles, we estimate the gauge fluctuation contained in the glueball correlators with $n_s = 8$ stout smearing steps. In the top row of figure 6.12, the 0^{++} glueball is analyzed. With 1000 configurations, the excited state at small t has already a good signal even though in the center of the lattice many data points with negative sign are missing. This gap in the lattice center is closed with an ensemble size of 3000, but the large relative uncertainties affect the fit of the ground state. Similarly, the pseudoscalar glueball in the bottom row of figure 6.12 has a clear signal at small t. Its correlator in the center of the lattice remains contaminated with negative numbers, which is qualitatively the same as data points with error bars crossing zero. Thus, an extraction of the ground state mass is demanding with the available statistics.

6.2.4 Chiral limit

To connect lattice results with the supersymmetric continuum theory, first an extrapolation to the critical point and then the thermodynamic and continuum limits are necessary. In what follows, all previously discussed results (see sections 6.2.1, 6.2.2 and 6.2.3) will be extrapolated to the critical point where the renormalized gluino mass vanishes. In the previous sections this extrapolation has been discussed for the individual states already. The focus here is to summarize and compare the extrapolated values of all supersymmetric partners in a multiplet, in particular to check if they coincide within uncertainties. The leading order of chiral perturbation theory suggests that the residual gluino mass m^{R} is given by the squared mass of the would-be Goldstone bosons, i.e. $m^{\mathrm{R}} \propto m^2_{\text{a-}\pi}$. In [219–222] it has been argued that the leading correction to non-zero meson and baryon masses in the chiral limit is also proportional to $m^2_{\text{a-}\pi}$ such that we assume a linear m^{R} dependency in our extrapolation to the critical point.

For the VY-supermultiplet, the linear extrapolations are depicted in the upper panel of figure 6.13 and the corresponding values are listed in table 6.1. We see that the lowest mass contributions of a-η', a-f_0 and $\tilde{\mathrm{g}}\mathrm{g}_{S8}$ (this index indicates the usage of 8 stout smearing steps) are degenerated within errors. For the first excited state of the VY-supermultiplet, the situation is less clear. Nonetheless, a tendency for a mass-degeneracy is seen which may be manifest in the continuum limit. Possibly the relatively small lattice size causes the second excited state to superpose with the first, resulting in larger contributions to $d^*_{\text{a-}\eta'}$ which we cannot resolve. Conversely, smearing the gluino-glue operator may have overly dampened the first excited state $d^*_{\tilde{\mathrm{g}}\mathrm{g}}$ such that its mass is underestimated.

The lower panel of figure 6.13 illustrates the extrapolation of the FGS-supermultiplet states. Looking at the lowest state, the scalar glueball 0^{++} has a clear mass-degeneracy with the gluino-glue. It is as heavy as the a-f_0 of the VY-supermultiplet, but slightly heavier than the a-η' state. A prediction which of the two multiplets is the lightest in the

Table 6.1: Results of the linear fits. The lowest mass contribution d, the next higher mass contribution d^*, the corresponding slopes s resp. s^* and their fit errors are rounded to 2 digits.

state	d	s	d^*	s^*
a-η'	0.14 ± 0.01	1.60 ± 0.04	1.09 ± 0.02	1.48 ± 0.23
a-f_0	0.19 ± 0.12	1.23 ± 1.49	–	–
$\tilde{\mathrm{g}}\mathrm{g}_{S8}$	0.21 ± 0.12	1.09 ± 0.40	0.89 ± 0.09	0.55 ± 0.43
0^{++}_{S8}	0.20 ± 0.05	0.73 ± 0.32	0.83 ± 0.05	0.14 ± 0.02
0^{-+}_{S8}	–	–	1.14 ± 0.06	-0.19 ± 0.25

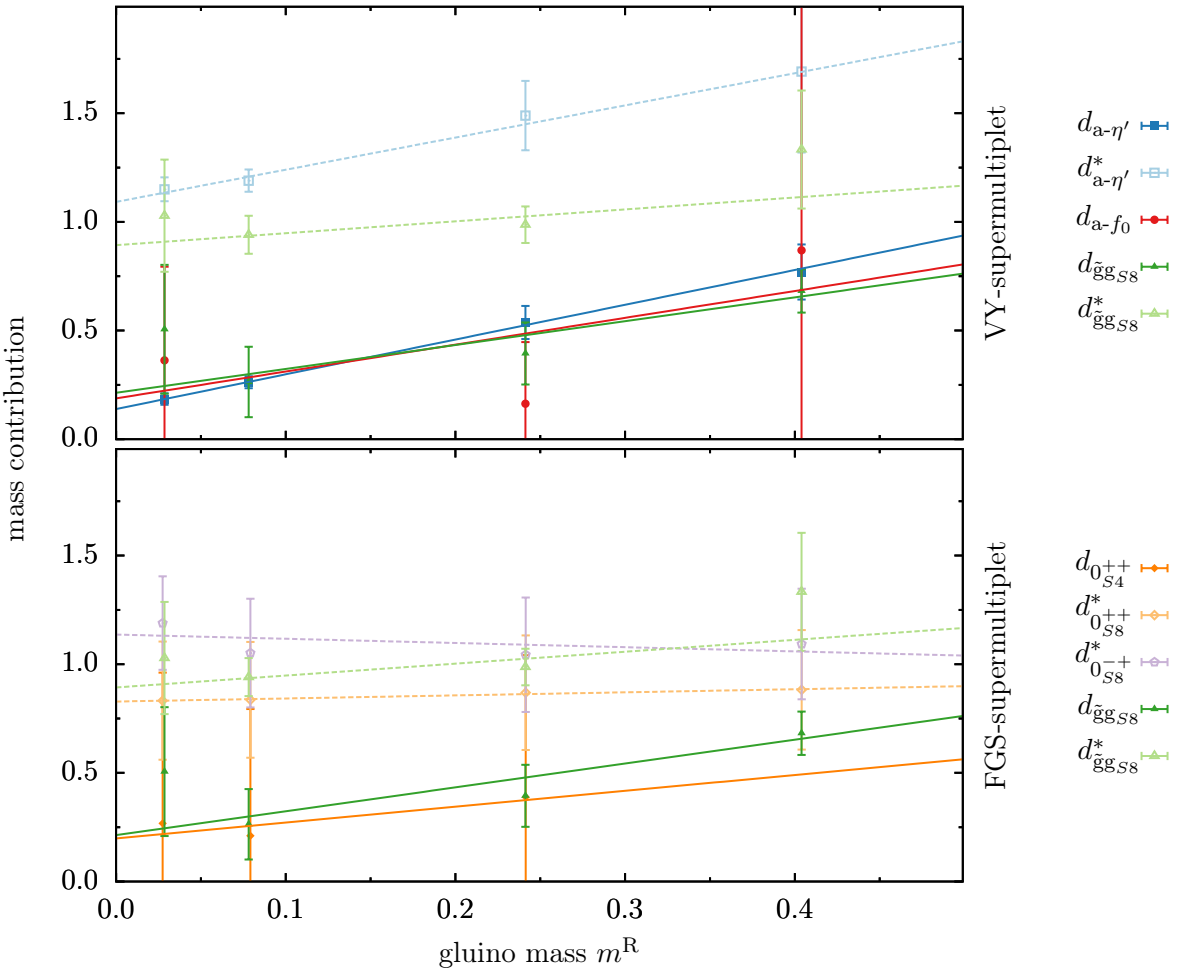

Figure 6.13: Top/Bottom: Chiral extrapolation of the VY/FGS-supermultiplet. Each particle is depicted with a different color. Solid/Dashed lines are linear fits to the lowest/next higher mass contribution. The amount of smearing steps is indicated in the indices, e.g. $\tilde{\mathrm{g}}\mathrm{g}_{S8}$ stands for 8 levels of stout smearing. For the gluino-glue only the symmetric operator is considered as discussed in section 6.2.2. Two resp. four time slices are ignored in all correlator fits at the lattice boundary resp. in the center, i.e., $t_{\mathrm{cut}} = (2, 4)$. All fits are 2-cosh except 0^{++}_{S8} and 0^{-+}_{S8}, which are fitted to a single cosh.

continuum limit is not possible with the present data. In the excited spectrum, 0^{++}_{S8}, $\tilde{\mathrm{g}}\mathrm{g}_{S8}$ and 0^{-+}_{S8} lie in the interval $[0.8, 1.2]$. If those states all belong to the first excitation, or if this excitation in fact is a superposition of multiple higher states, cannot be resolved. Simulations in larger volumes are required to address this in a reasonable manner. Finally, in addition to the chiral limit, the thermodynamic limit $V \to \infty$ and the continuum limit $a \to 0$ have to be performed.

In a study of SU(2) $\mathcal{N} = 1$ SYM theory [32], it was reported that the interpolation operators of a-η' and 0^{-+} weakly mix and hence project onto two different states with different masses. It was seen that the 0^{-+} operator generates a strong signal for the first excited state, while the overlap with the ground state is small. Furthermore, it was found that the lowest state of the 0^{-+} glueball has the same mass as the first excited state of the 0^{++} glueball. This is in agreement with our results, in which we identified the lowest contribution of the pseudoscalar glueball as its first excited state $d^*_{0^{-+}}$.

In further studies [33, 41], the same collaboration analyzed their lattice simulations using the variational method. They found that the a-η' and 0^{-+} operators do not mix in the variational basis and when analyzed individually the extracted mass of the excited a-η' agrees with the lowest mass of the pseudoscalar glueball. In the 0^{++} channel mixing between a-f_0 and the glueball is found and thus they are measured together in a variational basis. The authors report that the ground state is more glueball-like, while the excited state is more meson-like. In the pseudoscalar channel, the lowest state was dominated by the a-η' operator while the signal for the 0^{-+} operator was comparably small.

To conclude, our spectroscopic results of the VY- and FGS-supermultiplet with the twisted Wilson Dirac operator demonstrate that a mass-degeneracy of the ground states can be observed. Soft supersymmetry breaking through the gluino mass leads to positive mass shifts of the ground states in accordance to [108]. In future studies, the first excited states should be refined and with a continuum extrapolation the question, which of the supermultiplets is the lightest, should be addressed.

CHAPTER 7

Conclusion and outlook

In the context of this thesis we introduced, analyzed and applied a new type of Wilson Dirac operator for lattice calculations of $\mathcal{N} = 1$ Super-Yang-Mills (SYM) theory. Inspired by twisted-mass lattice Quantum Chromodynamics (QCD) and simulations of lower-dimensional supersymmetric theories, we added a twisted mass term to the fermionic lattice action and interpreted it as a deformation whose parameter requires tuning. We reasoned that this new lattice action still describes the same continuum theory. An analytical calculation revealed a special choice of the twist angle, $\alpha = 45°$, which leads to an improvement of the mass-degeneracy of the mesonic chiral partners. Furthermore, we checked analytically that a chiral transformation of the spinors does not spoil the supermultiplet structure.

Lattice simulations brought numerical evidence that the anticipated improvements hold at finite lattice spacing, although chiral symmetry as well as supersymmetry are broken. Fixing the twist angle, only one parameter has to be fine-tuned – like in the untwisted scenario. At $\alpha = 45°$, chiral symmetry as well as supersymmetry are improved, reducing the distance to the supersymmetric continuum limit. Along this direction we investigated the mesonic states, the gluino-glue and the glueballs of the Veneziano-Yankielowicz and Farrar-Gabadadze-Schwetz supermultiplets. Accordant ground state mass contributions were found and with some uncertainties also the excited masses are consistent.

In the analysis of the free Wilson Dirac operator we demonstrated that the discretization effects in the leading order $\mathcal{O}(a)$ are proportional to $\cos(\alpha)$. Therefore, this twisted approach has (like maximal-twisted lattice QCD) the potential to reduce discretization errors and improve the continuum extrapolation. Considering the phase of the Pfaffian, we assured in a test series that no problematic sign problem arises in twisted simulations.

During the end of our studies, we introduced the double-twisted Wilson Dirac operator with another angle φ for the Wilson term besides the twist angle α for the mass term. On the one hand, it was helpful for our analytical calculation, where we shifted the chiral rotation from the lattice action to the observable. While exploring the possibilities of

independently choosing both twist angles, we observed that a double-twist can reduce the numerical difference between the chiral partners a-η' and a-f_0. Optimally chosen twist angles reduce lattice artifacts such that the double-twisted scenario provides a promising improvement of $\mathcal{N} = 1$ SYM on the lattice.

On the other hand, a twist of the Wilson term into the complex (r, r_5)-plane can be dangerous. This may violate reflection positivity and thus the reconstruction theorem does not guarantee the correct continuum theory. Therefore, we preferred the more conventional Wilson Dirac operator with only a twist in the mass term.

Alternatively to the twisted fermions, we tried clover improvement. For the combination of the Lüscher-Weisz gauge action and the adjoint representation of SU(3), no results exist in the literature. In a parameter scan, we searched heuristically for a distinct clover coefficient. Our most promising value is determined non-perturbatively via the tree-level tadpole factor.

In a side project, we touched two-dimensional $\mathcal{N} = (2, 2)$ SYM theory. In the analytical part we covered the Kaluza-Klein reduction and the expected supermultiplet structure. Regarding the presentation of numerical observations, we selected the mass spectroscopy and the bosonic action. Further topics can be found in [55, 114].

Apart from modifications in the lattice action, we enhanced our code. With the implementation of the domain decomposition adaptive algebraic multigrid (DDαAMG) algorithm, the numerous inversions of the Wilson Dirac operator during the measurements of the observables could be accelerated significantly. In a benchmark test, speed-ups for $\mathcal{N} = 1$ SYM theory with gauge group SU(3) up to a factor of 20 were achieved. This way, we could reduce our computational cost considerably and at the same time increase the number of stochastic estimators and point sources. Compared to QCD, where the gauge group is in the fundamental representation, the percentage of the DDαAMG-setup is smaller in relation to the total time spent for the inversions.

In our exploratory simulations the lattice parameters were not optimally chosen. As a consequence, the presented lattice results are afflicted with non-negligible volume artifacts and a whole section is dedicated to discuss the origin and consequences. Nonetheless, on a qualitative level our findings presumably will not change and we leave it to forthcoming lattice studies to verify them on larger volumes. Concretely, those studies should start at larger gauge couplings (smaller lattice couplings) to increase the physical box size. Furthermore, a combination of ensembles with different couplings allows to extrapolate to the continuum limit and to determine the physical masses of the Veneziano-Yankielowicz and Farrar-Gabadadze-Schwetz supermultiplets. Additionally, with supersymmetric Ward identities the quality of the supersymmetry improvement at finite lattice spacing could be verified.

Besides the investigated mass spectrum of the supermultiplets, $\mathcal{N} = 1$ SYM theory exhibits a variety of non-perturbative effects. Further studies could include more composite states like baryons or vector mesons in the spectroscopy. Also a closer look at the breaking of chiral symmetry and the emergence of the chiral condensate could bring new insights. Addressing the theory at finite temperature, aspects like the occurrence of the confinement-deconfinement transition as well as the restoration of chiral symmetry can be studied.

Ultimately, dynamical supersymmetric quarks (squarks) should be added to $\mathcal{N} = 1$ SYM theory resulting in Supersymmetric Quantum Chromodynamics (Super-QCD). Lattice studies of this central building block of the Minimal Supersymmetric Standard Model (MSSM) are within one's grasp. First steps in that direction were presented in [223–228]. One-flavor SU(3) Super-QCD with Wilson fermions has nine relevant operators, but as proposed in [225], the one-loop potential of the squark field may simplify the fine-tuning of the parameters. In a study of two-flavor SU(2) Super-QCD with Wilson fermions, it was found that the marginal gauge couplings are well approximated by their tree-level values near the conformal window and the leading dependence is on the adjoint PCAC mass [228]. A plethora of states exists in Super-QCD and mixing brings a rich mass spectrum. Numerical predictions have the potential to guide experimental searches for supersymmetry, like nowadays in lattice QCD.

An experimental confirmation of supersymmetry is still missing despite an intensive search, for example, at the large hadron collider (LHC) by the ATLAS collaboration [229–231] and the CMS collaboration [232–234]. Supersymmetry may be broken softly, such that the superpartners are heavier than their counterparts of the standard model (SM). This could explain why they have not been observed at the accessible energy of approximately 13 TeV, but further questions arise. What is the supersymmetry breaking mechanism of nature? Which superpartner masses are natural?

Supersymmetry was, is and will be an interesting field for experimental, perturbative and lattice research.

APPENDIX A

Definitions and conventions

The Clifford algebra in Minkowski spacetime is $\{\gamma_\mu, \gamma_\nu\} = 2\eta_{\mu\nu}$ with the metric tensor $\eta_{\mu\nu} = \mathrm{diag}(1, -1, -1, -1)$. Greek indices $\mu, \nu, \ldots \in \{0, 1, 2, 3\}$ take values of the four-dimensional spacetime and roman letters indicate spatial components $i, j, \ldots \in \{1, 2, 3\}$. If not stated otherwise, Einstein's sum convention is assumed. The Dirac matrix with temporal index is Hermitean $\gamma_0^\dagger = \gamma_0$ and Dirac matrices with spatial indices are anti-Hermitean $\gamma_i^\dagger = -\gamma_i$, such that $\gamma_0\gamma_\mu\gamma_0 = \gamma_\mu^\dagger$. The matrix $\gamma_5^\dagger = \gamma_5 = -\mathrm{i}\gamma_0\gamma_1\gamma_2\gamma_3$ is also Hermitean and anti-commutes with all other Dirac matrices, $\{\gamma_5, \gamma_\mu\} = 0$. Taking the square of the Dirac matrices gives $\gamma_0^2 = \mathbb{1}$, $\gamma_i^2 = -\mathbb{1}$ and $\gamma_5^2 = \mathbb{1}$. Additionally we define $\Sigma_{\mu\nu} \equiv [\gamma_\mu, \gamma_\nu]$.

In the Euclidean spacetime, the metric is simply $\delta_{\mu\nu}$ and the Euclidean spacetime indices run over $1, \ldots, 4$. For the correlators we consider the last index as the temporal direction. In our numerical simulations, we employ the chiral basis for the gamma matrices

$$\gamma_1 = \begin{pmatrix} 0 & 0 & 0 & -\mathrm{i} \\ 0 & 0 & \mathrm{i} & 0 \\ 0 & -\mathrm{i} & 0 & 0 \\ \mathrm{i} & 0 & 0 & 0 \end{pmatrix}, \quad \gamma_2 = \begin{pmatrix} 0 & 0 & 1 & 0 \\ 0 & 0 & 0 & -1 \\ 1 & 0 & 0 & 0 \\ 0 & -1 & 0 & 0 \end{pmatrix}, \quad \gamma_3 = \begin{pmatrix} 0 & 0 & -\mathrm{i} & 0 \\ 0 & 0 & 0 & -\mathrm{i} \\ \mathrm{i} & 0 & 0 & 0 \\ 0 & \mathrm{i} & 0 & 0 \end{pmatrix},$$

$$\gamma_4 = \begin{pmatrix} 0 & 0 & 0 & 1 \\ 0 & 0 & 1 & 0 \\ 0 & 1 & 0 & 0 \\ 1 & 0 & 0 & 0 \end{pmatrix}, \quad \gamma_5 = \begin{pmatrix} 1 & 0 & 0 & 0 \\ 0 & 1 & 0 & 0 \\ 0 & 0 & -1 & 0 \\ 0 & 0 & 0 & -1 \end{pmatrix}.$$

The deduced charge conjugation matrix

$$\mathcal{C}_- = \gamma_4\gamma_2 = \begin{pmatrix} 0 & -1 & 0 & 0 \\ 1 & 0 & 0 & 0 \\ 0 & 0 & 0 & -1 \\ 0 & 0 & 1 & 0 \end{pmatrix} \tag{A.1}$$

has the properties $\mathcal{C}_- = -\mathcal{C}_-^{-1} = -\mathcal{C}_-^{\mathrm{T}}$, $\mathcal{C}_-^2 = -\mathbb{1}$, $\mathcal{C}_-\gamma_\mu^{\mathrm{T}}\mathcal{C}_-^{-1} = -\gamma_\mu$, $\mathcal{C}_-\gamma_5^{\mathrm{T}}\mathcal{C}_-^{-1} = \gamma_5$. In four spacetime dimensions a second charge conjugation matrix can be defined with

$$\mathcal{C}_+ = \gamma_1\gamma_3 = \begin{pmatrix} 0 & 1 & 0 & 0 \\ -1 & 0 & 0 & 0 \\ 0 & 0 & 0 & -1 \\ 0 & 0 & 1 & 0 \end{pmatrix} \tag{A.2}$$

and the properties $\mathcal{C}_+ = -\mathcal{C}_+^{-1} = -\mathcal{C}_+^{\mathrm{T}}$, $\mathcal{C}_+^2 = -\mathbb{1}$, $\mathcal{C}_+\gamma_\mu^{\mathrm{T}}\mathcal{C}_+^{-1} = +\gamma_\mu$, $\mathcal{C}_+\gamma_5^{\mathrm{T}}\mathcal{C}_+^{-1} = \gamma_5$. While $\mathcal{C}_-$ is used in our numerical calculations, $\mathcal{C}_+$ is used in the proof in section 4.3. Acting with a charge conjugation on a spinor we get $\psi^{\mathrm{C}} \equiv \mathcal{C}\bar{\psi}^{\mathrm{T}} = \mathcal{C}\gamma_0^{\mathrm{T}}\psi^*$ and the charge conjugation of an anti-spinor $\bar{\psi} \equiv \psi^\dagger\gamma_0$ is $\bar{\psi}^{\mathrm{C}} = -\psi^{\mathrm{T}}\mathcal{C}^{-1}$. Spinors are anti-commuting Grassmann variables and Majorana spinors fulfill $\lambda^{\mathrm{C}} = \lambda$. Choosing $\mathcal{C}_-$ in four spacetime dimensions, the following bilinears of Majorana spinors

$$\bar{\lambda}_1\lambda_2 = \bar{\lambda}_2\lambda_1\,,\ \bar{\lambda}_1\gamma_5\lambda_2 = \bar{\lambda}_2\gamma_5\lambda_1\,,\ \bar{\lambda}_1\gamma_5\gamma_\mu\lambda_2 = \bar{\lambda}_2\gamma_5\gamma_\mu\lambda_1 \tag{A.3}$$

are symmetric and the antisymmetric bilinears are

$$\bar{\lambda}_1\gamma_\mu\lambda_2 = -\bar{\lambda}_2\gamma_\mu\lambda_1\,,\ \bar{\lambda}_1\gamma_{\mu\nu}\lambda_2 = \bar{\lambda}_2\gamma_{\mu\nu}\lambda_1\,. \tag{A.4}$$

Additionally we can distinguish between Hermitean bilinears

$$\bar{\lambda}_1\lambda_2\,, \qquad \bar{\lambda}_1\gamma_{\mu\nu}\lambda_2\,, \qquad \bar{\lambda}_1\gamma_5\gamma^\mu\lambda_2 \tag{A.5}$$

and anti-Hermitean bilinears

$$\bar{\lambda}_1\gamma^\mu\lambda_2\,, \qquad \bar{\lambda}_1\gamma_5\lambda_2\,. \tag{A.6}$$

Finally we list the generators of the Lie group SU(3):

$$T^1 = \frac{1}{\sqrt{2}}\begin{pmatrix} 0 & 1 & 0 \\ 1 & 0 & 0 \\ 0 & 0 & 0 \end{pmatrix},\ T^2 = \frac{1}{\sqrt{2}}\begin{pmatrix} 0 & -\mathrm{i} & 0 \\ \mathrm{i} & 0 & 0 \\ 0 & 0 & 0 \end{pmatrix},\ T^3 = \frac{1}{\sqrt{2}}\begin{pmatrix} 0 & 0 & 1 \\ 0 & 0 & 0 \\ 1 & 0 & 0 \end{pmatrix},\ T^4 = \frac{1}{\sqrt{2}}\begin{pmatrix} 0 & 0 & -\mathrm{i} \\ 0 & 0 & 0 \\ \mathrm{i} & 0 & 0 \end{pmatrix},$$
$$T^5 = \frac{1}{\sqrt{2}}\begin{pmatrix} 0 & 0 & 0 \\ 0 & 0 & 1 \\ 0 & 1 & 0 \end{pmatrix},\ T^6 = \frac{1}{\sqrt{2}}\begin{pmatrix} 0 & 0 & 0 \\ 0 & 0 & -\mathrm{i} \\ 0 & \mathrm{i} & 0 \end{pmatrix},\ T^7 = \frac{1}{\sqrt{2}}\begin{pmatrix} 1 & 0 & 0 \\ 0 & -1 & 0 \\ 0 & 0 & 0 \end{pmatrix},\ T^8 = \frac{1}{\sqrt{6}}\begin{pmatrix} 1 & 0 & 0 \\ 0 & 1 & 0 \\ 0 & 0 & -2 \end{pmatrix}.$$

Except the prefactor of $\frac{1}{\sqrt{2}}$ they are given by the Hermitean and trace-less Gell-Mann matrices and their normalization is $\mathrm{tr}(T^aT^b) = \delta^{ab}$. The generators are related by the real and totally antisymmetric structure constants, $[T^a, T^b] = \mathrm{i}f^{ab}{}_cT^c$. The group-valued fields can be expressed as

$$\lambda(x) = \lambda^a(x)T^a\,, \qquad A_\mu(x) = A_\mu^a(x)T^a\,, \qquad F_{\mu\nu}(x) = F_{\mu\nu}^a(x)T^a\,. \tag{A.7}$$

APPENDIX B

Properties of the Wilson Dirac operators

In section 3.2.3, several properties of the Wilson Dirac operators were discussed. This chapter provides the according calculations.

B.1 Untwisted Dirac operator

First the untwisted Dirac operator is addressed. With

$$\begin{aligned}(\gamma_5 D_{\mathrm{W}})^\dagger &= \left(\gamma_5\Big(\frac{4}{a}+m\Big)\delta_{n,n'} - \frac{1}{2a}\gamma_5\sum_{\mu=1}^{4}\Big\{(\mathbb{1}-\gamma_\mu)\,\mathcal{V}_\mu(n)\,\delta_{n+\mu,n'} + (\mathbb{1}+\gamma_\mu)\,\mathcal{V}_\mu(n-\mu)^\dagger\,\delta_{n-\mu,n'}\Big\}\right)^\dagger \\ &= \gamma_5\Big(\frac{4}{a}+m\Big)\delta_{n,n'} - \frac{1}{2a}\sum_{\mu=1}^{4}\Big\{(\mathbb{1}-\gamma_\mu)\,\mathcal{V}_\mu(n)^\dagger\,\delta_{n,n'+\mu} + (\mathbb{1}+\gamma_\mu)\,\mathcal{V}_\mu(n-\mu)\,\delta_{n,n'-\mu}\Big\}\gamma_5 \\ &\overset{*}{=} \gamma_5\left(\Big(\frac{4}{a}+m\Big)\delta_{n,n'} - \frac{1}{2a}\sum_{\mu=1}^{4}\Big\{(\mathbb{1}+\gamma_\mu)\,\mathcal{V}_\mu(n-\mu)^\dagger\,\delta_{n-\mu,n'} + (\mathbb{1}-\gamma_\mu)\,\mathcal{V}_\mu(n)\,\delta_{n+\mu,n'}\Big\}\right) \\ &= \gamma_5 D_{\mathrm{W}} \end{aligned} \tag{B.1}$$

we can show γ_5-Hermiticity. In the step marked with the asterisk, we shifted the lattice index n, which is summed over in the fermion action. A direct consequence of eq. (B.1) is γ_5-Hermiticity of the inverse: $(D_{\mathrm{W}}^{-1})^\dagger = \gamma_5 D_{\mathrm{W}}^{-1}\gamma_5$. Next, we use that the gauge links $\mathcal{V} \in \mathrm{SO}(N_c^2\text{-}1)$ are in the real adjoint representation to calculate

$$\begin{aligned}\mathcal{C}_- D_{\mathrm{W}}\mathcal{C}_-^{-1} &= \mathcal{C}_-\Big(\frac{4}{a}+m\Big)\mathcal{C}_-^{-1}\delta_{n,n'} - \frac{1}{2a}\mathcal{C}_-\sum_{\mu=1}^{4}\Big\{(\mathbb{1}-\gamma_\mu)\mathcal{V}_\mu(n)\delta_{n+\mu,n'} + (\mathbb{1}+\gamma_\mu)\mathcal{V}_\mu(n-\mu)^{\mathrm{T}}\delta_{n-\mu,n'}\Big\}\,\mathcal{C}_-^{-1} \\ &= \Big(\frac{4}{a}+m\Big)\delta_{n,n'} - \frac{1}{2a}\sum_{\mu=1}^{4}\Big\{\Big(\mathbb{1}+\gamma_\mu^{\mathrm{T}}\Big)\,\mathcal{V}_\mu(n)\,\delta_{n+\mu,n'} + \Big(\mathbb{1}-\gamma_\mu^{\mathrm{T}}\Big)\,\mathcal{V}_\mu(n-\mu)^{\mathrm{T}}\,\delta_{n-\mu,n'}\Big\} \\ &\overset{*}{=} \Big(\frac{4}{a}+m\Big)\delta_{n,n'} - \frac{1}{2a}\sum_{\mu=1}^{4}\Big\{\Big(\mathbb{1}-\gamma_\mu^{\mathrm{T}}\Big)\,\mathcal{V}_\mu(n)^{\mathrm{T}}\,\delta_{n,n'+\mu} + \Big(\mathbb{1}+\gamma_\mu^{\mathrm{T}}\Big)\,\mathcal{V}_\mu(n-\mu)\,\delta_{n,n'-\mu}\Big\}\end{aligned}$$

$$= \left(\left(\frac{4}{a} + m\right)\delta_{n,n'} - \frac{1}{2a}\sum_{\mu=1}^{4} \left\{ (\mathbb{1} - \gamma_\mu)\, \mathcal{V}_\mu(n)\, \delta_{n+\mu,n'} + (\mathbb{1} + \gamma_\mu)\, \mathcal{V}_\mu(n-\mu)^{\mathrm{T}}\, \delta_{n-\mu,n'} \right\} \right)^{\mathrm{T}}$$
$$= D_{\mathrm{W}}^{\mathrm{T}}$$

and deduce $\mathcal{C}$-antisymmetry, $(\mathcal{C}_- D_{\mathrm{W}})^{\mathrm{T}} = -\mathcal{C}_- D_{\mathrm{W}}$. Again, we shifted the summation index n in the step marked with the asterisk. Note that the lattice actions of QCD and SYM are both invariant under charge conjugation, $S^{\mathrm{C}} = S$. In the former case, $\mathcal{U}_\mu(n)^{\mathrm{C}} = \mathcal{U}_\mu(n)^* = (\mathcal{U}_\mu(n)^\dagger)^{\mathrm{T}}$, $A_\mu(n) \to -A_\mu(n)^{\mathrm{T}}$ implies that the antiparticle has opposite charge [129]. For $\mathcal{N} = 1$ SYM theory $\mathcal{V}_\mu(n)^{\mathrm{C}} = \mathcal{V}_\mu(n)$ holds and the antiparticle has the same charge.

The eigenvalues of the untwisted Wilson Dirac operator can be analyzed in their entirety. Due to γ_5-Hermiticity the eigenvalues are either real or come in a complex pairs [129]. Furthermore, each eigenvalue is double-degenerated and hence the determinant is non-negative [31, 203, 235]. Consequently the Pfaffian $\mathrm{Pf}(\mathcal{C}_- D_{\mathrm{W}}) = \mathrm{sign}(\mathrm{Pf}(\mathcal{C}_- D_{\mathrm{W}}))\sqrt{\det(D_{\mathrm{W}})}$ is also real, but can be negative. For most simulation parameters, the fraction of configurations with negative Pfaffian is negligible [31].

B.2 Twisted Dirac operator

Performing the same calculations as in the previous section, we will encounter some differences for the mass-twisted Wilson Dirac operator $D_{\mathrm{W}}^{\mathrm{mtw}}$. First of all, the parity-breaking mass term destroys γ_5-Hermiticity:

$$\begin{aligned}
(\gamma_5 D_{\mathrm{W}}^{\mathrm{mtw}})^\dagger &= \left(\gamma_5 \left(\frac{4}{a} + m + \mathrm{i}m_5\gamma_5\right)\delta_{n,n'} - \frac{1}{2a}\gamma_5 \sum_{\mu=1}^{4} \left\{ (\mathbb{1} - \gamma_\mu)\, \mathcal{V}_\mu(n)\, \delta_{n+\mu,n'} + (\mathbb{1} + \gamma_\mu)\, \mathcal{V}_\mu(n-\mu)^\dagger\, \delta_{n-\mu,n'} \right\} \right)^\dagger \\
&= \gamma_5 \left(\frac{4}{a} + m - \mathrm{i}m_5\gamma_5\right)\delta_{n,n'} - \frac{1}{2a}\sum_{\mu=1}^{4} \left\{ (\mathbb{1} - \gamma_\mu)\, \mathcal{V}_\mu(n)^\dagger\, \delta_{n,n'+\mu} + (\mathbb{1} + \gamma_\mu)\, \mathcal{V}_\mu(n-\mu)\, \delta_{n,n'-\mu} \right\}\gamma_5 \\
&= \gamma_5 \left(\left(\frac{4}{a} + m + \mathrm{i}m_5\gamma_5\right)\delta_{n,n'} - \frac{1}{2a}\sum_{\mu=1}^{4} \left\{ (\mathbb{1}+\gamma_\mu)\mathcal{V}_\mu(n-\mu)^\dagger\, \delta_{n-\mu,n'} + (\mathbb{1}-\gamma_\mu)\mathcal{V}_\mu(n)\, \delta_{n+\mu,n'} \right\} \right) - 2\mathrm{i}m_5\delta_{n,n'} \\
&= \gamma_5 D_{\mathrm{W}}^{\mathrm{mtw}} - 2\mathrm{i}m_5\mathbb{1}\,. \qquad \text{(B.2)}
\end{aligned}$$

Only the modified form $(D_{\mathrm{W}}^{\mathrm{mtw}})^\dagger = \gamma_5 D_{\mathrm{W}}^{\mathrm{mtw}}\gamma_5 - 2\mathrm{i}m_5\gamma_5$ with the correction term holds. Alternative formulations are $(D_{\mathrm{W}}^{\mathrm{mtw}}(m_5))^\dagger = \gamma_5 D_{\mathrm{W}}^{\mathrm{mtw}}(-m_5)\gamma_5$ or[23]

$$\left(D_{\mathrm{W}}^{\mathrm{mtw}}(\alpha)\right)^\dagger = \gamma_5 D_{\mathrm{W}}^{\mathrm{mtw}}(-\alpha)\gamma_5\,. \qquad \text{(B.3)}$$

[23] This is generalized for the double-twist as $\left(D_{\mathrm{W}}^{\mathrm{dtw}}(\alpha,\varphi)\right)^\dagger = \gamma_5 D_{\mathrm{W}}^{\mathrm{dtw}}(-\alpha,-\varphi)\gamma_5$.

The complex conjugate of the inverse reads

$$\begin{aligned}\left((D_{\mathrm{W}}^{\mathrm{mtw}})^{-1}\right)^{\dagger} &= \left(D_{\mathrm{W}}^{\mathrm{mtw}} + 2\mathrm{i}m_5\gamma_5\right)\cdot\left(\gamma_5 D_{\mathrm{W}}^{\mathrm{mtw}}\gamma_5 D_{\mathrm{W}}^{\mathrm{mtw}} + 4m_5^2\mathbb{1}\right)^{-1} \\ &= \left(D_{\mathrm{W}}^{\mathrm{mtw}}\gamma_5 D_{\mathrm{W}}^{\mathrm{mtw}}\gamma_5 + 4m_5^2\mathbb{1}\right)^{-1}\cdot\left(D_{\mathrm{W}}^{\mathrm{mtw}} + 2\mathrm{i}m_5\gamma_5\right).\end{aligned}$$

Analogous to the untwisted scenario, the twisted Wilson Dirac operator is $\mathcal{C}$-antisymmetric, $(\mathcal{C}D_{\mathrm{W}}^{\mathrm{mtw}})^{\mathrm{T}} = -\mathcal{C}D_{\mathrm{W}}^{\mathrm{mtw}}$. In consequence of the lost γ_5-Hermiticity the complex eigenvalues are no longer arranged, thus in general $\det(D_{\mathrm{W}}^{\mathrm{mtw}}) \in \mathbb{C}$ and $\mathrm{Pf}(D_{\mathrm{W}}^{\mathrm{mtw}}) \in \mathbb{C}$. In section 5.3 we checked numerically that the phase of the Pfaffian is negligible and no sign-problem arises.

APPENDIX C

Supersymmetry transformation of the gluino-glue

In section 4.2, we transformed the scalar and pseudoscalar mesonic state with the supersymmetry into the gluino-glue (plus a term linear in the auxiliary field $\mathcal{G}$):

$$\delta_\epsilon O_{\text{a-}f_0} = \delta_\epsilon\Big(\bar\lambda\lambda\Big) = -2\mathrm{i}\bar\epsilon\,\mathrm{tr_c}\Big(\frac{1}{4\mathrm{i}}F_{\mu\nu}\Sigma^{\mu\nu}\lambda - \mathcal{G}\gamma_5\lambda\Big)\,, \tag{C.1}$$

$$\delta_\epsilon O_{\text{a-}\eta'} = \delta_\epsilon\Big(\bar\lambda\mathrm{i}\gamma_5\lambda\Big) = 2\bar\epsilon\gamma_5\,\mathrm{tr_c}\Big(\frac{1}{4\mathrm{i}}F_{\mu\nu}\Sigma^{\mu\nu}\lambda - \mathcal{G}\gamma_5\lambda\Big)\,. \tag{C.2}$$

For clarity, the spacetime argument x is suppressed. Here, we show that the supersymmetry transformation of the gluino-glue contains a linear combination of the scalar a-f_0 and the pseudoscalar a-η'. Hence the chiral Wess-Zumino supermultiplet is closed. The eqs. (C.1) and (C.2) suggest that for the gluino-glue we should start off-shell with

$$\begin{aligned}\delta_\epsilon\mathrm{tr_c}\Big(\frac{1}{4\mathrm{i}}F_{\mu\nu}\Sigma^{\mu\nu}\lambda-\mathcal{G}\gamma_5\lambda\Big) = {}& \frac{1}{4}\mathrm{tr_c}\Big(\bar\epsilon\gamma_\nu D_\mu\lambda-\bar\epsilon\gamma_\mu D_\nu\lambda\Big)\Sigma^{\mu\nu}\lambda + \frac{1}{4}\mathrm{tr_c}F_{\mu\nu}\Sigma^{\mu\nu}\Big(\frac{1}{4\mathrm{i}}F_{\alpha\beta}\Sigma^{\alpha\beta}+\mathcal{G}\gamma_5\Big)\epsilon\\ & - \mathrm{tr_c}\Big(\bar\epsilon\gamma_5\not{D}\lambda\Big)\gamma_5\lambda - \mathrm{tr_c}\gamma_5\mathcal{G}\Big(\frac{1}{4}F_{\mu\nu}\Sigma^{\mu\nu}\epsilon+\mathcal{G}\gamma_5\epsilon\Big)\,.\end{aligned}$$

The terms linear in $\mathcal{G}$ cancel and we get

$$\delta_\epsilon\mathrm{tr_c}\Big(\frac{1}{4\mathrm{i}}F_{\mu\nu}\Sigma^{\mu\nu}\lambda-\mathcal{G}\gamma_5\lambda\Big) = -\frac{1}{2}(\partial_\mu\bar\lambda_a\gamma_\nu\epsilon)\Sigma^{\mu\nu}\lambda_a - \frac{1}{2}f^{abc}A_{c\mu}(\bar\lambda_a\gamma_\nu\epsilon)\Sigma^{\mu\nu}\lambda_b \tag{C.3}$$

$$- \mathrm{tr_c}\Big(\bar\epsilon\gamma_5\not{D}\lambda\Big)\gamma_5\lambda \tag{C.4}$$

$$+ \frac{1}{16\mathrm{i}}\mathrm{tr_c}F_{\mu\nu}\Sigma^{\mu\nu}F_{\alpha\beta}\Sigma^{\alpha\beta}\epsilon - \mathrm{i}\,\mathrm{tr_c}\mathcal{G}^2\epsilon\,. \tag{C.5}$$

With the help of the general Fierz identity [236, 237]

$$4\psi^b\bar\psi^a = -(\bar\psi^a\psi^b) - \gamma_\rho(\bar\psi^a\gamma^\rho\psi^b) + \frac{1}{2}\gamma_{\rho\sigma}(\bar\psi^a\gamma^{\rho\sigma}\psi^b) + \gamma_5\gamma_\sigma(\bar\psi^a\gamma_5\gamma^\sigma\psi^b) - \gamma_5(\bar\psi^a\gamma_5\psi^b)\,, \tag{C.6}$$

expression (C.4) can be rewritten as

$$\begin{aligned}
-\mathrm{tr_c}\Big(\bar\epsilon\gamma_5 \not{D}\lambda\Big)\gamma_5\lambda &= (\bar\epsilon\gamma^\mu\partial_\mu\gamma_5\lambda_a)\gamma_5\lambda_a - \mathrm{i}\,\mathrm{tr_c}\Big(\bar\epsilon\gamma^\mu[A_\mu,\gamma_5\lambda]\gamma_5\lambda\Big)\\
&= (\partial_\mu\bar\lambda_a\gamma^\mu\gamma_5\epsilon)\gamma_5\lambda_a + f^{abc}A_{c\mu}(\bar\lambda_a\gamma^\mu\gamma_5\epsilon)\gamma_5\lambda_b\\
&= \frac{1}{4}(\partial_\mu\bar\lambda_a\lambda_a)\gamma^\mu\epsilon - \frac{1}{4}(\partial_\mu\bar\lambda_a\gamma_\rho\lambda_a)\gamma^\rho\gamma^\mu\epsilon - \frac{1}{8}(\partial_\mu\bar\lambda_a\gamma^{\rho\sigma}\lambda_a)\gamma_{\rho\sigma}\gamma^\mu\epsilon\\
&\quad + \frac{1}{4}(\partial_\mu\bar\lambda_a\gamma_5\gamma^\rho\lambda_a)\gamma_5\gamma_\rho\gamma^\mu\epsilon + \frac{1}{4}(\partial_\mu\bar\lambda_a\gamma_5\lambda_a)\gamma_5\gamma^\mu\epsilon\\
&\quad - \frac{1}{4}f^{abc}A_{c\mu}(\bar\lambda_a\gamma^\rho\lambda_b)\gamma_\rho\gamma^\mu\epsilon - \frac{1}{8}f^{abc}A_{c\mu}(\bar\lambda_a\gamma^{\rho\sigma}\lambda_b)\gamma_{\rho\sigma}\gamma^\mu\epsilon\,. \qquad \text{(C.7)}
\end{aligned}$$

Applying the Fierz identity (C.6) on the first term of (C.3) gives

$$\begin{aligned}
-\frac{1}{2}(\partial_\mu\bar\lambda_a\gamma_\nu\epsilon)\Sigma^{\mu\nu}\lambda_a &= \frac{1}{8}(\partial_\mu\bar\lambda_a\lambda_a)\Sigma^{\mu\nu}\gamma_\nu\epsilon + \frac{1}{8}(\partial_\mu\bar\lambda_a\gamma_\rho\lambda_a)\Sigma^{\mu\nu}\gamma^\rho\gamma_\nu\epsilon\\
&\quad - \frac{1}{16}(\partial_\mu\bar\lambda_a\gamma^{\rho\sigma}\lambda_a)\Sigma^{\mu\nu}\gamma_{\rho\sigma}\gamma_\nu\epsilon - \frac{1}{8}(\partial_\mu\bar\lambda_a\gamma_5\gamma^\rho\lambda_a)\Sigma^{\mu\nu}\gamma_5\gamma_\rho\gamma_\nu\epsilon\\
&\quad + \frac{1}{8}(\partial_\mu\bar\lambda_a\gamma_5\lambda_a)\Sigma^{\mu\nu}\gamma_5\gamma_\nu\epsilon\,.
\end{aligned}$$

With the help of

$$\Sigma^{\mu\nu}\gamma_\nu = 6\gamma^\mu\,, \quad \Sigma^{\mu\nu}\gamma^\rho\gamma_\nu = -\Sigma^{\mu\rho} - 6\eta^{\mu\rho}\,, \quad \Sigma^{\mu\nu}\gamma^{\rho\sigma}\gamma_\nu = -\Sigma^{\rho\sigma}\gamma^\mu \qquad \text{(C.8)}$$

and using $\partial_\mu(\bar\lambda_a\Gamma\lambda_a) = 2(\partial_\mu\bar\lambda_a)\Gamma\lambda_a$ for $\Gamma\in\{\mathbb{1},\gamma_5,\gamma_5\gamma^\mu\}$ we obtain

$$\begin{aligned}
-\frac{1}{2}(\partial_\mu\bar\lambda_a\gamma_\nu\epsilon)\Sigma^{\mu\nu}\lambda_a &= \frac{3}{8}\partial_\mu(\bar\lambda_a\lambda_a)\gamma^\mu\epsilon - \frac{1}{8}(\partial_\mu\bar\lambda_a\gamma_\rho\lambda_a)\Sigma^{\mu\rho}\epsilon - \frac{3}{4}(\partial_\mu\bar\lambda_a\gamma^\mu\lambda_a)\epsilon\\
&\quad + \frac{1}{16}(\partial_\mu\bar\lambda_a\gamma_{\rho\sigma}\lambda_a)\Sigma^{\rho\sigma}\gamma^\mu\epsilon\\
&\quad + \frac{1}{16}\partial_\mu(\bar\lambda_a\gamma_5\gamma_\rho\lambda_a)\Sigma^{\mu\rho}\gamma_5\epsilon + \frac{3}{8}\partial_\mu(\bar\lambda_a\gamma_5\gamma^\mu\lambda_a)\gamma_5\epsilon\\
&\quad + \frac{3}{8}\partial_\mu(\bar\lambda_a\gamma_5\lambda_a)\gamma_5\gamma^\mu\epsilon\,. \qquad \text{(C.9)}
\end{aligned}$$

The second term of eq. (C.3) with the Fierz identity (C.6) leads to

$$\begin{aligned}
-\frac{1}{2}f^{abc}A_{c\mu}(\bar\lambda_a\gamma_\nu\epsilon)\Sigma^{\mu\nu}\lambda_b &= \frac{1}{8}f^{abc}A_{c\mu}(\bar\lambda_a\gamma^\rho\lambda_b)\Sigma^{\mu\nu}\gamma_\rho\gamma_\nu\epsilon - \frac{1}{16}f^{abc}A_{c\mu}(\bar\lambda_a\gamma^{\rho\sigma}\lambda_b)\Sigma^{\mu\nu}\gamma_{\rho\sigma}\gamma_\nu\epsilon\\
&= -\frac{1}{8}f^{abc}A_{c\mu}(\bar\lambda_a\gamma_\rho\lambda_b)\Sigma^{\mu\rho}\epsilon - \frac{3}{4}f^{abc}A_{c\mu}(\bar\lambda_a\gamma^\mu\lambda_b)\epsilon\\
&\quad + \frac{1}{16}f^{abc}A_{c\mu}(\bar\lambda_a\gamma_{\rho\sigma}\lambda_b)\Sigma^{\rho\sigma}\gamma^\mu\epsilon\,. \qquad \text{(C.10)}
\end{aligned}$$

Finally we use $\gamma^{\mu\nu} = \frac{1}{2}\Sigma^{\mu\nu}$ and add up the terms

$$\begin{aligned}
\delta_\epsilon \mathrm{tr_c}\Big(\frac{1}{4\mathrm{i}}F_{\mu\nu}\Sigma^{\mu\nu}\lambda - \mathcal{G}\gamma_5\lambda\Big) &= (C.9) + (C.10) + (C.7) + (C.5) \\
&= \Big(\frac{3}{8}\partial_\mu(\bar\lambda_a\lambda_a)\gamma^\mu\epsilon - \frac{1}{8}(\partial_\mu\bar\lambda_a\gamma_\rho\lambda_a)\Sigma^{\mu\rho}\epsilon - \frac{3}{4}(\partial_\mu\bar\lambda_a\gamma^\mu\lambda_a)\epsilon \\
&\quad + \frac{1}{32}(\partial_\mu\bar\lambda_a\Sigma_{\rho\sigma}\lambda_a)\Sigma^{\rho\sigma}\gamma^\mu\epsilon + \frac{1}{16}\partial_\mu(\bar\lambda_a\gamma_5\gamma_\rho\lambda_a)\Sigma^{\mu\rho}\gamma_5\epsilon \\
&\quad + \frac{3}{8}\partial_\mu(\bar\lambda_a\gamma_5\gamma^\mu\lambda_a)\gamma_5\epsilon + \frac{3}{8}\partial_\mu(\bar\lambda_a\gamma_5\lambda_a)\gamma_5\gamma^\mu\epsilon\Big) \\
&\quad + \Big(-\frac{1}{8}f^{abc}A_{c\mu}(\bar\lambda_a\gamma_\rho\lambda_b)\Sigma^{\mu\rho}\epsilon - \frac{3}{4}f^{abc}A_{c\mu}(\bar\lambda_a\gamma^\mu\lambda_b)\epsilon \\
&\quad + \frac{1}{32}f^{abc}A_{c\mu}(\bar\lambda_a\Sigma_{\rho\sigma}\lambda_b)\Sigma^{\rho\sigma}\gamma^\mu\epsilon\Big) \\
&\quad + \Big(\frac{1}{8}\partial_\mu(\bar\lambda_a\lambda_a)\gamma^\mu\epsilon - \frac{1}{4}(\partial_\mu\bar\lambda_a\gamma_\rho\lambda_a)\gamma^\rho\gamma^\mu\epsilon - \frac{1}{32}(\partial_\mu\bar\lambda_a\Sigma^{\rho\sigma}\lambda_a)\Sigma_{\rho\sigma}\gamma^\mu\epsilon \\
&\quad + \frac{1}{8}\partial_\mu(\bar\lambda_a\gamma_5\gamma^\rho\lambda_a)\gamma_5\gamma_\rho\gamma^\mu\epsilon + \frac{1}{8}\partial_\mu(\bar\lambda_a\gamma_5\lambda_a)\gamma_5\gamma^\mu\epsilon \\
&\quad - \frac{1}{4}f^{abc}A_{c\mu}(\bar\lambda_a\gamma^\rho\lambda_b)\gamma_\rho\gamma^\mu\epsilon - \frac{1}{32}f^{abc}A_{c\mu}(\bar\lambda_a\Sigma^{\rho\sigma}\lambda_b)\Sigma_{\rho\sigma}\gamma^\mu\epsilon\Big) \\
&\quad + \Big(\frac{1}{16\mathrm{i}}\,\mathrm{tr_c}F_{\mu\nu}F_{\alpha\beta}\Sigma^{\mu\nu}\Sigma^{\alpha\beta}\epsilon - \mathrm{i}\,\mathrm{tr_c}\,\mathcal{G}^2\epsilon\Big)\,.
\end{aligned}$$

We collect terms of the same type

$$\begin{aligned}
\delta_\epsilon \mathrm{tr_c}\Big(\frac{1}{4\mathrm{i}}F_{\mu\nu}\Sigma^{\mu\nu}\lambda - \mathcal{G}\gamma_5\lambda\Big) &= \frac{1}{2}\partial_\mu(\bar\lambda_a\lambda_a)\gamma^\mu\epsilon + \frac{1}{2}\partial_\mu(\bar\lambda_a\gamma_5\lambda_a)\gamma_5\gamma^\mu\epsilon \\
&\quad + \frac{1}{4}(\partial_\mu\bar\lambda_a\gamma_\rho\lambda_a)\Big(-\gamma^\rho\gamma^\mu - \frac{1}{2}\Sigma^{\mu\rho} - 3\eta^{\mu\rho}\Big)\epsilon \\
&\quad + \frac{1}{32}(\partial_\mu\bar\lambda_a\Sigma_{\rho\sigma}\lambda_a)\Sigma^{\rho\sigma}\gamma^\mu\epsilon - \frac{1}{32}(\partial_\mu\bar\lambda_a\Sigma_{\rho\sigma}\lambda_a)\Sigma^{\rho\sigma}\gamma^\mu\epsilon \\
&\quad + \frac{1}{8}\partial_\mu(\bar\lambda_a\gamma_5\gamma_\rho\lambda_a)\Big(\frac{1}{2}\Sigma^{\mu\rho}\gamma_5 + 3\gamma_5\eta^{\mu\rho} + \gamma_5\gamma^\rho\gamma^\mu\Big)\epsilon \\
&\quad - \frac{1}{8}f^{abc}A_{c\mu}(\bar\lambda_a\gamma_\rho\lambda_b)\Sigma^{\mu\rho}\epsilon - \frac{3}{4}f^{abc}A_{c\mu}(\bar\lambda_a\gamma^\mu\lambda_b)\epsilon \\
&\quad + \frac{1}{32}f^{abc}A_{c\mu}(\bar\lambda_a\Sigma_{\rho\sigma}\lambda_b)\Sigma^{\rho\sigma}\gamma^\mu\epsilon \\
&\quad - \frac{1}{4}f^{abc}A_{c\mu}(\bar\lambda_a\gamma_\rho\lambda_b)\gamma^\rho\gamma^\mu\epsilon - \frac{1}{32}f^{abc}A_{c\mu}(\bar\lambda_a\Sigma_{\rho\sigma}\lambda_b)\Sigma^{\rho\sigma}\gamma^\mu\epsilon \\
&\quad + \frac{1}{16\mathrm{i}}\,\mathrm{tr_c}F_{\mu\nu}F_{\alpha\beta}\Sigma^{\mu\nu}\Sigma^{\alpha\beta}\epsilon - \mathrm{i}\,\mathrm{tr_c}\,\mathcal{G}^2\epsilon
\end{aligned}$$

and simplify to

$$\begin{aligned}
\delta_\epsilon \mathrm{tr_c}\Big(\frac{1}{4\mathrm{i}}F_{\mu\nu}\Sigma^{\mu\nu}\lambda - \mathcal{G}\gamma_5\lambda\Big) &= \frac{1}{2}\not\partial(\bar\lambda_a\lambda_a)\epsilon + \frac{1}{2}\gamma_5\not\partial(\bar\lambda_a\gamma_5\lambda_a)\epsilon \\
&\quad + \Big(\bar\lambda_a(\not D\lambda)_a\Big)\epsilon + \Big(\bar\lambda_a\gamma_5(\not D\lambda)_a\Big)\gamma_5\epsilon \\
&\quad + \frac{1}{16\mathrm{i}}\,\mathrm{tr_c}F_{\mu\nu}F_{\alpha\beta}\Sigma^{\mu\nu}\Sigma^{\alpha\beta}\epsilon - \mathrm{i}\,\mathrm{tr_c}\,\mathcal{G}^2\epsilon\,. \qquad \text{(C.11)}
\end{aligned}$$

APPENDIX D

Supersymmetry transformation of the action

The gluino mass term breaks supersymmetry softly in the Euclidean continuum action (2.38). To prove that the $\mathcal{N} = 1$ SYM action without gluino mass is invariant under supersymmetry transformations, we use the on-shell formulation of the Lagrangian

$$\mathcal{L}_{\mathrm{E}}(x) = \frac{1}{4} F^a_{\mu\nu}(x) F^{a\mu\nu}(x) + \frac{1}{2} \bar{\lambda}^a(x) \not{D} \lambda^a(x) \tag{D.1}$$

and the corresponding supersymmetry transformations given in eq. (4.21). In the following we do not distinguish between contravariant and covariant indices since they can be lowered and raised trivially with the Euclidean metric. We still assume Einstein's sum convention over doubled indices – also if both indices are contravariant resp. covariant. First, we calculate the infinitesimal transformation of the gauge term

$$\begin{aligned} \delta_\epsilon \left(\frac{1}{4} F^a_{\mu\nu}(x) F^a_{\mu\nu}(x) \right) = \frac{1}{2} F^a_{\mu\nu}(x) \, \delta_\epsilon F^a_{\mu\nu}(x) &\overset{(4.19)}{=} \frac{\mathrm{i}}{2} F^a_{\mu\nu}(x) \, \bar{\epsilon} \left(\gamma_\nu D_\mu - \gamma_\mu D_\nu \right) \lambda^a(x) \\ &= \mathrm{i} \, F^a_{\mu\nu}(x) \, \bar{\epsilon} \gamma_\nu D_\mu \lambda^a(x) \, . \end{aligned} \tag{D.2}$$

With the help of

$$\begin{aligned} \delta_\epsilon \left(D_\mu \lambda(x) \right) &= \partial_\mu \delta_\epsilon \lambda(x) - \mathrm{i} g [\delta_\epsilon A_\mu(x), \lambda(x)] - \mathrm{i} g [A_\mu(x), \delta_\epsilon \lambda(x)] \\ &= D_\mu \delta_\epsilon \lambda(x) - \mathrm{i} g [\delta_\epsilon A_\mu(x), \lambda(x)] \\ &= \frac{1}{4\mathrm{i}} D_\mu \left(\Sigma_{\alpha\beta} F_{\alpha\beta}(x) \epsilon \right) + g [\bar{\epsilon} \gamma_\mu \lambda(x), \lambda(x)] \end{aligned} \tag{D.3}$$

the transformation of the fermionic term proceeds:

$$\begin{aligned}\delta_\epsilon\left(\frac{1}{2}\bar{\lambda}^a(x)\gamma_\mu D_\mu\lambda^a(x)\right) &= \frac{-1}{8\mathrm{i}}\bar{\epsilon}\,\Sigma_{\alpha\beta}F^a_{\alpha\beta}(x)\gamma_\mu D_\mu\lambda^a(x) + \frac{1}{8\mathrm{i}}\bar{\lambda}^a(x)\gamma_\mu D_\mu\Sigma_{\alpha\beta}F^a_{\alpha\beta}(x)\epsilon \\ &\quad + \frac{1}{2}\bar{\lambda}^a(x)\gamma_\mu g f_{abc}\bar{\epsilon}\gamma_\mu\lambda^b(x)\lambda^c(x) \\ &= \left\{\frac{\mathrm{i}}{8}\bar{\epsilon}\,\Sigma_{\alpha\beta}\gamma_\mu F^a_{\alpha\beta}(x)D_\mu\lambda^a(x) - \frac{\mathrm{i}}{8}\bar{\epsilon}\,\Sigma_{\alpha\beta}\gamma_\mu\Big(D_\mu F^a_{\alpha\beta}(x)\Big)\lambda^a(x)\right\} \\ &\quad + \left[\frac{g}{2}\bar{\lambda}^a(x)\gamma_\mu f_{abc}\bar{\epsilon}\gamma_\mu\lambda^b(x)\lambda_c(x)\right]. \end{aligned} \tag{D.4}$$

To further simplify this expression we rewrite the second term in $\{\ldots\}$ as

$$\begin{aligned}\bar{\epsilon}\,\Sigma_{\alpha\beta}\gamma_\mu\Big(D_\mu F^a_{\alpha\beta}(x)\Big)\lambda^a(x) &= \bar{\epsilon}\,\Sigma_{\alpha\beta}\gamma_\mu\Big(\Big(\partial_\mu F^a_{\alpha\beta}(x)\Big)\lambda^a(x) + g f_{abc}A^b_\mu(x)F^c_{\alpha\beta}(x)\lambda^a(x)\Big) \\ &= \bar{\epsilon}\,\Sigma_{\alpha\beta}\gamma_\mu\Big(\partial_\mu\Big(F^a_{\alpha\beta}(x)\lambda^a(x)\Big) - F^a_{\alpha\beta}(x)D_\mu\lambda^a(x) \\ &\quad + F^a_{\alpha\beta}(x)g f_{abc}A^b_\mu(x)\lambda^c(x) + g f_{abc}A^b_\mu(x)F^c_{\alpha\beta}(x)\lambda^a(x)\Big).\end{aligned} \tag{D.5}$$

The first term of eq. (D.5) is a divergence and the two last terms cancel each other. Then eq. (D.4) becomes

$$\begin{aligned}\delta_\epsilon\left(\frac{1}{2}\bar{\lambda}^a(x)\gamma_\mu D_\mu\lambda^a(x)\right) &= \left\{\frac{\mathrm{i}}{4}\bar{\epsilon}\,\Sigma_{\alpha\beta}F^a_{\alpha\beta}(x)\not{D}\lambda^a(x)\right\} + \left[\frac{g}{2}\bar{\lambda}^a(x)\gamma_\mu f_{abc}\bar{\epsilon}\gamma_\mu\lambda^b(x)\lambda^c(x)\right] \\ &\quad + \text{divergence}\,.\end{aligned} \tag{D.6}$$

Using the relation

$$\frac{1}{2}\Sigma_{\mu\nu}\gamma_\rho = \delta_{\nu\rho}\gamma_\mu - \delta_{\mu\rho}\gamma_\nu + \epsilon_{\mu\nu\rho\sigma}\gamma_\sigma\gamma_5,\ \ \epsilon_{0123} = 1 \tag{D.7}$$

of the Euclidean Dirac matrices, the term in $\{\ldots\}$ of eq. (D.6) can be rearranged:

$$\begin{aligned}\frac{\mathrm{i}}{4}\bar{\epsilon}\,\Sigma_{\alpha\beta}F^a_{\alpha\beta}(x)\not{D}\lambda^a(x) &= \frac{\mathrm{i}}{2}\bar{\epsilon}F^a_{\alpha\beta}(x)\left(\delta_{\beta\rho}\gamma_\alpha - \delta_{\alpha\rho}\gamma_\beta + \epsilon_{\alpha\beta\rho\sigma}\gamma_\sigma\gamma_5\right)D_\rho\lambda^a(x) \\ &= \frac{\mathrm{i}}{2}\bar{\epsilon}\left(F^a_{\alpha\rho}(x)\gamma_\alpha - F^a_{\rho\beta}(x)\gamma_\beta + F^a_{\alpha\beta}(x)\epsilon_{\alpha\beta\rho\sigma}\gamma_\sigma\gamma_5\right)D_\rho\lambda^a(x) \\ &= \mathrm{i}\bar{\epsilon}\left(F^a_{\alpha\rho}(x)\gamma_\alpha D_\rho\lambda^a(x) + \frac{1}{2}F^a_{\alpha\beta}(x)\epsilon_{\alpha\beta\rho\sigma}\gamma_\sigma\gamma_5 D_\rho\lambda^a(x)\right).\end{aligned} \tag{D.8}$$

The second term of the last equation gives

$$\begin{aligned}\frac{\mathrm{i}}{2}\bar{\epsilon}F^a_{\alpha\beta}(x)\epsilon_{\alpha\beta\rho\sigma}\gamma_\sigma\gamma_5 D_\rho\lambda^a(x) &= \frac{\mathrm{i}}{2}\bar{\epsilon}\Big(F^a_{\alpha\beta}(x)\epsilon_{\alpha\beta\rho\sigma}\gamma_\sigma\gamma_5\Big(\partial_\rho\lambda^a(x) + g f_{abc}A^b_\rho(x)\lambda^c(x)\Big)\Big) \\ &= \frac{\mathrm{i}}{2}\epsilon_{\alpha\beta\rho\sigma}\bar{\epsilon}\Big(\partial_\rho\Big(F^a_{\alpha\beta}(x)\gamma_\sigma\gamma_5\lambda^a(x)\Big) - \Big(D_\rho F^a_{\alpha\beta}(x)\Big)\gamma_\sigma\gamma_5\lambda^a(x) \\ &\quad + F^a_{\alpha\beta}(x)\gamma_\sigma\gamma_5 g f_{abc}A^b_\rho(x)\lambda^c(x) + g f_{abc}A^b_\rho(x)F^c_{\alpha\beta}(x)\gamma_\sigma\gamma_5\lambda^a(x)\Big).\end{aligned}$$

In the previous equation, the first term is a divergence, the second term vanishes due to the Bianchi identity [238] and the third and fourth terms cancel each other. Finally, the term in [...] of eq. (D.6) can be rewritten with the general Fierz identity[24] (C.6), the properties of the bilinears (4.22) and (4.23), and the sums

$$\gamma_\mu\gamma^\mu = 4\,\mathbb{1}_4\,, \quad \gamma_\mu\gamma_5\gamma^\mu = -4\gamma_5\,, \quad \gamma_\mu\gamma_\rho\gamma^\mu = -2\gamma_\rho\,, \quad \gamma_\mu\gamma_{\rho\sigma}\gamma^\mu = 0\,, \quad \gamma_\mu\gamma_5\gamma_\rho\gamma^\mu = -2\gamma_\rho\gamma_5\,.$$

A short calculation

$$\begin{aligned}\frac{g}{2}f_{abc}\bar\epsilon\gamma_\mu\lambda^b(x)\bar\lambda^a(x)\gamma^\mu\lambda^c(x) &= \frac{g}{4}\Big(\bar\epsilon\gamma_\mu\lambda^c(x)\Big)\Big(\bar\lambda^a(x)\gamma^\mu\lambda^b(x)\Big)f_{abc}\\ &= \frac{g}{4}\Big(\bar\epsilon\gamma_\mu\lambda^b(x)\Big)\Big(\bar\lambda^a(x)\gamma^\mu\lambda^c(x)\Big)f_{acb}\\ &= -\frac{g}{4}\Big(\bar\epsilon\gamma_\mu\lambda^b(x)\Big)\Big(\bar\lambda^a(x)\gamma^\mu\lambda^c(x)\Big)f_{abc}\end{aligned} \tag{D.9}$$

shows that lhs $= -\frac{1}{2}\cdot$ lhs and hence this term has to vanish. Collecting all terms, the transformation of the Euclidean Lagrangian density is

$$\begin{aligned}\delta_\epsilon\mathcal{L}_\mathrm{E} &= (\text{D.2}) + (\text{D.6})\\ &= \mathrm{i}F^a_{\mu\nu}(x)\bar\epsilon\gamma_\nu D_\mu\lambda^a(x) + \mathrm{i}\bar\epsilon F^a_{\alpha\rho}(x)\gamma_\alpha D_\rho\lambda^a(x) + \text{divergence}\\ &= \text{divergence}\end{aligned} \tag{D.10}$$

only a divergence and consequently the Euclidean action is invariant. For the proof of the invariance of the lattice action, see for example [205].

[24] We checked explicitly that the Fierz identity holds with our Euclidean Dirac matrices given in appendix A.

APPENDIX E

Why the pion is the lightest mesonic state

The subsequent formulation of the proof can be found in the textbooks [239, 240], both citing the original publication of Don Weingarten [241]. To prove that the pion is in the untwisted scenario the lightest mesonic state on the lattice, we consider two-point correlators. If two different correlators obey $|C_1(0,x)| > |C_2(0,x)|$ for large enough separations $x \gg 1$ (where excited states do not contribute), then the exponential decay of C_2 is faster and thus the ground state mass of the corresponding particle is heavier. Starting from a generic mesonic interpolators with mass-degenerated fermions ψ_1 and ψ_2, the mesonic correlator is

$$\begin{aligned} C(0,x) = \left\langle \bar{\psi}_1(0)\Gamma\psi_2(0)\,\bar{\psi}_2(x)\tilde{\Gamma}\psi_1(x)\right\rangle &= \left\langle \mathrm{tr}\Big(G(0,x)\Gamma G(x,0)\tilde{\Gamma}\Big)\right\rangle_{\mathcal{U}} \\ &= \left\langle \mathrm{tr}\Big(G(0,x)\Gamma\gamma_5 G^{\dagger sc}(0,x)\gamma_5\tilde{\Gamma}\Big)\right\rangle_{\mathcal{U}}. \end{aligned} \tag{E.1}$$

In the last step we used γ_5-Hermiticity and we explicitly transposed the spatial part of the propagator – thus the Hermitean conjugate has still to be applied in spinor and color space as indicated by the indices *sc*. For the four-dimensional complex spinor space we can choose the basis $\gamma_A \in \{\mathbb{1}_4, \gamma^\mu, \gamma^{\mu\nu}, \gamma_5\gamma^\mu, \gamma_5\}$ and expand the propagator

$$G(0,x) = \sum_{A=1}^{16} c_A(x)\gamma_A\,. \tag{E.2}$$

In case of the a-π, $\Gamma = \tilde{\Gamma} = \gamma_5$, the trace simplifies to

$$\mathrm{tr}\left(\sum_{A,B=1}^{16} c_A(x)\gamma_A\, c_B^\dagger(x)\gamma_B^\dagger\right) = \sum_{A,B=1}^{16} \mathrm{tr_c}\Big(c_A(x)c_B^\dagger(x)\Big)\mathrm{tr}\Big(\gamma_A\gamma_B^\dagger\Big) = 4\sum_{A=1}^{16}\mathrm{tr_c}\Big(|c_A(x)|^2\Big)\,.$$

Consequently all coefficients $c_A(x)$ lead to a positive contribution. To calculate the sum for the a-a with $\Gamma = \tilde{\Gamma} = \mathbb{1}_4$, we rename the coefficients in the expansion

$$G(0,x) = a(x)\mathbb{1}_4 + \sum_{\mu=1}^{4} b_\mu(x)\gamma^\mu + \sum_{\substack{\mu,\nu=1\\ \mu<\nu}}^{4} c_{\mu\nu}(x)\gamma^{\mu\nu} + \sum_{\mu=1}^{4} d_\mu(x)\gamma_5\gamma^\mu + e(x)\gamma_5 \tag{E.3}$$

and notice that

$$\gamma_5 G(0,x)\gamma_5 = a(x)\mathbb{1}_4 - \sum_{\mu=1}^{4} b_\mu(x)\gamma^\mu + \sum_{\substack{\mu,\nu=1 \\ \mu<\nu}}^{4} c_{\mu\nu}(x)\gamma^{\mu\nu} - \sum_{\mu=1}^{4} d_\mu(x)\gamma_5\gamma^\mu + e(x)\gamma_5\,. \quad \text{(E.4)}$$

In comparison to the a-π, the trace of the expanded a-a correlator

$$\mathrm{tr}\Big(G(0,x)\gamma_5 G^{\dagger_{sc}}(0,x)\gamma_5\Big) =$$
$$4\mathrm{tr_c}\Big(|a(x)|^2\Big) - \sum_{\mu=1}^{4}\mathrm{tr_c}\Big(|b_\mu(x)|^2\Big) + \sum_{\substack{\mu,\nu=1 \\ \mu<\nu}}^{4}\mathrm{tr_c}\Big(|c_{\mu\nu}(x)|^2\Big) - \sum_{\mu=1}^{4}\mathrm{tr_c}\Big(|d_\mu(x)|^2\Big) + \mathrm{tr_c}\Big(|e(x)|^2\Big)$$

has negative summands and thus is always smaller. In conclusion, the a-a (and analogously all other mesonic states) are heavier than the a-π. Note that this proof is only valid in the untwisted scenario, where γ_5-Hermiticity is intact. Furthermore this proof is only exact for zero temperature and in an infinite volume, when all connected correlators approach zero. In a finite volume the correlators are cosh-shaped and $|C_{\text{a-}a}(0,x)| < |C_{\text{a-}\pi}(0,x)|$ would not imply $m_{\text{a-}a} > m_{\text{a-}\pi}$. Note also that this proof requires a positive measure and its validity ends when a sign problem occurs.

To check if the results in section 6.2 are in line with this proof, we have a closer look at the correlators of a-π and a-a. This way we can check whether the unexpected mass-hierarchy originates from problems with fitting the correlators. Figure E.1 depicts the correlators of both connected mesonic states without normalization. We see that the correlator of the a-π is always above the corresponding a-a correlator and in the range $t \in [2, 12]$ the a-a correlator falls off faster than the a-π correlator. Thus $m_{\text{a-}a} > m_{\text{a-}\pi}$ is expected. With an appropriate fit range, the influence of excited contributions at small t and the lattice artifacts around $t = T/2$ can be reduced. See section 5.5 for a further discussion of the mass extraction and finite size effects. Similar observations hold for the other lattice couplings $\beta \in \{4.5, 5.4\}$.

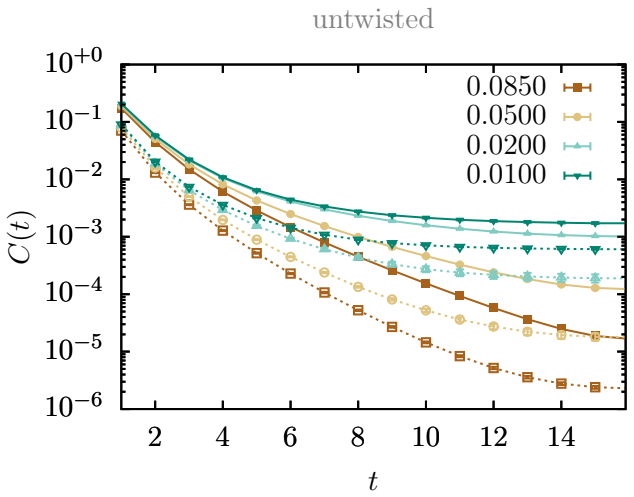

Figure E.1: Unnormalized correlators from untwisted simulations on the $16^3 \times 32$ lattice for our four mass parameters at $\beta = 5.0$, see top four rows of table G.5b. Solid/dotted lines with filled/open markers connect the data points of a-π resp. a-a to guide the eye. The labels indicate the distance $m - m_{\text{crit}}$ to the critical point. Errors are mostly smaller than the marker size.

APPENDIX F

Influence of the twist on the connected correlators

To investigate the effect of the mass twist α and the dependence on the distance $m - m_{\text{crit}}$ to the critical point, the effective masses and the corresponding raw correlators of a-π and a-a are plotted in figure F.1.

Without any twist, the effective mass of a-a seems to be lighter than the a-π. This is most probably a signal of finite size effects as discussed in section 5.5. With an appropriate choice of the fit range of the correlator, the influence of the finite size may be reduced. Furthermore, excited states lead to kinks in the effective masses. Approaching the critical point, the contribution of the excited states decreases and the length of the mass plateau increases.

At 90°-twist, the roles of a-π and a-a interchange and the adjoint pion is harder to determine. Comparing the effective mass results of figure F.1 in a diagonal manner (i.e. a-π at $\alpha = 0°$ with a-a at $\alpha = 90°$ and vice versa a-a at $\alpha = 0°$ with a-π at $\alpha = 90°$) reveals a small discrepancy. In the m_5-"direction" at $\alpha = 90°$ the effective mass of a-π grows faster with the distance from the critical point than in the untwisted m-"direction", see black arrows. Consequently, the kinks in the brown data of the a-π at 90° are a little bit more pronounced than in the corresponding a-a data at 0°.

For the optimal twist $\alpha = 45°$, all effective masses of a-π and a-a look identical. At this special choice long effective mass plateaus can be seen; without any kinks arising from excited contributions. This may originate from reduced discretization errors, see the discussion in section 4.3.

In summary, the mass-twisted Wilson Dirac operator improves the situation, because it leads to a mixing of the mesonic a-π and a-a. At optimal twist angle $\alpha = 45°$, the correlators of a-π and a-a have identical shapes and finite size effects are reduced.

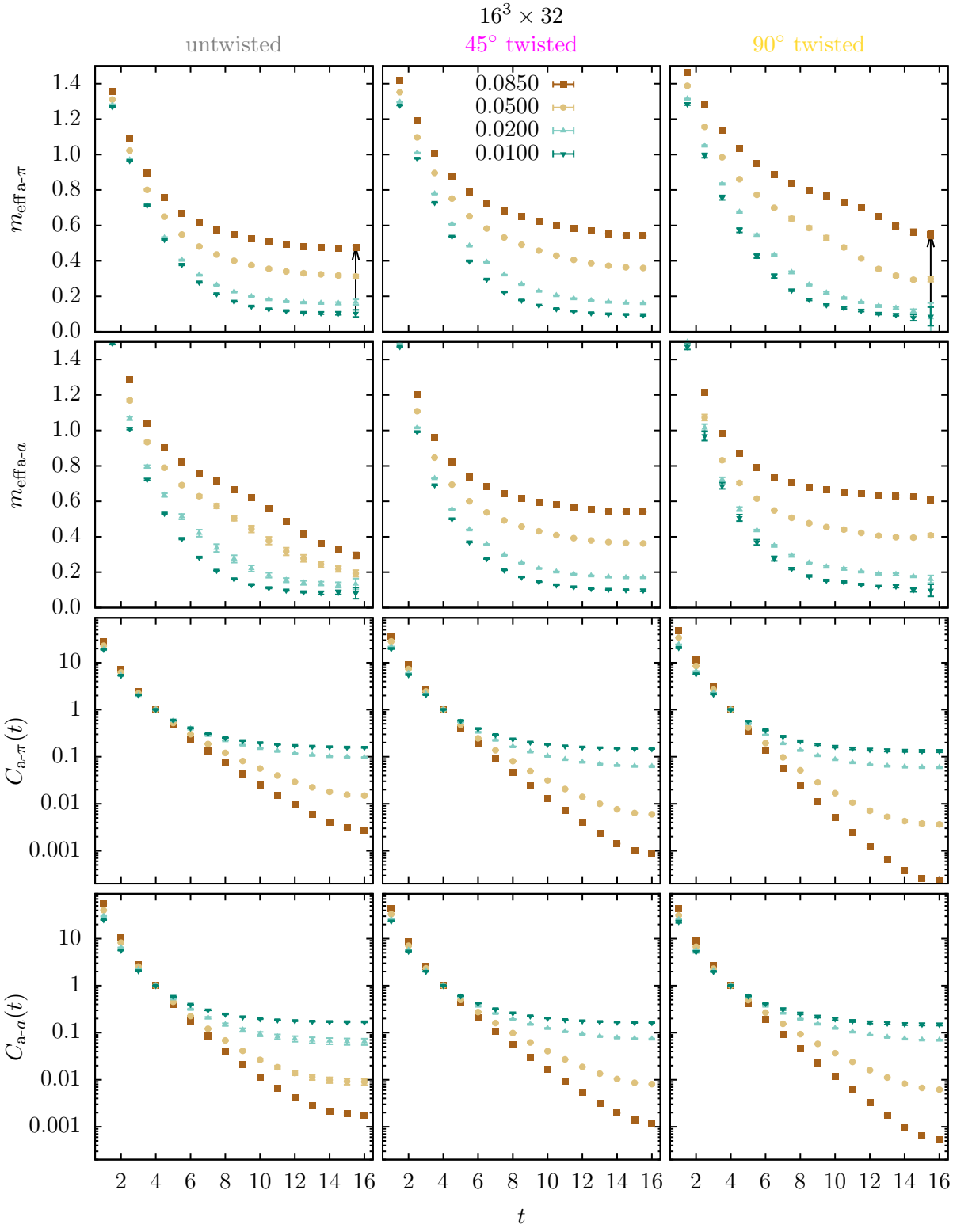

Figure F.1: From top to bottom: Effective mass of a-π / Effective mass of a-a / Correlator of a-π / Correlator of a-a on the $16^3 \times 32$ lattice for different mass parameters at lattice coupling $\beta = 5.0$. Left/Center/Right: Twist angle $\alpha = 0°, 45°, 90°$. The different colors indicate the distance $m - m_{\text{crit}}$ to the critical point, see legend. Most error bars are smaller than the marker size. All correlators are normalized at $t = 4$ to magnitude one. The black arrows are discussed in the text.

APPENDIX G

Overview of numerical data

G.1 Clover fermions

Table G.1 summarizes the parameter ranges of the broad scan in the (m, c_{SW})-plane. For a deeper analysis, several mass parameters for three different lattice couplings $\beta \in \{4.20, 4.59, 4.98\}$ on a $16^3 \times 32$ lattice were chosen, see table G.3. Additionally we performed a little study with 2-flavor QCD to compare with the literature. See table G.2 for the parameters and figure 5.6 for the clover values.

Table G.1: Parameter ranges for $\beta = 4.2$ on the $8^3 \times 16$ lattice. In total more than 80 combinations, on average 250 configurations per ensembles.

m	c_{SW}	#
$[-1.65, 0.00]$	$[0.0, 3.7]$	$[80, 2000]$

Table G.2: Parameters on the 8^4 lattice for 2-flavor QCD.

β	m	#
5.20	−0.322 40	1000
5.29	−0.332 16	400

Table G.3: Ensemble parameters on the $16^3 \times 32$ lattice. The clover values are calculated with the tree-level tadpole formula given in table 3.3.

(a) $\beta = 4.20$

m	c_{SW}	#
−0.550	2.2058326	360
−0.600	2.1916195	275
−0.625	2.1815920	50
−0.650	2.1732948	180
−0.675	2.1640857	50

(b) $\beta = 4.59$

m	c_{SW}	#
−0.525	2.0005457	50
−0.550	1.9968514	50
−0.575	1.9923141	50
−0.600	1.9852185	50
−0.625	1.9833238	50
−0.675	1.9743650	50

(c) $\beta = 4.98$

m	c_{SW}	#
−0.500	1.8607814	50
−0.525	1.8582152	50
−0.550	1.8497537	50
−0.575	1.8525834	50

Table G.4: Overview of the parameter sets. Three different lattice couplings β, two different lattice volumes $V = L^3 \times T$ and two different combinations of (r, r_5) are listed. For each setting, the mass parameter m_{crit} of the critical point as well as the ranges of m and m_5 are given.

ID	β	$L^3 \times T$	m_{crit}	m	m_5	r	r_5
(I)	4.5	$16^3 \times 32$	-1.22428	[-1.1443, -1.22428]	[0.0000, 0.0800]	1.0000	0.0000
(II)	5.0	$16^3 \times 32$	-1.0706	[-0.9856, -1.0706]	[0.0000, 0.0850]	1.0000	0.0000
(III)	5.0	$16^3 \times 32$	-0.7570	[-0.6156, -0.8277]	[-0.6156, -0.8277]	0.7071	0.7071
(IV)	5.4	$8^3 \times 16$	-0.967	[-1.4000, -0.6000]	[-0.4000, 0.4000]	1.0000	0.0000
(V)	5.4	$16^3 \times 32$	-0.9750	[-0.8450, -0.9750]	[0.0000, 0.1300]	1.0000	0.0000

Table G.5: Ensemble sizes of the sets (I), (II) & (V) on the $16^3 \times 32$ lattice.

(a) $\beta = 4.5$

m	m_5	#
-1.2143	0.0000	100
-1.2043	0.0000	100
-1.1743	0.0000	100
-1.1443	0.0000	100
-1.2172	0.0071	100
-1.2101	0.0141	100
-1.1889	0.0354	100
-1.1677	0.0566	100
-1.22428	0.0100	50
-1.22428	0.0200	50
-1.22428	0.0500	50
-1.22428	0.0800	50

(b) $\beta = 5.0$

m	m_5	#
-1.0606	0.0000	200
-1.0506	0.0000	200
-1.0206	0.0000	200
-0.9856	0.0000	200
-1.0635	0.0071	2110
-1.0565	0.0141	2370
-1.0352	0.0354	2705
-1.0105	0.0601	3100
-1.0706	0.0100	50
-1.0706	0.0200	100
-1.0706	0.0500	50
-1.0706	0.0850	50

(c) $\beta = 5.4$

m	m_5	#
-0.9650	0.0000	100
-0.9500	0.0000	100
-0.8950	0.0000	100
-0.8450	0.0000	100
-0.9679	0.0071	100
-0.9573	0.0177	100
-0.9184	0.0566	100
-0.8831	0.0919	100
-0.9750	0.0100	100
-0.9750	0.0250	100
-0.9750	0.0800	100
-0.9750	0.1300	100

G.2 Twisted-mass fermions

In table G.4, we summarize the parameters of the simulations with twisted Wilson Dirac operator. Mainly, three different lattice couplings $\beta \in \{4.5, 5.0, 5.4\}$ are used. Parameter set (IV) consists of approximately 500 combinations of m and m_5 with each ensemble containing around 200 configurations. Table G.5 contains the values of the bare mass m, the twisted mass m_5 as well as the number of configurations for the various lattice couplings β on the $16^3 \times 32$ lattice. There, we focused on the three "directions" $\alpha \in \{0°, 45°, 90°\}$. For high statistics we have chosen 45° mass twist at lattice coupling $\beta = 5.0$, see table G.5b.

APPENDIX H

Data analysis

Binning is used to estimate the autocorrelation and to reduce its influence [129]. Therefore the N_{conf} configurations $C_n[\mathcal{U}]$ are divided into N_{b} blocks of a chosen bin size s_{b}. Then for each block, the averages of all observables are calculated and considered as new random variables. If the block size is large enough, then the blocked variables can be considered as uncorrelated. On the blocked data a jackknife analysis is performed to estimate the statistical error [242, 243]. This method can be applied directly to observables like the plaquette as well as results obtained by a fit, for example the masses extracted from a correlator.

In the jackknife analysis, we first calculate the jackknife samples, where each sample consists of the observable evaluated on $N_{\text{b}} - 1$ bins; i.e. one bin is left out:

$$\bar{O}_i(x) = \frac{1}{N_{\text{b}} - 1} \frac{1}{s_{\text{b}}} \sum_{\substack{n=1 \\ n \notin \text{bin}(i)}}^{N_{\text{conf}}} O[C_n] \,, \quad i = 1, \ldots, N_{\text{b}} \,. \tag{H.1}$$

Afterwards the parameter $\bar{\theta}_i$ is fitted on each sample $\bar{O}_i(x)$ resulting in its mean

$$\hat{\theta} = \frac{1}{N_{\text{b}}} \sum_{i=1}^{N_{\text{b}}} \bar{\theta}_i \tag{H.2}$$

and the corresponding jackknife uncertainty

$$\sigma_{\hat{\theta}}^2 = \frac{N_{\text{b}} - 1}{N_{\text{b}}} \sum_{i=1}^{N_{\text{b}}} (\bar{\theta}_i - \hat{\theta})^2 \,. \tag{H.3}$$

The fit [244] on the individual jackknife samples is performed as an uncorrelated fit by minimizing $\chi_i^2 = \sum_x \frac{(f(\bar{\theta}_i, x) - \bar{O}_i(x))^2}{\sigma^2(x)}$ with $\sigma^2(x) = \frac{1}{N_{\text{b}}} \sum_i (\hat{O}(x) - \bar{O}_i(x))^2$. A correlated fit with $\chi_i^2 = \sum_{x,x'} \Big(f(\bar{\theta}_i, x) - \bar{O}_i(x)\Big)\Big(f(\bar{\theta}_i, x') - \bar{O}_i(x')\Big) C^{-1}(x, x')$ and the correlation matrix $C(x, x') = \frac{N_{\text{b}} - 1}{N_{\text{b}}} \sum_i \Big(\hat{O}(x) - \bar{O}_i(x)\Big)\Big(\hat{O}(x') - \bar{O}_i(x')\Big)$ can consider correlations between $O(x)$ and $O(x + 1)$. If the correlation matrix C has good condition number and can be inverted, a correlated fit should be preferred.

APPENDIX I

Benchmark tests

After the start of SuperMUC-NG, we performed some benchmark runs on the new system. In a simulation of $\mathcal{N} = 1$ SYM theory on a $12^3 \times 24$ lattice with 648 cores, a speed-up of approximately 35 % could be achieved compared to SuperMUC Phase 2. In the left panel of figure I.2, a strong scaling analysis with this lattice size is shown including the fraction spent in MPI communication. Figure I.1 shows the same data as speedup with respect to a single node. The included fit is inspired by Amdahl's law [245] and can be interpreted that 3% of the code is intrinsically on one node, i.e. serial or master-only. This portion remains even with infinitely many nodes. In the right panel of figure I.2 a weak scaling analysis is depicted, where we fixed the problem size to 256 lattice sites per core.

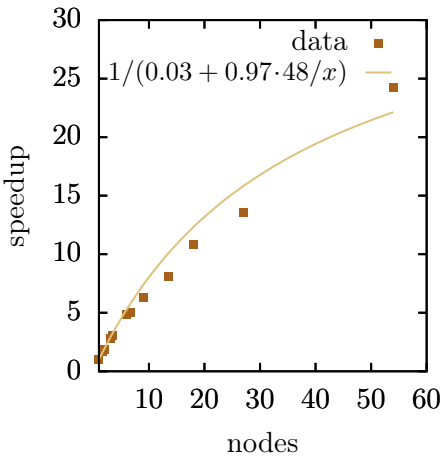

Figure I.1: Speedup in relation to one node with 48 cores.

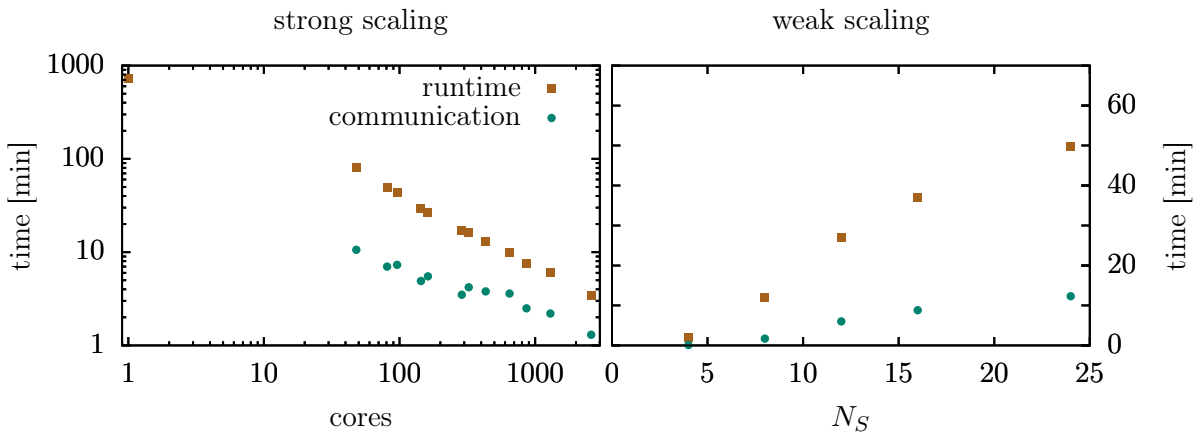

Figure I.2: Left: Strong scaling with a $12^3 \times 24$ lattice on SuperMUC-NG as average runtime (including MPI communication) per configuration in minutes vs. number of cores. Right: Weak scaling with a $N_S^3 \times 2N_S$ lattice and 256 lattice sites per core on SuperMUC-NG as average runtime per configuration in minutes vs. spatial lattice extent N_S.

References

[1] G. Aad et al. "Observation of a new particle in the search for the Standard Model Higgs boson with the ATLAS detector at the LHC." In: *Phys. Lett.* Vol. B716 (2012), pp. 1–29. DOI: 10.1016/j.physletb.2012.08.020. arXiv: 1207.7214 [hep-ex].

[2] S. Chatrchyan et al. "Observation of a New Boson at a Mass of 125 GeV with the CMS Experiment at the LHC." In: *Phys. Lett.* Vol. B716 (2012), pp. 30–61. DOI: 10.1016/j.physletb.2012.08.021. arXiv: 1207.7235 [hep-ex].

[3] M. Tanabashi et al. "Review of Particle Physics." In: *Phys. Rev.* Vol. D98, no. 3 (2018), p. 030001. DOI: 10.1103/PhysRevD.98.030001.

[4] K. G. Wilson. "The Renormalization Group and Strong Interactions." In: *Phys. Rev. D* vol. 3 (1971), p. 1818. DOI: 10.1103/PhysRevD.3.1818.

[5] L. Susskind. "Dynamics of Spontaneous Symmetry Breaking in the Weinberg-Salam Theory." In: *Phys. Rev. D* vol. 20 (1979), pp. 2619–2625. DOI: 10.1103/PhysRevD.20.2619.

[6] E. Witten. "Dynamical breaking of supersymmetry." In: *Nuclear Physics B* vol. 188, no. 3 (1981), pp. 513–554. ISSN: 0550-3213. DOI: 10.1016/0550-3213(81)90006-7. URL: http://www.sciencedirect.com/science/article/pii/0550321381900067 (visited on 11/15/2019).

[7] M. Veltman. "The Infrared - Ultraviolet Connection." In: *Acta Phys. Polon. B* vol. 12 (1981), p. 437.

[8] R. K. Kaul. "Gauge Hierarchy in a Supersymmetric Model." In: *Phys. Lett. B* vol. 109 (1982), pp. 19–24. DOI: 10.1016/0370-2693(82)90453-1.

[9] D. Clowe, A. Gonzalez, and M. Markevitch. "Weak lensing mass reconstruction of the interacting cluster 1E0657-558: Direct evidence for the existence of dark matter." In: *Astrophys. J.* Vol. 604 (2004), pp. 596–603. DOI: 10.1086/381970. arXiv: astro-ph/0312273.

[10] V. Springel et al. “Simulating the joint evolution of quasars, galaxies and their large-scale distribution.” In: *Nature* vol. 435 (2005), pp. 629–636. DOI: 10.1038/nature03597. arXiv: astro-ph/0504097.

[11] P. A. R. Ade et al. “Planck 2015 results. XIII. Cosmological parameters.” In: *Astron. Astrophys.* Vol. 594 (2016), A13. DOI: 10.1051/0004-6361/201525830. arXiv: 1502.01589 [astro-ph.CO].

[12] J. Ellis et al. “Supersymmetric relics from the big bang.” In: *Nuclear Physics B* vol. 238, no. 2 (1984), pp. 453–476. ISSN: 0550-3213. DOI: 10.1016/0550-3213(84)90461-9. URL: http://www.sciencedirect.com/science/article/pii/0550321384904619 (visited on 11/15/2019).

[13] S. Dimopoulos and H. Georgi. “Softly broken supersymmetry and SU(5).” In: *Nuclear Physics B* vol. 193, no. 1 (1981), pp. 150–162. ISSN: 0550-3213. DOI: 10.1016/0550-3213(81)90522-8. URL: http://www.sciencedirect.com/science/article/pii/0550321381905228 (visited on 11/15/2019).

[14] I. Aitchison. *Supersymmetry in Particle Physics. An Elementary Introduction.* Cambridge: Cambridge University Press, 2007. ISBN: 978-0-511-61925-0. DOI: 10.1017/CBO9780511619250.

[15] R. Peccei and H. R. Quinn. “CP Conservation in the Presence of Instantons.” In: *Phys. Rev. Lett.* Vol. 38 (1977), pp. 1440–1443. DOI: 10.1103/PhysRevLett.38.1440.

[16] M. A. Shifman, A. Vainshtein, and V. I. Zakharov. “Can Confinement Ensure Natural CP Invariance of Strong Interactions?” In: *Nucl. Phys. B* vol. 166 (1980), pp. 493–506. DOI: 10.1016/0550-3213(80)90209-6.

[17] H. P. Nilles and S. Raby. “Supersymmetry and the strong CP problem.” In: *Nucl. Phys. B* vol. 198 (1982), pp. 102–112. DOI: 10.1016/0550-3213(82)90547-8.

[18] R. Kuchimanchi. “Solution to the strong CP problem: Supersymmetry with parity.” In: *Phys. Rev. Lett.* Vol. 76 (1996), pp. 3486–3489. DOI: 10.1103/PhysRevLett.76.3486. arXiv: hep-ph/9511376.

[19] P. Dondi and H. Nicolai. “Lattice Supersymmetry.” In: *Nuovo Cim. A* vol. 41 (1977), p. 1. DOI: 10.1007/BF02730448.

[20] S. Catterall and S. Karamov. “Exact lattice supersymmetry: The Two-dimensional N=2 Wess-Zumino model.” In: *Phys. Rev. D* vol. 65 (2002), p. 094501. DOI: 10.1103/PhysRevD.65.094501. arXiv: hep-lat/0108024.

[21] M. Bonini and A. Feo. “Wess-Zumino model with exact supersymmetry on the lattice.” In: *JHEP* vol. 09 (2004), p. 011. DOI: 10.1088/1126-6708/2004/09/011. arXiv: hep-lat/0402034.

[22] G. Bergner et al. "Low-dimensional Supersymmetric Lattice Models." In: *Annals Phys.* Vol. 323 (2008), pp. 946–988. DOI: 10.1016/j.aop.2007.06.010. arXiv: 0705.2212 [hep-lat].

[23] T. Kastner et al. "Two-Dimensional Wess-Zumino Models at Intermediate Couplings." In: *Phys. Rev. D* vol. 78 (2008), p. 095001. DOI: 10.1103/PhysRevD.78.095001. arXiv: 0807.1905 [hep-lat].

[24] I. Kanamori, F. Sugino, and H. Suzuki. "Observing dynamical supersymmetry breaking with euclidean lattice simulations." In: *Prog. Theor. Phys.* Vol. 119 (2008), pp. 797–827. DOI: 10.1143/PTP.119.797. arXiv: 0711.2132 [hep-lat].

[25] K. Steinhauer and U. Wenger. "Loop formulation of supersymmetric Yang-Mills quantum mechanics." In: *JHEP* vol. 12 (2014), p. 044. DOI: 10.1007/JHEP12(2014)044. arXiv: 1410.0235 [hep-lat].

[26] K. Steinhauer and U. Wenger. "Spontaneous supersymmetry breaking in the 2D $\mathcal{N}$ =1 Wess-Zumino model." In: *Phys. Rev. Lett.* Vol. 113, no. 23 (2014), p. 231601. DOI: 10.1103/PhysRevLett.113.231601. arXiv: 1410.6665 [hep-lat].

[27] G. Koutsoumbas and I. Montvay. "Gluinos on the lattice: Quenched calculations." In: *Phys. Lett. B* vol. 398 (1997), pp. 130–134. DOI: 10.1016/S0370-2693(97)00178-0. arXiv: hep-lat/9612003.

[28] A. Donini et al. "Towards N=1 superYang-Mills on the lattice." In: *Nucl. Phys.* Vol. B523 (1998), pp. 529–552. DOI: 10.1016/S0550-3213(98)00166-7.

[29] A. Donini, E. Gabrielli, and M. Gavela. "Quenched supersymmetry." In: *Nucl. Phys. B* vol. 546 (1999), pp. 119–134. DOI: 10.1016/S0550-3213(99)00030-9. arXiv: hep-th/9810127.

[30] R. Kirchner et al. "Evidence for discrete chiral symmetry breaking in N=1 supersymmetric Yang-Mills theory." In: *Phys. Lett. B* vol. 446 (1999), pp. 209–215. DOI: 10.1016/S0370-2693(98)01523-8. arXiv: hep-lat/9810062.

[31] I. Campos et al. "Monte Carlo simulation of SU(2) Yang-Mills theory with light gluinos." In: *Eur. Phys. J. C* vol. 11 (1999), pp. 507–527. DOI: 10.1007/s100520050651. arXiv: hep-lat/9903014.

[32] G. Bergner et al. "The light bound states of supersymmetric SU(2) Yang-Mills theory." In: *JHEP* vol. 03 (2016), p. 080. DOI: 10.1007/JHEP03(2016)080. arXiv: 1512.07014 [hep-lat].

[33] S. Ali et al. "Variational analysis of low-lying states in supersymmetric Yang-Mills theory." In: *JHEP* vol. 04 (2019), p. 150. DOI: 10.1007/JHEP04(2019)150. arXiv: 1901.02416 [hep-lat].

[34] F. Farchioni et al. "The Supersymmetric Ward identities on the lattice." In: *Eur. Phys. J. C* vol. 23 (2002), pp. 719–734. DOI: 10.1007/s100520200898. arXiv: hep-lat/0111008.

[35] G. Bergner et al. "Phase structure of the $\mathcal{N} = 1$ supersymmetric Yang-Mills theory at finite temperature." In: *JHEP* vol. 11 (2014), p. 049. DOI: 10.1007/JHEP11(2014)049. arXiv: 1405.3180 [hep-lat].

[36] G. Bergner, C. López, and S. Piemonte. "Study of center and chiral symmetry realization in thermal $\mathcal{N} = 1$ super Yang-Mills theory using the gradient flow." In: *Phys. Rev.* Vol. D100, no. 7 (2019), p. 074501. DOI: 10.1103/PhysRevD.100.074501. arXiv: 1902.08469 [hep-lat].

[37] G. Bergner and S. Piemonte. "Compactified $\mathcal{N} = 1$ supersymmetric Yang-Mills theory on the lattice: continuity and the disappearance of the deconfinement transition." In: *JHEP* vol. 12 (2014), p. 133. DOI: 10.1007/JHEP12(2014)133. arXiv: 1410.3668 [hep-lat].

[38] F. Farchioni et al. "SUSY Ward identities in 1 loop perturbation theory." In: *Nucl. Phys. B Proc. Suppl.* Vol. 106 (2002). Ed. by M. Muller-Preussker et al., pp. 941–943. DOI: 10.1016/S0920-5632(01)01892-8. arXiv: hep-lat/0110113.

[39] G. Münster and H. Stüwe. "The mass of the adjoint pion in $\mathcal{N} = 1$ supersymmetric Yang-Mills theory." In: *JHEP* vol. 05 (2014), p. 034. DOI: 10.1007/JHEP05(2014)034. arXiv: 1402.6616 [hep-th].

[40] S. Musberg, G. Münster, and S. Piemonte. "Perturbative calculation of the clover term for Wilson fermions in any representation of the gauge group SU(N)." In: *JHEP* vol. 05 (2013), p. 143. DOI: 10.1007/JHEP05(2013)143. arXiv: 1304.5741 [hep-lat].

[41] S. Ali et al. "Numerical results for the lightest bound states in $\mathcal{N} = 1$ supersymmetric SU(3) Yang-Mills theory." In: *Phys. Rev. Lett.* Vol. 122, no. 22 (2019), p. 221601. DOI: 10.1103/PhysRevLett.122.221601. arXiv: 1902.11127 [hep-lat].

[42] S. Ali et al. "Analysis of Ward identities in supersymmetric Yang–Mills theory." In: *Eur. Phys. J. C* vol. 78, no. 5 (2018), p. 404. DOI: 10.1140/epjc/s10052-018-5887-9. arXiv: 1802.07067 [hep-lat].

[43] S. Ali et al. "Baryonic states in supersymmetric Yang-Mills theory." In: *PoS* vol. LATTICE2018 (2018), p. 207. DOI: 10.22323/1.334.0207. arXiv: 1811.02297 [hep-lat].

[44] S. Ali. "Ward Identities and Baryonic States in $\mathcal{N} = 1$ Supersymmetric Yang-Mills Theory on the Lattice." Dissertation. University Münster, 2019.

[45] H. Neuberger. "Vector-like gauge theories with almost massless fermions on the lattice." In: *Phys. Rev. D* vol. 57 (1998), pp. 5417–5433. DOI: 10.1103/PhysRevD.57.5417. arXiv: hep-lat/9710089.

[46] D. B. Kaplan and M. Schmaltz. "Supersymmetric Yang-Mills theories from domain wall fermions." In: *Chin. J. Phys.* Vol. 38 (2000). Ed. by T.-W. Chiu, pp. 543–550. arXiv: hep-lat/0002030.

[47] J. Giedt et al. "Lattice super-Yang-Mills using domain wall fermions in the chiral limit." In: *Phys. Rev. D* vol. 79 (2009), p. 025015. DOI: 10.1103/PhysRevD.79.025015. arXiv: 0810.5746 [hep-lat].

[48] M. G. Endres. "Dynamical simulation of N=1 supersymmetric Yang-Mills theory with domain wall fermions." In: *Phys. Rev. D* vol. 79 (2009), p. 094503. DOI: 10.1103/PhysRevD.79.094503. arXiv: 0902.4267 [hep-lat].

[49] S. Kim et al. "Lattice study of 4d N=1 super Yang-Mills theory with dynamical overlap gluino." In: *PoS* vol. LATTICE2011 (2011). Ed. by P. Vranas, p. 069. DOI: 10.22323/1.139.0069. arXiv: 1111.2180 [hep-lat].

[50] S. Ali et al. "Continuum limit of SU(3) $\mathcal{N} = 1$ supersymmetric Yang-Mills theory and supersymmetric gauge theories on the lattice." In: *37th International Symposium on Lattice Field Theory*. Jan. 2020. arXiv: 2001.09682 [hep-lat].

[51] G. T. Fleming, J. B. Kogut, and P. M. Vranas. "SuperYang-Mills on the lattice with domain wall fermions." In: *Phys. Rev. D* vol. 64 (2001), p. 034510. DOI: 10.1103/PhysRevD.64.034510. arXiv: hep-lat/0008009.

[52] V. A. Novikov et al. "Exact Gell-Mann-Low Function of Supersymmetric Yang-Mills Theories from Instanton Calculus." In: *Nucl. Phys.* Vol. B229 (1983), pp. 381–393. DOI: 10.1016/0550-3213(83)90338-3.

[53] A. Armoni, M. Shifman, and G. Veneziano. "SUSY relics in one flavor QCD from a new 1/N expansion." In: *Phys. Rev. Lett.* Vol. 91 (2003), p. 191601. DOI: 10.1103/PhysRevLett.91.191601. arXiv: hep-th/0307097 [hep-th].

[54] A. Armoni, M. Shifman, and G. Veneziano. "From Super-Yang-Mills theory to QCD: Planar equivalence and its implications." In: *Shifman, M. (ed.) et al.: From fields to strings, vol. 1 353-444* (2004). arXiv: hep-th/0403071 [hep-th]. URL: http://weblib.cern.ch/abstract?CERN-PH-TH-2004-022.

[55] D. August et al. "Mass spectrum of 2-dimensional $\mathcal{N} = (2, 2)$ super Yang-Mills theory on the lattice." In: *JHEP* vol. 01 (2019), p. 099. DOI: 10.1007/JHEP01(2019)099. arXiv: 1802.07797v2 [hep-lat].

[56] D. Kadoh and H. Suzuki. "SUSY WT identity in a lattice formulation of 2D = (2,2) SYM." In: *Phys. Lett. B* vol. 682 (2010), pp. 466–471. DOI: 10.1016/j.physletb.2009.11.028. arXiv: 0908.2274 [hep-lat].

[57] S. Catterall, R. G. Jha, and A. Joseph. "Nonperturbative study of dynamical SUSY breaking in N=(2,2) Yang-Mills theory." In: *Phys. Rev. D* vol. 97, no. 5 (2018), p. 054504. DOI: 10.1103/PhysRevD.97.054504. arXiv: 1801.00012 [hep-lat].

[58] M. Hanada and I. Kanamori. "Lattice study of two-dimensional N=(2,2) super Yang-Mills at large-N." In: *Phys. Rev. D* vol. 80 (2009), p. 065014. DOI: 10.1103/PhysRevD.80.065014. arXiv: 0907.4966 [hep-lat].

[59] S. Catterall, D. B. Kaplan, and M. Unsal. "Exact lattice supersymmetry." In: *Phys. Rept.* Vol. 484 (2009), pp. 71–130. DOI: 10.1016/j.physrep.2009.09.001. arXiv: 0903.4881 [hep-lat].

[60] A. Joseph. "Supersymmetric Yang-Mills theories with exact supersymmetry on the lattice." In: *Int. J. Mod. Phys. A* vol. 26 (2011), pp. 5057–5132. DOI: 10.1142/S0217751X11054863. arXiv: 1110.5983 [hep-lat].

[61] A. G. Cohen et al. "Supersymmetry on a Euclidean space-time lattice. 1. A Target theory with four supercharges." In: *JHEP* vol. 08 (2003), p. 024. DOI: 10.1088/1126-6708/2003/08/024. arXiv: hep-lat/0302017.

[62] F. Sugino. "SuperYang-Mills theories on the two-dimensional lattice with exact supersymmetry." In: *JHEP* vol. 03 (2004), p. 067. DOI: 10.1088/1126-6708/2004/03/067. arXiv: hep-lat/0401017.

[63] S. Catterall. "A Geometrical approach to N=2 super Yang-Mills theory on the two dimensional lattice." In: *JHEP* vol. 11 (2004), p. 006. DOI: 10.1088/1126-6708/2004/11/006. arXiv: hep-lat/0410052.

[64] A. D'Adda et al. "Exact extended supersymmetry on a lattice: Twisted N=2 super Yang-Mills in two dimensions." In: *Phys. Lett. B* vol. 633 (2006), pp. 645–652. DOI: 10.1016/j.physletb.2005.12.034. arXiv: hep-lat/0507029.

[65] M. Hanada et al. "O(a) Improvement of 2D N=(2,2) Lattice SYM Theory." In: *Nucl. Phys. B* vol. 929 (2018), pp. 266–297. DOI: 10.1016/j.nuclphysb.2018.02.008. arXiv: 1711.02319 [hep-lat].

[66] F. Sugino. "Lattice Formulation of Two-Dimensional N=(2,2) SQCD with Exact Supersymmetry." In: *Nucl. Phys. B* vol. 808 (2009), pp. 292–325. DOI: 10.1016/j.nuclphysb.2008.09.035. arXiv: 0807.2683 [hep-lat].

[67] S. Catterall and A. Veernala. "Spontaneous supersymmetry breaking in two dimensional lattice super QCD." In: *JHEP* vol. 10 (2015), p. 013. DOI: 10.1007/JHEP10(2015)013. arXiv: 1505.00467 [hep-lat].

[68] A. Joseph. "Two-dimensional $\mathcal{N} = (2, 2)$ lattice gauge theories with matter in higher representations." In: *JHEP* vol. 07 (2014), p. 067. DOI: 10.1007/JHEP07(2014)067. arXiv: 1403.4390 [hep-lat].

[69] D. B. Kaplan, E. Katz, and M. Unsal. "Supersymmetry on a spatial lattice." In: *JHEP* vol. 05 (2003), p. 037. DOI: 10.1088/1126-6708/2003/05/037. arXiv: hep-lat/0206019.

[70] M. Hanada. "A proposal of a fine tuning free formulation of 4d N = 4 super Yang-Mills." In: *JHEP* vol. 11 (2010), p. 112. DOI: 10.1007/JHEP11(2010)112. arXiv: 1009.0901 [hep-lat].

[71] S. Catterall, J. Giedt, and A. Joseph. "Twisted supersymmetries in lattice $\mathcal{N} = 4$ super Yang-Mills theory." In: *JHEP* vol. 10 (2013), p. 166. DOI: 10.1007/JHEP10(2013)166. arXiv: 1306.3891 [hep-lat].

[72] D. Schaich et al. "Latest results from lattice N=4 supersymmetric Yang–Mills." In: *PoS* vol. LATTICE2016 (2016), p. 221. DOI: 10.22323/1.256.0221. arXiv: 1611.06561 [hep-lat].

[73] S. Catterall, J. Giedt, and G. c. Toga. "Lattice N=4 super Yang-Mills at Strong Coupling." In: (Sept. 2020). arXiv: 2009.07334 [hep-lat].

[74] A. Joseph. "Lattice formulation of N=2* Yang-Mills." In: *Phys. Rev. D* vol. 97, no. 9 (2018), p. 094508. DOI: 10.1103/PhysRevD.97.094508. arXiv: 1710.10172 [hep-lat].

[75] D. B. Kaplan and M. Unsal. "A Euclidean lattice construction of supersymmetric Yang-Mills theories with sixteen supercharges." In: *JHEP* vol. 09 (2005), p. 042. DOI: 10.1088/1126-6708/2005/09/042. arXiv: hep-lat/0503039.

[76] E. Giguère and D. Kadoh. "Restoration of supersymmetry in two-dimensional SYM with sixteen supercharges on the lattice." In: *JHEP* vol. 05 (2015), p. 082. DOI: 10.1007/JHEP05(2015)082. arXiv: 1503.04416 [hep-lat].

[77] O. Morikawa and H. Suzuki. "Numerical study of the $\mathcal{N} = 2$ Landau–Ginzburg model." In: *PTEP* vol. 2018, no. 8 (2018), 083B05. DOI: 10.1093/ptep/pty088. arXiv: 1805.10735 [hep-lat].

[78] R. Flore et al. "Supersymmetric Nonlinear O(3) Sigma Model on the Lattice." In: *JHEP* vol. 11 (2012), p. 159. DOI: 10.1007/JHEP11(2012)159. arXiv: 1207.6947 [hep-lat].

[79] K. Steinhauer and U. Wenger. "Loop formulation of the supersymmetric nonlinear O(N) sigma model." In: *PoS* vol. LATTICE2013 (2014), p. 092. DOI: 10.22323/1.187.0092. arXiv: 1311.5403 [hep-lat].

[80] S. Catterall, A. Joseph, and T. Wiseman. "Thermal phases of D1-branes on a circle from lattice super Yang-Mills." In: *JHEP* vol. 12 (2010), p. 022. DOI: 10.1007/JHEP12(2010)022. arXiv: 1008.4964 [hep-th].

[81] A. Joseph. "Review of Lattice Supersymmetry and Gauge-Gravity Duality." In: *Int. J. Mod. Phys. A* vol. 30, no. 27 (2015), p. 1530054. DOI: 10.1142/S0217751X15300549. arXiv: 1509.01440 [hep-th].

[82] R. Frezzotti et al. "Lattice QCD with a chirally twisted mass term." In: *JHEP* vol. 08 (2001), p. 058. arXiv: hep-lat/0101001.

[83] R. Frezzotti and G. Rossi. "Chirally improving Wilson fermions. 1. O(a) improvement." In: *JHEP* vol. 08 (2004), p. 007. DOI: 10.1088/1126-6708/2004/08/007. arXiv: hep-lat/0306014.

[84] M. Lüscher and P. Weisz. "On-Shell Improved Lattice Gauge Theories." In: *Commun. Math. Phys.* Vol. 97 (1985). [Erratum: Commun.Math.Phys. 98, 433 (1985)], p. 59. DOI: 10.1007/BF01206178.

[85] B. Sheikholeslami and R. Wohlert. "Improved Continuum Limit Lattice Action for QCD with Wilson Fermions." In: *Nucl. Phys.* Vol. B259 (1985), p. 572. DOI: 10.1016/0550-3213(85)90002-1.

[86] R. Wohlert. "Improved continuum limit lattice action for quarks." In: *DESY-87-069* (1987).

[87] M. Steinhauser et al. "Spectroscopy of four-dimensional $\mathcal{N} = 1$ supersymmetric SU(3) Yang-Mills theory." In: *EPJ Web Conf.* Vol. 175 (2018). Ed. by M. Della Morte et al., p. 08022. DOI: 10.1051/epjconf/201817508022. arXiv: 1711.05086 [hep-lat].

[88] M. Steinhauser et al. "$\mathcal{N} = 1$ Supersymmetric $SU(3)$ Gauge Theory – Pure Gauge sector with a twist." In: *PoS* vol. LATTICE2018 (2018), p. 211. DOI: 10.22323/1.334.0211. arXiv: 1811.01785 [hep-lat].

[89] M. Steinhauser et al. "$\mathcal{N} = 1$ Supersymmetric SU(3) Gauge Theory with a Twist." In: *37th International Symposium on Lattice Field Theory*. 2019. arXiv: 1912.09979 [hep-lat].

[90] M. Steinhauser et al. "$\mathcal{N} = 1$ Super-Yang-Mills theory on the lattice with twisted mass fermions." In: (Oct. 2020). arXiv: 2010.00946 [hep-lat].

[91] C.-N. Yang and R. L. Mills. "Conservation of Isotopic Spin and Isotopic Gauge Invariance." In: *Phys. Rev.* Vol. 96 (1954). Ed. by J.-P. Hsu and D. Fine, pp. 191–195. DOI: 10.1103/PhysRev.96.191.

[92] S. Coleman and J. Mandula. "All Possible Symmetries of the S Matrix." In: *Phys. Rev.* Vol. 159 (5 July 1967), pp. 1251–1256. DOI: 10.1103/PhysRev.159.1251. URL: http://link.aps.org/doi/10.1103/PhysRev.159.1251.

[93] Yu. A. Golfand and E. P. Likhtman. "Extension of the Algebra of Poincare Group Generators and Violation of p Invariance." In: *JETP Lett.* Vol. 13 (1971). [Pisma Zh. Eksp. Teor. Fiz.13,452(1971)], pp. 323–326.

[94] R. Haag, J. T. Lopuszanski, and M. Sohnius. "All Possible Generators of Supersymmetries of the S-Matrix." In: *Nucl. Phys.* Vol. B88 (1975), p. 257. DOI: 10.1016/0550-3213(75)90279-5.

[95] M. Sohnius. "Introducing Supersymmetry." In: *Phys. Rept.* Vol. 128 (1985), pp. 39–204. DOI: 10.1016/0370-1573(85)90023-7.

[96] L. O'Raifeartaigh. "Mass differences and Lie Algebras of Finite Order." In: *Phys. Rev. Lett.* Vol. 14, no. 14 (1965), p. 575. DOI: 10.1103/PhysRevLett.14.575.

[97] S. Weinberg. "The Cosmological Constant Problem." In: *Rev. Mod. Phys.* Vol. 61 (1989), pp. 1–23. DOI: 10.1103/RevModPhys.61.1.

[98] E. Witten. "Constraints on Supersymmetry Breaking." In: *Nucl. Phys.* Vol. B202 (1982), p. 253. DOI: 10.1016/0550-3213(82)90071-2.

[99] N. Seiberg. "Naturalness versus supersymmetric nonrenormalization theorems." In: *Phys. Lett.* Vol. B318 (1993), pp. 469–475. DOI: 10.1016/0370-2693(93)91541-T. arXiv: hep-ph/9309335 [hep-ph].

[100] M. Dine. *Supersymmetry and String Theory: Beyond the Standard Model*. 2nd ed. Cambridge University Press, 2016. DOI: 10.1017/CBO9781107261426.

[101] I. Affleck, M. Dine, and N. Seiberg. "Dynamical Supersymmetry Breaking in Four-Dimensions and Its Phenomenological Implications." In: *Nucl. Phys. B* vol. 256 (1985), pp. 557–599. DOI: 10.1016/0550-3213(85)90408-0.

[102] S. P. Martin. "A Supersymmetry primer." In: *Adv. Ser. Direct. High Energy Phys.* Vol. 21 (2010). Ed. by G. L. Kane, pp. 1–153. DOI: 10.1142/9789812839657_0001. arXiv: hep-ph/9709356.

[103] D. Amati, G. Rossi, and G. Veneziano. "Instanton Effects in Supersymmetric Gauge Theories." In: *Nucl. Phys. B* vol. 249 (1985), pp. 1–41. DOI: 10.1016/0550-3213(85)90037-9.

[104] M. A. Shifman and A. Vainshtein. "On Gluino Condensation in Supersymmetric Gauge Theories. SU(N) and O(N) Groups." In: *Sov. Phys. JETP* vol. 66 (1987), p. 1100. DOI: 10.1016/0550-3213(88)90680-3.

[105] G. Veneziano and S. Yankielowicz. "An effective Lagrangian for the pure N = 1 supersymmetric Yang-Mills theory." In: *Physics Letters B* vol. 113, no. 3 (1982), pp. 231 –236. ISSN: 0370-2693. DOI: http://dx.doi.org/10.1016/0370-2693(82)90828-0. URL: http://www.sciencedirect.com/science/article/pii/0370269382908280.

[106] S. Weinberg. *The Quantum theory of fields. Vol. 1: Foundations*. Cambridge University Press, June 2005. ISBN: 978-0-521-67053-1, 978-0-511-25204-4.

[107] G. R. Farrar, G. Gabadadze, and M. Schwetz. "On the effective action of N=1 supersymmetric Yang-Mills theory." In: *Phys. Rev.* Vol. D58 (1998), p. 015009. DOI: 10.1103/PhysRevD.58.015009. arXiv: hep-th/9711166 [hep-th].

[108] G. R. Farrar, G. Gabadadze, and M. Schwetz. "The spectrum of softly broken N=1 supersymmetric Yang-Mills theory." In: *Phys. Rev.* Vol. D60 (1999), p. 035002. DOI: 10.1103/PhysRevD.60.035002. arXiv: hep-th/9806204 [hep-th].

[109] G. B. West. "Theorem on the lightest glueball state." In: *Phys. Rev. Lett.* Vol. 77 (1996), pp. 2622–2625. DOI: 10.1103/PhysRevLett.77.2622. arXiv: hep-ph/9603316.

[110] A. Feo, P. Merlatti, and F. Sannino. "Information on the super Yang-Mills spectrum." In: *Phys. Rev. D* vol. 70 (2004), p. 096004. DOI: 10.1103/PhysRevD.70.096004. arXiv: hep-th/0408214.

[111] T. Kaluza. "Zum Unitätsproblem der Physik." In: *Int. J. Mod. Phys. D* vol. 27, no. 14 (2018), p. 1870001. DOI: 10.1142/S0218271818700017. arXiv: 1803.08616 [physics.hist-ph].

[112] O. Klein. "Quantentheorie und fünfdimensionale Relativitätstheorie." In: *Z. Phys.* Vol. 37 (1926). Ed. by J. Taylor, pp. 895–906. DOI: 10.1007/BF01397481.

[113] P. C. West. *Introduction to supersymmetry and supergravity*. 1990.

[114] D. August. "Two-dimensional $\mathcal{N} = (2, 2)$ super Yang-Mills theory on the lattice." Dissertation. Friedrich Schiller University Jena, 2019.

[115] A. M. Jaffe. "Euclidean Quantum Field Theory." In: *Nucl. Phys.* Vol. B254 (1985), pp. 31–43. DOI: 10.1016/0550-3213(85)90208-1.

[116] R. Jost. *The general theory of quantized fields*. Vol. 4. American Mathematical Society, 1965.

[117] R. F. Streater and A. S. Wightman. *PCT, spin and statistics, and all that*. Vol. 52. Princeton University Press, 2000.

[118] M. Lüscher. "Construction of a Selfadjoint, Strictly Positive Transfer Matrix for Euclidean Lattice Gauge Theories." In: *Commun. Math. Phys.* Vol. 54 (1977), p. 283. DOI: 10.1007/BF01614090.

[119] K Osterwalder and E Seiler. "Gauge field theories on a lattice." In: *Annals of Physics* vol. 110, no. 2 (Feb. 1, 1978), pp. 440–471. ISSN: 0003-4916. DOI: 10.1016/0003-4916(78)90039-8. URL: http://www.sciencedirect.com/science/article/pii/0003491678900398 (visited on 01/13/2020).

[120] P. Menotti and A. Pelissetto. "General proof of Osterwalder-Schrader positivity for the Wilson action." In: *Communications in Mathematical Physics* vol. 113, no. 3 (Sept. 1, 1987), pp. 369–373. ISSN: 1432-0916. DOI: 10.1007/BF01221251. URL: https://doi.org/10.1007/BF01221251 (visited on 12/20/2019).

[121] K. Symanzik. "A Modified Model of Euclidean Quantum Field Theory." In: *MATSCIENCE-35* (1964).

[122] K. Symanzik. "Euclidean Quantum Field Theory. I. Equations for a Scalar Model." In: *Journal of Mathematical Physics* vol. 7, no. 3 (1966), pp. 510–525. DOI: 10.1063/1.1704960. eprint: https://doi.org/10.1063/1.1704960. URL: https://doi.org/10.1063/1.1704960.

[123] K. Osterwalder and R. Schrader. "Axioms for Euclidean Green's Functions. 2." In: *Commun. Math. Phys.* Vol. 42 (1975), p. 281. DOI: 10.1007/BF01608978.

[124] I. Montvay and G. Münster. *Quantum fields on a lattice*. Cambridge Monographs on Mathematical Physics. Cambridge University Press, 1997. ISBN: 9780521599177, 9780511879197. DOI: 10.1017/CBO9780511470783. URL: http://www.cambridge.org/uk/catalogue/catalogue.asp?isbn=0521404320.

[125] T. Kugo and P. K. Townsend. "Supersymmetry and the Division Algebras." In: *Nucl. Phys. B* vol. 221 (1983), pp. 357–380. DOI: 10.1016/0550-3213(83)90584-9.

[126] H. Nicolai. "A Possible constructive approach to (super-ϕ^3) in four-dimensions. 1. Euclidean formulation of the model." In: *Nucl. Phys. B* vol. 140 (1978), pp. 294–300. DOI: 10.1016/0550-3213(78)90537-0.

[127] P. van Nieuwenhuizen and A. Waldron. "On Euclidean spinors and Wick rotations." In: *Phys. Lett. B* vol. 389 (1996), pp. 29–36. DOI: 10.1016/S0370-2693(96)01251-8. arXiv: hep-th/9608174.

[128] I. Montvay. "Majorana fermions on the lattice." In: Aug. 2001. arXiv: hep-lat/0108011.

[129] C. Gattringer and C. B. Lang. *Quantum chromodynamics on the lattice*. Vol. 788. Lect. Notes Phys. 2010, pp. 1–343. DOI: 10.1007/978-3-642-01850-3.

[130] T. DeGrand and C. E. Detar. *Lattice methods for quantum chromodynamics*. 2006.

[131] F. Knechtli, M. Günther, and M. Peardon. *Lattice Quantum Chromodynamics: Practical Essentials*. SpringerBriefs in Physics. Springer, 2017. ISBN: 978-94-024-0997-0, 978-94-024-0999-4. DOI: 10.1007/978-94-024-0999-4.

[132] W. Hastings. "Monte Carlo Sampling Methods Using Markov Chains and Their Applications." In: *Biometrika* vol. 57 (1970), pp. 97–109. DOI: 10.1093/biomet/57.1.97.

[133] T. Müller-Gronbach, E. Novak, and K. Ritter. *Monte Carlo-Algorithmen*. Springer, 2012. ISBN: 978-3-540-89141-3. DOI: 10.1007/978-3-540-89141-3.

[134] M. Karowski, R. Schrader, and H. Thun. "Monte Carlo Simulations for Quantum Field Theories Involving Fermions." In: *Commun. Math. Phys.* Vol. 97 (1985), p. 5. DOI: 10.1007/BF01206176.

[135] I. Montvay. "Simulation of Staggered Fermions by Polymer Averaging." In: *Phys. Lett. B* vol. 227 (1989), pp. 260–265. DOI: 10.1016/S0370-2693(89)80033-4.

[136] A. Wipf. "Statistical approach to quantum field theory." In: *Lect. Notes Phys.* Vol. 864 (2013), pp.1–390. DOI: 10.1007/978-3-642-33105-3.

[137] B. Wellegehausen. "Phase diagrams of exceptional and supersymmetric lattice gauge theories." Dissertation. Friedrich Schiller University Jena, 2012.

[138] M. Troyer and U.-J. Wiese. "Computational complexity and fundamental limitations to fermionic quantum Monte Carlo simulations." In: *Phys. Rev. Lett.* Vol. 94 (2005), p. 170201. DOI: 10.1103/PhysRevLett.94.170201. arXiv: cond-mat/0408370 [cond-mat].

[139] D. H. Weingarten and D. N. Petcher. "Monte Carlo Integration for Lattice Gauge Theories with Fermions." In: *Phys. Lett.* Vol. B99 (1981), pp. 333–338. DOI: 10.1016/0370-2693(81)90112-X.

[140] G. Wick. "The Evaluation of the Collision Matrix." In: *Phys. Rev.* Vol. 80 (1950), pp. 268–272. DOI: 10.1103/PhysRev.80.268.

[141] S. Duane et al. "Hybrid Monte Carlo." In: *Phys. Lett.* Vol. B195 (1987), pp. 216–222. DOI: 10.1016/0370-2693(87)91197-X.

[142] A. D. Kennedy, I. Horvath, and S. Sint. "A new exact method for dynamical fermion computations with nonlocal actions." In: *Nucl. Phys. Proc. Suppl.* Vol. 73 (1999), pp. 834–836. DOI: 10.1016/S0920-5632(99)85217-7. arXiv: hep-lat/9809092 [hep-lat].

[143] D. J. Callaway and A. Rahman. "The Microcanonical Ensemble: A New Formulation of Lattice Gauge Theory." In: *Phys. Rev. Lett.* Vol. 49 (1982), p. 613. DOI: 10.1103/PhysRevLett.49.613.

[144] D. J. Callaway and A. Rahman. "Lattice Gauge Theory in Microcanonical Ensemble." In: *Phys. Rev. D* vol. 28 (1983), p. 1506. DOI: 10.1103/PhysRevD.28.1506.

[145] N. Metropolis et al. "Equation of state calculations by fast computing machines." In: *J. Chem. Phys.* Vol. 21 (1953), pp. 1087–1092. DOI: 10.1063/1.1699114.

[146] A. D. Kennedy. "Algorithms for dynamical fermions." In: (2006). arXiv: hep-lat/0607038 [hep-lat].

[147] R. D. Ruth. "A Canonical Integration Technique." In: *IEEE Transactions on Nuclear Science* vol. 30 (4 Aug. 1983), pp. 2669 –2671.

[148] J. C. Sexton and D. H. Weingarten. "Hamiltonian evolution for the hybrid Monte Carlo algorithm." In: *Nucl. Phys.* Vol. B380 (1992), pp. 665–677. DOI: 10.1016/0550-3213(92)90263-B.

[149] C. Urbach et al. "HMC algorithm with multiple time scale integration and mass preconditioning." In: *Comput. Phys. Commun.* Vol. 174 (2006), pp. 87–98. DOI: 10.1016/j.cpc.2005.08.006. arXiv: hep-lat/0506011 [hep-lat].

[150] H. Yoshida. "Construction of higher order symplectic integrators." In: *Phys. Lett. A* vol. 150 (1990), pp. 262–268. DOI: 10.1016/0375-9601(90)90092-3.

[151] E. Y. Remez. "Sur le calcul effectif des polynômes d'approximation de Tschebyscheff." In: *C. P. Paris* (1934), pp. 337–340.

[152] W. Fraser. "A Survey of Methods of Computing Minimax and Near-Minimax Polynomial Approximations for Functions of a Single Independent Variable." In: *J. ACM* vol. 12, no. 3 (July 1965), pp. 295–314. ISSN: 0004-5411. DOI: 10.1145/321281.321282. URL: http://doi.acm.org/10.1145/321281.321282.

[153] M. R. Hestenes and E. Stiefel. "Methods of conjugate gradients for solving linear systems." In: *Journal of research of the National Bureau of Standards* vol. 49 (1952), pp. 409–436. DOI: 10.6028/jres.049.044.

[154] B. Jegerlehner. "Krylov space solvers for shifted linear systems." In: *ArXiv High Energy Physics - Lattice e-prints* (1996). arXiv: hep-lat/9612014 [hep-lat].

[155] T. A. DeGrand. "A Conditioning Technique for Matrix Inversion for Wilson Fermions." In: *Comput. Phys. Commun.* Vol. 52 (1988), pp. 161–164. DOI: 10.1016/0010-4655(88)90180-4.

[156] R. Gupta et al. “QCD With Dynamical Wilson Fermions.” In: *Phys. Rev. D* vol. 40 (1989), p. 2072. DOI: 10.1103/PhysRevD.40.2072.

[157] T. A. DeGrand and P. Rossi. “Conditioning Techniques for Dynamical Fermions.” In: *Comput. Phys. Commun.* Vol. 60 (1990), pp. 211–214. DOI: 10.1016/0010-4655(90)90006-M.

[158] C. Alexandrou et al. “Adaptive Aggregation-based Domain Decomposition Multigrid for Twisted Mass Fermions.” In: *Phys. Rev.* Vol. D94, no. 11 (2016), p. 114509. DOI: 10.1103/PhysRevD.94.114509. arXiv: 1610.02370 [hep-lat].

[159] S. Bacchio. “DDalphaAMG library including twisted mass fermions.” In: *Github* (2018). URL: https://github.com/sbacchio/DDalphaAMG.

[160] A. Frommer et al. “Adaptive Aggregation Based Domain Decomposition Multigrid for the Lattice Wilson Dirac Operator.” In: *SIAM J. Sci. Comput.* Vol. 36 (2014), A1581–A1608. DOI: 10.1137/130919507. arXiv: 1303.1377 [hep-lat].

[161] H. A. Schwarz. *Gesammelte mathematische Abhandlungen*. Vol. 2. Berlin: Springer Verlag, 1890.

[162] M. Lüscher. “Lattice QCD and the Schwarz alternating procedure.” In: *JHEP* vol. 05 (2003), p. 052. DOI: 10.1088/1126-6708/2003/05/052. arXiv: hep-lat/0304007.

[163] M. Lüscher. “Local coherence and deflation of the low quark modes in lattice QCD.” In: *JHEP* vol. 07 (2007), p. 081. DOI: 10.1088/1126-6708/2007/07/081. arXiv: 0706.2298 [hep-lat].

[164] A. Frommer et al. “An adaptive aggregation based domain decomposition multilevel method for the lattice wilson dirac operator: multilevel results.” In: (2013). arXiv: 1307.6101 [hep-lat].

[165] S. Heybrock et al. “Adaptive algebraic multigrid on SIMD architectures.” In: *PoS* vol. LATTICE2015 (2016), p. 036. DOI: 10.22323/1.251.0036. arXiv: 1512.04506 [physics.comp-ph].

[166] M. Lüscher. “Schwarz-preconditioned HMC algorithm for two-flavour lattice QCD.” In: *Comput. Phys. Commun.* Vol. 165 (2005), pp. 199–220. DOI: 10.1016/j.cpc.2004.10.004. arXiv: hep-lat/0409106.

[167] C. Alexandrou, S. Bacchio, and J. Finkenrath. “Multigrid approach in shifted linear systems for the non-degenerated twisted mass operator.” In: *Comput. Phys. Commun.* Vol. 236 (2019), pp. 51–64. DOI: 10.1016/j.cpc.2018.10.013. arXiv: 1805.09584 [hep-lat].

[168] A. Frommer et al. “A multigrid accelerated eigensolver for the Hermitian Wilson-Dirac operator in lattice QCD.” In: (Apr. 2020). arXiv: 2004.08146 [hep-lat].

[169] K. Bitar et al. “The QCD Finite Temperature Transition and Hybrid Monte Carlo.” In: *Nucl. Phys.* Vol. B313 (1989), pp. 348–376. DOI: 10.1016/0550-3213(89)90323-4.

[170] S.-J. Dong and K.-F. Liu. “Stochastic estimation with Z(2) noise.” In: *Phys. Lett.* Vol. B328 (1994), pp. 130–136. DOI: 10.1016/0370-2693(94)90440-5. arXiv: hep-lat/9308015 [hep-lat].

[171] C. Morningstar and M. J. Peardon. “Analytic smearing of SU(3) link variables in lattice QCD.” In: *Phys. Rev. D* vol. 69 (2004), p. 054501. DOI: 10.1103/PhysRevD.69.054501. arXiv: hep-lat/0311018.

[172] M. Albanese et al. “Glueball Masses and String Tension in Lattice QCD.” In: *Phys. Lett. B* vol. 192 (1987), pp. 163–169. DOI: 10.1016/0370-2693(87)91160-9.

[173] A. Hasenfratz and F. Knechtli. “Flavor symmetry and the static potential with hypercubic blocking.” In: *Phys. Rev. D* vol. 64 (2001), p. 034504. DOI: 10.1103/PhysRevD.64.034504. arXiv: hep-lat/0103029.

[174] S. Gusken et al. “Nonsinglet Axial Vector Couplings of the Baryon Octet in Lattice QCD.” In: *Phys. Lett. B* vol. 227 (1989), pp. 266–269. DOI: 10.1016/S0370-2693(89)80034-6.

[175] G. S. Bali et al. “The moment $\langle x \rangle_{u-d}$ of the nucleon from $N_f = 2$ lattice QCD down to nearly physical quark masses.” In: *Phys. Rev. D* vol. 90, no. 7 (2014), p. 074510. DOI: 10.1103/PhysRevD.90.074510. arXiv: 1408.6850 [hep-lat].

[176] S. Gusken. “A Study of smearing techniques for hadron correlation functions.” In: *Nucl. Phys. B Proc. Suppl.* Vol. 17 (1990). Ed. by N. Cabibbo et al., pp. 361–364. DOI: 10.1016/0920-5632(90)90273-W.

[177] C. Allton et al. “Gauge invariant smearing and matrix correlators using Wilson fermions at Beta = 6.2.” In: *Phys. Rev. D* vol. 47 (1993), pp. 5128–5137. DOI: 10.1103/PhysRevD.47.5128. arXiv: hep-lat/9303009.

[178] C. Best et al. “Pion and rho structure functions from lattice QCD.” In: *Phys. Rev. D* vol. 56 (1997), pp. 2743–2754. DOI: 10.1103/PhysRevD.56.2743. arXiv: hep-lat/9703014.

[179] S. Collins. “Gauge invariant smearing and the extraction of excited state masses using Wilson fermions at Beta = 6.2.” In: *The International Symposium on Lattice Field Theory: Lattice 92*. Sept. 1992. arXiv: hep-lat/9211039.

[180] A. Feo. “Supersymmetry on the lattice: Where do predictions and results stand?” In: *Light-Cone Workshop: Hadrons and Beyond (LC 03)*. Nov. 2003. arXiv: hep-lat/0311037.

[181] G. Curci and G. Veneziano. "Supersymmetry and the Lattice: A Reconciliation?" In: *Nucl. Phys.* Vol. B292 (1987), pp. 555–572. DOI: 10.1016/0550-3213(87)90660-2.

[182] M. Gell-Mann, R. Oakes, and B. Renner. "Behavior of current divergences under SU(3) x SU(3)." In: *Phys. Rev.* Vol. 175 (1968), pp. 2195–2199. DOI: 10.1103/PhysRev.175.2195.

[183] K. G. Wilson. "Confinement of Quarks." In: (Feb. 1974). Ed. by J. Taylor, pp. 45–59. DOI: 10.1103/PhysRevD.10.2445.

[184] K. Symanzik. "Continuum Limit and Improved Action in Lattice Theories. 1. Principles and ϕ^4 Theory." In: *Nucl. Phys.* Vol. B226 (1983), pp. 187–204. DOI: 10.1016/0550-3213(83)90468-6.

[185] K. Symanzik. "Continuum Limit and Improved Action in Lattice Theories. 2. O(N) Nonlinear Sigma Model in Perturbation Theory." In: *Nucl. Phys.* Vol. B226 (1983), pp. 205–227. DOI: 10.1016/0550-3213(83)90469-8.

[186] Y. Iwasaki. "Renormalization Group Analysis of Lattice Theories and Improved Lattice Action. II. Four-dimensional non-Abelian SU(N) gauge model." In: (Dec. 1983). arXiv: 1111.7054 [hep-lat].

[187] L. H. Karsten and J. Smit. "Lattice Fermions: Species Doubling, Chiral Invariance, and the Triangle Anomaly." In: (Sept. 1980). Ed. by J. Julve and M. Ramón-Medrano, pp. 495–532. DOI: 10.1016/0550-3213(81)90549-6.

[188] H. B. Nielsen and M. Ninomiya. "Absence of Neutrinos on a Lattice. 1. Proof by Homotopy Theory." In: (Nov. 1980). Ed. by J. Julve and M. Ramón-Medrano. [Erratum: Nucl.Phys.B 195, 541 (1982)], pp. 533–555. DOI: 10.1016/0550-3213(82)90011-6.

[189] H. B. Nielsen and M. Ninomiya. "Absence of Neutrinos on a Lattice. 2. Intuitive Topological Proof." In: *Nucl. Phys. B* vol. 193 (1981), pp. 173–194. DOI: 10.1016/0550-3213(81)90524-1.

[190] G. P. Lepage and P. B. Mackenzie. "On the viability of lattice perturbation theory." In: *Phys. Rev.* Vol. D48 (1993), pp. 2250–2264. DOI: 10.1103/PhysRevD.48.2250. arXiv: hep-lat/9209022 [hep-lat].

[191] M. Lüscher et al. "Nonperturbative O(a) improvement of lattice QCD." In: *Nucl. Phys.* Vol. B491 (1997), pp. 323–343. DOI: 10.1016/S0550-3213(97)00080-1. arXiv: hep-lat/9609035 [hep-lat].

[192] T. Karavirta et al. "Non-perturbatively improved clover action for SU(2) gauge + fundamental and adjoint representation fermions." In: *PoS* vol. LATTICE2010 (2010). Ed. by G. Rossi, p. 064. DOI: 10.22323/1.105.0064. arXiv: 1011.1781 [hep-lat].

[193] S. Aoki, R. Frezzotti, and P. Weisz. "Computation of the improvement coefficient c(SW) to one loop with improved gluon actions." In: *Nucl. Phys. B* vol. 540 (1999), pp. 501–519. DOI: 10.1016/S0550-3213(98)00742-1. arXiv: hep-lat/9808007.

[194] J. Bulava and S. Schaefer. "Improvement of $N_f = 3$ lattice QCD with Wilson fermions and tree-level improved gauge action." In: *Nucl. Phys. B* vol. 874 (2013), pp. 188–197. DOI: 10.1016/j.nuclphysb.2013.05.019. arXiv: 1304.7093 [hep-lat].

[195] G. Immirzi and K. Yoshida. "Generalized Lattice Fermion Actions And Applications." In: *Nucl. Phys.* Vol. B210 (1982), pp. 499–512. DOI: 10.1016/0550-3213(82)90175-4.

[196] S. Catterall. "First results from simulations of supersymmetric lattices." In: *JHEP* vol. 01 (2009), p. 040. DOI: 10.1088/1126-6708/2009/01/040. arXiv: 0811.1203 [hep-lat].

[197] D. August, B. Wellegehausen, and A. Wipf. "Two-dimensional N=2 Super-Yang-Mills theory." In: (). in *Proceedings, 35th International Symposium on Lattice Field Theory (Lattice2017): Granada, Spain*, to appear in EPJ Web Conf. arXiv: 1710.01000 [hep-lat].

[198] K. Demmouche et al. "Simulation of 4d N=1 supersymmetric Yang-Mills theory with Symanzik improved gauge action and stout smearing." In: *Eur. Phys. J. C* vol. 69 (2010), pp. 147–157. DOI: 10.1140/epjc/s10052-010-1390-7. arXiv: 1003.2073 [hep-lat].

[199] S. Kuberski. "Bestimmung von Massen in der supersymmetrischen Yang-Mills-Theorie mit der Variationsmethode." Master Thesis. University Münster, 2017. URL: https://www.uni-muenster.de/imperia/md/content/physik_tp/theses/muenster/kuberski_ma.pdf.

[200] B. Berg and A. Billoire. "Glueball Spectroscopy in Four-Dimensional SU(3) Lattice Gauge Theory (I)." In: *Nucl. Phys. B* vol. 221 (1983), pp. 109–140. DOI: 10.1016/0550-3213(83)90620-X.

[201] F. Heitger. "Darstellungstheorie der kubischen Gruppe in Anwendung auf Operatoren der N=1 SUSY-Yang-Mills-Theorie auf dem Gitter." Dissertation. University Münster, 2000. URL: https://www.uni-muenster.de/Physik.TP/archive/fileadmin/Arbeiten/heitgerf.pdf.

[202] J. Wess and B. Zumino. "Supergauge Transformations in Four-Dimensions." In: *Nucl. Phys. B* vol. 70 (1974). Ed. by A. Salam and E. Sezgin, pp. 39–50. DOI: 10.1016/0550-3213(74)90355-1.

[203] I. Montvay. "Supersymmetric Yang-Mills theory on the lattice." In: *Int. J. Mod. Phys. A* vol. 17 (2002), pp. 2377–2412. DOI: 10.1142/S0217751X0201090X. arXiv: hep-lat/0112007.

[204] S. Luckmann. "Ward-Identitäten in der N = 1 Super-Yang-Mills-Theorie." Diploma Thesis. Westfälische Wilhelms-Universität Münster, 1997.

[205] R. Kirchner. "Ward Identities and Mass Spectrum of N=1 Super Yang-Mills Theory on the Lattice." Dissertation. University Hamburg, 2000.

[206] Y. Taniguchi. "One loop calculation of SUSY Ward-Takahashi identity on lattice with Wilson fermion." In: *Physical Review D* vol. 63, no. 1 (2000), p. 014502. ISSN: 0556-2821, 1089-4918. DOI: 10.1103/PhysRevD.63.014502. arXiv: hep-lat/9906026. URL: http://arxiv.org/abs/hep-lat/9906026 (visited on 03/06/2020).

[207] T. Kästner. "Supersymmetry on a space-time lattice." Dissertation. Friedrich Schiller University Jena, 2008. URL: http://www.tpi.uni-jena.de/qfphysics/homepage/wipf/abschlussarbeiten/kaestner_diss.pdf.

[208] M. Wimmer. "Algorithm 923: Efficient Numerical Computation of the Pfaffian for Dense and Banded Skew-Symmetric Matrices." In: *ACM Transactions on Mathematical Software* vol. 38, no. 4 (Aug. 2012), 1–17. ISSN: 1557-7295. DOI: 10.1145/2331130.2331138. URL: http://dx.doi.org/10.1145/2331130.2331138.

[209] R. Sommer. "A New way to set the energy scale in lattice gauge theories and its applications to the static force and alpha-s in SU(2) Yang-Mills theory." In: *Nucl. Phys. B* vol. 411 (1994), pp. 839–854. DOI: 10.1016/0550-3213(94)90473-1. arXiv: hep-lat/9310022.

[210] J. Greensite. "The Confinement problem in lattice gauge theory." In: *Prog. Part. Nucl. Phys.* Vol. 51 (2003), p. 1. DOI: 10.1016/S0146-6410(03)90012-3. arXiv: hep-lat/0301023.

[211] S. Ali et al. "The light bound states of $\mathcal{N} = 1$ supersymmetric SU(3) Yang-Mills theory on the lattice." In: *JHEP* vol. 03 (2018), p. 113. DOI: 10.1007/JHEP03(2018)113. arXiv: 1801.08062 [hep-lat].

[212] F. Farchioni and R. Peetz. "The Low-lying mass spectrum of the N=1 SU(2) SUSY Yang-Mills theory with Wilson fermions." In: *Eur. Phys. J. C* vol. 39 (2005), pp. 87–94. DOI: 10.1140/epjc/s2004-02081-2. arXiv: hep-lat/0407036.

[213] G. Bergner et al. "The gluino-glue particle and finite size effects in supersymmetric Yang-Mills theory." In: *JHEP* vol. 09 (2012), p. 108. DOI: 10.1007/JHEP09(2012)108. arXiv: 1206.2341 [hep-lat].

[214] G. Bergner et al. "Influence of topology on the scale setting." In: *Eur. Phys. J. Plus* vol. 130, no. 11 (2015), p. 229. DOI: 10.1140/epjp/i2015-15229-7. arXiv: 1411.6995 [hep-lat].

[215] H. Suzuki and Y. Taniguchi. "Two-dimensional N = (2,2) super Yang-Mills theory on the lattice via dimensional reduction." In: *JHEP* vol. 10 (2005), p. 082. DOI: 10.1088/1126-6708/2005/10/082. arXiv: hep-lat/0507019.

[216] A. A. Migdal. "Recursion Equations in Gauge Theories." In: *Sov. Phys. JETP* vol. 42 (1975). Ed. by I. Khalatnikov and V. Mineev, p. 413.

[217] N. E. Bralic. "Exact Computation of Loop Averages in Two-Dimensional Yang-Mills Theory." In: (1980). DOI: 10.1103/PhysRevD.22.3090.

[218] M. Steinhauser. "Voruntersuchungen zur Simulation von supersymmetrischen Yang-Mills-Theorien." Master Thesis. University Jena, 2016. URL: http://www.tpi.uni-jena.de/qfphysics/homepage/wipf/abschlussarbeiten/steinhauser_master_16.pdf.

[219] N. J. Evans, S. D. Hsu, and M. Schwetz. "Lattice tests of supersymmetric Yang-Mills theory?" In: (July 1997). arXiv: hep-th/9707260.

[220] G. S. Bali et al. "Direct determinations of the nucleon and pion σ terms at nearly physical quark masses." In: *Phys. Rev. D* vol. 93, no. 9 (2016), p. 094504. DOI: 10.1103/PhysRevD.93.094504. arXiv: 1603.00827 [hep-lat].

[221] S. Aoki et al. "Pseudo scalar meson masses in Wilson chiral perturbation theory for 2+1 flavors." In: *Phys. Rev. D* vol. 73 (2006), p. 014511. DOI: 10.1103/PhysRevD.73.014511. arXiv: hep-lat/0509049.

[222] F. Farchioni et al. "Hadron masses in QCD with one quark flavour." In: *Eur. Phys. J. C* vol. 52 (2007), pp. 305–314. DOI: 10.1140/epjc/s10052-007-0394-4. arXiv: 0706.1131 [hep-lat].

[223] J. Giedt. "Progress in four-dimensional lattice supersymmetry." In: *Int. J. Mod. Phys. A* vol. 24 (2009), pp. 4045–4095. DOI: 10.1142/S0217751X09045492. arXiv: 0903.2443 [hep-lat].

[224] M. Costa and H. Panagopoulos. "Supersymmetric QCD on the Lattice: An Exploratory Study." In: *Phys. Rev. D* vol. 96, no. 3 (2017), p. 034507. DOI: 10.1103/PhysRevD.96.034507. arXiv: 1706.05222 [hep-lat].

[225] B. Wellegehausen and A. Wipf. "$\mathcal{N} = 1$ Supersymmetric $SU(3)$ Gauge Theory - Towards simulations of Super-QCD." In: *PoS* vol. LATTICE2018 (2018), p. 210. DOI: 10.22323/1.334.0210. arXiv: 1811.01784 [hep-lat].

[226] G. Bergner and S. Piemonte. "Supersymmetric and conformal theories on the lattice: from super Yang-Mills towards super QCD." In: *PoS* vol. LATTICE2018 (2019), p. 209. DOI: 10.22323/1.334.0209. arXiv: 1811.01797 [hep-lat].

[227] M. Costa and H. Panagopoulos. "Supersymmetric QCD: Renormalization and Mixing of Composite Operators." In: *Phys. Rev. D* vol. 99, no. 7 (2019), p. 074512. DOI: 10.1103/PhysRevD.99.074512. arXiv: 1812.06770 [hep-lat].

[228] G. Bergner and S. Piemonte. "Lattice simulations of a gauge theory with mixed adjoint-fundamental matter." In: (Aug. 2020). arXiv: 2008.02855 [hep-lat].

[229] G. Aad et al. "Search for chargino-neutralino production with mass splittings near the electroweak scale in three-lepton final states in $\sqrt{s}$=13 TeV pp collisions with the ATLAS detector." In: *Phys. Rev. D* vol. 101, no. 7 (2020), p. 072001. DOI: 10.1103/PhysRevD.101.072001. arXiv: 1912.08479 [hep-ex].

[230] G. Aad et al. "Searches for electroweak production of supersymmetric particles with compressed mass spectra in $\sqrt{s} = 13$ TeV pp collisions with the ATLAS detector." In: *Phys. Rev. D* vol. 101, no. 5 (2020), p. 052005. DOI: 10.1103/PhysRevD.101.052005. arXiv: 1911.12606 [hep-ex].

[231] G. Aad et al. "Search for direct stau production in events with two hadronic τ-leptons in $\sqrt{s} = 13$ TeV pp collisions with the ATLAS detector." In: *Phys. Rev. D* vol. 101, no. 3 (2020), p. 032009. DOI: 10.1103/PhysRevD.101.032009. arXiv: 1911.06660 [hep-ex].

[232] A. M. Sirunyan et al. "Search for supersymmetry in proton-proton collisions at $\sqrt{s} = 13$ TeV in events with high-momentum Z bosons and missing transverse momentum." In: *JHEP* vol. 09 (2020), p. 149. DOI: 10.1007/JHEP09(2020)149. arXiv: 2008.04422 [hep-ex].

[233] A. M. Sirunyan et al. "Search for supersymmetry using Higgs boson to diphoton decays at $\sqrt{s} = 13$ TeV." In: *JHEP* vol. 11 (2019), p. 109. DOI: 10.1007/JHEP11(2019)109. arXiv: 1908.08500 [hep-ex].

[234] A. M. Sirunyan et al. "Combined search for supersymmetry with photons in proton-proton collisions at $\sqrt{s} = 13$ TeV." In: *Phys. Lett. B* vol. 801 (2020), p. 135183. DOI: 10.1016/j.physletb.2019.135183. arXiv: 1907.00857 [hep-ex].

[235] S. Piemonte. "N=1 supersymmetric Yang-Mills theory on the lattice." Dissertation. University Münster, 2015.

[236] M. Fierz. "Zur Fermischen Theorie des β-Zerfalls." In: *Zeitschrift für Physik* vol. 104 (1937), pp. 553–565. DOI: 10.1007/BF01330070.

[237] P. B. Pal. "Representation-independent manipulations with Dirac spinors." In: (Mar. 2007). arXiv: physics/0703214.

[238] S. Weinberg. *The quantum theory of fields. Vol. 2: Modern applications*. Cambridge University Press, Aug. 2013. ISBN: 978-1-139-63247-8, 978-0-521-67054-8, 978-0-521-55002-4.

[239] G. Kilcup and S. R. Sharpe, eds. *Phenomenology and lattice QCD. Proceedings: Uehling Summer School, Seattle, USA, Jun 21-Jul 2, 1993*. 1995.

[240] E. V. Shuryak. *The QCD vacuum, hadrons and the superdense matter*. Vol. 71. World Scientific, Oct. 2004. DOI: 10.1142/5367.

[241] D. Weingarten. "Mass Inequalities for QCD." In: *Phys. Rev. Lett.* Vol. 51 (1983), p. 1830. DOI: 10.1103/PhysRevLett.51.1830.

[242] M. H. Quenouille. "Notes on Bias in Estimation." In: *Biometrika* vol. 43, no. 3/4 (1956), pp. 353–360. ISSN: 00063444. URL: http://www.jstor.org/stable/2332914.

[243] J. W. Tukey. "Abstracts of Papers." In: *Ann. Math. Statist.* Vol. 29, no. 2 (June 1958), pp. 614–623. DOI: 10.1214/aoms/1177706647. URL: https://doi.org/10.1214/aoms/1177706647.

[244] Z. Bai. "Neutral Kaon Mixing from Lattice QCD." Dissertation. Columbia University, 2018. URL: https://s3.cern.ch/inspire-prod-files-2/208ac613b20b9c7bb845b05c76e26351.

[245] G. M. Amdahl. "Validity of the Single Processor Approach to Achieving Large Scale Computing Capabilities." In: *Proceedings of the April 18-20, 1967, Spring Joint Computer Conference*. AFIPS '67 (Spring). New York, NY, USA: Association for Computing Machinery, 1967, 483–485. ISBN: 9781450378956. DOI: 10.1145/1465482.1465560. URL: https://doi.org/10.1145/1465482.1465560.

[246] M. Helsø. "Template for master's theses written at the Department of Geosciences at the University of Oslo." In: *overleaf* (2019). URL: https://de.overleaf.com/latex/templates/geoscience-masters-thesis/rdwnkmgfkjnx.

Danksagung

Mein größter Dank gilt meinem Betreuer Prof. Wipf, von dem ich während meiner Promotionszeit viel gelernt habe und gut unterstützt wurde. Fachlich und persönlich habe ich mich bei ihm stets wohlgefühlt. Auch mit André, der für mich so etwas wie ein zweiter Betreuer war, habe ich immer gerne zusammengearbeitet. Ohne ihn hätte ich viele IT-Probleme und algorithmische Konzepte nicht so gut verstanden oder mir daran die Zähne ausgebissen. Am nächsten dran an meinen alltäglichen Problemen der Physik und Simulation war Björn. Vielen Dank für die vielen lehrreichen Antworten und insbesondere für den "Gauge Theory Simulator" als numerische Grundlage für meine komplette Forschung. Bei Georg bedanke ich mich für nützliche Hinweise und insbesondere für den Beweis in Appendix E, dass ohne Twist das Pion das leichteste Meson auf dem Gitter sein muss.

Für die konstruktive Arbeitsatmosphäre und vielzähligen Diskussionen möchte ich mich bei meinen ehemaligen Bürokollegen Daniel & Daniel und bei meinen derzeitigen Bürokollegen Julian und Michael bedanken. Als Korrekturleser waren mir Björn, Julian und Michael eine große Hilfe. Um keinen zu vergessen gilt mein Dank auch dem ganzen TPI mit seinen offenen Türen und dem gut strukturiertem Institutsleben.

Auch für die Finanzierung meiner Landesstelle und die Vorteile beider DFG-Graduiertenkollegs GRK1523/2 und RTG2522/1 bin ich dankbar. Dadurch waren mir diverse Teilnahmen an Konferenzen, Workshops und Vorträgen möglich. An dieser Stelle vielen Dank, Camilo, für die gemeinsamen Dienstreisen und den Austausch über die $\mathcal{N} = 1$ SYM -Theorie.

Darüber hinaus möchte ich mich bei allen Rechen-Ressourcen bedanken. Insbesondere beim Leibniz-Rechenzentrum (LRZ, www.lrz.de) für die Bereitstellung der Rechenzeit im Rahmen des Projekts pr48ji. Der Super-MUC ist ein super Partner für die Supersymmetrie-Simulation. Ebenfalls habe ich Rechenkapazitäten der Universität Jena auf den Clustern Ara und Omega sowie auf den Rechenservern des TPIs genutzt.

Zuletzt möchte ich noch die Code-Bibliotheken DDαAMG [159] und Pfapack [208] sowie dieses LaTeX-Template [246] dankend erwähnen, auf die ich mich stützen konnte.

Publications & proceedings

- M. Steinhauser, A. Sternbeck, B. Wellegehausen, A. Wipf. $\mathcal{N} = 1$ *Super-Yang-Mills theory on the lattice with twisted mass fermions.* J. High Energ. Phys. 2021, 154, https://arxiv.org/abs/2010.00946
- M. Steinhauser, A. Sternbeck, B. Wellegehausen, A. Wipf. $\mathcal{N} = 1$ *Supersymmetric SU(3) Gauge Theory with a Twist.* PoS LATTICE2019, 201, https://arxiv.org/abs/1912.09979
- D. August, M. Steinhauser, B. Wellegehausen, A. Wipf. *Mass spectrum of* 2*-dimensional* $\mathcal{N} = (2, 2)$ *super Yang-Mills theory on the lattice.* JHEP 2019 01, 99, https://arxiv.org/abs/1802.07797v2
- M. Steinhauser, A. Sternbeck, B. Wellegehausen, A. Wipf. $\mathcal{N} = 1$ *Supersymmetric* $SU(3)$ *Gauge Theory – Pure Gauge sector with a twist.* PoS LATTICE2018, 211, https://arxiv.org/abs/1811.01785
- M. Steinhauser, A. Sternbeck, B. Wellegehausen, A. Wipf. *Spectroscopy of four-dimensional* $\mathcal{N} = 1$ *supersymmetric SU(3) Yang-Mills theory.* EPJ Web Conf. 2018, 175, 8022, https://arxiv.org/abs/1711.05086

Ehrenwörtliche Erklärung

Ich erkläre hiermit ehrenwörtlich, dass ich die vorliegende Arbeit selbstständig, ohne unzulässige Hilfe Dritter und ohne Benutzung anderer als der angegebenen Hilfsmittel und Literatur angefertigt habe. Die aus anderen Quellen direkt oder indirekt übernommenen Daten und Konzepte sind unter Angabe der Quelle gekennzeichnet.

Bei der Auswahl und Auswertung folgenden Materials haben mir die nachstehend aufgeführten Personen in der jeweils beschriebenen Weise unentgeltlich geholfen:

- Andreas Wipf, Betreuung der Arbeit über die gesamte Dauer der Promotion als betreuender Hochschullehrer und Unterstützung insbesondere bei den analytischen Rechnungen.
- Björn Wellegehausen, enge Kooperation über die gesamte Dauer der Promotion, insbesondere Bereitstellung des Code-Frameworks und Hilfe bei der Software-Entwicklung sowie numerischen Simulation.
- André Sternbeck, Kooperation über die gesamte Dauer der Promotion und Beratung bei numerischen Problemen und der Datenauswertung.
- Daniel August, hat die $\mathcal{N} = (2, 2)$ Simulationen durchgeführt.

Weitere Personen waren an der inhaltlich-materiellen Erstellung der vorliegenden Arbeit nicht beteiligt. Insbesondere habe ich hierfür nicht die entgeltliche Hilfe von Vermittlungs- bzw. Beratungsdiensten (Promotionsberater oder andere Personen) in Anspruch genommen. Niemand hat von mir unmittelbar oder mittelbar geldwerte Leistungen für Arbeiten erhalten, die im Zusammenhang mit dem Inhalt der vorgelegten Dissertation stehen.

Die Arbeit wurde bisher weder im In- noch im Ausland in gleicher oder ähnlicher Form einer anderen Prüfungsbehörde vorgelegt. Die geltende Promotionsordnung der Physikalisch-Astronomischen Fakultät ist mir bekannt.

Ich versichere ehrenwörtlich, dass ich nach bestem Wissen die reine Wahrheit gesagt und nichts verschwiegen habe.

Ort, Datum Unterschrift des Verfassers